Scale model seismicity: A detailed study of deformation localisation from laboratory acoustic emission data

Caroline C. Graham

BSc. (Hons) Geophysics (Edinburgh) 2004
MRes. Physics of the Earth and Atmosphere 2005

Thesis submitted for the degree of
Doctor of Philosophy

University of Edinburgh
2010

Abstract

Acoustic emissions (AE) can provide information relating to the internal state of a deforming rock sample during laboratory testing and have been utilised to quantify damage progression for time-dependent failure modeling. However, the underlying physical mechanisms that produce AE in different materials and their evolution during the process of damage localisation are not fully understood, particularly in porous media. In order to investigate the sources of laboratory acoustic emissions, a moment tensor inversion was applied to data from triaxial compression experiments on Aue granite and Clashach sandstone. The moment tensor inversion was verified for granite, by comparison with results obtained using a more simplistic source analysis technique. In the non-porous Aue granite, AE sources exhibited a predominantly tensile behaviour in the early stages of AE activity. However, shear sources become dominant in the vicinity of the peak stress. In contrast, during deformation of the Clashach sandstone, which has a significant pre-existing porosity, AE sources are dominated by a collapse signature and generally involve a notable shear component. AE that have a predominantly shear mechanism are also a major contributor to the microscale deformation imaged by the technique, and dominate during shear localisation. A combination of correlation analysis and source analysis was used to elucidate the temporal and spatial evolution of the AE source mechanisms involved in the localisation process, as well as during a temporary hiatus in the progression to failure. The results support the concept that the cascade to failure requires the simultaneous involvement of a range of micromechanical behaviours to maintain the progression of localised damage, and eventual formation of a fault. Localisation of collapse mechanisms was not observed until the final approach to failure.

Finally, AE sources produced during brittle deformation of the Clashach sandstone were characterised in detail and compared to microstructural observations representing the integrated effect of all times up to the end of the test, and including smaller structures that may have been formed insufficiently dynamically to produce AE. Equivalent focal mechanisms for these events are presented and the relative proportions of their volumetric and shear components considered. The results indicate that AE sources display a wide spectrum of micromechanical behaviour that is consistent with microstructural observations, indicating that AE mechanisms are representative of ongoing deformation processes within the sandstone. It is argued that moment tensor inversion of acoustic emissions is a powerful tool for elucidating the micromechanical evolution of damage, during the brittle deformation of rock.

Declaration

I declare that this thesis has been composed solely by myself and that it has not been submitted, either in whole or in part, in any previous application for a degree. Except where otherwise acknowledged, the work presented is entirely my own.

Caroline C. Graham
June 2010

Acknowledgements

Firstly, I would like to thank my supervisors for their assistance during the course of this project. Ian Main's enthusiastic discussion, guidance and speedy return of chapters is much appreciated. This project would not have been possible without the involvement of the GFZ and, as such, the support of Georg Dresen and the Deformation and Rheology group has been invaluable. Thanks also to Steve Elphick, who introduced me to the world of experimental rock mechanics. Mike Forde's support in the School of Engineering is appreciated, as was the opportunity to explore the application of acoustic emissions to masonry. The kind provision of their SiGMA source code by Mitsuhiro Shigeishi and Masayasu Ohtsu is much appreciated. This project was funded by the Natural Environment Research Council (NER/S/A/2005/13745).

In addition, thanks are due to Sergei Stanchits, who has provided assistance, guidance and an enthusiastic ear over the course of this project. Thanks also to Jerome Fortin, for helpful discussions during a coincident visit to the GFZ and to Stephan Gehrman for fantastic thin section preparation skills, as well putting up with my terrible German! Back in Edinburgh, the support of Ian Butler and Bryne Ngwenya is much appreciated, as are the technical skills and assistance of Mike Hall, Nicola Cayzer, John Craven and Alex Jackson. Also, the members of the Earthquake Physics Group have provided much fruitful discussion and debate; Mark Naylor, Andy Bell, Jon Greenhough, Sarah Touati, Yusuke Kawada and (in an honorary capacity) John McCloskey. I would also like to thank Moray Stone Cutters who very kindly provided me with a sizeable quantity of the Clashach sandstone and even arranged for its delivery to the Central Belt.

On a more personal note I would like to thank my flatmates Jen and Lou for feeding me copious amounts of food and Dan for generally being tall. In Germany, Agathe's friendship and translation skills were much appreciated. In Edinburgh, Ciaran Beggan has not only been a fantastic alcove buddy, but also helped me move more times than can ever be reasonably expected! Also, thanks to all my friends in the Grant Institute for much fun and support over the past few years, including in roughly chronological order; Alex, Tim I., Sarah B., Sarah A., Clare B, Jon, Dave, Janette, Andy B., Pete, Zana, Natasha, Emma P., Steve, Rich, Hannah, Natalie, David, Isabel, Adam, Mikael, Emma Mac., Ruth, Tanya, Tom, Amber, Gijs, Matt U., Rhian, Margaret, Simon, Luke, Andrew M., JJ, Nick, Janet, Martin, Matt H., Sian and Skippy. As well as many, very entertaining undergraduates. The kind proof-reading of my chapters by a number of people is also greatly appreciated. Many members of staff also deserve thanks including Heather Hooker, Helena Sim, Roger Scrutton, Andrew Curtis and Barry Dawson. Outside of the university, I would like to thank my friends for being patient during periods of poor correspondence and, in particular my parents and Victoria and Graeme, for all their support and understanding. Thanks also to the t-mail ladies at Keyworth. Finally, many thanks are due to the British Geological Survey who have been incredibly supportive during the final stages of my write-up, particularly the TPRL lab members who have provided both time and advice.

Contents

List of figures

List of tables

Chapter 1

Introduction

Brittle fracture occurs in the Earth's crust on a wide range of length scales; from the microscopic to the tectonic. The resulting fracture networks are intrinsically related to the distribution of stress and strongly influence energy transfer within the crust. They are of interest in the field of geoscience for three primary reasons; i.) on the largest scale they are a major mechanism for strain accommodation within the planet's lithosphere, ii.) the release of energy, by movement along these fractures, can be disruptive, whether a high-magnitude earthquake, or a rock burst in an active mine, iii.) they often provide efficient pathways for fluid migration, including water and hydrocarbons, and can drastically affect both the rate and spatial distribution of such fluid flow.

One approach to studying the phenomenon of brittle failure in geological media is to conduct rock deformation experiments, simulating conditions in the Earth's crust. Such laboratory tests can provide detailed information, using a range of techniques, about both the whole-rock and microscopic behaviour that leads to the formation of a fault. Perhaps, most importantly, rock mechanics tests provide us with an opportunity to study the behaviour of rock under *controlled* and *pre-selected* conditions; generally unknown or uncertain quantities in the real earth.

The primary emphasis in this study is on the use of 'acoustic emissions' (AE) for determining information about damage progression in rock deformation tests. AE are high-frequency pressure disturbances that may be recorded in real-time during laboratory experiments. They are thought to be produced by the release of energy during microcracking within the material (*Scholz*, 1968a; *Ohnaka and Mogi*, 1982) and, therefore, can provide us with an abundance of information about the internal state of a loaded specimen. Modern AE data sets can contain tens of thousands of events from just one experiment and are generally detailed enough to be considered comparable to an earthquake catalogue in a tectonic region; providing a rich and detailed source of data relating to inelastic deformation on a microscopic scale.

When a rock sample is loaded in compression, and under confinement, its macroscopic rheology is dependent on a number of controlling environmental factors, including temperature, strain-rate, confining pressure and pore-fluid pressure (discussed in further detail in section 2.2). Given the correct conditions, for brittle behaviour, deformation may become spatially concentrated, or 'localised', in a planar or sub-planar arrangement with the potential to form a fault. This thesis is focused on the evolution of microscopic damage in the *brittle* field, from its onset, through localisation to the eventual failure of the material.

In a *compact* rock experiencing compression, the stress-strain behaviour of the material can be separated into a number of stages leading up to the formation of a macroscopic fracture or fault (*Brace et al.*, 1966; *Paterson and Wong*, 2005):

I. A period of rapid strain-hardening, due to the closure of pre-existing fractures. This effect is more commonly observed in unconfined samples, as the application of a confining pressure can lead to the earlier closure of any pre-existing microcracks. There may also be some collapse of pore-spaces in samples with a small porosity.

II. A phase of apparent linear elasticity, due predominantly to the reversible deformation of grains. However, there may also be a degree of irreversible deformation occurring at this time, indicated by the observation of hysteresis on re-loading the sample (*Cook and Hodgson*, 1965).

III. Significant inelastic deformation starts to occur. Microfracturing begins, observable from microstructural analysis and variations in P-wave velocity, leading to dilatancy. There is also an increase in the level of acoustic emission activity.

IV. Localisation of microfracturing leads to unstable growth and the eventual development of a macroscopic fracture.

The corresponding evolution of various physical properties during these four stages of compressive loading of a compact rock is illustrated in Figure 1.1. Similar behaviour is also observed in porous rock, such as sandstone, but the approach to failure differs in a number of ways. In particular, the permeability of the sample may in fact *decrease* during the dilatancy phase. Moreover, microstructural studies indicate that

microfracturing is not as pervasive as in a compact rock. Instead, dilatancy arises primarily from the movement of grains, enabled by the rupturing of the contacts between them.

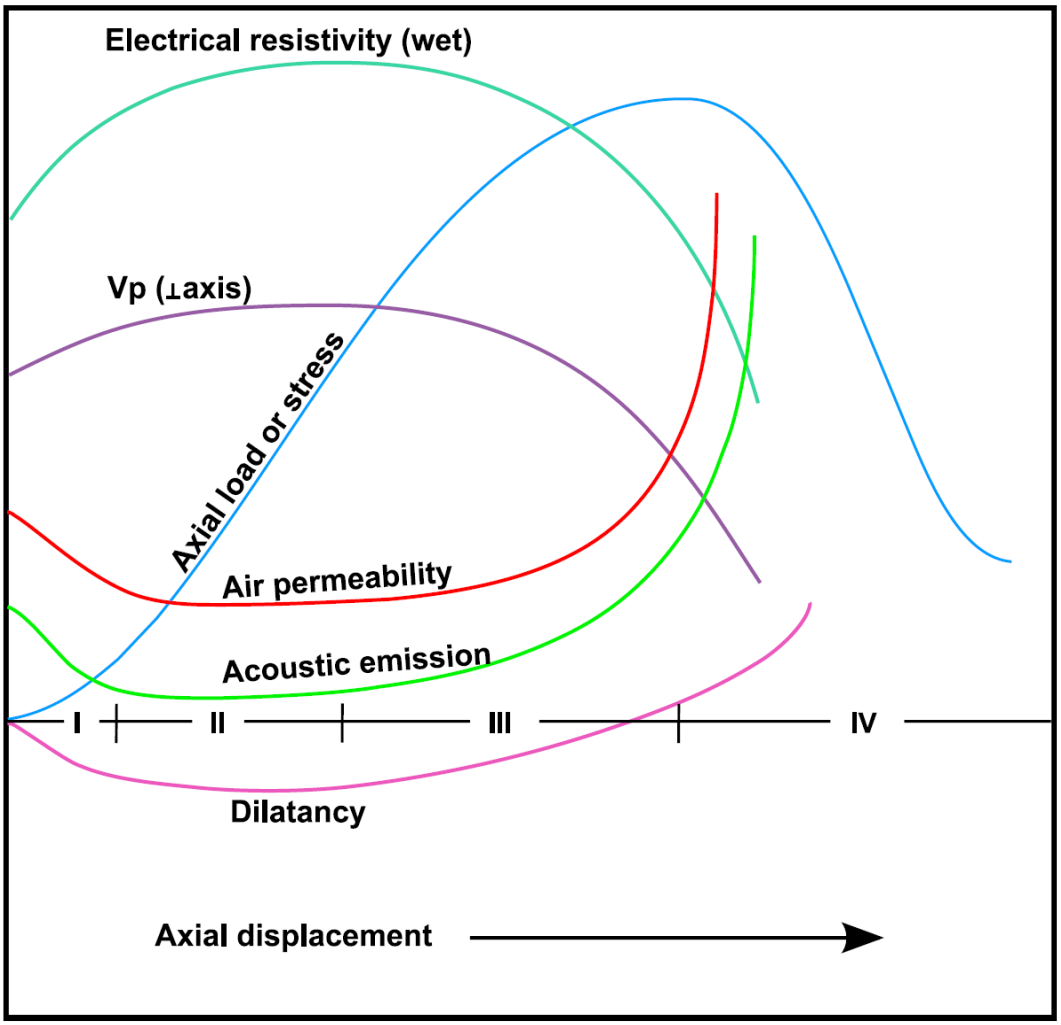

Figure 1.1. The generalised evolution of various physical parameters during the compressive loading of compact rock (after Paterson and Wong, 2005). The material behaviour is divided into four main stages: I-IV.

In this thesis, the data discussed comes from experiments conducted on: i.) a compact rock with no significant pre-existing porosity, in this case the Aue granite from Germany, and ii.) a low-porosity sandstone at low effective pressure, from the Clashach quarry in Scotland. Recent work mentioned in the discussion chapter (section 6.7) and presented in the appendix, is from experiments conducted on the high-porosity Bleurswiller sandstone, at a range of moderate to high effective pressures. These materials were chosen as controls to allow comparison of the micromechanical evolution of damage, up to and during localisation, in porous and non-porous media. All three materials are used regularly in rock mechanics testing, due to their relatively homogeneous nature.

1.1 Thesis rationale

One approach to modelling the brittle failure of rock is the application of continuum damage mechanics (*Kachanov*, 1986). This method defines an internal state variable, relating to the irreversible weakening experienced by a material as it deforms. A suitable analogy for this approach is the development of the 'ideal gas law'. In this experiment we consider a box filled with gas molecules. In order to describe the behaviour of the system using Newtonian mechanics, detailed information about the state of each individual gas molecule is required, and each collision between molecules must be anticipated and accounted for. However, the complexity of this system as a whole can be simplified by considering its collective behaviour at a larger scale, where

strong averaging produces remarkably consistent behaviour. Macroscopic parameters can then be assigned, which describe the 'average' state of the gas inside the box at any given time; pressure and temperature.

In the case of the brittle deformation of rock, rather than modelling the propagation and interaction of each individual microcrack, the continuum damage mechanics approach is used to describe the internal state of the material using a parameter that reflects the degree of permanent, irreversible 'damage' it has experienced. This parameter is usually related to some micromechanical property, such as the average density of microfractures in the rock at any given time. In general, as the rock becomes increasingly damaged on a microscopic scale, the weaker it will become on a macroscopic scale, until it finally fails.

There are a number of different techniques that can be used to estimate damage within a laboratory rock sample, including microstructural analysis and monitoring of changes in ultrasonic velocity. These are discussed in greater detail in section 2.3. In particular, several techniques have been developed to extract a damage parameter from acoustic emission catalogues, which can then be used to reconstruct the stress-strain history of a rock from initial loading through to sample failure (*Cox and Meredith*, 1993). The predicted results are very similar to experimental observations, particularly in the initial to intermediate stages of loading. However, there is also a consistent over-estimation of the peak stress (*Cox and Meredith*, 1993; *Ojala et al*., 2003; *Ojala*, 2003). One possible explanation is that AE damage parameters do not account for the total amount of

damage during the final stages of loading, either due to incompleteness in the AE record or aseismic microfracturing. However, *Ojala et al*. (2003) argue that it is most likely an effect of the localisation process; in the region of damage coalescence a sample will be much closer to failure than in the surrounding rock. An isotropic damage parameter will, therefore, overestimate the sample's strength before failure.

It has been proposed that this problem may be overcome by the application of a tensorial measure of damage (*Bažant*, 1986, *Ju*, 1990; *Shah and Labuz*, 1995), which accounts for the orientation and mechanism of each individual acoustic emission. Describing an earthquake mechanism in such terms is a standard technique in seismology, further details of which are given in section 2.3.4.3. Summation of earthquake mechanisms on a regional scale has been effectively used to estimate the inelastic strains experienced by tectonic plates (*Jackson and McKenzie*, 1988). However, the mechanisms that produce acoustic emissions are still not understood as sufficiently well as for earthquakes. To date, laboratory studies of composite materials investigating AE mechanisms have focused primarily on compact rocks in the geosciences, such as granite, or concrete and masonry in civil engineering. Such studies rarely involve a full tensorial description of the AE source mechanisms. It is the nature of these damage mechanisms, and the resulting implications for damage mechanics modelling with acoustic emission data, which are the primary focus of this thesis. Particular focus is on the damage evolution process in sandstone, with a pre-existing porosity, in comparison to the behaviour of non-porous granite.

The aims of this study are three-fold:

i.) To validate the application of a moment tensor inversion technique to acoustic emission data, and to utilise this approach to characterise source evolution in a compact rock.

ii.) To use moment tensor inversion to investigate damage evolution in a porous rock, in this case sandstone, with particular focus on the role of different micromechanical mechanisms during the localisation process (Stage IV).

iii.) To characterise the microscale mechanisms that produce acoustic emissions during the brittle failure of sandstone, and to relate them to physical mechanisms and microscopic observations.

1.2 Thesis structure

The core of this thesis has been written in the form of three papers. Chapter 2 contains background theory, relevant to these papers. The third chapter then closely follows the format of a technical note that has recently been published (*Graham et al*., 2010) and compares two methods for analysing source mechanisms. Here, the methodology for obtaining information about microfracturing mechanisms, from acoustic emission data, is outlined and the results validated with a simpler, but more established technique. This

chapter also demonstrates the 'ideal' evolution of damage in a crystalline rock (Aue granite) with effectively no initial porosity or pre-existing fracture network; from diffuse microfracturing, through to localised damage, shear band formation and eventual failure.

Chapter 4 is written in the style of a Tectonophysics paper, which will shortly be submitted for review. This chapter is also concerned with shear localisation, but is complicated by the addition of porosity to the material; in this case, the Clashach sandstone. Damage is characterised using the moment tensor inversion approach and the role of different source types within the localisation process are investigated. The final results chapter (chapter 5) is written as a short paper for the Journal of Structural Geology and focuses on characterising the physical mechanisms responsible for acoustic emissions and comparing AE focal mechanisms with microstructural observations.

As publication styles vary between different journals, each of the results chapters ends with a section summarising findings, rather than beginning with an abstract. The sixth chapter is written as a discussion, which draws together the results of chapters 3-5 and returns to the initial aims of the thesis. More recent work concerning source characterisation of AE from laboratory tests involving compaction localisation in sandstone at higher effective pressures is also discussed. Additionally, outstanding questions and possible directions for future work are highlighted. The primary conclusions of this study are then summarised in chapter 7.

This was a collaborative project between the University of Edinburgh and the GFZ German Research Centre for Geosciences (Potsdam, Germany), during the course of which I have spent a total of approximately four months in Potsdam. The Clashach sandstone experiment described in chapters 4 and 5 was conducted by me, with the assistance of Dr. Sergei Stanchits, at the GFZ. All other data is from tests conducted in, and kindly provided by, the Deformation and Rheology laboratory at the GFZ, as was Figure 3.4. The AE hypocentre location procedure was carried out by Dr. Sergei Stanchits. The automated moment tensor inversion procedure was developed by adapting source code that was kindly provided by Mitsuhiro Shigeishi (Department of Civil and Environmental Engineering, Kumamoto University, Japan). I have also spent 3 months carrying out an internship in the Exploration and Mining Group at the Commonwealth Scientific and Industrial Research Organisation (CSIRO), in Perth, Australia. The work I was involved in there was concerned with Discrete Element Modelling (DEM) of shear localisation in sandstone, with the eventual aim of simulating acoustic emissions, and I may draw some of my ideas in this thesis from my time spent there.

Chapter 2

Background theory

2.1 Introduction

This background chapter is split into two main sections. The first deals with the theory of macroscopic rock failure, before going on to discuss fracture in the laboratory and the phenomenon of damage localisation. The second section concerns the monitoring of damage evolution in the laboratory by observing variations in certain physical parameters. In particular, the emphasis is on the phenomenon of acoustic emission, which is the primary focus of this thesis. As such, a significant part of this second section also involves the seismological theory that underpins the source analysis of acoustic emissions.

2.2 Mechanics of faulting

This section describes the background theory around the mechanics of failure on the macroscopic scale, followed by discussing brittle fracture on the laboratory scale in rock deformation experiments.

2.2.1 Stress and strain

Lithostatic and hydrostatic forces are capable of generating significant differential and effective stresses in the Earth's crust, onto which tectonic forces may in turn be superimposed. Rocks subjected to these forces may deform as a result. However, the nature of such deformation can vary greatly, depending upon a number of physical and chemical conditions. In order to study this process, it therefore becomes necessary to quantify both the forces applied to, and the resulting deformation of, the material by introducing the concepts of *stress* and *strain*. If we consider a cube of rock (Figure 2.1), subjected to external forces acting upon its faces, the stress exerted upon each face may be defined as the force per unit area applied to that face. Any force applied to a face of the cube may be expressed as the combination of a normal stress, acting orthogonally to the face, and a shear stress, acting parallel to the face (*Hobbs et al*., 1976). It therefore follows that we can fully describe the stress, $\boldsymbol{\sigma}$, experienced by the cube as a tensor, consisting of nine stress components, such that:

$$\underline{\sigma} = \begin{pmatrix} \sigma_{11} & \sigma_{21} & \sigma_{31} \\ \sigma_{12} & \sigma_{22} & \sigma_{32} \\ \sigma_{13} & \sigma_{23} & \sigma_{33} \end{pmatrix} \tag{2.1}$$

Those elements on the diagonal of the tensor represent normal stresses, whilst the remaining six elements represent shear stresses. Conservation of angular momentum

requires that the tensor must be symmetric, such that the summation of all moments involved is zero. As a result, the *stress tensor* involves only six unique components (*Anderson*, 1942). Diagonalisation of the stress tensor allows a further reduction, such that only its three eigenvalues, σ_1, σ_2, σ_3, are sufficient to describe the stress state of the material:

$$\underline{\sigma} = \begin{pmatrix} \sigma_1 & 0 & 0 \\ 0 & \sigma_2 & 0 \\ 0 & 0 & \sigma_3 \end{pmatrix} \tag{2.2}$$

The diagonal elements, σ_1, σ_2, σ_3, are called the *principal stresses* and are conventionally described in geology as the *maximum*, *intermediate* and *minimum* principal stresses, respectively (*Hobbs et al*., 1976). They are all, by definition, orthogonal to one another. A further useful term is the *differential stress*, which is defined as the difference between the *maximum* and *minimum* principal stresses (σ_1-σ_3).

Once a system for describing the forces *exerted* upon a rock has been defined, it then becomes necessary to prescribe a similar approach to deal with the *response* of the rock to such forces. Consequently, *strain* is defined as the change in length of the rock, normalised by its initial length:

$$\varepsilon = \frac{\Delta l}{l_0} \tag{2.3}$$

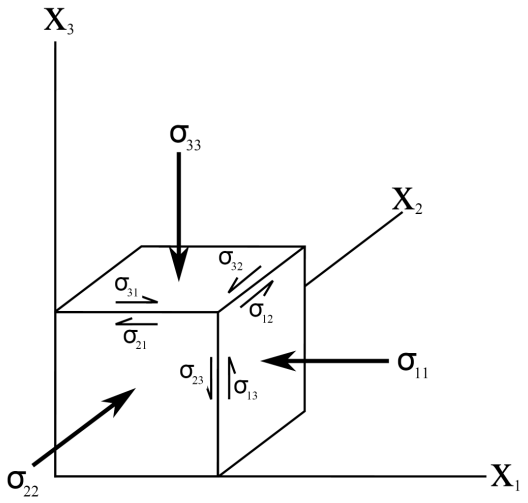

Figure 2.1. Stress acting on an infinitesimal cube in three-dimensional Cartesian space, after Hobbs, et al. (1976).

Alternatively, the *volumetric* strain can be found from the change in volume, Δv, normalized with respect to the initial volume of the rock, v_o;

$$\varepsilon = \frac{\Delta v}{v_0} \tag{2.4}$$

Alternatively, if the deformation of an elemental cubic volume is considered for each elemental face in three dimensions, it is then possible to describe the response of a rock to external stresses by way of the *strain tensor* (*Hobbs et al*., 1976):

$$\underline{\varepsilon} = \begin{pmatrix} \varepsilon_{11} & \varepsilon_{21} & \varepsilon_{31} \\ \varepsilon_{12} & \varepsilon_{22} & \varepsilon_{32} \\ \varepsilon_{13} & \varepsilon_{23} & \varepsilon_{33} \end{pmatrix} \tag{2.5}$$

Now the response of a rock to an applied stress may be described in terms of the relationship between $\boldsymbol{\sigma}$ and $\boldsymbol{\varepsilon}$. If we initially consider deformation in only one direction, for an isotropic material responding in a purely linear elastic fashion, this relationship is known as '*Hooke's Law*':

$$\sigma = E\varepsilon \tag{2.6}$$

In this instance, the relationship is linear and dependent upon the material property, $\boldsymbol{E}$, known as the Young's modulus of elasticity. If we then consider the deformation of an elemental cube in terms of the stress and strain tensors, *Hooke's Law* is then expressed as;

$$\underline{\sigma} = \underline{E}\underline{\varepsilon} \tag{2.7}$$

where, $\underline{E}$ is a fourth order tensor. Such elastic behaviour is characterised by the material's ability to return to its original state, once the applied load is removed. All associated deformation is instantaneous and reversible.

2.2.2 Mode of deformation and macroscopic failure

The mode of deformation by which a rock, subjected to sufficient differential stress, may fail is dependent upon a number of conditions including temperature, strain rate, confining pressure and pore fluid pressure (discussed in further detail in section 2.2.3.2). Macroscopic failure may be by *brittle* fracture (along a zone of localised deformation) or *ductile* (involving the continuous delocalised, *plastic* flow of the rock). An idealised definition of failure by brittle fracture is that it occurs with no significant permanent deformation beforehand (Fig. 2.2), although the reality is that some inelastic damage is often observed prior to failure in the laboratory (*Paterson and Wong*, 2005). Brittle failure is also expected to result in a significant stress drop.

In contrast, *ideal ductile* failure is irreversible and results in constant stress, post-yield. However, in practice laboratory experiments may result in either an increase (strain-hardening) or a decrease (strain-softening) in stress. In general, low pressures and temperatures favour brittle deformation, whilst high pressures and temperatures favour ductile deformation, though the nature of the brittle-ductile transition is, in reality, dependent on a range of environmental and material parameters. It should also be noted that macroscopic *irreversible* flow may also occur as the result of *brittle* fracture during cataclastic flow (Fig. 2.7).

The focus of this thesis is on the *brittle* fracture of rock and, in particular, those microscopic processes that lead up to and are involved in the localisation of damage on the macroscopic scale. This subject is discussed in more detail in section 2.2.3.3 of this chapter. However, it is helpful to first place the problem of rock fracture into its macroscopic context. Within the brittle field it is possible to predict the strength of a rock and hence, the likelihood of its failure under a given loading condition, by utilising the *'Coulomb-Navier' macroscopic failure criterion*. This empirical construction requires no information about the microscopic state of the material and can be visually represented by the construction of the '*Mohr Circle*' (Fig. 2.3) and an empirically derived failure envelope (*Jaeger and Cook*, 2007). On a graph of shear stress, τ, as a function of normal stress, σ_n, Mohr's circle can be used to geometrically describe the stress state of a rock, based on the values of the minimum and maximum principal stresses. Whilst not strictly linear, a failure envelope for the rock may then generally be reasonably represented by a straight line, dependent upon the empirically derived coefficient of internal friction, μ, and the material's cohesion, τ_0, such that;

$$\tau = \tau_0 + \mu\sigma_n \tag{2.8}$$

It therefore follows that τ_0 is the shear stress required for failure to occur when σ_n is equal to zero. The coefficient of internal friction may also be expressed in terms of the slope of the failure envelope, φ, such that;

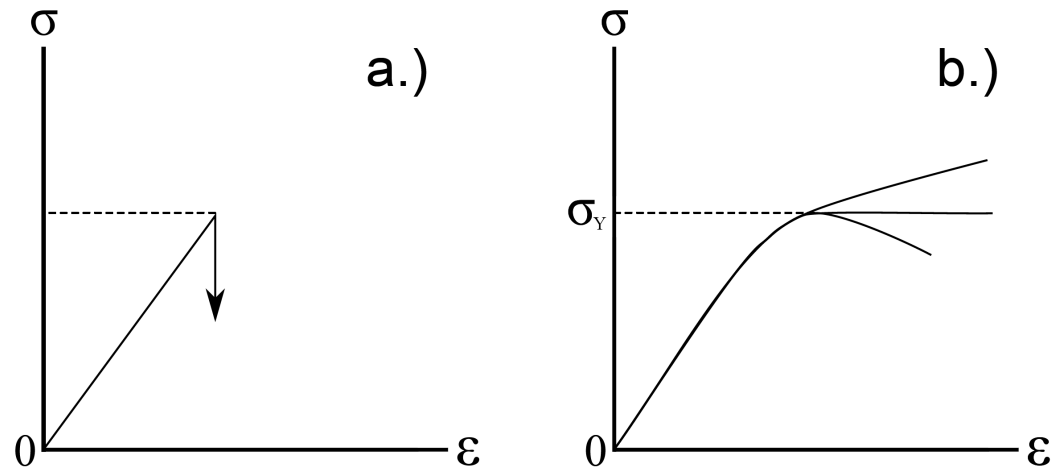

Figure 2.2. Idealised stress-strain curves for: a.) ideal brittle failure and b.) ductile failure (after Ranalli, 1995). b.) demonstrates three possible post-yield behaviours: i.) ideal ductile behaviour (straight line), ii.) strain-hardening (curved upward) and iii.) strain-softening (curved downward).

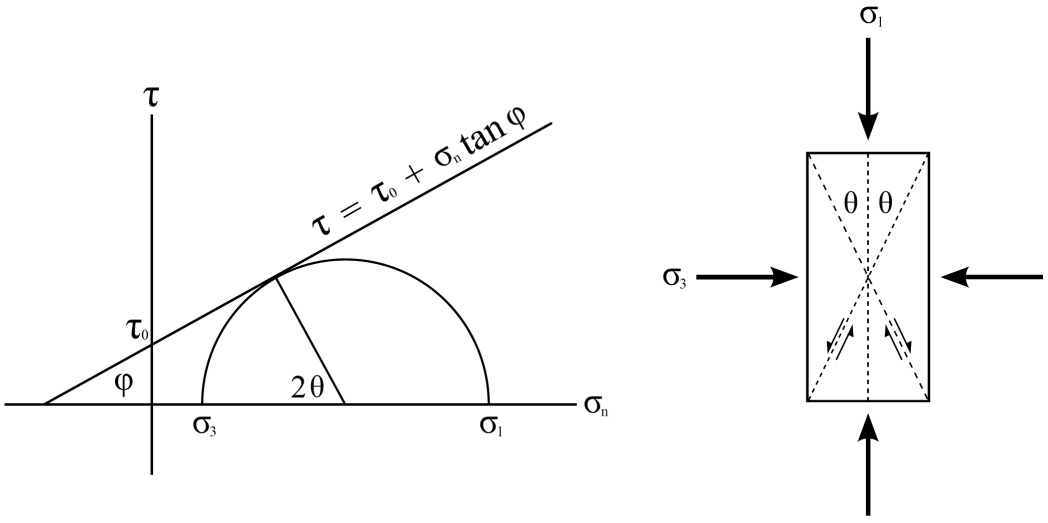

Figure 2.3. The Mohr circle construction (left), illustrating the Coulomb-Navier failure criterion (redrawn after Scholz, 2003). To the right is a profile through a loaded rock, indicating the orientation of failure planes and their angular relationship to the principal stresses.

$$\mu = \tan \varphi \tag{2.9}$$

leading to the expression:

$$\tau = \tau_0 + \sigma_n \tan \varphi \tag{2.10}$$

If the Mohr circle comes into contact with the failure envelope, the stress state is sufficient to meet the Coulomb-Navier failure criterion and the sample will fail along a plane orientated at an angle, θ, from σ_1. Whilst this approach does neglect the intermediate principal stress, it is generally sufficient to describe the failure behaviour of rock in traditional laboratory experiments and has been successfully applied to a wide range of field based problems, from natural faulting to tunnel excavations.

However, for a porous rock this concept must be further adapted to allow for the effects of pore fluid pressure, P_p. If the rock is saturated, the pressure of fluid within the pores acts in the opposite sense to the applied stress, σ_{ij}. As a result, if pore pressure is isotropic, then the 'effectiveness' of the applied stress is reduced in all directions by P_p. As such the law of effective stress (*Jaeger and Cook,* 2007; *Paterson and Wong*, 2005), states that;

$$\sigma_{ij}^{e} = \sigma_{ij} - P_p \delta_{ij} \tag{2.11}$$

where δ_{ij} is Kronecker's delta, and α is a constant and σ^e_{ij} is known as the '*effective stress*'. In this thesis, where fluid is present, we are dealing with *water* in a *fully* saturated material and as such we can assume α=1. This is a standard approximation for such conditions (Terzaghi's Principle), in which the term '*simple* effective stress' is utilised to describe σ^e_{ij}. In addition, since pore fluid effects are isotropic here, only its influence on normal stresses must be considered. As a result the principal effective stress components are: σ_1-P_p, σ_2-P_p, and σ_3-P_p. The effect of increasing pore fluid pressure can, therefore, be demonstrated geometrically by shifting the Mohr's circle along the normal stress axis (towards the origin), by an increment equal to P_p. As a result, the Mohr's circle moves closer to the Coulomb failure envelope and, potentially, towards failure at a lower stress than would have otherwise been anticipated.

2.2.3 Faulting in the laboratory

One approach to investigating the failure of rock under stress is to carry out rock deformation tests in the laboratory. By applying different stress states to samples, a range of different types of fracturing can be investigated (Fig. 2.4), including shear fracture and extension fracture. The loading arrangements in an experiment are generally described in terms of the relative size and polarity of the principal stresses; the convention in rock mechanics testing being that compressive stresses are positive. The experiments described in this thesis involve sample loading with entirely compressional principal stresses, or *triaxial compression* (Fig. 2.5).

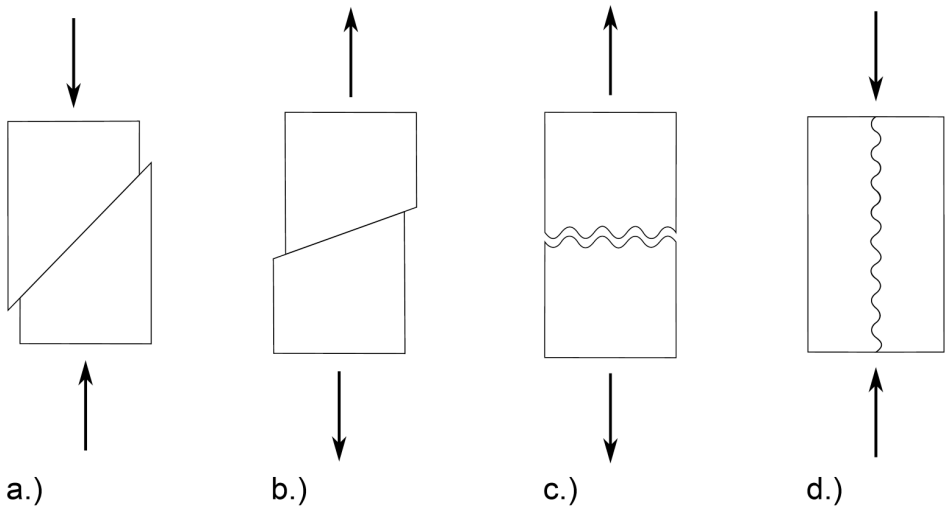

Figure 2.4. Types of fractures (redrawn after Paterson and Wong, 2005). a.) Shear fracture in compression, b.) shear fracture in extension, c.) extension fracture in extension and d.) extension or 'axial splitting' fracture in compression test.

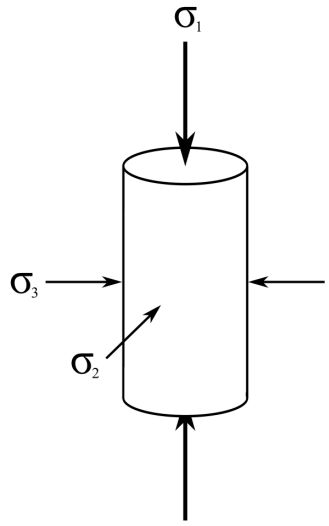

Figure 2.5. Stress arrangement for triaxial compression of a cylindrical sample. For a conventional triaxial compression test $\sigma_2=\sigma_3$.

Triaxial compression tests have been developed to simulate stress conditions that a rock might experience in the crust, due to loading by the material above. A *true triaxial* test involves the application of three independently variable compressive stresses, such that $\sigma_1>\sigma_2>\sigma_3$. Whilst it has been shown that the intermediate principal stress cannot always be ignored (*Haimson and Chang*, 2000; *Haimson and Chang*, 2002), carrying out a true triaxial test is experimentally complex and, as a result, this has yet to become the conventional arrangement for compressional testing. More widely used within the field of rock deformation is the *axisymmetric* or *conventional triaxial* test. In this case a cylindrical sample is subjected to a maximum compressive stress orientated parallel to the axis of the cylinder, whilst the minimum and intermediate principal stresses are equal to one another (generally provided by a confining fluid surrounding the cylinder) and perpendicular to the loading axis. This arrangement is conventionally written as $\sigma_1>\sigma_2=\sigma_3$. Failure of a rock sample loaded under this arrangement of stresses occurs along a shear fracture, which is often termed a 'fault', due to its similarity with geological faults observed in the field (*Griggs and Handin*, 1960). Under low to moderate confinement ($\sigma_2=\sigma_3$), this failure plane will be oriented at an angle $\theta<45°$.

2.2.3.1 Loading evolution

As discussed in chapter 1, the evolution of physical properties of a compact rock sample during compression are conventionally separated into four main stages (*Brace et al.*,

1966; *Paterson and Wong*, 2005). Figure 2.6 illustrates a typical stress-strain curve for such a test and highlights the onset of each of these stages, a brief description of which is given below:

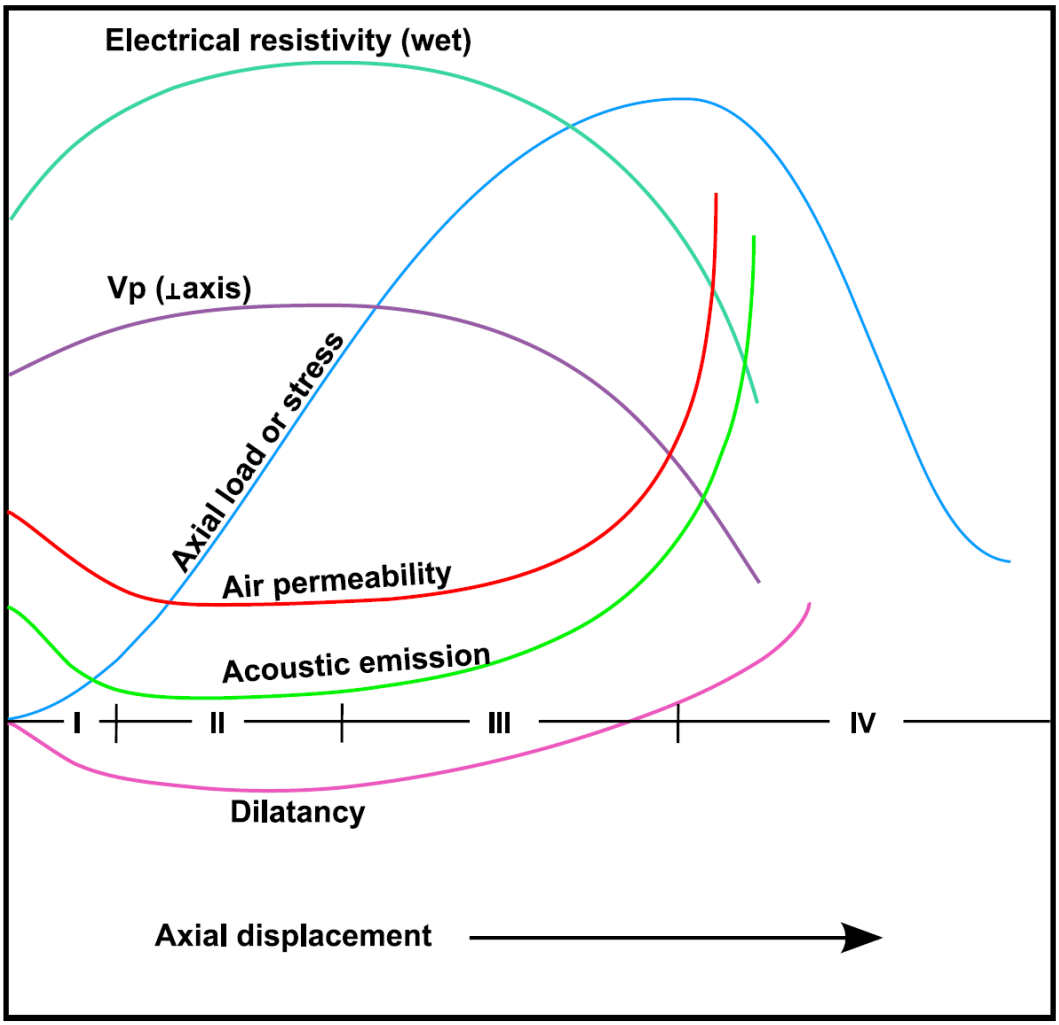

Figure 2.6. The generalised evolution of various physical parameters during the compressive loading of compact rock (after Paterson and Wong, 2005). The material behaviour is divided into four main stages: I-IV.

I. Strain-hardening due to closure of pre-existing fractures. Porous rocks may also experience some pore-collapse, leading to negative dilatancy.

II. A period of essentially linear, near-elastic deformation, albeit with some ongoing inelastic damage indicated by a low level of acoustic emissions.

III. The onset of significant dilatancy, due to microcracking (*Brace et al.*, 1966). Microfractures propagate in a stable fashion, leading to a notable reduction in P-wave velocities (see Vp in Fig. 2.6). In wet samples, a decrease in electrical resistivity may also occur, as a result of microcracking. Significant acoustic emission activity generally begins at this stage. These emissions are discussed in depth later in this chapter (section 2.3.3). The sample stiffness decreases during this stage until it reaches zero, at the peak stress, C_o, which is also the sample strength. In the case of high-porosity rocks, microfracturing is not thought to be the primary cause of dilatancy, but instead rupturing of grain contacts, leading to sliding and rotation of grains (*Menéndez et al.*, 1996).

IV. Microcracking becomes unstable as damage is increasingly spatially localised, eventually leading to the formation of a fracture plane. The rate of acoustic emissions increases rapidly prior to sample failure.

The transition from stage III to stage IV is generally thought to occur close to the peak load. However, whilst strain observations indicate that localisation occurs before this peak, location of acoustic emissions (section 2.3.3.2 of this chapter) and microstructural

analysis indicate that the transition occurs post-peak stress. *Paterson and Wong* (2005) suggest that 'Closer study of the initiation of localisation and thus of the transition from Stage II to Stage IV integrating different measurement techniques would be useful to resolve this apparent discrepancy '. It is the transition from stages III to IV that is the main focus in chapter 4 of this thesis. This study has involved a detailed investigation of the progression of damage during this phase, for triaxial compression of both granite and sandstone. In particular, damage localisation in a low-porosity sandstone is examined utilising a range of techniques, including spatial analysis of acoustic emission hypocentres, source analysis of AE waveforms, monitoring of porosity volume and microstructural analysis.

2.2.3.2 Controls on rock strength

The strength of rock and mode of failure have been the subject of intense laboratory study and are dependent upon a number of controlling factors, including confining pressure, temperature and pore-fluid pressure. Comparison of uniaxial (unconfined) and triaxial compression strengths for different rock types clearly demonstrates that confining pressure increases rock strength (Table 2.1).

Over a moderate range of confining pressures, p, this relationship may be approximated as linear by;

$$\sigma_1 - \sigma_3 = \sigma_0 + p \tan \psi \qquad (2.12)$$

where the differential stress at failure is expressed as a function of the uniaxial compressive strength, σ_0, and a constant, $\tan \psi$ (*Paterson and Wong*, 2005). This is essentially the same relationship as that described by the Mohr Circle (equation 2.8, section 2.2.2).

Rock type	**Uniaxial compressive strength (MPa)**	**Differential stress at failure (MPa), for confining pressure = 100MPa**
Igneous and high-grade metamorphic rocks	≈ 100-200	≈ 500-800
Low-porosity sedimentary and low- to medium-grade metamorphic rocks (including limestone and marble)	≈ 50-100	≈ 200-300 (if still brittle)
High-porosity sedimentary and some low-grade metamorphic rocks	≈ 10-50	———
Low-porosity dolomites and quartzites	300 +	≈ 500-1000

Table 2.1. Comparison of confined and unconfined failure strengths for different rock types (*Paterson and Wong*, 2005).

In reality, the relationship observed in the laboratory between compressive strength and confining pressure is not necessarily linear, particularly over wide ranges of p. Instead, a concave curve is regularly observed. In many cases this may be a result of the approach of the brittle-ductile transition, although this not always a satisfactory explanation. However, a linear approximation may still be used as a first degree approximation in many situations, especially over small ranges of confinement pressures. For a porous rock, where pore fluid is present, it is the difference between the confining pressure and the pore fluid pressure, or the *effective pressure*, which affects failure strength (as described in section 2.2.2 above).

Brittle fracture is also influenced by the rate at which deformation occurs. Increased strength has been observed at higher strain rates during uniaxial compression of a wide range of rock types including marble (*Mogi*, 1959) and granite (*Mogi*, 1962; *Li et al*., 1999; *Masuda*, 2001). *Masuda* (2001) also observed a similar effect during triaxial loading of granite, across a range of strain rates and confining pressures. The same study demonstrated that the observed strain rate dependence of failure strength was greater in water-saturated samples than dry samples, particularly at lower confining pressures. They also suggest that the responsible mechanism for their observation of time-dependent strength of samples is sub-critical crack growth by stress corrosion. *Ojala et al*. (2003) also observed strain rate dependence of failure strength for triaxial compression of samples of Locharbriggs sandstone.

In addition, the effect of temperature upon deformation of rock is a well-established phenomenon. At high temperatures, above around 500°C, rock behaves in a ductile fashion and plastic flow becomes the primary mode of deformation (*Jaeger and Cook*, 2007). In the ductile regime, increased temperature leads to a notable decrease in strength. However, at lower temperatures, and hence in the brittle field, such an effect is not nearly as significant. In spite of this, a number of studies have observed some decrease in strength with increased temperature in the brittle regime (*Tullis and Yund*, 1997; *Caristan*, 1982; *Fischer and Paterson*, 1989; *Gottschalk et al*., 1990; *Hirth and Tullis*, 1994).

2.2.3.3 Inelastic deformation and localisation

Of particular importance in laboratory experiments on rock, is the observation of the volumetric strain. Inelastic deformation during brittle compression of rock is thought to be a direct consequence of microstructural damage of the material. Such a change is described as *dilation*, for an increase in volume, and *compaction*, for a decrease in volume. If we first consider a rock under hydrostatic conditions, the likelihood of dilation is low, as is that of compaction if there is no significant porosity present. If, however, a deviatoric stress is then applied, the sample may exhibit dilatant behaviour, or *dilatancy*, as inelastic deformation takes place. This is also the case for a porous rock, although it may instead experience *compactancy* if the inelastic deformation is associated with a decrease in volume.

Brace et al. (1966) demonstrated that, in the brittle regime, failure of compact rock is preceded by a period of dilatant behaviour. A number of methods have been proposed for determining the onset of dilatancy, usually designated *C'*, though perhaps the most effective approach is to identify the point of deviation from the hydrostatic response of the material (*Schock, Heard and Stephens*, 1973). Alternatively, a line may be fitted through the elastic segment of the stress-strain curve, assuming a significant initial period of linear behaviour is observed. In addition, the results presented in this thesis suggest that it may be possible to determine the onset of dilatancy from moment tensor inversion of acoustic emission data.

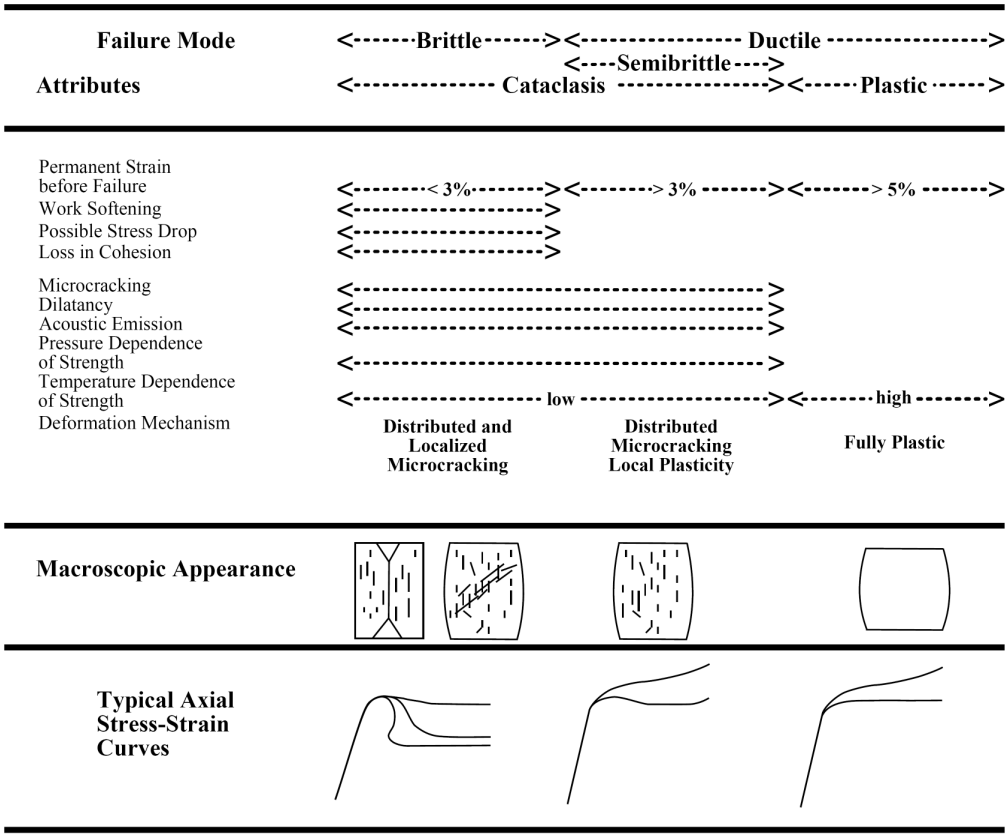

Figure 2.7. The phenomenology of the brittle-ductile transition (after Evans et al., 1990).

In a compact, non-porous crystalline rock, with no significant pre-existing damage, compressive differential loading in the brittle regime will generally lead to initially distributed, dilatant microcracking, followed by localisation of damage and brittle failure. Damage tends to localise in the plane of the future shear fracture and this mode of deformation is often termed *shear localisation* (*Kranz*, 1983). In the region of the brittle-ductile transition, damage becomes more delocalised and local ductility may occur (Fig. 2.7). Once in the ductile regime, damage becomes fully delocalised.

Similar behaviour, from the brittle to the ductile regime, may also be observed for porous rocks, although they may also undergo negative dilatancy greater than that expected from hydrostatic loading. This process is termed '*shear-enhanced compaction*' (*Paterson and Wong*, 2005). In a compressed sandstone, with a high porosity and under a sufficient effective pressure, compactancy may become concentrated into deformation bands; a process known as *compaction localisation* (*Paterson and Wong*, 2005). The importance of this form of localisation has become increasingly recognised, primarily due to the potential for compaction bands to affect permeability characteristics of reservoir rocks (*Mair et al*., 2000; *Main et al*., 2000; *Mair et al*., 2002).

Whether dilatancy or compaction dominates during loading is controlled by the effective pressure, sample porosity and grain size (*Wong et al*., 1997), although they need not necessarily be mutually exclusive processes (*Baud et al*., 2000). The macroscopic deformation of porous rock, approaching the brittle-ductile transition, and the effects of

porosity and effective pressure on the transition from dilatant to compactive behaviour, has been the subject of intense study (*Wong et al.*, 1992; *Menéndez et al*., 1996; *Wong et al*., 1997; *Baud et al*., 2000; *Besuelle*, 2001; *Klein et al*., 2001; *Besuelle et al*., 2003; *Fortin et al*., 2009). A detailed acoustic emission study of micromechanics of shear localisation in the Clashach sandstone is presented in chapter 4 of this thesis. The approach utilised in this chapter also shows significant potential for further elucidating the micromechanical processes involved in compaction localisation (see section 6.7).

2.3 Small scale seismicity

In order to investigate the progression to failure of compressed rock, the evolution of a number of physical properties may be monitored during laboratory experiments. As well as regional mechanical data, local volumetric strain may be monitored, either with strain gauges or by estimation from interconnected porosity volume. Active techniques may be applied, such as monitoring electrical resistivity of wet samples or changes in ultrasonic velocities across the sample. Acoustic emissions produced during microscale damage events also provide information about the internal state of a sample. After a sample has been unloaded, microscopic analysis can provide additional quantitative data relating to microcrack densities and orientations within different parts of the material.

This section describes some of these techniques and their findings, with particular focus on acoustic emissions; the primary tool for this study. The modelling of failure by

estimation of damage progression, utilising acoustic emission data, is also discussed. Source analysis methods from the field of seismology, which are applied to acoustic emissions in this thesis, are then described, with particular emphasis on the moment tensor.

2.3.1 Ultrasonic velocities

Monitoring of ultrasonic velocities by the emission of regular pulses from piezoelectric transducers is now standard practice in laboratory studies. Changes in P-wave and S-wave velocities, V_p and V_s respectively, during deformation experiments provide useful information about the evolution of the sample's mechanical properties (*Ayling et al*., 1995). There is also a correlation between the reduction in ultrasonic velocities during sample loading, and the increase in crack density during dilatancy (*Hadley*, 1975; *Hadley*, 1976). If both axial-parallel and axial-normal velocities are monitored, development of acoustic anisotropy during triaxial loading may be observed (Fig. 2.6). This phenomenon can be explained by the preferential orientation of microcracking, in alignment with the maximum compressive stress (*Anderson et al*., 1974).

In addition, *Benson et al*. (2005) demonstrated that pore-space anisotropy in hydrostatically loaded sandstone can be accurately inferred from acoustic velocity anisotropy. *Stanchits et al*. (2003) monitored P-wave velocities and attenuation in a triaxially loaded Westerly granite as it was injected with water, so as to investigate pore-

fluid pressure effects. The sample was loaded in discretely increasing steps until failure took place. Their results demonstrate that P-wave velocities and attenuation respond significantly to the saturation of microcracks. *Hadley* (1976) also demonstrated that changes in acoustic velocities could be used to estimate microcrack densities during the laboratory deformation of a rock in the brittle regime.

However, whilst monitoring of ultrasonic velocities can provide information pertaining to the orientation and density of microcracking, this approach is less suited to investigating the microscale mechanisms involved in damage evolution. This is because the velocities involved are dependent not only on processes occurring at a given time within a sample, but also on all previous damage that has occurred. As such, monitoring of changes in ultrasonic velocities gives information only about *bulk* changes in damage within the material.

In contrast, acoustic emissions are generated by *instantaneous* deformation events occurring during loading and, as a result, are not dependent upon accumulated damage. Consequently this study is primarily concerned with the analysis of acoustic emission data, to obtain highly detailed information concerning the micromechanical processes involved in shear localisation, as well as their spatial and temporal evolution.

2.3.2 Microstructural analysis

2.3.2.1 Mechanisms of microcracking

The formation of a single fracture may be broken down into three fundamental modes (Fig. 2.8); I.) *Opening* mode, or *tensile* fracture, II.) *Sliding* mode, or *in-plane shear*, and III.) *tearing* mode, or *anti-plane shear*. Such fracturing occurs in rock when the 'local stress exceeds the local strength' (*Simmons and Richter*, 1976). The formation of a macroscopic fault is preceded by the growth and coalescence of many microscopic fractures, or *microcracks*. In this context, it is important to consider a fracture's relationship with the grain or crystal it is contained in. *Kranz* (1983) subdivides microcracks into; i.) *grain boundary* cracks, ii.) *intragranular* cracks (contained entirely within a grain), iii.) *intergranular* cracks (extending from a grain boundary and passing through a grain, or several grains), iv.) *transgranular* cracks (cutting across a grain from one grain boundary to another). In general, low-porosity, well-cemented rocks tend to have transgranular microcracking, whilst intragranular cracks are characteristic of high-porosity, poorly-cemented rocks.

These different types of microcracking are caused by a range of mechanisms. *Blenkinsop* (2000) identified nine different mechanisms for microcrack formation. Of particular interest to this study are:

i.) *Impingement* microcracking is generally intragranular and connects points of contact between neighbouring grains. Multiple points of contact may lead to multiple microcracks if loaded (Fig. 2.9). Evidence suggests that such microcracks are the result

of the stress applied by an indentor impacting upon the surface of the grain (Fig. 2.10). This mechanism is capable of producing both tensile (*Lawn and Wilshaw*, 1975) and shear (*McEwen*, 1981) fracturing.

ii.) *Flaw-induced* microcracks are diagnosed by being joined to a flaw, which may be another microcrack, a pore or a grain boundary. They may be intragranular, transgranular or grain-boundary microcracks and are thought to form due to increased tensile stresses on the surface of the flaw, induced by a more remote stress. Analytical solutions indicate that growth of fractures from both ends of a flaw will lead to the formation of a 'wing crack' (*Baud et al*., 1996) as is illustrated in Figure 2.11.

iii.) Microfracturing of pre-existing flaws (such as grain boundaries), or *refracture*, is a highly significant mechanism for microcracking. In particular, the observation of *Pittman* (1981) that quartz overgrowth material constitutes a primary component of fault matrix, indicates that even where a grain-boundary has been strengthened by quartz overgrowth cement, this boundary may still represent a notable zone of weakness for fracture to occur along.

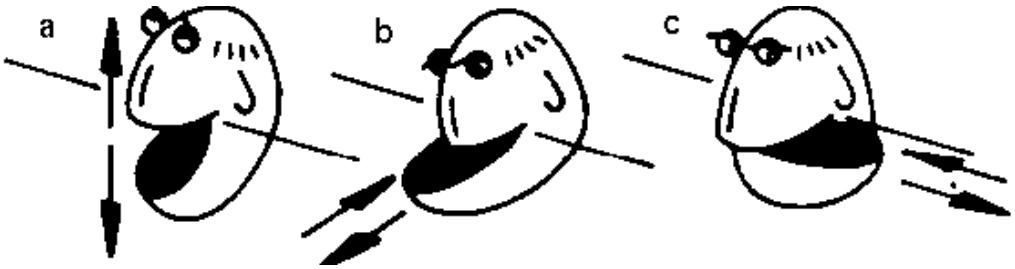

Figure 2.8. Crack opening modes (after Guéguen et al., 1990). a.) tensile, b.) in-plane shear and c.) anti-plane shear.

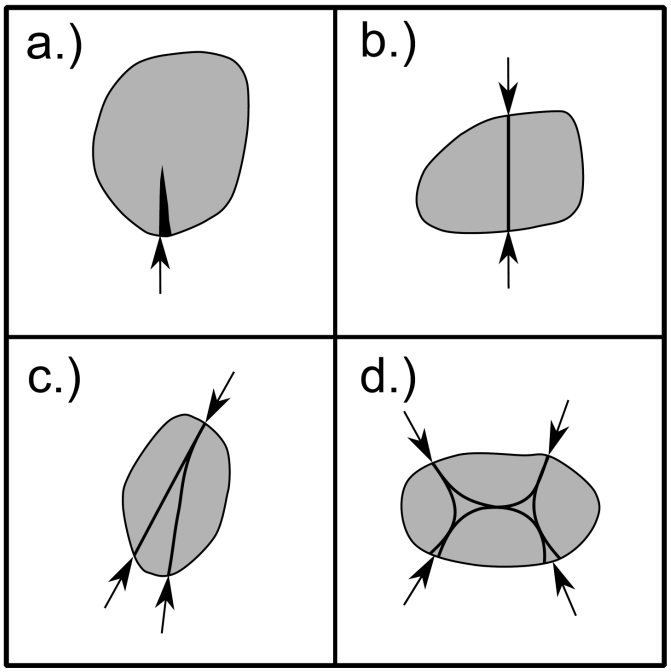

Figure 2.9. Impingement crack geometry (redrawn after Blenkinsop, 2000), in relation to contact points with adjacent grains (indicated by arrows). a.) single load, b.) double load, c.) triple load and d.) quadruple load.

2.3.2.2 Statistics of microcracking

Kranz (1983) argues that 'understanding crack interaction and coalescence is…essential to understanding the formation of fracture in rock'. As such, quantitative microscopic observations of microcracks are an important tool for informing us about these processes. Observations of microfractures in compact rock samples, post-compression, generally indicate a preferred orientation, even when none is observed in the original pre-loading material. For uniaxial loading, the majority of microcracks are orientated

within 10° of the maximum compressive stress axis, whilst after triaxial loading microfractures display a preferred orientation of within 30° of the maximum compressive stress axis (*Kranz*, 1983). However, the mean angle of microcrack orientation observations, and the associated standard deviation, may vary during the progression to failure. Another commonly quantified observation is that of crack length. However, interpretation of length distributions may be complicated by uncertainties inherent in the two dimensional nature of a thin section, and its associated orientation.

In addition, the observation of *crack densities* (generally based on the number of cracks per grain or per specified unit area) allows the degree of spatial localisation of damage to be quantified, at different stages of the loading process. A notable increase in spatial concentration is observed before failure (*Kranz*, 1983). Such detailed and quantitative data, concerning the progression of microcracking, is invaluable to the study of damage evolution.

However, one disadvantage of this technique is the inability to collect data before unloading. As such, the effects of unloading on the sample can never be fully known and, in order to investigate microcracking at different stages during the loading process, more than one sample must be used. In chapter 5, microstructural analysis of damage in a low-porosity sandstone is compared to acoustic emission focal mechanisms from the same experiment, providing the first comparison of these two types of observation for a sandstone.

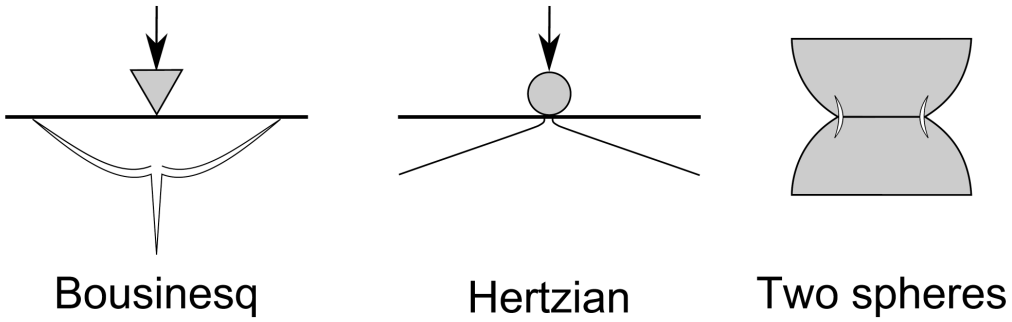

Figure 2.10. The formation of impingement microcracking by indentation with a sharp indentor, a spherical indentor and between two spheres (redrawn after Blenkinsop, 2000).

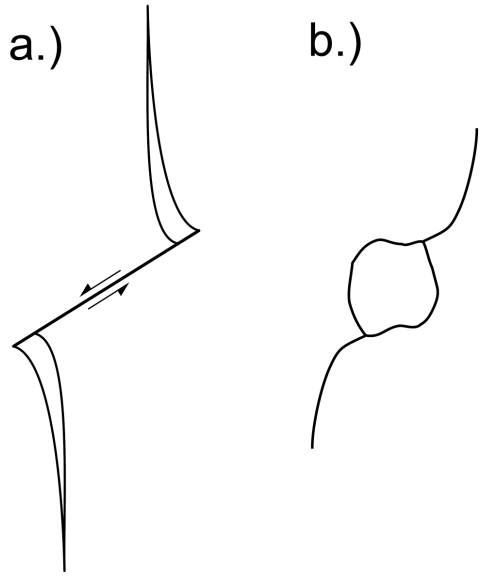

Figure 2.11. Flaw induced microcracking (redrawn after Blenkinsop, 2000). a.) An idealised 'wing crack' and b.) An example of microcrack/pore interaction.

2.3.3 Laboratory acoustic emissions

2.3.3.1 The phenomenon of acoustic emission

An alternative method for investigating microcracking, during the laboratory deformation of rock, is the monitoring of acoustic emissions (or AE). These high-frequency pressure disturbances are thought to be produced by the dynamic release of energy during the formation of microcracks. A comprehensive review of this phenomenon is given by *Lockner* (1993). In early AE experiments, recording systems were generally set to monitor the occurrence of AE '*hits*' at each sensor; detected when the output signal of the sensor superceded a preselected amplitude threshold. The onset time and peak amplitude of these hits were typically recorded. However, with the increased memory of modern systems the recording of full waveform data has become common place. Such systems generally record data from an array of AE sensors and the focus tends to be on each unique AE '*event*', which may be recorded at one or more sensors, producing many '*hits*' as a result. In this thesis, AE data is dealt with as '*events*'. For example, the term 'AE rate' is used to describe the rate of acoustic emission *events*, as opposed to *hits*.

A primary reason for studying acoustic emissions in the laboratory is to infer information about earthquake scale processes. Whilst such experiments are dissimilar to earthquake sources in that they involve the initial failure of a previously intact sample,

as opposed to rupture along a pre-existing fault, *Lockner* (1993) argues that the approach is valid for the following reasons:

i.) Between earthquakes, faults are thought to heal and strengthen.

ii.) Regions of rock interlock with one another along natural faults (as they are not smooth planes). These zones must be broken through during a rupturing event. Laboratory experiments may, therefore, be considered as representing fracture in these fault zone asperities.

iii.) There is a similarity between the statistical behaviour of both earthquakes and AE events.

iv.) Similar micromechanical processes are at work during failure of initially intact rock samples and slip on large-scale faults. However, caution should always be taken when inferring analogous behaviour.

As such, methodology applied in the study of acoustic emissions has developed in synchrony with that utilised in earthquake seismology.

2.3.3.2 Hypocentre locations

By employing hypocentre location techniques originally developed for analysis of earthquakes, it is possible to obtain information about the spatial and temporal occurrence of damage and the process of crack coalescence. Sensors must respond to frequencies in the MHz range, in order to provide sufficient resolution for first arrival times and, hence, acceptable location uncertainties. With increases in computer memory, came the ability to record significant numbers of AE waveforms at an array of sensors and, as such, a number of different techniques for determining the first arrival time have been developed. All are carried out automatically, as the vast number of acoustic emissions recorded in laboratory experiments (~10^3-10^4 events) makes manual picking unviable.

Scholz (1968b) located acoustic emissions produced during compression of Westerly granite and noted that, whilst initially delocalised, sources became spatially concentrated in the region of the eventual fault plane as failure was approached. *Lockner et al*. (1991) found hypocentre locations (with an uncertainty of ±3mm) for acoustic emissions recorded during the triaxial loading of Westerly granite. The rate of AEs was used as a feedback control on the axial stress, thereby extending the failure process. The results clearly demonstrated a marked transition from relatively distributed AE hypocentres, during dilation, to a notably planar arrangement of sources, in the final stages of loading (Fig. 2.12).

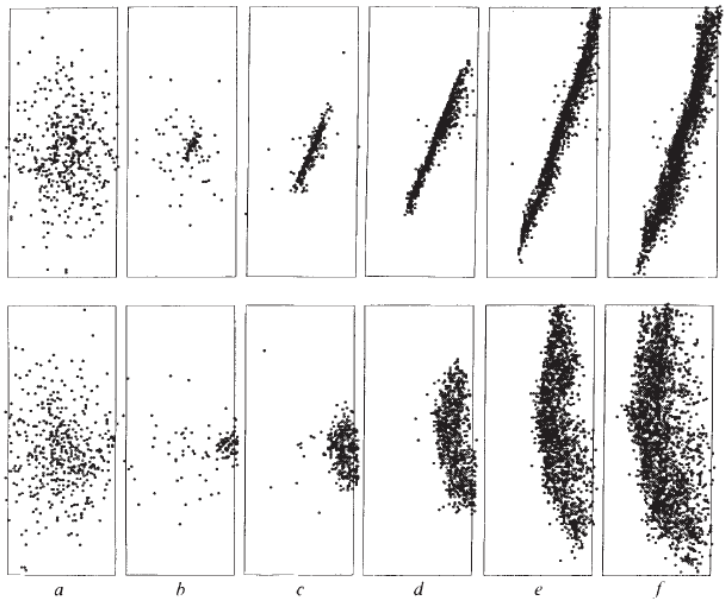

Figure 2.12. Hypocentre locations of acoustic emissions produced during quasi-static loading of Westerly granite (after Lockner et al., 1991). Upper plots are viewed along-strike of the final failure plane. Lower plots are face on to the fault plane. Plots are taken from different intervals along the stress-strain curve, with plot b.) being in the vicinity of the peak stress.

Whilst locating acoustic emission sources has been proven as a highly effective tool for elucidating the localisation of damage, this technique is reliant upon a good knowledge of the velocity field through which the AE signals travel. As such, regular monitoring of ultrasonic velocities through a deforming sample must be carried out, in order to correct for the development of acoustic anisotropy during loading. After hypocentres have been located during an experiment, coalescence of damage can be quantified by determining the '*correlation exponent*'. *Hirata et al*. (1987) used this approach to demonstrate that the spatial distribution of microcracks could be approximated as fractal, in deforming Oshima granite. A drop in the correlation coefficient is also generally observed as a consequence of damage localisation in samples (*Hirata et al*., 1987; *Zang et al*., 1996).

This technique will be described in greater detail in chapter 4, where spatial analysis is utilised to investigate the micromechanics of shear localisation in deforming sandstone. The results given there represent the first spatial analysis of individual AE source types during damage localisation in sandstone.

2.3.3.3 Time-dependent behaviour of acoustic emissions

There is a direct correlation between the rate of acoustic emission, during sample deformation, and the inelastic strain rate (*Mogi*, 1962; *Scholz*, 1968a). This phenomenon is therefore a highly informative monitoring tool for the passive collection of data in laboratory experiments. The relationship between AE event rate and inelastic strain rate is consistent with the general observation of the onset of significant AE activity at the initiation of dilation. However, *Lockner* (1993) reported that detected acoustic emissions represented only 0.2% of microcracks directly observed in deformed Westerly granite. Whilst the number of AE detected is limited by the amplitude threshold set for recording purposes, they argue that such a large discrepancy may call into question how representative AE events are of the general behaviour of the microcrack population. This is a question that is considered in more detail in chapter 5.

In spite of this discrepancy, acoustic emissions and earthquakes display a number of similarities in their statistical behaviour, leading to suggestions that the source processes

involved may be analogous. The rate of acoustic emissions has been shown to exhibit power-law behaviour, similar to that observed for earthquake aftershock sequences.

$$\nu(t) = \kappa/(t+c)^{P} \tag{2.13}$$

The modified Omori's law (equation 2.13) implies that the aftershock event rate after an earthquake, υ, decays approximately as the reciprocal of the time since the mainshock, t. The constants, κ and c control the amplitude and offset of the decay, respectively, whilst the constant P was introduced to the original Omori Law equation and is empirically derived (generally ranging from 0-2 in value). *Hirata* (1987) demonstrated that this relationship could be applied to AE data by considering bursts of AE events as foreshock and aftershock sequences, and observed a transition from firstly exponential to power-law behaviour in aftershock sequences. This approach has also been applied to whole AE rate curves, by taking the time of the main shock as the failure point (*Ojala et al*., 2004). In addition, it has been widely reported that laboratory AE exhibit power-law frequency-magnitude distributions (*Mogi*, 1967; *Scholz*, 1968c). This is comparable to the Gutenberg-Richter relation (*Gutenberg and Richter*, 1949), which describes the number of earthquakes, N, of magnitude, M;

$$\log N(M) = a - bM \tag{2.14}$$

with the empirical constants a and b. This has lead to speculation that microcracking may involve self-similarity on laboratory scales. As with earthquakes, AE frequency-magnitude distributions may be used to determine b-value evolution in the approach to failure, which has been observed to drop before failure during laboratory experiments (*Main et al*., 1989; *Meredith et al*., 1990; *Colombo et al*., 2003).

The clear association of acoustic emissions, microcracking, and hence, inelastic strain (*Scholz*, 1968a), has led to the application of AE data to time-dependent failure models. A number of AE-derived damage parameters have been proposed. For example, the cumulative number of acoustic emissions, N, has been utillised as such, due to its direct correlation with inelastic strain, as has the cumulative energy, E, of AE events. Such parameters provide an opportunity to account for the deviation from elastic behaviour as a consequence of the development of microfracturing within a rock sample. Damage parameter values can also be applied to predictive models, which can then be compared against mechanical observations for similarity. Of primary interest is the volume fraction of cracks within the material at a given time, which can be expressed in terms of the crack density parameter, χ, such that;

$$\chi = \frac{n_c < c >^3}{V} = \frac{\Sigma c^3}{V} \tag{2.15}$$

where n_c is the number of cracks with half length c, within a given volume, V. *Cox and Meredith* (1993) utilised seismic source dislocation theory to define a damage parameter

similar to that given above (equation 2.15), which could be derived from acoustic emission magnitude data. They were then able to successfully reconstruct stress-strain curves by applying the dilute crack model of *Walsh* (1965) and the self-consistent model of *Bruner* (1976) to calculate the effective Young's modulus. They noted that the stress-strain behaviour predicted by Bruner's model better fitted observations, due to the consideration of crack interactions. However, there was also a tendency for damage to be underestimated in the vicinity of the peak stress. This may be explained either by; i.) aseismic, inelastic deformation becoming increasingly dominant during the strain softening phase, or ii.) the coalescence of damage leading to localised weakening, which is not considered by an isotropic damage parameter. An improved understanding of the interactions and contributions of AE-associated damage in the strain-softening phase would aide attempts to solve this discrepancy.

2.3.3.4 Mechanisms of acoustic emissions

With the rapid increase of data storage capacity in recent times, the recording of full waveforms at a high sampling frequency has become a standard practice in AE studies. As a result, a number of approaches have been developed for the separation of AE events into different waveform types, which are attributed with different source characteristics. Most studies involve analysis of P-wave polarities and distinguish between sources based on the predominance of an implosive or explosive component. In seismology, the polarity of a detected P-wave is described in terms of the ground

motion at the recording site (Fig. 2.14), as opposed to the behaviour at the source. For example an isotropically *explosive* source will produce a *compressional* first motion as a consequence, as the material surrounding the source will be compressed. Throughout this thesis, first-motions and radiation patterns are described using this terminology, as *dilational* or *compressional* (see section 2.3.4.2 for further details). This should not be confused with descriptions of source behaviour, which are concerned with *local* dilational or compressional deformations and follow the standard terminology used in rock mechanics.

First-motion analysis of AE waveform data has identified the presence of at least four types of behaviour; i.) *tensile* cracking, where the first motions are predominantly compressional (*Kranz et al*., 1990; *Zang et al*., 2000; *Lei et al*., 2004), ii.) *collapse* sources, where the first motions are predominantly dilatational (*Zang et al*., 1998; *Stanchits et al*., 2006; *Fortin et al*., 2009), iii.) *shear* cracking, where the first motions of waveforms do not exhibit a dominant implosive or explosive signature (*Zang et al*., 1998; *Lei et al*., 2004), and iv.) '*complex*' events, which cannot be classified as a specific source behaviour with this method (*Kranz et al*., 1990). This approach allows the broad characterisation of source behaviour, but provides only basic information about the mechanisms which generate the emissions. Once shear sources have been identified, mechanisms for these events may also be obtained by fitting a '*double-couple*' mechanism to them (*Zang et al*., 1998; also see section 2.3.4.2 below). Whilst this method does allow orientations of shear cracks to be determined, it assumes the

source is entirely shear and does not allow for source complexity. In addition, a double-couple cannot be applied to other types of microcracking.

One alternative method is to utilise waveforms to invert for a more detailed description of source behaviour (see sections 2.3.4.3 and 2.3.4.4 below). Such an approach can provide useful information about source complexities (*Shah and Labuz*, 1995; *Chang and Lee*, 2004), but has yet to be applied to many rock types. In this thesis, an inversion technique is utilised to characterise damage evolution in triaxial loading of granite and sandstone, giving an insight into source complexity and interaction in compact and low-porosity rocks. In chapter 3, the moment tensor inversion technique is validated by its comparison with the results of a more simplistic, polarity-based technique. Furthermore, chapters 4 and 5 provide the first moment tensor inversion results for a triaxially compressed sandstone, and a comprehensive characterisation of the micromechanical evolution of damage localisation, involving acoustic emission, microstructural, mechanical and ultrasonic velocity observations.

2.3.4 Source analysis in seismology

Modern recording techniques allow the collection of acoustic emission data sets that are comparable in detail, and the number of events involved, to a regional earthquake catalogue. As a result, many of the techniques developed in the field of seismology are now applicable to laboratory acoustic emission data. In this section, standard source

analysis theory from the field of seismology is described, in order to give context to later chapters.

2.3.4.1 Fault geometry and the seismic source

Earthquakes are generated by the release of energy, during the displacement of rock along faults in the Earth's crust. Whilst natural faults may involve curvature or irregularities along their length, it is generally considered a reasonable approximation to describe them as planar in the first instance. As such, the geometry of a fault plane (Fig. 2.13), in relation to a geographic coordinate system, can be defined in terms of only two parameters; the strike, Φ , or orientation from North, and the dip, δ, or angle below the horizontal, perpendicular to the strike.

In addition, the direction of slip along the fault plane is described as the *rake*, λ, the sign of which is designated by convention. *Aki and Richards* (2002) propose $-180° < \lambda < 0°$ for a normal fault and $0° < \lambda < 180°$ for a reverse/thrust fault. Additionally, if the fault motion is strike-slip then $\lambda = 0°$ and $\lambda = 180°$ represent left-lateral and right-lateral motion respectively. Alternatively, the fault motion can be described with respect to the fault using two vectors: $\boldsymbol{n}$, the normal vector to the fault plane and $\boldsymbol{d}$, the slip vector in the fault plane.

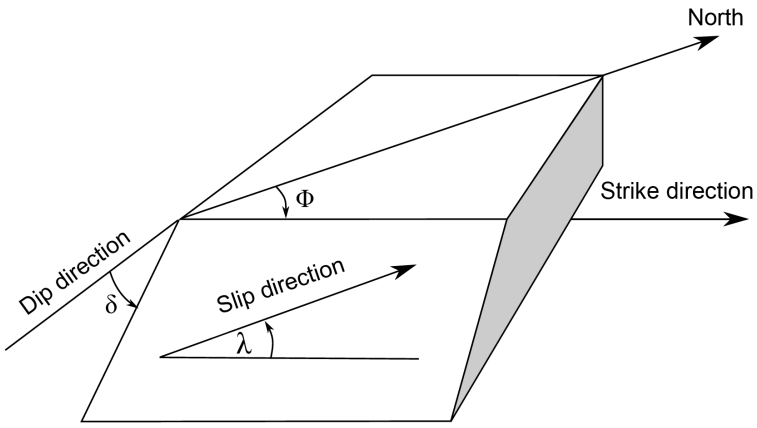

Figure 2.13. Illustration of the geometry of a fault in terms of the dip, strike and rake of the fault plane (after Aki and Richards, 2002).

2.3.4.2 First motion analysis and the double couple

The pattern of radiated seismic waves produced during an earthquake is directly related to the geometry of the fault along which the displacement occurred. Consequently, it is possible to derive information relating to fault geometry from the waveforms recorded over a number of seismic recording stations. The simplest approach to this inverse problem is based solely on the polarity, or 'first motion', of recorded body waves, in relation to the station distribution. Depending on the orientation of the seismic source, seismographs recorded at different locations may receive either a positive or negative first motion, relating to whether the effect of the displacement was compressional or dilatational within that part of the crust (Fig. 2.14).

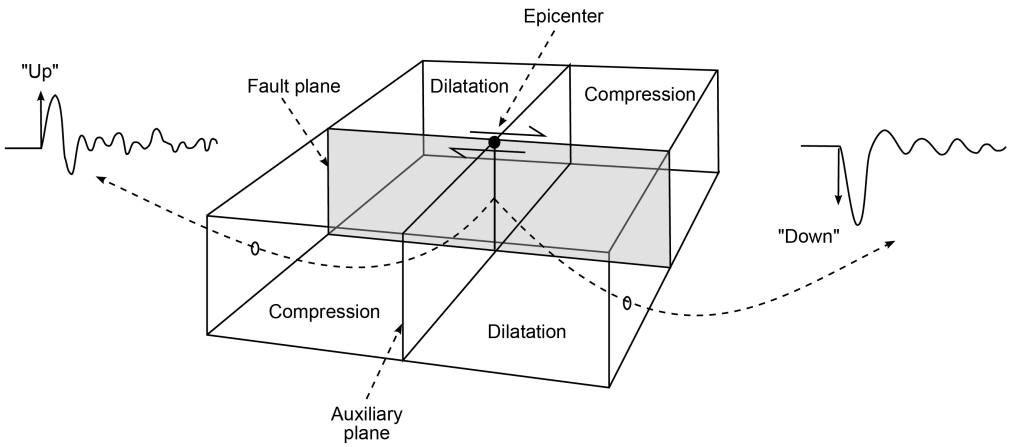

Figure 2.14. First motion observations of P-waves recorded due to a slip on a planar fault (redrawn after Stein and Wysession, 2007).

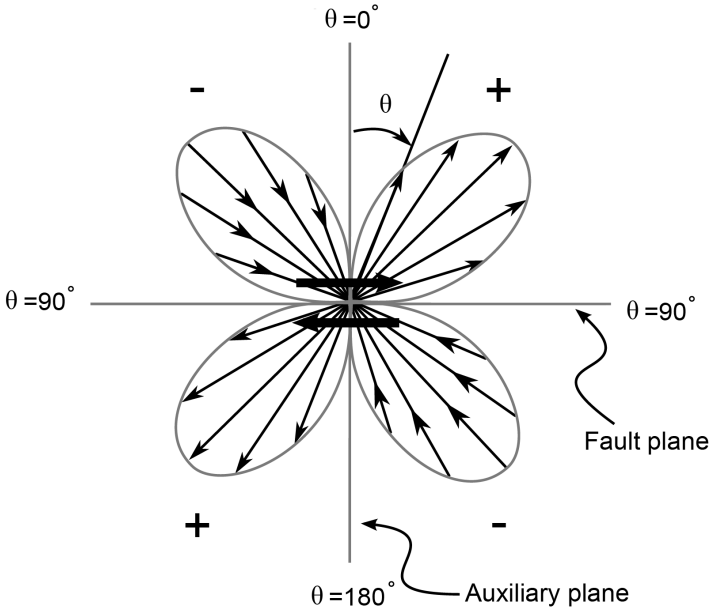

Figure 2.15. The two-dimensional P-wave radiation pattern for a double-couple source (modified after Aki and Richards, 2002). Two lobes are compressional and two dilatational, going to zero at the nodal planes. Either nodal plane may be the fault plane and cannot be distinguished from the radiation pattern alone.

The radiation pattern produced by a planar fault consists of four quadrants, two compressional and two dilatational, which are divided by the fault plane and a plane perpendicular to the fault plane, or *auxiliary plane*. As a result, first motions detected along these planes may be small or undetected, due to destructive interference between the compressional and dilatational behaviour, and they are often termed the *nodal planes*. In order to satisfy such a radiation pattern (Fig. 2.15) two '*force-couples*' must be invoked; pairs of forces acting close to one another with an opposite sense (Fig. 2.16). One force-couple acts parallel to the fault plane and a second force-couple acts perpendicular to the first, along the auxiliary plane. Such an arrangement produces the desired radiation pattern, whilst inhibiting any change in volume at the source. The resulting *double-couple* mechanism is regularly used in seismology to approximate slip along a fault plane.

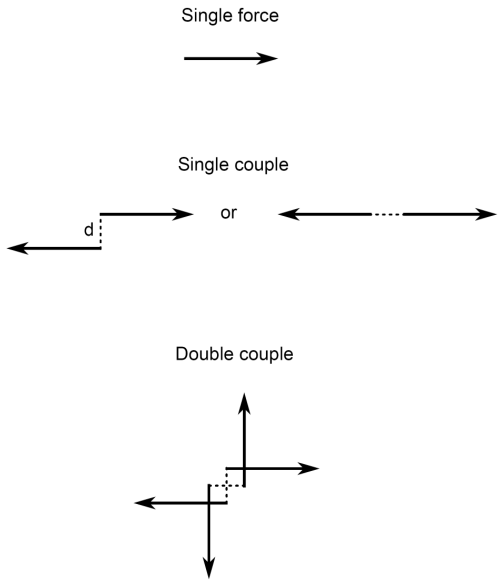

Figure 2.16. Equivalent body forces for a single force, a single couple and a double couple (modified after Stein and Wysession, 2007). The single couple forces may be offset so that a torque is exerted (left) or so that no torque is exerted (right).

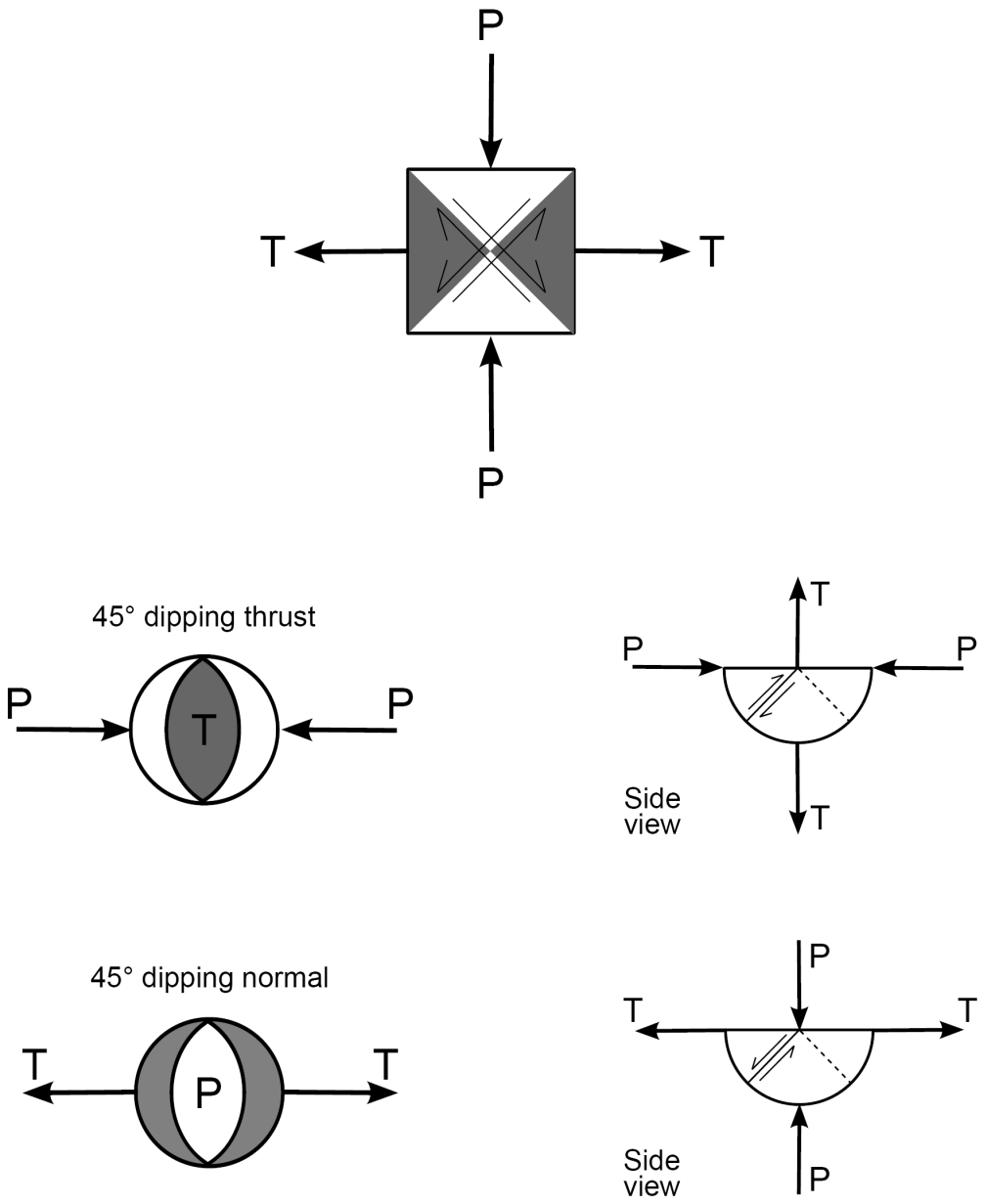

Figure 2.17. Schematic diagram showing two example focal mechanisms (left) for thrust and normal faulting on fault plane dipping by 45 degrees (modified after Stein and Wysession, 2007). The geometric relationship between the fault plane (solid line), the auxiliary plane (dashed line) and the pressure (P) and tension (T) axes is also illustrated.

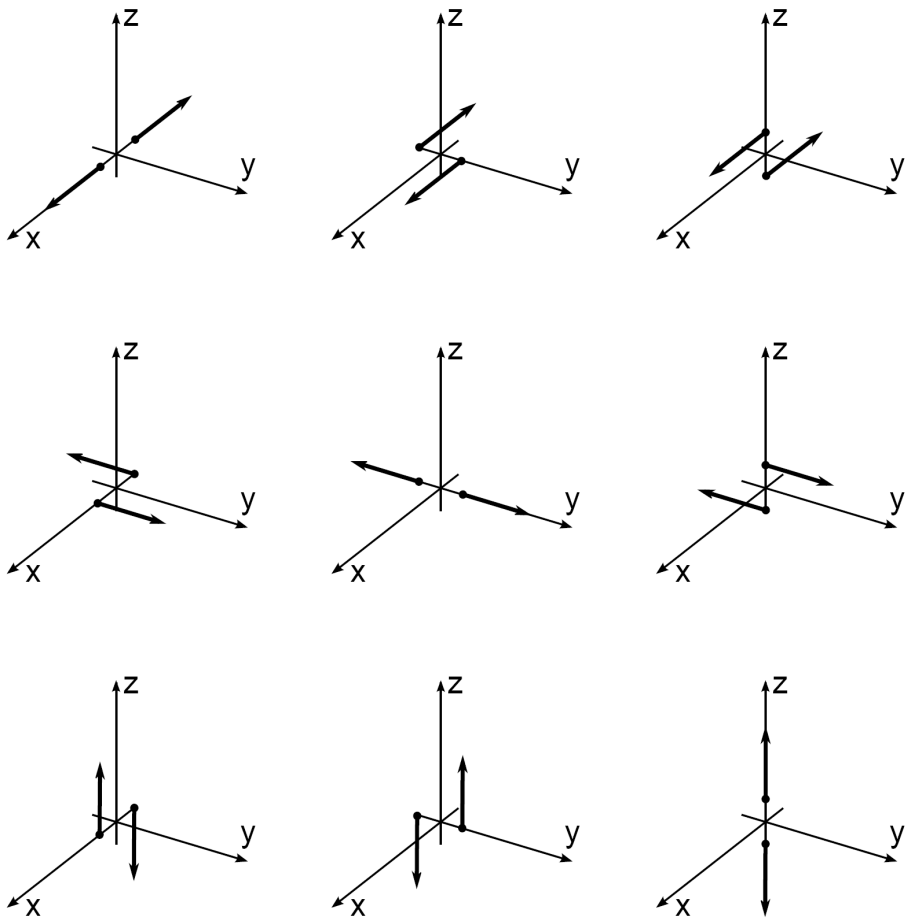

Figure 2.18. The nine force couples that make up the moment tensor (modified after Aki and Richards, 2002).

By fitting a double-couple mechanism to the first motion distribution for an earthquake, the *fault plane solution* or *focal mechanism* can be found. This is usually visualised by plotting the fault plane and auxiliary plane as great circles on a Lambert spherical projection (Fig. 2.17), allowing the type of faulting to be assessed. The compressional and dilatational quadrants are conventionally shaded black and white respectively.

Whilst the fault plane cannot be differentiated from the auxiliary plane, in terms of the radiation pattern generated, additional information, such as geological and geodetic data, can often indicate which nodal plane is the true fault orientation.

In addition, fault plane solutions can be utilised to infer the stress state that led to the production of an earthquake. The maximum compressive stress axis must bisect the dilatational quadrants of a double-couple mechanism, and is conventionally called the '*P*' axis. Likewise, the minimum compressive stress axis, or '*T*' axis must be orientated half-way between the nodal planes, but instead bisects the compressional quadrants. Additionally, the intermediate stress axis must be orthogonal to the other two axes and is, therefore, orientated along the intersection between the nodal planes, leading to its designation as the '*null*' axis. In this way the local stress field responsible for faulting can be inferred. A vertical P, T or null axis will lead to normal, thrust and strike-slip faulting respectively. (Fig. 2.17). However, it should be noted that such an interpretation, which involves slip at 45° to the maximum compressive stress, is directly at odds with the standard rock mechanics theory (as described in section 2.2.2). An explanation for these conflicting interpretations is not apparent at present and this discrepancy has yet to be resolved.

2.3.4.3 The moment tensor

In the previous section, the approximation of a seismic source in terms of a '*double-couple*' mechanism was described; where two pairs of force couples act orthogonally to one another along the fault plane and auxiliary plane. Such an approximation is based on the model of slip along a planar surface, leading to a net change in volume of zero, and is sufficient to allow fitting of a fault plane solution for most earthquakes. However, a number of seismic sources, such as those produced by volcanic systems and nuclear explosions, may require a different arrangement of body forces to represent their mechanisms. They may involve single force, a force-couple exerting a torque, a force-couple exerting no torque, a double-couple or a combination of all four of these (Fig. 2.16). As a result, the moment tensor was developed to allow these sources to be represented mathematically.

The seismic moment tensor, $\boldsymbol{M}$, is a 3x3 tensor, representing the orientation and magnitude of nine possible force-couples (Fig. 2.18);

$$M = \begin{pmatrix} m_{11} & m_{21} & m_{31} \\ m_{12} & m_{22} & m_{32} \\ m_{13} & m_{23} & m_{33} \end{pmatrix} \tag{2.16}$$

The diagonal elements represent normal force-couples, which exert no torque, whilst the remaining elements represent shear force-couples (*Aki and Richards*, 2002). Thus for a double-couple source, requiring no net change in volume, the sum of the diagonal elements must be zero. In addition, conservation of angular momentum requires that the

tensor must be symmetric, with the result that a seismic source may be represented by only six unique elements; three shear and three normal in nature. The magnitude of the moment tensor is called the scalar moment, M_o;

$$M_0 = \frac{1}{\sqrt{2}} (\sum_{ij} M_{ij}^2)^{1/2} \tag{2.17}$$

and is a function of the shear modulus, μ, and the average scalar slip, $\bar{u}$, on a fault rupture of area, A (eq 2.18 below).

$$M_0 = \mu \bar{u} A \tag{2.18}$$

If moment tensors have been found for a regional catalogue of earthquakes, the regional inelastic volumetric strain can be found by carrying out a summation of the tensors. This method was originally proposed by *Kostrov* (1974). *Jackson and McKenzie* (1988) describe its application to plate tectonics in the Mediterranean. By assuming that all the deformation in a region is seismic in nature, summation of the moment tensors elements, m_{ij}, of all the earthquakes occurring in that region during a specified length of time, T, yields the average volumetric strain rate tensor;

$$\dot{\varepsilon} = \frac{1}{2\mu VT} \sum M_0 m_{ij} \tag{2.19}$$

where μ is the shear modulus and V is the region's volume. It has been suggested that a similar tensorial summation approach could be applied to acoustic emission data.

Moment Tensor	Beachball	Moment Tensor	Beachball
$\frac{1}{\sqrt{3}}\begin{pmatrix}1&0&0\\0&1&0\\0&0&1\end{pmatrix}$		$-\frac{1}{\sqrt{3}}\begin{pmatrix}1&0&0\\0&1&0\\0&0&1\end{pmatrix}$	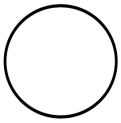
$-\frac{1}{\sqrt{2}}\begin{pmatrix}0&1&0\\1&0&0\\0&0&0\end{pmatrix}$		$\frac{1}{\sqrt{2}}\begin{pmatrix}1&0&0\\0&-1&0\\0&0&0\end{pmatrix}$	
$\frac{1}{\sqrt{2}}\begin{pmatrix}0&0&-1\\0&0&0\\-1&0&0\end{pmatrix}$	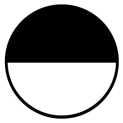	$\frac{1}{\sqrt{2}}\begin{pmatrix}0&0&0\\0&0&-1\\0&-1&0\end{pmatrix}$	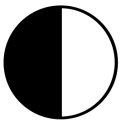
$\frac{1}{\sqrt{2}}\begin{pmatrix}-1&0&0\\0&0&0\\0&0&1\end{pmatrix}$		$\frac{1}{\sqrt{2}}\begin{pmatrix}0&0&0\\0&-1&0\\0&0&1\end{pmatrix}$	
$\frac{1}{\sqrt{6}}\begin{pmatrix}1&0&0\\0&-2&0\\0&0&1\end{pmatrix}$		$\frac{1}{\sqrt{6}}\begin{pmatrix}-2&0&0\\0&1&0\\0&0&1\end{pmatrix}$	
$\frac{1}{\sqrt{6}}\begin{pmatrix}1&0&0\\0&1&0\\0&0&-2\end{pmatrix}$		$-\frac{1}{\sqrt{6}}\begin{pmatrix}1&0&0\\0&1&0\\0&0&-2\end{pmatrix}$	

Figure 2.19. Example moment tensors and their associated focal mechanisms (modified after Dahlen and Tromp, 1998; coordinate system has been altered to north, west and up). The top two rows are an explosion (left) and an implosion (right). The bottom two rows are Compensated Linear Vector Dipole (CLVD) sources and the other rows illustrate examples of double-couple mechanisms.

2.3.4.4 Moment tensor inversion and decomposition

The moment tensor of a seismic source can be inverted for from seismic data if we know the Earth's elastodynamic response to an impulse at the source; generally termed the '*Green's function*' in seismology (*Gilbert*, 1971). *Moment tensor inversion*, as it is now referred to, is the process of determining the moment tensor elements required to produce the observed seismic waveforms recorded in response to an earthquake (*Gilbert*, 1973). This approach was first utilised by *Dziewonski and Gilbert* (1974) and has since become a standard procedure in the field of seismology. The specific methodology applied to acoustic emission data in this thesis, is provided within chapters 3, 4 and 5. However, here the general theory behind moment tensor inversion is given.

As described in section 2.3.4.3, conservation of angular momentum requires that the moment tensor be symmetric. Consequently, we are only required to solve for the *six* unique elements of the tensor. If we consider the Green's functions, $G_{ij}(t)$ for the ith seismometer responding to the jth moment tensor component, m_j, we can define a seismogram, $u_i(t)$, at the ith seismometer, such that;

$$u_i(t) = \sum_{j=1}^{6} G_{ij}(t) m_j \tag{2.20}$$

The Green's functions are defined simply as an impulsive spike, delayed by the travel time between the source and each seismometer. If the locations of the receivers and the source are known, we can therefore define a set of simultaneous equations where, $\boldsymbol{u}$, is a vector containing $u_i(t)$ at n seismometers and G is a matrix containing the Green's functions for each seismometer:

$$\mathbf{u} = \mathbf{Gm} \tag{2.21}$$

or;

$$\begin{pmatrix} u_1 \\ u_2 \\ . \\ . \\ . \\ u_n \end{pmatrix} = \begin{pmatrix} G_{11} & . & . & . & G_{16} \\ G_{21} & . & & & G_{26} \\ . & & . & & . \\ . & & & . & . \\ . & & & & . \\ G_{n1} & . & . & . & G_{n6} \end{pmatrix} \begin{pmatrix} m_1 \\ m_2 \\ . \\ . \\ . \\ m_6 \end{pmatrix} \tag{2.22}$$

If n>6, then the system is over-determined and we can invert for, $\boldsymbol{m}$, by solving in a least squares sense:

$$\mathbf{m} = (\mathbf{G}^T\mathbf{G})^{-1}\mathbf{G}^T\mathbf{u} \tag{2.23}$$

Due to the inherent symmetry of the moment tensor, as with the stress tensor (equation 2.2, section 2.2.1) it can be rotated to find its principal-axis system;

$$\mathbf{M} = \begin{pmatrix} M_1 & 0 & 0 \\ 0 & M_2 & 0 \\ 0 & 0 & M_3 \end{pmatrix} \tag{2.24}$$

Diagonalisation of ***M***, gives us three eigenvalues, each with an associated eigenvector, which are sufficient to describe the behaviour of the source. For a double-couple, the pressure axis, *P*, the intermediate axis, *B*, and the tension axis, *T*, are the associated eigenvectors of the maximum, intermediate and minimum eigenvalues, respectively. Once the moment tensor has been diagonalised, a seismic source can be interpreted by '*decomposing*' it into specified parts, defined as certain linear combinations of eigenvalues. For example, the trace of ***M***, tr(***M***), provides us with the isotropic change in volume of the source and, as such, represents the explosive, or implosive, component of the source. In other words, we can separate the diagonalised moment tensor into an isotropic part and a deviatoric part, such that:

$$\mathbf{M} = (1/3)\begin{pmatrix} tr(\mathbf{m}) & 0 & 0 \\ 0 & tr(\mathbf{m}) & 0 \\ 0 & 0 & tr(\mathbf{m}) \end{pmatrix} + \begin{pmatrix} M_1^1 & 0 & 0 \\ 0 & M_2^1 & 0 \\ 0 & 0 & M_3^1 \end{pmatrix} \tag{2.25}$$

where the remaining terms, M_i^1, are the deviatoric eigenvalues of ***M***.

As faulting involves slip along a plane, such events rarely generate significant isotropic components. However, volumetric change occurs during microcracking in rock deformation experiments (*Kranz and Scholz*, 1977; see sections 2.2.3.3 and 2.3.2.1) and, as such, the isotropic component is of greater significance at laboratory scales. This may be due to the large differences in sample size to grain size ratio and/or in the applied strain rate. A number of different decomposition schemes are used in seismology, for example decomposing into an isotropic part and three vector dipoles or into an isotropic part and three double couples. However, one of the most commonly used approaches is to invoke a '*compensated linear vector dipole*' part (or CLVD), which involves three dipoles; one of strength two in one direction and two of strength one in the opposing direction. The result is a trace of zero, so there is no net change in volume due to the CLVD. The diagonalised moment tensor may therefore be separated into an isotropic part, a double-couple part and a CLVD part as follows;

$$\mathbf{M} = (1/3)\begin{pmatrix} tr(\mathbf{m}) & 0 & 0 \\ 0 & tr(\mathbf{m}) & 0 \\ 0 & 0 & tr(\mathbf{m}) \end{pmatrix} + (1-2\varepsilon)\begin{pmatrix} 0 & 0 & 0 \\ 0 & -M_3 & 0 \\ 0 & 0 & M_3 \end{pmatrix} + \varepsilon\begin{pmatrix} -M_3 & 0 & 0 \\ 0 & -M_3 & 0 \\ 0 & 0 & 2M_3 \end{pmatrix} \tag{2.26}$$

where $\varepsilon = -M_2^1/M_3^1$. The decomposition applied in this thesis follows such an approach and is described in more detail in section 3.4.2. Some examples of moment tensors and their focal mechanisms are given in Figure 2.19. In chapter 5, example focal

mechanisms of acoustic emissions generated in sandstone are presented and decomposition of full moment tensors is utilised to demonstrate the complexity of acoustic emission sources.

2.4 Summary

Compressive loading of rock in the brittle regime can lead to the formation of faults. The failure criteria for this process can be reasonably well estimated on the macroscopic scale by considering the confining pressure, pore fluid pressure and the intrinsic properties of the material. During laboratory compression of rock in the brittle field, deviation from perfectly elastic behaviour has been observed before macroscopic failure; an effect attributed to the occurrence of microcracking and resulting in the material become weakened or 'damaged'. Given the correct conditions, these microfractures may begin to coalesce, leading to localised interaction and the eventual formation of a fault. High-frequency 'acoustic emissions' (AE), observed in laboratory experiments, have been widely attributed to the release of energy during the microfracturing of deforming rock samples. As such, a damage parameter can be derived from AE data, which may be used to predict time-dependent failure of a rock sample. However, where a period of strain-softening is observed before sample failure, such an approach leads to a consistent over-estimation of the peak stress, during the final stages of loading. Two possible causes for this are: i.) the ratio of seismic to aseismic damage decreases after

the peak stress, or ii.) the localisation of microcracking leads to the underestimation of damage estimates in the region of failure.

Localisation is the process by which this inelastic deformation goes from being distributed in a diffuse manner, throughout the material, to a coalesced and spatially distinct arrangement. It is this process which, at low effective pressures, leads to the formation of shear bands and, if loading continues, the eventual faulting of the rock. At higher effective pressures, and where sufficient porosity is present, shear bands are superseded by compaction bands as the preferred mechanism for strain localisation. The majority of information about the micromechanical behaviour of damage during localisation is derived from microstructural analysis (*Kranz*, 1983). However, this approach can only provide information pertaining to the damage state of the sample at the time of unloading. Capturing detailed information relating to the evolution of damage during the rapid process of localisation is, therefore, extremely difficult and can only be done for a suite of rocks, loaded to a range of stress levels.

However, source analysis of high quality AE data can provide an insight into the micromechanical behaviour of samples during the approach to failure. Characterisation of earthquake sources, by inversion of waveform data for a moment tensor, is regularly carried out in the field of earthquake seismology. The high quality of modern acoustic emission recording systems now provides an opportunity for the application of a similar approach to characterise the mechanisms that generate acoustic emissions in laboratory deformation experiments. Such an approach may aide attempts to improve our

understanding of natural faulting processes, as well as developing our understanding of the micromechanical processes that occur during damage localisation. In this thesis, a comprehensive description of the shear localisation process in compact and low-porosity rock is given, combining spatial analysis of AE, mechanical data, pore volume data, microstructural observations and a detailed source analysis of acoustic emissions by moment tensor inversion.

Chapter 3

Comparison of polarity and moment tensor inversion methods for source analysis of acoustic emission data

The work described in this chapter has recently been published with the citation: *Graham CC, et al*. Comparison of polarity and moment tensor inversion methods for source analysis of acoustic emission data. Int J Rock Mech Mining Sci 47 (2010) 161-169. The structure of this chapter closely follows that of the technical note (Appendix C), except that the conclusions section has been replaced with a summary section, to match the format of the other chapters.

3.1 Introduction

During rock deformation tests, energy may be released as high-frequency acoustic emissions (AE) from microfractures within the sample. These emissions provide a passive indicator of the progression of inelastic damage, during the approach to sample failure. Characterisation of the sources that produce AE can provide us with an insight into the microscopic processes that are involved in the initiation and coalescence of damage within a loaded rock sample. Such work has relevance within the field of seismology and earthquake physics; earthquakes and acoustic emissions display similar, power law, frequency-magnitude distributions (*Scholz*, 1968c; *Main et* al., 1989;

Meredith et al., 1990) and Omori Law aftershock behaviour (*Hirata*, 1987). Laboratory AE waveforms also exhibit some remarkable similarities with large scale seismological events, and monitoring and characterisation of them during experiments can improve our understanding of a wide range of processes, including fault asperity rupture (*Lei*, 2003) and volcano-seismic events (*Burlini et al*., 2007; *Benson et al*., 2008). In addition, as the search for new prospects leads to exploration in increasingly deeper closed-pit mines, so our need to understand fracture system evolution, and the processes that lead to mining-induced earthquakes, likewise increases. However, in such field-based situations, placement of sensor arrays is governed by physical constraints and may be non-ideal. Acoustic emission studies in the laboratory can give us an insight into the fracture network evolution processes that take place in such situations and provide us with an opportunity to develop laws suitable for testing at larger scales.

This paper describes two techniques used to characterise microscale fracturing, using acoustic emission data, generated within triaxially compressed granite. These microscopic processes show significant spatial and temporal development up to, and during, the period of macroscopic sample failure. Comparing the results produced by both methods shows that they are consistent with one another and demonstrates the value of the moment tensor inversion approach.

3.2 Current source analysis methods

Detailed information relating to fracture network evolution, and the onset of sample failure, can be obtained under controlled conditions during rock fracture experiments. The behaviour of this material does not depend solely upon mean field properties, such as crack density, but also the microscopic processes and feedbacks involved in cracking, how the cracks are organised and how they interact under different external conditions. In order to understand these effects, we need to have reliable information about the location, geometry and orientations of these cracks, the type of motion associated with them and the evolution of these properties with loading. Whilst samples compressed under brittle conditions will fail in a shear fashion along a macroscopic fault, microscopic analysis indicates that damage by tensile fracture also occurs on the microscale. One such study (*Katz and Reches*, 2004) focused on dry samples of triaxially compressed Mount Scott granite. Microstructural analysis indicated predominantly tensile microcracks in the early stages of loading, whilst shear fracturing became more intense and spatially concentrated with increasing load.

However, microstructural observations have the disadvantage of only being recoverable after sample unloading and do not provide us with real-time information about microcrack evolution. Alternatively, variations in horizontal and vertical ultrasonic velocities, across different regions of the sample, can be measured during the course of an experiment. As a result, the observed increase in seismic anisotropy can be used to monitor changes in bulk physical properties of the sample. P and S wave velocities may be significantly decreased by the presence of microcracks (*Hadley*, 1976), providing us with an opportunity to infer crack density values (*Stanchits et al*., 2006).

A complementary approach is the study of high-frequency pressure disturbances termed acoustic emissions (AE), which may be recorded during deformation experiments, and exhibit a rate of occurrence that is correlated with the inelastic strain rate (*Lockner*, 1993). These emissions have been attributed to the dynamic release of energy during microcracking events (*Scholz*, 1968a; *Ohnaka and Mogi*, 1982) and provide us with passively collected information about damage processes occurring within laboratory samples. Such processes can be highly complicated in nature, for instance being related to the collapse of pore-spaces and crushing of grains at high confining pressures.

Reches and Lockner (1994) propose a model of fault nucleation and growth in brittle rocks, based on observations of AE hypocentre distributions and stress-field modelling. They suggest that the nucleation and propagation of faults in granite is a consequence of the interaction of tensile microcracks, prior to the peak stress, within a ‘process zone’. The dilating microcracks lead to changes in the local stress field which, in turn, cause the interaction of cracks to spread unstably, resulting in the propagation of the process zone. As this zone grows, the material yields in a shear fashion within its central part and this creates a 'fault nucleus', which then proceeds to grow behind the process zone as it propagates through the rock. However, as mechanisms and orientations of microcracks were obtained from microstructural analysis, real time data was not available.

Improving our knowledge of these mechanisms is essential in any attempts to understand progression towards brittle failure. Source analysis of AE can elucidate the

temporal and spatial evolution of these processes. A number of approaches to the characterisation of laboratory AE sources have been taken. One such technique (*Lei et al*., 2000) utilises the distribution of P wave first motions to classify sources coarsely into four categories. A distinction is made between tensile sources and all other AE types, by finding the ratio between up (dilatational) and down (compressional) first motions. A similar method to this (*Zang et al*., 1998) assigns an average 'polarity' to each event.

Alternatively a more quantitative approach to AE source analysis is that of moment tensor inversion (MTI), which provides a tensor that describes the forces acting at the source. Such inversion has been widely utilised in the field of seismology, particularly for analysing events with a large non-double-couple component (*Dziewonski et al*., 1981; *Frolich*, 1995), such as those observed in volcanically active regions (*Julian*, 1983; *Nettles and Ekström*, 1998). It has the advantage of providing information about, not only the type of motion acting at the source, but also the associated change in volume. One study (*Feignier and Young*, 1992) applied moment tensor inversion to microseismic events recorded in the Underground Research Laboratory (URL) in Pinawa, Manitoba, where a tunnelling operation was underway. They found evidence for failure mechanisms with a non-shear component to them and reported a correlation between the location of a breakout in the tunnel roof and a region of failure mechanisms with a high tensile component. Similarly, (*McGarr*, 1992) inverted for moment tensors from ground motions in two of the South African gold mining districts. He found two very distinct sets of mechanisms; the first, predominantly double-couple in nature, the

second, displaying a substantial, coseismic reduction in volume. In addition, moment tensor decomposition has been carried out (*Ohtsu*, 1991) using AE waveforms recorded during an in situ hydrofracture test. It was shown that sources could be separated into those that were primarily shear in nature and those with a significant tensile component.

Inversion of laboratory AE data for moment tensors has also been carried out for material deformation experiments. For example, (*Shigeishi and Ohtsu*, 2001) utilised moment tensor analysis to characterise microcracking events in unconfined mortar and concrete plates. They determined crack types, orientations and volumes using this method and demonstrated a technique for damage evolution estimation from moment tensor data. AE source analysis by moment tensor inversion has also been applied successfully to other laboratory media, including salt rock (*Dahm*, et al., 1999; *Manthei*, 2005; *Manthei et al*., 2001), granite and marble (*Chang and Lee*, 2004).

Whilst a number of source analysis techniques have been proposed for AE laboratory data, the authors are unaware of any studies applying and comparing inversion with other approaches, whilst utilising the same data set. This study compares the application and results of two methods of first motion analysis and source classification, using AE data collected during the triaxial compression of granite in the brittle regime. It is a polarity technique (*Zang et al*., 1998) and the 'simplified green's function moment tensor analysis' (*Ohtsu*, 1991), which are compared in this study. The former, is a simple method for estimating the predominant source movement, based on the mean polarity of the first motions recorded across an array of AE sensors. Whilst this

approach is simple and fast, it can only provide limited information about the source type. The latter approach is a moment tensor inversion method that utilises first motion amplitudes to invert for a moment tensor. The tensor can then be decomposed and classified depending on the predominance of its constituent parts. A moment tensor inversion approach has the advantage of providing detailed information about the source mechanism of an event, including the associated degree of volume change, which is of particular use in the application of damage mechanics (*Chang and Lee*, 2004). Furthermore, eigenvalue analysis of the moment tensor allows the determination of source orientations and opening directions for all source types; information which is not obtained without a moment tensor inversion approach. A more detailed description of the methods used is given in section 3.4 (below).

In this study we compare the results of these two techniques using the same data set, in order to test the robustness and value of both an inversion approach and a more simplified method.

3.3 Experimental technique

In this section, sample selection, characteristics and preparation are discussed. This is followed by a description of the experimental set-up, the data acquisition system and the method of location of acoustic emission hypocentres.

3.3.1 Sample description

Due to the large number of acoustic emissions produced in laboratory experiments, their classification into specified source mechanisms relies on selecting generalised categories into which, in reality much more complicated, microscale events are placed. Rock types with a significant porosity will exhibit dilatant behaviour, shear localisation and compaction during compressional loading. For the purposes of this study, a low-porosity crystalline rock, in this case a granite, was utilised so as to focus primarily on the two former processes. By choosing a crystalline rock with very little pre-existing damage, this study focuses on AE source type evolution from the initiation of the damage process, through the creation of dilatancy, to the onset of localisation and eventual failure. The relatively simple source mechanisms observed in such a scenario provide a suitable data set for comparing source analysis techniques. In a material such as sandstone, with a significant porosity present, pore-collapse type sources become a major mechanism for microscopic deformation. The application of the moment tensor inversion technique discussed in this paper, to AE from sandstone in compression, will be presented elsewhere.

The rock used in this work is a red granite, sourced from Aue, Erzgebirge, Germany. It is composed of 30% quartz, 40% plagioclase, 20% K feldspar and 10% mica (*Zang et al*., 1998). The grain size within this rock type varies between 0.9 and 1.8mm, with an average value of 1.3mm. The uniaxial compressive strength of the Aue granite is in the range of 127-141 MPa (*Zang*, 1999). Porosity was measured as 1.3% and the Poisson's

ratio was estimated as 0.17. A cylindrical sample was used with a length, *l*, of 125mm and diameter, *d*, of 50mm, giving a ratio *l*/*d* of 2.5. The test was carried out at a confining pressure of 20MPa on a dry sample, which failed in a brittle fashion with relatively localised damage. The resulting fault trace was orientated at an angle of approximately 30º from the maximum compressive stress (Figure 3.1a).

3.3.2 Equipment set-up

A servo-operated MTS 4600kN loading frame (MTS Systems Corporation 1996) was used to apply the maximum stress to a cylindrical sample of red Aue granite. The surrounding hydraulic oil within the pressure vessel, provided a confining pressure of 20MPa to the sides of the cylinder whilst the sample was protected in a rubber jacket. The loading frame and pressure vessel are shown in Figure 3.2. Eleven piezoelectric crystal transducers (PZT) were contained within brass housings with conformably shaped bases, so as to give a tight contact with the sample. These housings were then bonded to the sample surface with epoxy in the arrangement shown in Figure 3.1b. The transducers, with a frequency range of 0.1-2MHz, provided acoustic emission waveforms, which were then subjected to an amplification of 40dB by Physical Acoustics Corporation preamplifiers. The waveforms were then digitised and recorded by a 16 bit data acquisition system (DaxBox, Prökel GmbH). The amplitude recording threshold was set to ±300mV. However, a further, floating threshold was applied during the P-wave arrival time picking procedure, which is described below.

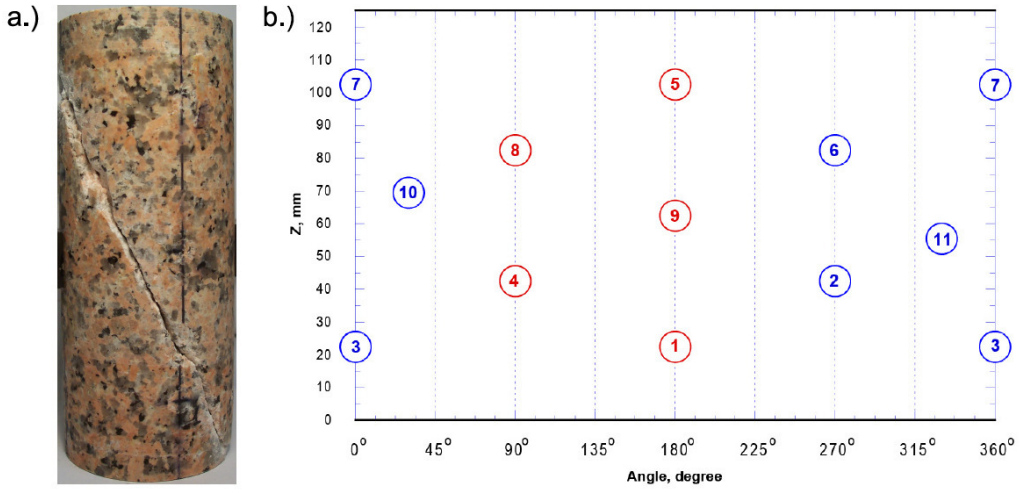

Figure 3.1. a.) Aue granite sample after failure and unloading (125mm height). b.) Projected sample surface showing position of AE sensors during testing. Sensors highlighted in red were used as transmitters for ultrasonic velocity measurement.

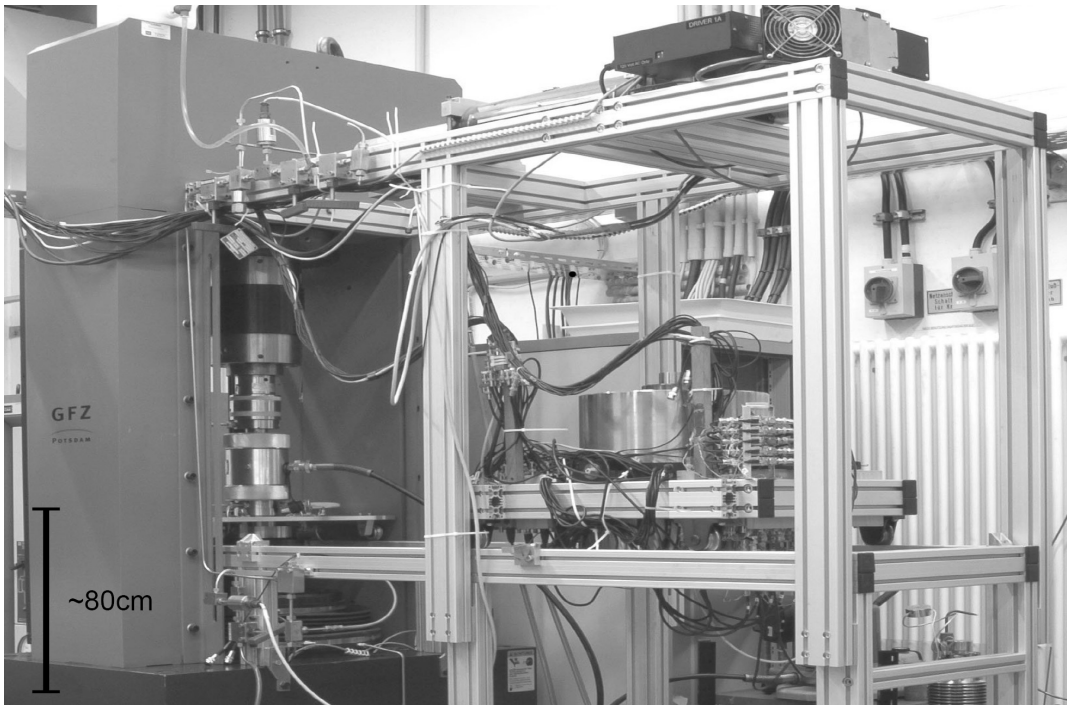

Figure 3.2. The MTS loading frame and confining pressure vessel used for the triaxial compression of the Aue granite.

Following *Lockner et al*. (1991), the rate of acoustic emissions was used as a feedback control for the press, thereby drawing out the length of the failure process and allowing a greater number of the AE to be successfully located, up to and during the post-peak stress phase. This process leads to a decrease in strain rate before failure and a resultant decrease in sample strength, making the data unsuitable for carrying out time-dependent modelling. However, it is particularly useful when investigating source behaviour of acoustic emissions in compact rock, as a more extensive AE catalogue is recorded.

Variations in P-wave velocity were monitored during loading by applying an electrical pulse to three PZTs at minute intervals. The resulting arrival times and amplitudes were then recorded at each sensor in the array, allowing vertical and horizontal velocities to be determined for a number of different regions within the sample. P-wave arrival times of AE waveforms were then picked automatically, using an Akaike Information Criterion (AIC) based approach (*Leonard and Kennett*, 1999). A floating threshold was applied, depending on the local noise level for each particular channel. A more detailed account of the setup for this experiment, and the onset time picking process, can be found in *Stanchits et al*. (2006).

3.3.3 Event location

Source location was based on automatic picking of P-waves for a minimum of eight sensors. After selection of P-wave arrival times and amplitudes, as described in section

3.2, hypocentre determination was carried out automatically using a procedure based on the downhill simplex algorithm (*Nelder and Mead*, 1965), which includes consideration of changes in the anisotropic velocity field. The resulting location precision was estimated at ±2.5mm.

3.4 Methodology

After successful location of events was carried out, two different techniques for characterising and classifying sources were applied to the data. The first method used is that of *Zang et al*. (1998), where events are classified according to the polarity of the first motions at each sensor. The second approach involves a full moment tensor inversion, the methodology for which is described by *Ohtsu* (1991). In this section, a description of both of these approaches is given.

3.4.1 Polarity technique

The polarity classification method used in this study is described by (*Zang et al*., 1998). Here, the first motion amplitude, A_i, at k sensors, is used to find an average polarity for each event, according to:

$$pol = \frac{1}{k}\sum_{i=1}^{k} sign(A_i) \tag{3.1}$$

This provides us with an estimate of the net polarity of the volume change at the location of the source. Classification is then carried out within three selected ranges, which are ascribed to the formation of different types of microcracks. AE are described as S-type events (shear) for a polarity between -0.25 and +0.25, T-type (tensile) for pol<-0.25, or C-type (collapse) for pol>+0.25. Once sources have been classified, the best-fitting double-couple total mechanism can be fitted to the first motion amplitudes for those events identified as shear. Orientations of shear fractures can then be determined from the resulting focal mechanisms (*Zang et al*., 1998), as they should correspond to one of the two nodal planes. This assumption (pure double-couple) is analogous to the typical focal mechanism in earthquake seismology, prior to the digital era. For natural tectonic seismicity it is often a very good assumption. However, this is not the case for laboratory or mining-scale induced events.

3.4.2 Moment tensor inversion technique

Moment tensor inversion has been regularly applied in the field of seismology, since the advent of digital recordings, and allows analysis of the mechanism acting at the source of the earthquake (*Dziewonski et al*., 1981; *Frolich*, 1995). The source is represented as a 3 by 3 tensor, known as the moment tensor, **M**, which is a function of the orientation

and size of the source. Each element in the array represents one of 9 force-couples acting at the source. To conserve angular momentum **M** is symmetric and, therefore, contains six independent elements; 3 tensile or compressional couples along the diagonal and a remaining 3 shear couples off the diagonal. The scalar moment M_0 gives us the magnitude of the moment tensor and is the product of the shear modulus, μ, rupture area, A, and average scalar slip on the fault, $\bar{u}$, (eq. 3.2).

$$M_0 = \mu \bar{u} A \tag{3.2}$$

The full moment tensor describes a range of source types that include shear, tensile, mixed-mode and compaction events. A number of methods have been developed to invert for these elements from seismic waveforms, using arrival times and amplitudes of, generally, several seismic phases.

However, for acoustic emission waveforms the effects of reflections and ringing within the sample often lead to a complicated coda, or tail, to the seismograms, where shear and surface waves / normal modes are not readily distinguishable. Therefore, any moment tensor inversion based on laboratory measurements should, preferably, require only P-wave data; the only reliable phase. If the double-couple approximation holds (i.e. the source is pure or simple shear) then there will be no volumetric change at the source and the trace of **M** will be zero.

For macroscopic earthquakes, the volumetric component is rarely distinguishable from zero. However, microstructural analysis of experimentally deformed rock samples, regularly demonstrates that such sources can be much more complicated than most earthquake sources and are often associated with a significant volume change. A great advantage of moment tensor inversion of AE is that it determines a volumetric component, where one exists above the detection limit. Furthermore, unlike some techniques, it can provide information on the orientation of all sources.

Standard elastic wave theory (*Aki and Richard*, 2002) allows us to express the elastic displacement **u**(**x**,t), recorded at position **x** and time *t* and due to a displacement continuity **b**(**y**, t) at position **y**, as a function of the moment tensor **M**. Let us consider **M** to be the product of the initial discontinuity and the elastic constants of the medium, such that;

$$M_{pq} = C_{pqkl} b_k n_1 \,, \tag{3.3}$$

where **n** is the normal vector, defined positive outward from the surface of the crack. We can then represent the resultant waveform as;

$$u_i(\underline{x},t) = G_{ip,q}(\underline{x},\underline{y},t) M_{pq} * S(t), \tag{3.4}$$

where the product of **M** and the spatial derivative of the associated Green's functions, is convolved with the source-time function *S(t)*. The Green's function describes the impulse response of the medium to a spike, measured at location **x** on the sample boundary. In the SiGMA method (*Ohtsu*, 1991; *Ohtsu*, 1995; *Shigeishi and Ohstu*, 2001), only the P-wave part of the full-space Green's function is selected, allowing for a simplification of the problem when applied to an isotropic, homogenous medium. This is a reasonable assumption for the Aue granite, which at these frequencies can be considered as seismically isotropic to within ~1ms^{-1} (V_{rad}/V_{ax}~0.9991). We are then left with an equation for P-wave amplitude, dependent upon **M**, but not upon time;

$$A(\underline{x}) = \frac{C_s \mathrm{Ref}(\underline{t},\underline{r})}{4\pi\rho R v_p^3}(r_1, r_2, r_3)\begin{pmatrix} m_{11} & m_{12} & m_{13} \\ m_{12} & m_{22} & m_{23} \\ m_{13} & m_{23} & m_{33} \end{pmatrix}\begin{pmatrix} r_1 \\ r_2 \\ r_3 \end{pmatrix} \tag{3.5}$$

Here, A is the displacement produced by an AE source (Fig. 3.3a) at point **y** and recorded at a position, **x**, which is a distance *R* away, in a direction **r** = (r_1, r_2, r_3). It is important to note that in the notation here, **t** is not time but the direction of AE sensor sensitivity, such that *Ref(t, r)* is the reflection coefficient at the observation surface. In addition, ρ is the density of the medium, v_p is the P-wave velocity and C_s is a calibration coefficient. With observations of P-phase amplitudes from six or more receivers, it is therefore possible to solve for the unique moment tensor elements. *Ohtsu* (1991) argues that, since they are not dependent upon time, the resulting solutions are inherently stable.

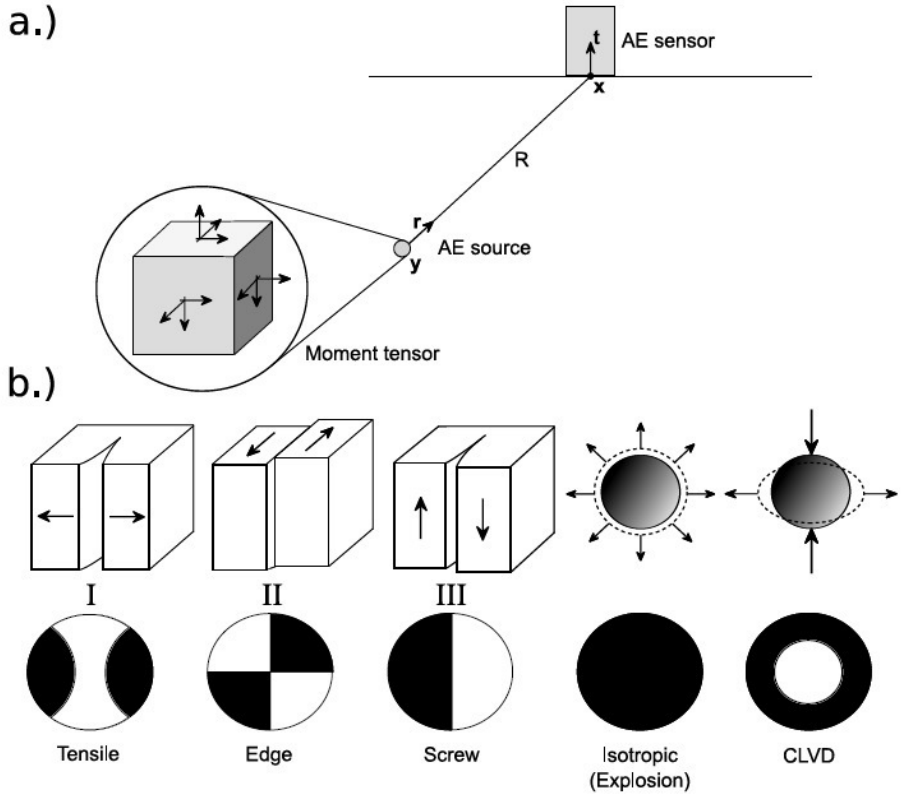

Figure 3.3. a.) Source-receiver geometry assumed for the moment tensor inversion. b.) Idealised acoustic emission sources and their associated focal mechanisms, including the 'Compensated Linear Vector Dipole (CLVD) mode.

Once the moment tensor of a source has been found, decomposition can be carried out using its eigenvalues (λ_{max}, λ_{int}, λ_{min}), to resolve the double-couple (DC) and non-double-couple (NDC) parts of the source (Fig. 3.3b). For example, *Knopoff and Randall* (1970) proposed that the tensor be split into a double-couple (DC) component, an isotropic component (ISO) and a deviatoric or 'Compensated Linear Vector Dipole' component (CLVD). In Ohtsu (1991) the maximum shear and CLVD components are defined as X and Y respectively, giving a DC part (X, 0, -X) and a CLVD part (Y, -0.5Y, -0.5Y). This leaves the remaining isotropic part in all directions, Z. The relative proportions of X, Y

and *Z* can then by found by first normalizing with respect to the maximum eigenvalue, such that;

$$\lambda_{max} / \lambda_{max} = 1 = X + Y + Z \quad (3.6)$$

and then solving simultaneously with;

$$\lambda_{int} / \lambda_{max} = 0 - 0.5Y + Z \quad (3.7)$$

$$\lambda_{min} / \lambda_{max} = -X - 0.5Y + Z \quad (3.8)$$

Hence, values of X=0, Y+Z=1, would represent an entirely tensile source, whilst a purely shear source would lead to X=1 and Y=Z=0. Sources can then be classified using criterion suggested and tested by (*Ohtsu*, 1995); for X>60% the source is considered to be predominantly shear, for X<40% it is classified as tensile and for 40%<X<60% it is termed 'mixed-mode' in nature, having both significant shear and tensile components.

Finally, in this study the trace of the moment tensor was used to find those events leading to a net loss in volume, which are classified as 'collapse' sources. It should, however, be noted when interpreting the results that this, by definition, excludes collapse sources with a significant CLVD component, which lead to no net change in volume. There also remains the possibility of some aseismic component to a source, which cannot be determined. However, the major advantage of the moment tensor technique is

that the associated eigenvectors can then be used to obtain crack opening directions for *all* source types. Having the full tensor also allows detailed comparison of the inferred fracture or fault directions with microstructural data, or principal components with applied strain direction.

3.5 Results

3.5.1 Spatial progression of fracture

Triaxial compression was carried out on a cylindrical sample of red Aue granite with AE feedback controlling the loading rate. Initially a constant displacement rate of 20μm/min was applied until significant acoustic emissions were detected for feedback control to begin. The peak differential stress applied during the test was 365MPa and failure occurred just before 7000s, along a macroscale fault plane with an orientation of approximately 30º to the maximum principal stress. Whilst AE feedback control lead to a significant decrease in the rate of piston displacement (with displacement eventually becoming constant just before failure), a notable increase in the rate of acoustic emissions was still observed before failure. However, this increase in AE rate was significantly less than that produced during a constant displacement rate test. Figure 3.4 shows the loading curve for the experiment and the variation in the vertical and horizontal P-wave velocities through the sample, V_{ax}, V_{h1}, V_{h2}, V_{h3}, respectively.

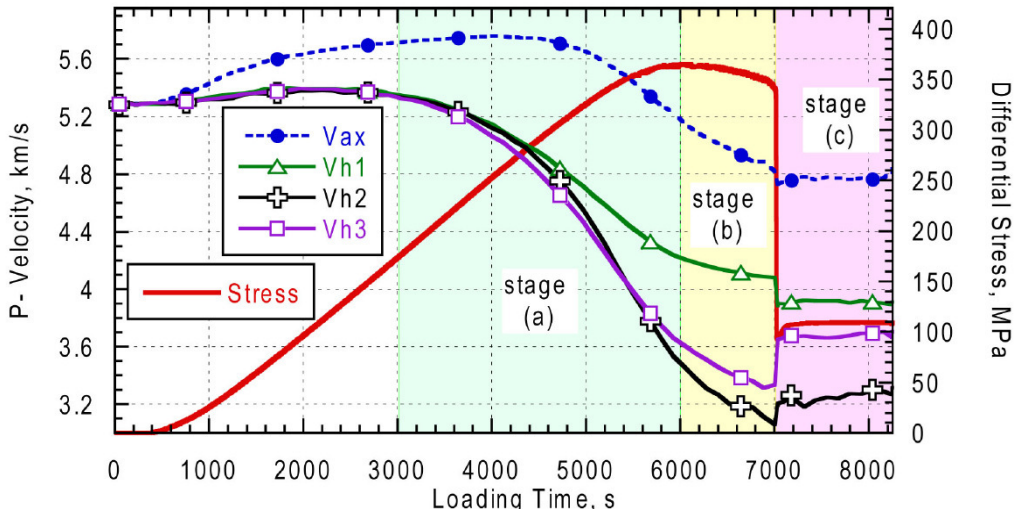

Figure 3.4. Differential stress applied to the sample during the course of the experiment. P-wave velocities are also shown for three horizontal zones (Vh1, Vh2, Vh3) and the axial P wave velocity (Vax). Three stages (a-c) of the loading process are highlighted.

Hypocentre locations (Figures 3.5 and 3.6) of large magnitude events, from different time windows during the loading process, show a progressive change from diffuse (stage a) to more localised (stage b) AE-associated damage, concentrated near the eventual macroscopic fault plane. Localised fracturing starts at the side of the cylinder, and progresses towards its bottom corner during failure. It should be noted that the uncertainty in source location is clearly visible, as some events are located outwith the sample box. The variation in event locations and source types are shown for both the polarity (Fig. 3.5a-c) and MTI methods (Fig. 3.6a-c). Both indicate a significantly higher proportion of tensile to shear events in the initial loading phase, followed by an increase in microshearing over time. Only shear and tensile sources are shown here for clarity, but other events were also classified as collapses (both techniques) or mixed-

mode sources (MTI only). It should also be noted that both techniques indicate a degree of tensile activity within the failure zone, even during the final stages of loading.

3.5.2 Temporal variation of sources

Due to the large number of AE events produced during loading of the Aue granite, the source mechanisms were analysed in terms of temporal variation in the relative proportions of each mechanism type. After events were classified into different source types, a rolling average of the number of events for each source type was calculated, for every hundred events and with a quarter overlap between windows. As the inversion process requires a number of events to be discarded, due to the lack of a well-fitting solution, the number of events for each source type was normalised by the total number of events within each window.

The resulting plots (Fig. 3.7 and 3.8), derived from both the polarity and MTI classifications, have many similarities. Both techniques clearly show that, during the early stages of acoustic emission (stage a), predominantly distributed tensile motion is the preferred mode of fracture on the microscopic scale. However, close to peak strength (stage b), a change to primarily shear microfracture, localised near the eventual fault plane, is also observed. Similar findings have been reported in a number of other studies involving low-porosity materials with little pre-existing damage (*Stanchits et al.*, 2006; *Reches and Lockner*, 1994).

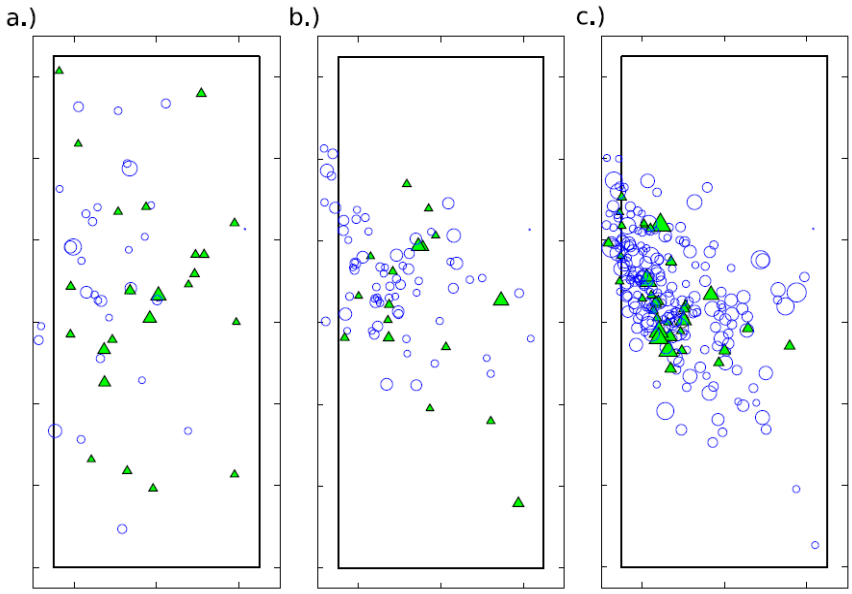

Figure 3.5. a-c.) Hypocentre locations for granite sample, Ag72r. Source types are shown as derived by the average polarity technique. Predominantly shear and tensile source types are indicated by open circles and closed triangles respectively. Symbol size is directly related to event magnitude and small magnitude events are not shown, for clarity. Slices are through the Y-Z plane during different time intervals; a.) 3000-6000s (stage a), b.) 6000-7000s (stage b), c.) 7000-8620s (stage c). The inner rectangle denotes the location and size of the sample.

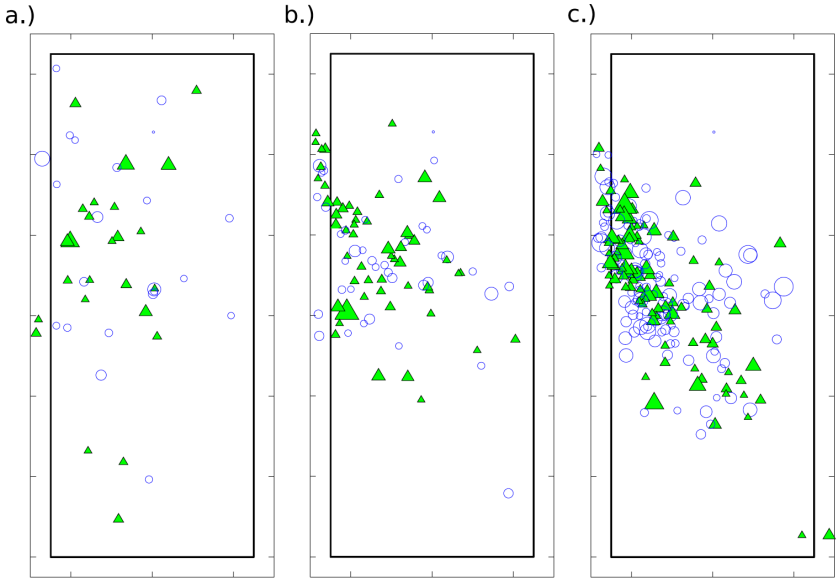

Figure 3.6. a-c.) Hypocentre locations for granite sample, Ag72r. Source types are shown as derived by moment tensor inversion. Predominantly shear and tensile source types are indicated by open circles and closed triangles respectively. Symbol size is directly related to event magnitude and small magnitude events are not own, for clarity. Slices are through the Y-Z plane during different time intervals; a.) 3000-6000s (stage a), b.) 6000-7000s (stage b), c.) 7000-8620s (stage c). The inner rectangle denotes the location and size of the sample.

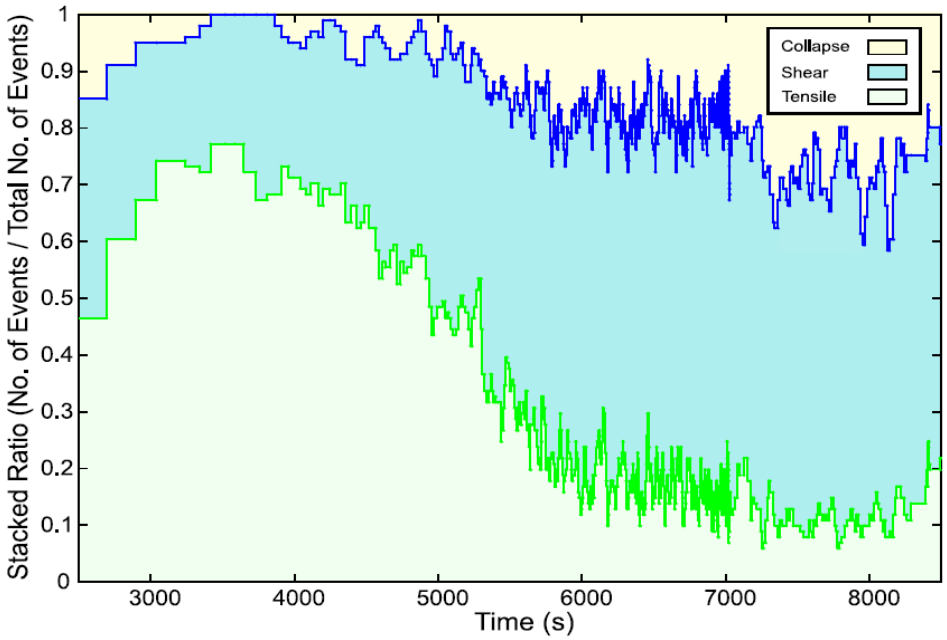

Figure 3.7. Temporal variation in source type dominance, as classified by the average polarity method.

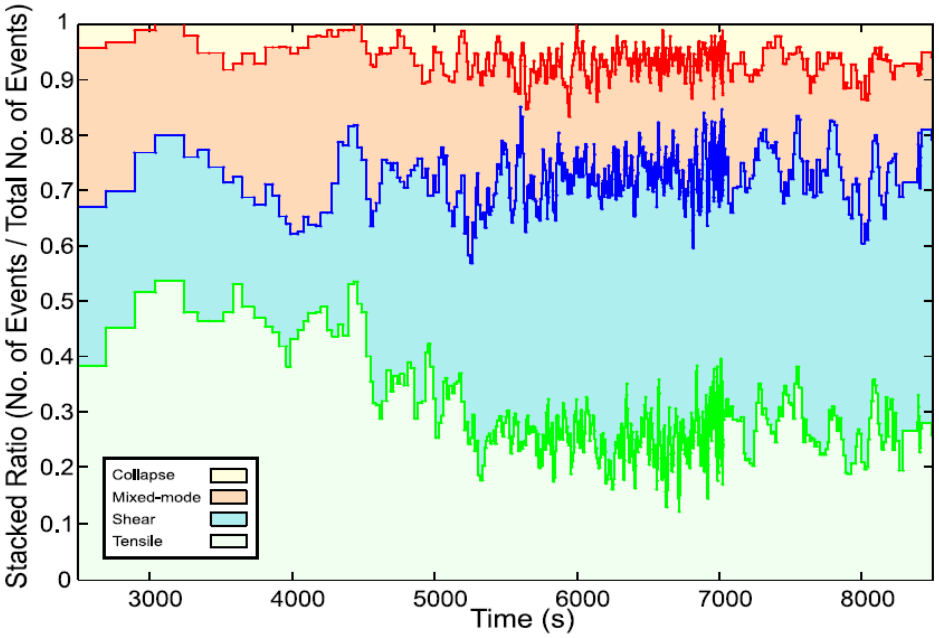

Figure 3.8. Temporal variation in source type dominance, as classified using moment tensor inversion.

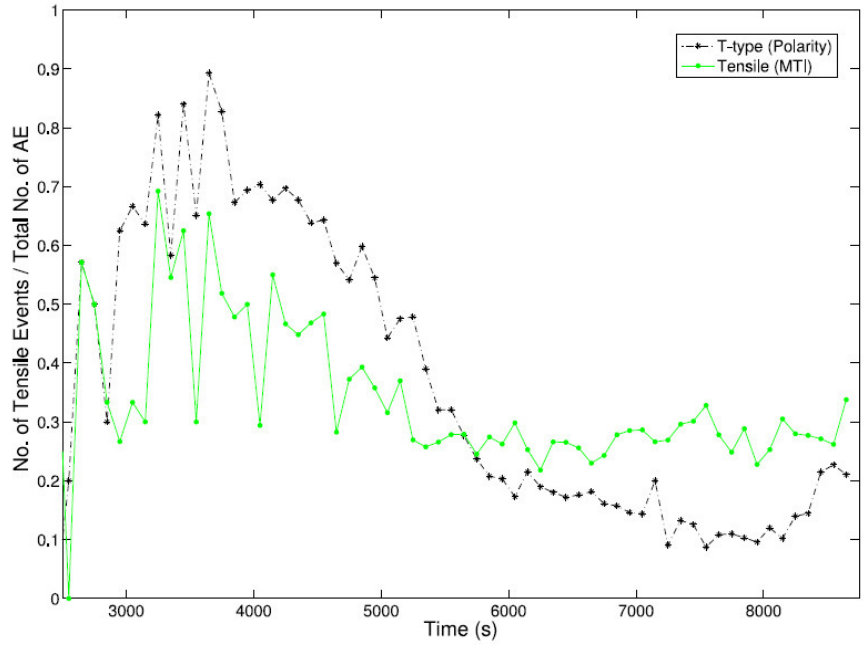

Figure 3.9. Variations in the proportion of tensile to total number of AE events. The dotted line and crosses represents results of the average polarity method. The straight line and circles indicate the results for moment tensor inversion.

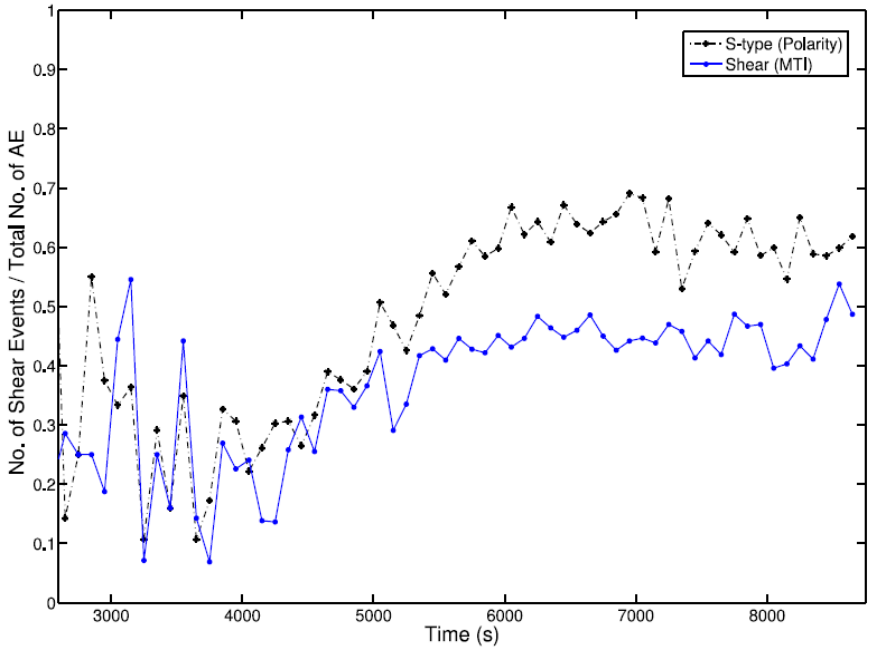

Figure 3.10. Variations in the proportion of shear to total number of AE events. The dotted line and crosses represents results of the average polarity method. The straight line and circles indicate the results for moment tensor inversion.

Figures 3.9 and 3.10 show the similarity between the resulting source type variability determined by both methods, with tensile sources initially dominating, before being superseded by shear sources. The results for the behaviour of shear sources are particularly similar, and this may be a reflection of the simplicity of the source type. In other words, a relatively shear dominant source is more common than a relatively tensile dominant source. In addition, the peak in tensile events in Fig. 3.9 is somewhat smaller for the MTI method, and is attributed to the addition of a 'mixed-mode' source type, with both a significant shear and tensile component. Whilst the gradient in the variation in MTI tensile events is shallower, the general trends are still very similar in both Figures 3.7 and 3.8. In addition, the percentage of 'collapse' type sources is somewhat smaller in the MTI case, as is discussed below (section 3.6.1).

3.6 Discussion

3.6.1 Physical mechanisms

Whilst we can separate sources into different classes, using either of the techniques described in this paper, we must also consider the physical mechanisms that generate such signals before attempting to utilise the results. In the case of the average polarity technique, we must be aware that we cannot necessarily, for example, differentiate between a shear source with no tensile component and a shear with a small tensile

component. Equally, C-type events that are described as 'collapse' mechanisms are sources containing a predominant collapse component, yet they will also require shearing between grains to be physically achievable in reality. Conversely, the moment tensor technique allows those events with an implosive net volume change to be identified as collapse sources, by using the trace of M. As a consequence, we would expect the average polarity technique to classify somewhat different proportions of event types. Additionally, the presence of a third class of source, the mixed-mode type, in the MTI method must reduce the percentage of shear or tensile sources that are identified. This illustrates the advantages of the full moment tensor technique for discriminating in more detail between competing microstructural processes.

3.6.2 Comparison of the two techniques

The results of this study are encouraging for the field of AE source analysis. When applying two dissimilar techniques to an AE laboratory data set, we see a concurrent set of results from both methods. For large datasets, finding the average polarity of events provides a quick and simple method to analyse sources, demonstrating similar results, albeit less informative results, to the full moment tensor inversion. Unlike the polarity technique of *Zang et al*. (1998), the SiGMA approach may not always produce a solution, as it is more sensitive to issues such as the uncertainty in source location. This uncertainty is of the order of ±2.5mm, meaning that it is possible for an event near the sample edge to be located outwith the cylinder. However, where a solution is

achievable, MTI provides a greater degree of information about the source involved, such as orientations of non-DC events and a full description of the source in terms of its 6 independent force couples. In addition, moment tensors provide a description of the volumetric change at the source and can be used to sum up AE-associated damage within the rock, during the loading process (*Shigeishi and Ohtsu*, 2001; *Chang and Lee*, 2004). Such an approach is clearly a powerful tool when investigating damage progression, in terms of the characteristics, organisation and evolution of microcracking.

One of the major challenges within this field is that of processing increasing amounts of data. In order to overcome this during analysis, a wide range of sources with a spectrum of different mechanism components must be reduced to a small number of source types, by placing them into a number of broad categories. The tendency is to consider them as specific and distinct mechanisms, whereas the reality is closer to a continuum of source types, which are placed in certain classification 'bins', associated with common behavioural elements. This should always be considered when using such an approach, particularly when comparing data from distinctly different materials. Further work into the nature of such sources in different media and under different laboratory conditions would help to elucidate any differences.

3.7 Summary

Temporal and spatial changes in acoustic emissions in rock deformation experiments can elucidate the processes that produce microseismic events in the earth, such as those observed in mining structures and hydrocarbons reservoirs. In order to properly understand the evolution of these changes, the microscale mechanisms involved must also be considered. This can, in part, be done by analysing experimentally produced AE sources. A number of techniques have been applied in this way, but with very little comparison between methods. In this study, two different methods were applied to the same data set in order to make such a comparison; one based upon polarity of first motions, the other involving a moment tensor inversion from the amplitudes of the first motions.

Sources were located, analysed, classified and their varying proportions plotted against time. Whilst the categories that sources were sorted into, for each technique, are somewhat different in their meaning, the results are still encouragingly similar. Both indicate that for this data set, produced during the triaxial compression of a granite, tensile sources dominate during the early stages of loading, but are superseded by shear sources prior to failure. Such behaviour is only expected in materials with a low-porosity and no pre-existing crack fabric. The following two chapters demonstrate this by investigating source behaviour in a sandstone. The results from this study suggest that both the average polarity and SiGMA methods provide useful information about the characteristics of AE sources and, hence, the associated damage within a deforming

rock. Source analysis of acoustic emissions, and moment tensor inversion in particular, shows significant potential for characterising and elucidating the processes involved in brittle damage in laboratory rock fracture tests.

Chapter 4

Moment tensor characterisation of damage localisation in triaxially loaded sandstone from acoustic emission data

4.1 Introduction

During the deviatoric compressive loading of rock beyond its elastic yield strength, the material may begin to accommodate strain in an inelastic and permanent fashion. This accommodation is made possible by a range of microscale mechanisms, dependent upon the environmental and material conditions. Given the correct circumstances, this damage will become increasingly localised within the material, until the rock becomes sufficiently weakened for fault propagation and sample failure to occur. The micromechanical evolution of damage during this localisation process is still not fully understood, but varies significantly from material to material (*Paterson and Wong, Chapter 5*, 2005).

A number of laboratory techniques can elucidate this process. By monitoring variations in ultrasonic velocities across a loaded sample, it is possible to infer the density of microcracking (*Hadley*, 1976; *Ayling et al*., 1996; *Stanchits et al*., 2006) and its variation with time. Detailed investigation of damage coalescence has also be carried out by the direct observation of rock sample microstructure, after loading has been completed

(*Kranz*, 1983). A number of studies involving such microstructural analysis provide evidence of a transition from diffuse to more spatially concentrated microcracking as the failure stress is approached, for both compact and porous materials, including granite (*Peng and Johnson*, 1972; *Tapponnier and Brace*, 1976; *Kranz*, 1979; *Katz and Reches*, 2004) and sandstone (*Sangha et al*., 1974; *Bésuelle, et al*., 2003; *Menéndez et al*., 1996). However, there are a number of disadvantages to this approach, including the possibility of additional sample damage during unloading and thin section preparation, as well as the non-trivial problem of interpreting a 2-dimensional slice taken from a 3-dimensional sample. Furthermore, damage at different stages in the loading process cannot be observed for the same sample.

In contrast, the dynamic release of energy during microcracking, as high-frequency pressure disturbances (*Scholz*, 1968a; *Ohnaka and Mogi*, 1982), or 'acoustic emissions' (AE), can provide real-time information about the accumulation of inelastic damage within a rock-mass. The rate of emission of these events has been shown to correlate with the inelastic strain rate during such tests (*Lockner*, 1993). The advantages of such an approach include the passive nature of the monitoring process and the reproducibility of the phenomenon in the laboratory, providing the opportunity for investigation under controlled conditions. A significant number of studies have utilised AE-derived damage parameters to successfully invert for the stress-strain history of a sample (*Cox and Meredith*, 1993; *Ojala et al*., 2003). However, such an approach can lead to an over-estimation of the peak stress, possibly due to the weakening affect of microcrack coalescence (*Ojala*, 2003).

By locating acoustic emission sources, this coalescence of inelastic damage can be observed (*Lockner*, 1993; *Rao and Kusunose*, 1995; *Lei et al*., 2000; *Vinciguerra et al*., 2004; *Benson et al*., 2007). *Lockner* (1991) demonstrated that utilising the rate of AE to control loading rate can lengthen the post-peak stress phase, providing enhanced detail of the fracture nucleation period. Damage localisation can be investigated by quantifying the degree of spatial clustering of AE source locations. *Hirata* (1987) determined the correlation integral from the locations of acoustic emissions, produced during a creep test on the Oshima granite, and demonstrated that their spatial distribution was approximately fractal. They also observed a decrease in the fractal dimension of the distribution during the evolution of the fracture process, indicating a progression from a volume-filling to a more planar spatial distribution.

This drop in fractal dimension has since been observed in a range of materials, including the Flechtingen sandstone (*Zang et al*., 1996). *Reches and Lockner* (1994) proposed a model for fault nucleation and growth, based on stress-field modelling and the locations of AE produced by Westerly Granite. Their model involved the development of a damage-rich 'process zone' that preceded the propagation of the growing fault. They argued that the increasing density of diffusely growing tensile fractures during the initial stages of loading would lead to their eventual interaction, resulting in shearing and the propagation of the process zone through the sample. Observations of AE hypocentre locations during the quasi-static loading of granite appear to support this hypothesis (*Zang et al*., 2000).

It is therefore reasonable to expect that the sources responsible for producing acoustic emissions may include a range of mechanisms with varying degrees of tensile or shear behaviour. One approach to characterising AE sources is to develop a parameter based on the average polarity of first motions recorded across an array of AE sensors. This provides a metric that is essentially related to the net degree of implosive or explosive volume change at the source. *Zang et al*. (1998) used one such approach to characterise damage evolution in symmetric and asymmetric uniaxial tests on Aue granite. This method is discussed in more detail in chapter 3 (section 3.4.1). *Lei et al*. (2000) used a similar approach, based on the distribution and polarity of first motions of AE waveforms recorded during the triaxial compression of hornblende schist. *Stanchits et al*. (2006) analysed first motion polarities to characterise inelastic damage in samples of granite and basalt, observing a change in the dominant microscopic mechanism, from tensile to shear cracking, prior to failure.

However, this approach to source analysis is limited in the detail it can provide, being insufficient to distinguish the constituent components of a mixed-mode mechanism. In the study of earthquakes, source analysis from waveform data is routinely carried out. The simplest approach here is also a polarity method, where the source mechanism is considered to be the result of the action of two force-couples, orientated orthogonally to one another. The best-fit of such a 'double-couple' to the first motion polarities is then found, given the spatial distribution of the recording sensors. This is known as the 'double-couple' approximation and is generally sufficient to represent an earthquake

source where slip is along the surface of a plane, with zero change in volume occurring during the event (*Aki and Richards*, 2002).

However, in situations where a volumetric component to the source *is* present, proper characterisation of the source requires a more general full moment tensor inversion (MTI). In this case a tensor, representing the forces acting at the source, is derived by inverting from waveform data (*Dziewonski et al*., 1981; *Frohlich*, 1995). *Julian* (1983) and *Nettles and Ekström* (1998) used moment tensor inversion to demonstrate that volcanic sources can contain a volumetric component and may be intrinsically non-double-couple (NDC) in nature. Moment tensor inversion has also been used to demonstrate that microseismics, produced in underground structures such as mines, can have mechanisms with a significant volumetric component (*Feignier and Young*, 1992; *McGarr*, 1992). This approach to source analysis has also been successfully applied to hydraulically induced microseismics (*Dahm et al*.,1999; *Ohtsu*, 1991).

Consequentially, a number of MTI techniques have been developed and applied to a range of materials including salt rock (*Manthei et al*., 2001; *Manthei*, 2005), concrete (*Ohtsu*, 1995; *Yuyama*, 2005; *Shigeishi and Ohtsu*, 2001) and rock (*Chang and Lee*, 2004; *Carvalho and Labuz*, 2002; *Shah and Labuz*, 1995; *Benson et al*., 2008).

Shah and Labuz (1995) used moment tensor inversion to show that in unconfined charcoal granite, the dominant failure mechanism from AE was sliding on inclined planes. They also found evidence for a further group of sources, which were orientated

parallel to the loading axis and an inhibition of crack growth perpendicular to the loading axis. In section 3.5.2 (Figure 3.8), moment tensor inversion was applied to AE data from triaxial compression of granite and a clear shift in the dominant damage mechanism was observed, from sources with a high tensile component to those with a high shear component, during the lead-up towards failure. In essence, the tensile component to microfracturing in the early stages of acoustic emission, might be considered to be a prerequisite for shear localisation, essentially 'making space' for large scale micro-shearing to take place. Such dilatancy associated with incipient failure is consistent with preferential fluid flow in boreholes, along fractures that are critically orientated with respect to the tectonic stress field (*Vernik and Zoback*, 1992; *Boness and Zoback*, 2004).

As a consequence, one might intuitively expect that the introduction of porosity or pre-existing damage, might significantly affect the mechanistic behaviour of microcracking during the localisation process. *Menéndez et al*. (1996) proposed that in brittle deformation of sandstone, early AE activity may be due to the rupture of lithified grain boundaries, leading to slip and rotation of grains. Whilst detection of such mechanisms with microanalysis is non-trivial, they suggest that source analysis of AE may provide an opportunity for more detailed investigation. *Fortin et al*. (2009) used an average polarity method to demonstrate that the most common type of AE produced during shear localisation in triaxially compressed Bleurswillers sandstone is a 'C-type' (implosion) event. This contrasts markedly to observations of AE sources in compact rock. They propose that a pore-collapse is a mixed-mode event, requiring a component of shear in

order for material to infill a pore-space, but it was not possible to resolve this using an average polarity source analysis.

In order to explore in more detail the evolution of AE-inducing damage in compressed sandstone, this study utilises a combined approach involving quantification of coalescence from AE hypocentres and moment tensor inversion for source mechanisms to characterise and elucidate the localisation of damage, a hiatus in its development and the eventual failure of the sample.

4.2 Methodology

This section describes the experimental approach, including the selection and preparation of the sample, the equipment used for the test and the set-up for collection of ultrasonic, AE and pore fluid data. Finally, the treatment of the AE waveforms is discussed, from the location of hypocentres and the moment tensors inversion process, to the decomposition and classification of sources into selected source types.

4.2.1 Sample description

In order to investigate the source mechanisms of acoustic emission during loading of low-porosity rock a clean, massive sandstone, with low clay-content was selected for

testing. The Permo-Triassic Hopeman sandstone was obtained from the Clashach quarry, in the Northeast of Scotland. This aeolian sandstone is an onshore analogue for hydrocarbon reservoir rocks in the Moray Firth, UK. A detailed characterisation is provided by *Crawford et al*. (1995). It is a medium-coarse grained, well-sorted, subarkosic arenite (Figure 4.1), composed of sub-rounded quartz grains (89%) and K-feldspar (11%). It has a porosity of approximately 13% and the grains are cemented together by secondary quartz overgrowths. As a result, samples have a significantly high uniaxial strength, for sandstone, of 105.8MPa (*Crawford et al*., 1995). The simple mineralogy and homogeneous nature of the Clashach sandstone make it a suitable material for investigating damage mechanisms in a porous rock. A cylindrical sample, 105mm in length and 50mm in diameter, was cored perpendicular to the bedding planes.

4.2.2 Experimental set-up

Prior to the test, the sample was left under vacuum overnight. It was then saturated with water and flushed through to remove any loose particles. During the course of the test, pore fluid pressure was maintained at a constant value of 10.5MPa. A volumometer could then be used to monitor changes in pore fluid volume and, hence, interconnected porosity during the course of the experiment. The sandstone sample was deformed under triaxial compression in the Deformation and Rheology Laboratory at the GeoForschungsZentrum Potsdam. We used a servo-operated MTS 4600 kN loading frame (MTS Systems Corporation, 1996) and carried out the test at room temperature.

The loading frame and pressure vessel are shown in chapter 3, Figure 3.2. A confining pressure of 50.5MPa was applied to the sample with hydraulic oil, giving an effective pressure of 40MPa.

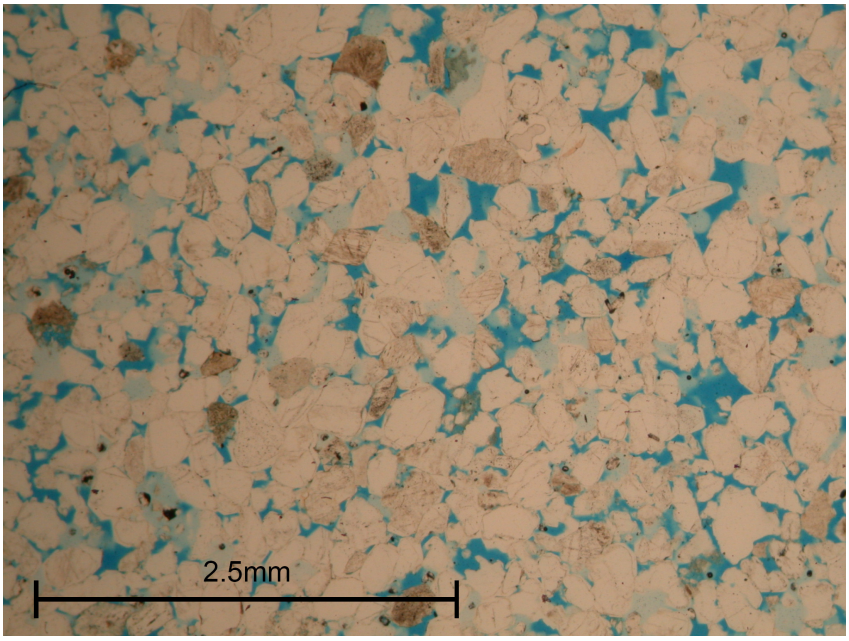

Figure 4.1. Photomicrograph of the Clashach sandstone in thin section. The sample was impregnated with blue resin to highlight porosity. The width of the field of view is 5mm.

Figure 4.2 shows the sensor arrangement on the surface of the sample. Twenty piezoelectric transducers (PZT), for detecting acoustic emissions, were either embedded within the pistons or fixed to the sample inside brass housings with conformable bases. Twelve of these PZTs were P-wave sensors and eight were S-wave sensors. Additionally, five of the P-wave transducers were set-up to act as transmitters, providing an ultrasonic pulse every minute, thereby allowing velocity changes within the sample to

be monitored. Figure 4.3 shows the final sample stack, with the sensor array in place, before insertion into the pressure vessel.

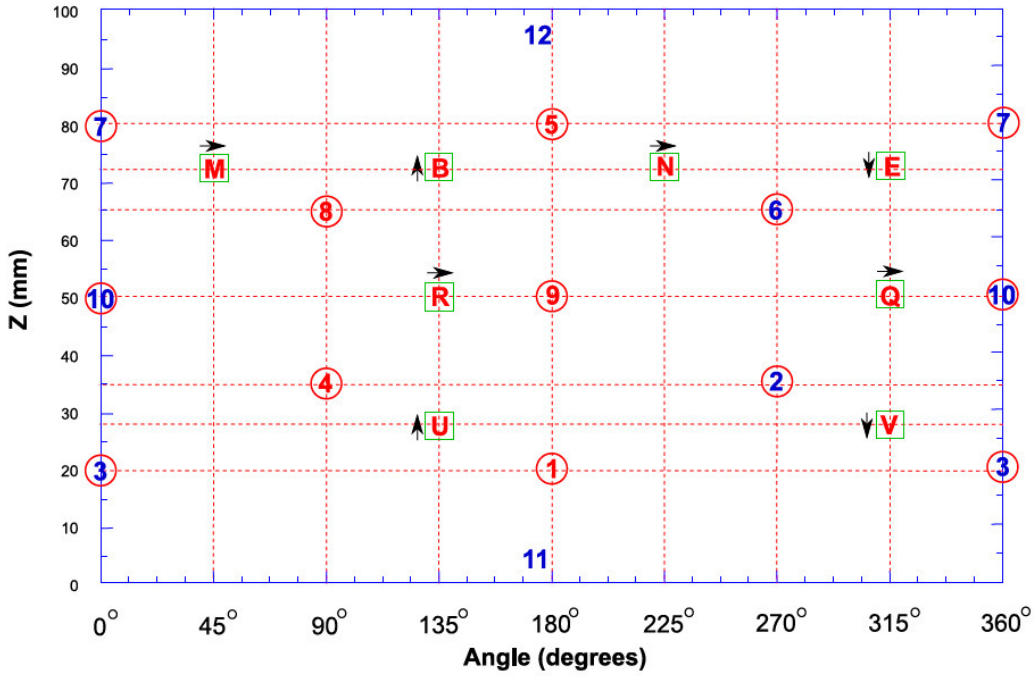

Figure 4.2. Sensor arrangement used for the experiment. Cylindrical projection of the sample surface given in terms of azimuth around the base (in degrees) and height from the base, Z (in mm). Circles indicate P-wave sensors and squares represent S-wave sensors. Transducers which acted as transmitters as well as receivers are highlighted in blue. The arrows indicate direction of polarisation for S-wave sensors.

4.2.3 Event location

Picking P-waves and locating AE events are discussed here briefly, as they have been previously described in more detail in sections 3.3.2 and 3.3.3. Automated picking of P-wave arrival times and amplitudes was carried out by an automatic algorithm, utilising

the approach of *Leonard and Kennett* (1999). For all AE events detected at a minimum of eight sensors, hypocentres were then located automatically using a downhill simplex algorithm (*Nelder and Mead*, 1965) that considers temporal variations in velocity anisotropy. The resulting source hypocentres are estimated to have a location uncertainty of ±1mm (*Stanchits et al*., 2006).

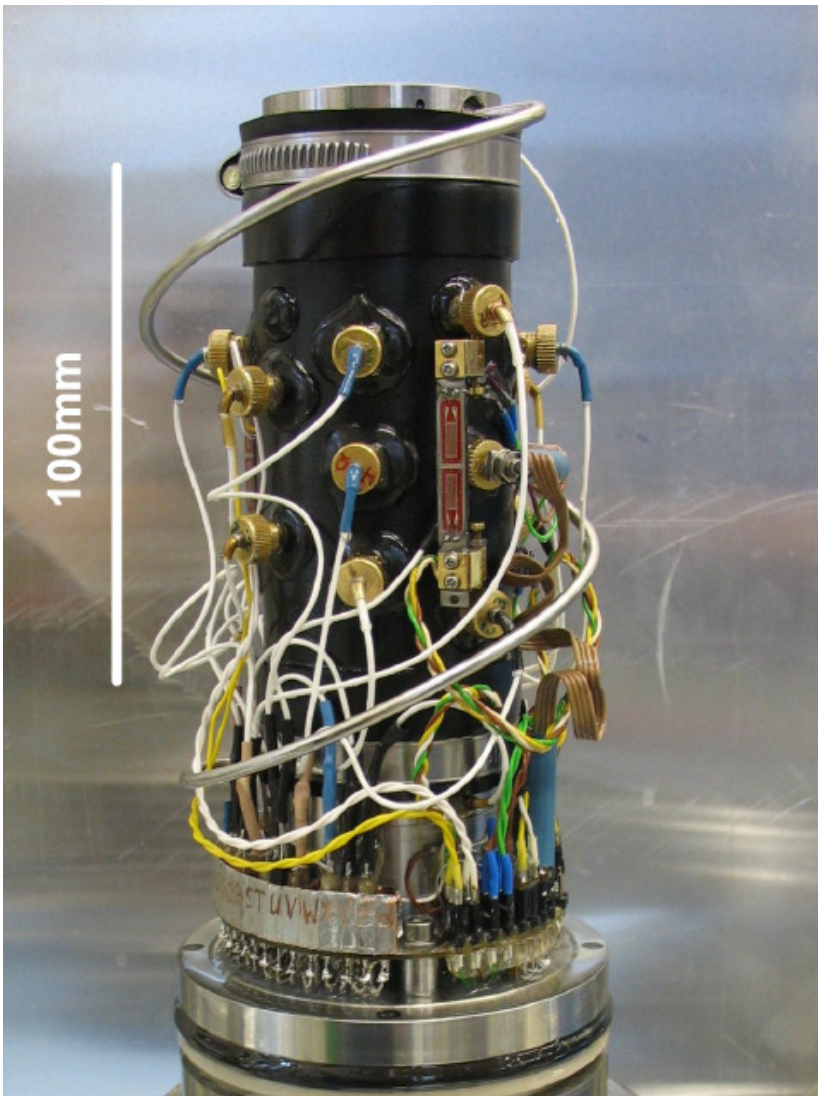

Figure 4.3. The sample stack before insertion into the pressure vessel. AE sensors are contained within brass housings, which are in direct contact with the sandstone sample.

4.2.4 Moment tensor inversion of acoustic emissions

The source analysis technique used in this study is a moment tensor inversion approach developed for acoustic emission data by *Ohtsu* (1991). A detailed description of the moment tensor and related seismic source theory is given in section 2.3.4.3. The moment tensor, **M**, is a three by three tensor, which represents a source as a function of its size and orientation. Conservation of angular momentum requires that **M** must be symmetric, hence containing six *unique* elements. The elements along the diagonal are the normal force-couples and the remaining three unique elements represent the shear force-couples. Hence, for a shear source with no net change in volume, the trace of **M** will be zero. The moment tensor is therefore capable of describing a spectrum of different source types that may include both negative and positive volumetric components, as well as shear. This capacity for characterising sources with a volumetric component makes moment tensor inversion highly suitable for analysis of acoustic emission data, particularly in porous media. In this section, we briefly describe the moment tensor inversion approach utilised during this study. Further detail on the application of this method has previously been given in section 3.4.2.

If we consider a displacement continuity **b**(**y**, t) at position **y** and time *t*, standard elastic wave theory (*Aki and Richards*, 2002) allows us to describe the elastic displacement **u**(**x**,t), recorded at position **x**, as a function of the moment tensor, **M**. If we define a normal vector, **n**, to the surface of the crack as being positive away from the crack and

take **M** to be the product of the initial discontinuity and the elastic constants of the medium, we get;

$$M_{pq} = C_{pqkl} b_k n_1 \,, \tag{4.1}$$

The waveform recorded at **x** is then represented by the product of **M** with the associated Green's functions, convolved with the source-time function, such that;

$$u_i(\underline{x},t) = G_{ip,q}(\underline{x},\underline{y},t) M_{pq} * S(t), \tag{4.2}$$

The Green's functions represent the medium's response, recorded at location **x**, to an impulsive function. In this study, the moment tensor inversion utilised is the SiGMA method of *Ohtsu* (1991). This approach was developed for analysis of acoustic emissions and is dependent only on P-wave data. When selecting the P-wave part of the full-space Green's function, we can describe the P-wave amplitude as a function of **M**, independent of time;

$$A(\underline{x}) = \frac{C_s \mathrm{Ref}(\underline{t},\underline{r})}{4\pi\rho R v_p^3} (r_1, r_2, r_3) \begin{pmatrix} m_{11} & m_{12} & m_{13} \\ m_{12} & m_{22} & m_{23} \\ m_{13} & m_{23} & m_{33} \end{pmatrix} \begin{pmatrix} r_1 \\ r_2 \\ r_3 \end{pmatrix} \tag{4.3}$$

The distance between the source and the receiver is *R*, in the direction given by **r** = (r_1, r_2, r_3). The affect of the sample boundary at the point of observation is accounted for by

the reflection coefficient, *Ref(t, r)*, which is dependent upon the direction of the AE sensor sensitivity, **t**. Additionally, C_s is a calibration coefficient, ρ is the density of the medium and v_p is the P-wave velocity through the sample at the time of emission. Given recorded amplitudes at a minimum of six sensors, we can then solve for the six unique moment tensor elements.

In order to classify an AE event, we decompose **M** into a double-couple (DC) part, an isotropic (ISO) part and a deviatoric or 'Compensated Linear Vector Dipole' (CLVD) part (*Knopoff and Randall*, 1970). This is done using the eigenvalues (λ_{max}, λ_{int}, λ_{min}), of **M**. *Ohtsu* (1991) defines the maximum shear and CLVD components as *X* and *Y* respectively, giving a DC part (*X*, 0, -*X*) and a CLVD part (*Y*, -0.5*Y*, -0.5*Y*). The remaining component, *Z*, is in all directions and is the isotropic part. By normalising with respect to the maximum eigenvalue, the relative proportions of *X*, *Y* and *Z* can then be determined by simultaneous solution of;

$$\lambda_{max} / \lambda_{max} = 1 = X + Y + Z \tag{4.4}$$

$$\lambda_{int} / \lambda_{max} = 0 - 0.5Y + Z \tag{4.5}$$

$$\lambda_{min} / \lambda_{max} = -X - 0.5Y + Z \tag{4.6}$$

Classification of sources is then based on selected proportions of *X*, *Y* and *Z*. Here we use the criteria described in section 3.4.2, which are based on those suggested and tested

by *Ohtsu* (1995). If X>60%, the source is considered to be predominantly 'shear' in nature, whilst if X<40% it is taken to be predominantly 'tensile'. If a source has 40%<X<60%, then it is described as being 'mixed-mode' as it contains both shear and volumetric components of relatively similar proportions. In addition, the physical mechanism for a pore-collapse event is likely to require a component of shear, for example along grain boundaries or pre-existing microfractures (*Fortin et al*., 2009). Therefore, we include a further source type, defined as those events that have X<60% (i.e. not predominantly shear) *and* that have a negative trace of **M**. Such AE are described in this study as 'collapse' events as they are events which lead to a net loss in volume. Events of this type are of particular importance in sandstone deformation tests, due to the presence of pores.

4.3 Results

In this section we describe the approach to failure in the Clashach sandstone in terms of mechanical and AE data. The localisation of damage is discussed and the temporal variation in different source mechanisms is described. Finally, spatial coalescence is reconsidered in terms of different AE source types.

4.3.1 Macroscopic progression to failure

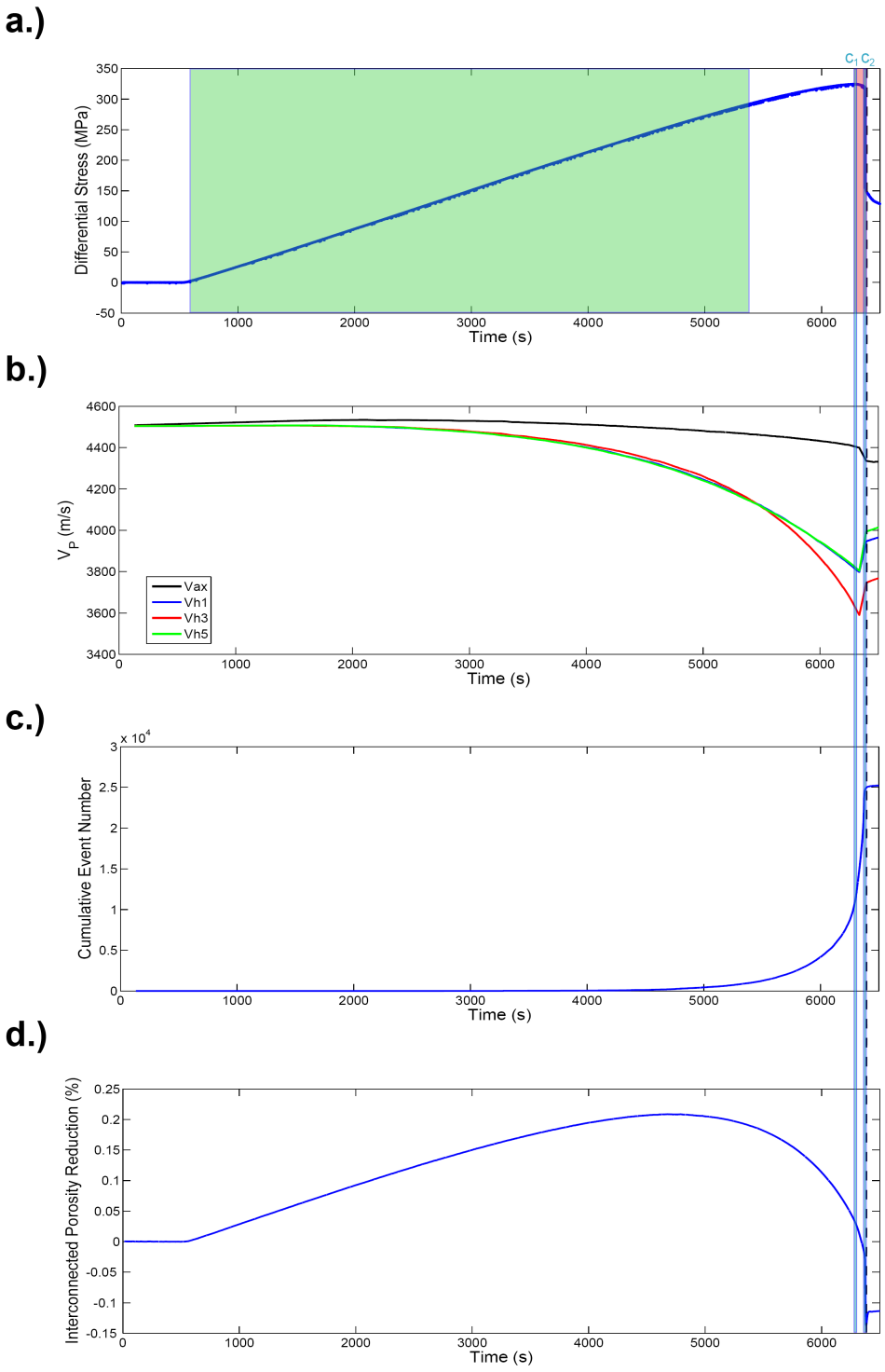

Figure 4.4. a-d.) Evolution of physical properties of the Clashach sandstone, during triaxial compression. a.) Differential Stress (MPa). The areas shaded in green and pink are the timeframes used for comparisons between delocalised and localised damage, respectively, b.) P-wave velocities (m/s): axial, V_{ax} and three horizontal zones, Vh_1, Vh_3, Vh_5, c.) Cumulative number of acoustic emissions, d.) Interconnected porosity reduction (%). Vh_1 is overlayed by Vh_5 and can only be observed after failure. The two periods of intense hypocentre clustering, C_1 and C_2 are highlighted in a-d.) by the blue lines and failure is indicated by the black dashed line.

T

The sample was loaded at a constant axial strain rate of 1.7×10^{-6} s^{-1}, at room temperature and under an effective pressure of 40MPa. Peak stress was followed by a brief period of strain-softening before the formation of a fault plane and sample failure (Fig. 4.7). A stress-drop of approximately 200MPa took place at this time (Fig. 4.4a). Pore fluid volume data indicates a clear reduction in interconnected porosity (Fig. 4.4d) up to approximately 4750s, whereupon it increases rapidly, as microcracking intensifies, during the approach to failure. This change is correlated with a notable increase in the cumulative number of acoustic emissions (Fig. 4.4c).

A significant reduction in ultrasonic velocities, due to microcrack formation, was also observed during the later stages of loading (Fig. 4.4b). Atypically however, the *rate* of acoustic emissions (Fig. 4.5) displays a brief period of deceleration during the later stages of loading, before accelerating again to failure. For the purposes of descriptive clarity in this paper, the time frame of the first and second peaks in AE rate will be described as phases C_1 and C_2 respectively.

4.3.2 Damage coalescence from AE hypocentres

4.3.2.1 Distribution of hypocentres

Hypocentre locations of acoustic emissions provide a real-time indicator of the spatial progression of damage during rock deformation experiments. In this experiment, over 25,000 AE were recorded before the Clashach sandstone failed. The resulting source locations clearly indicate spatial coalescence of damage; from an initially diffuse distribution, to a localised distribution in the vicinity of the eventual macrofracture plane (Fig. 4.6). A small number of events were located out with the sample region and are a reflection of the uncertainty in source location. Figure 4.8a-b demonstrates that localisation concentrated initially on one side of the sample, during the C_1 phase. A further region of clustered damage then intensified on the opposing side of the sample, during the C_2 phase (Figure 4.8c-d). These two zones both appear to be active in the final stages of failure. This behaviour suggests that the first period of coalescence was hindered in some manner, perhaps by a heterogeneity acting as a barrier to the damage process zone. The macroscopic fault could only be formed once the zone of localised damage had successfully progressed across the whole sample.

In this study, we investigate this hiatus and the final approach to failure, in terms of damage clustering and micromechanics, by combining correlation analysis with moment tensor characterisation of AE data.

4.3.2.2 Localisation from the correlation integral

In order to elucidate the damage localisation process, spatial coalescence of acoustic emissions can be quantified by determining the correlation integral (*Hirata et al.*, 1987), *C(r)*;

$$C(r) = \frac{2}{N(N-1)} N(R < r) \tag{4.7}$$

where $N(R<r)$ is the number of hypocentre pairs (p_i, p_k) separated by a distance of less than r and belonging to a set of hypocentres $(p_1, p_2, ..., p_N)$. The resulting correlation coefficient provides a measure of the degree of clustering of hypocentres, for a chosen maximum associated distance, r, between hypocentre pairs.

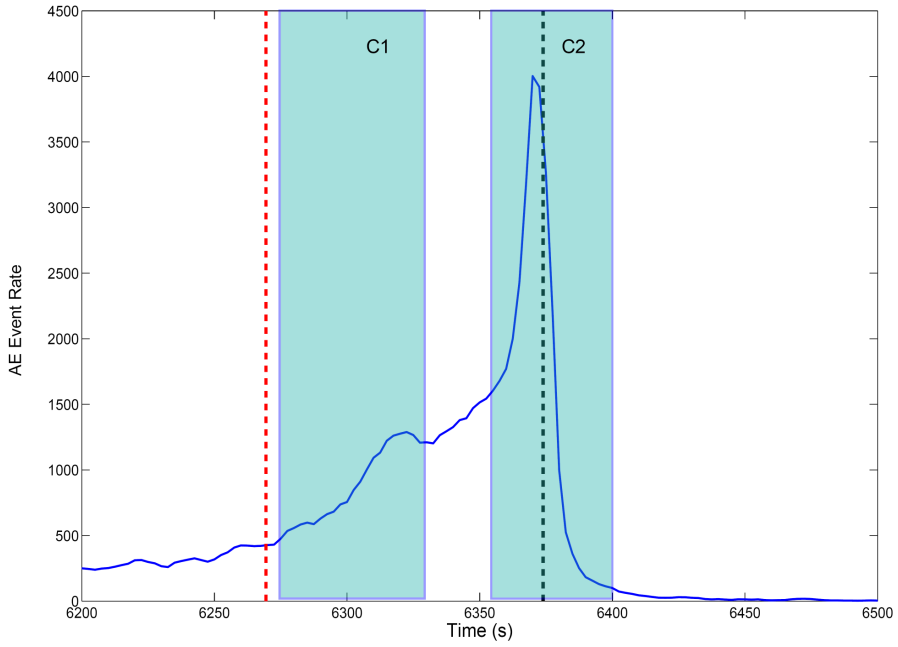

Figure 4.5. Rate of acoustic emissions with time, during the final stages of loading. Peak stress is indicated by the dashed red line and failure by the black dashed line. Two phases of significantly clustered damage are highlighted in blue; phases C_1 and C_2.

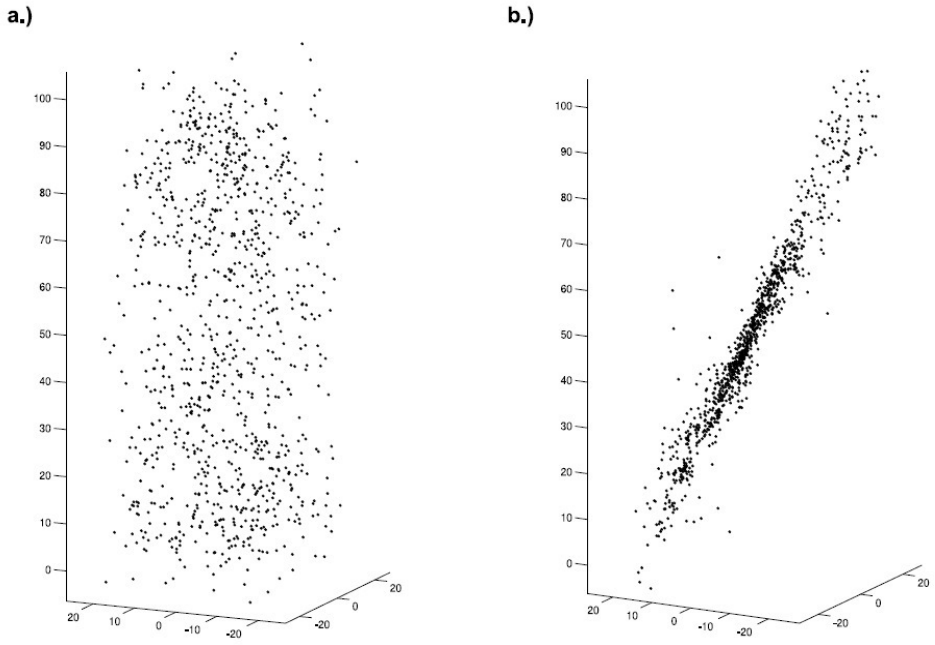

Figure 4.6. a-b.) Hypocentre locations of acoustic emissions, plotted in 3D space (axes labels are in mm). a.) The distribution of AE-associated damage during the early stages of acoustic emission (shaded in green in Fig. 4.4a). AE activity is spatially delocalised. b.) During the final stages of loading (shaded in pink in Fig. 4.4a), AE hypocentres become clearly spatially localised (here observed parallel to the eventual fault plane orientation).

Figure 4.7. The Clashach sandstone sample after shear fracture by triaxial compression (diameter of 50mm, height of 105mm).

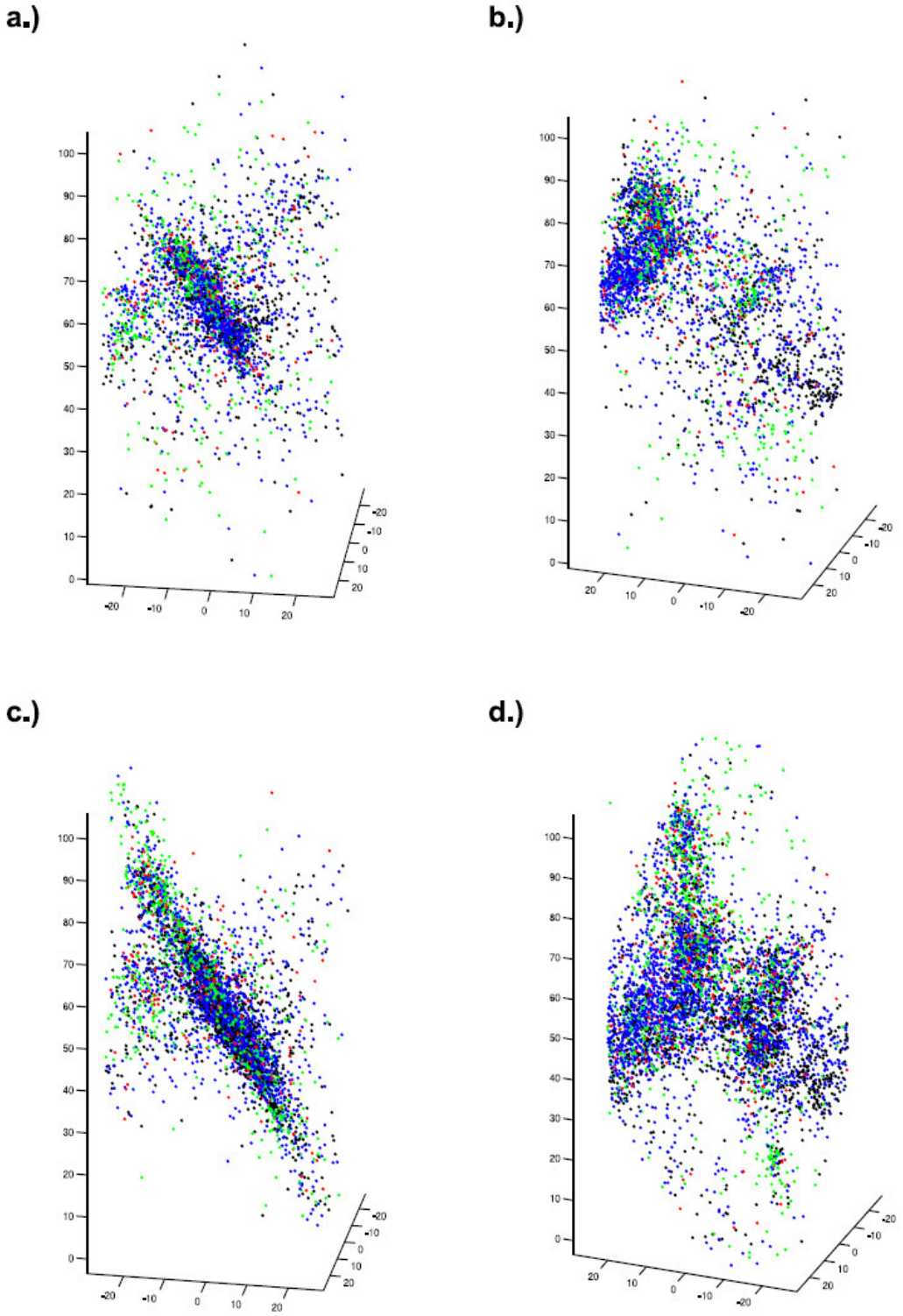

Figure 4.8. a-d.) Hypocentre locations, in 3D space, of acoustic emissions during coalescence periods C_1 and C_2 (Fig. 4.4). a.) Perpendicular to the eventual fault plane, during the first coalescence period, C_1 (see Fig. 4.7 for an image of the sample, post-failure at a similar orientation), b.) Face-on to the eventual fault plane, during the first coalescence period, C_1. Damage is concentrated to one side of the cylinder, c.) Perpendicular to the eventual fault, during the second coalescence period, C_2, d.) Face-on to the eventual fault plane, during the second coalescence period, C_2. Damage is more uniformly concentrated across the plane of localisation. Colours refer to source type, as described in section 4.3.3 and indicated in Figure 4.12.

If the damage distribution is fractal, then $C(r)$ is proportional to r^D, where D is the fractal dimension. A uniform hypocentre distribution leads to a D value of about three and a drop in this value is indicative of change from a volume-filling to a planar arrangement. Such a drop has been observed before in a number of rock deformation studies (*Shah and Labuz*., 1995; *Zang et al*., 1996) and has been proposed as a possible precursor to failure (*Hirata*, 1987).

Here we show $C(r)$ calculated for a range of values of r (1-100mm) on a log-log plot (Fig. 4.9). Two curves are shown, calculated for hypocentre locations from two different time frames during the test. The blue line shows $C(r)$ calculated for AE events during the early- to mid-stages of loading, whilst AE activity is relatively delocalised (see Fig 4.4a for the time frame used). The red line shows $C(r)$ calculated for AE events during the final stages of loading, whilst AE activity is intense and localised (see Fig 4.4a for the time frame used). The results clearly show a significant change in the relationship between $C(r)$ and r as damage becomes localised. The limited range in values of r, which is constrained by the uncertainty in source location (at small values of r) and the physical size of the rock (at large values of r), limits the potential for making a statistically satisfactory fit for D. However, the linear trend, prior to localisation, is nominally consistent with a power-law, indicating a fractal distribution of damage. In contrast, the trend post-localisation is notably more curved, suggesting a reduction in self-similarity at larger values of r. *Main* (1992) argued that uniformly distributed damage along an incipient fault plane produces a significantly different correlation integral from damage clustered about asperities and jogs on a pre-existing fault plane

(Fig. 4.10). Inspection of the shape and slope of the curves in Fig. 4.9, particularly the notable shallowing of slope with localisation, suggests that the former was true for this experiment.

In order to investigate in more detail the variation in AE source clustering during sample deformation, the correlation coefficient (equation 4.7) was also calculated for every 100 events, for a range of values of r (5mm-100mm) and plotted against time. The temporal variation in the degree of clustering could then be observed for different values of r. However, remarkably similar curves were obtained across the range of values for r, indicating that the selection of this parameter (the minimum distance required for pairs to be considered as clustered) has relatively little effect upon the resulting correlation coefficient value for this experiment. As such, only the results for r=10mm are shown here (Fig. 4.11).

The results indicate significant clustering of new damage approximately 6250s into the experiment, in the proximity of the peak stress. In these final stages before failure (Fig. 4.12), two peaks are seen in the correlation coefficient; a broader one (≈6250-6330s), which correlates with the first peak in AE rate (phase C_1), and more narrow one (≈6360-6380s) that correlates with the second peak in AE rate (phase C_2) and occurs prior to and during sample failure. Both periods of clustered activity occurred during the strain-softening phase.

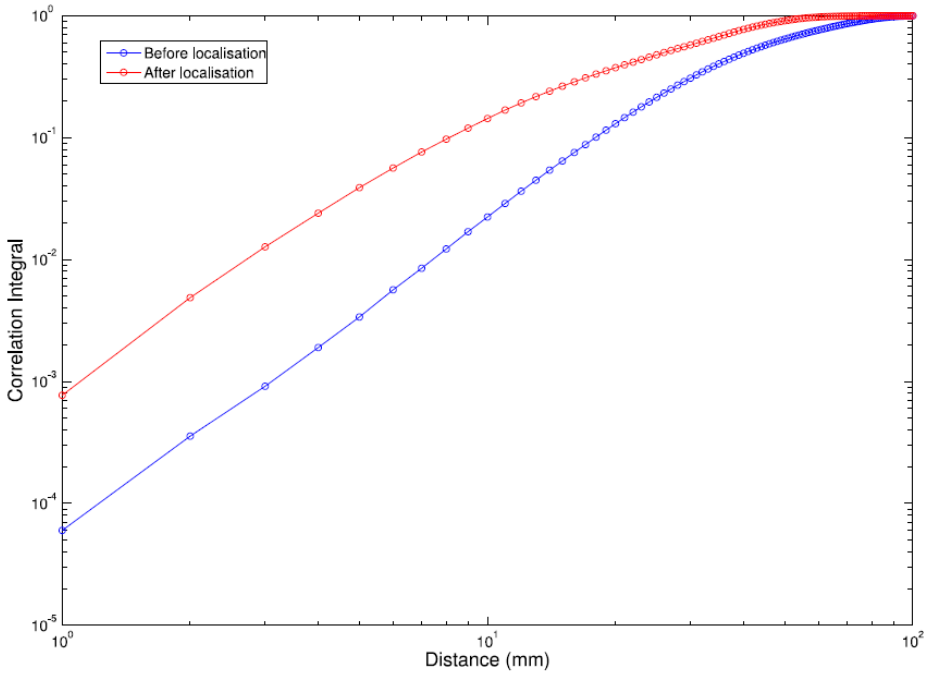

Figure 4.9. Spatial clustering of acoustic emission hypocentres. The variation in correlation integral with distance between pairs, before and after localisation has taken place (for the time frames used for this comparison, see Fig 4.4a).

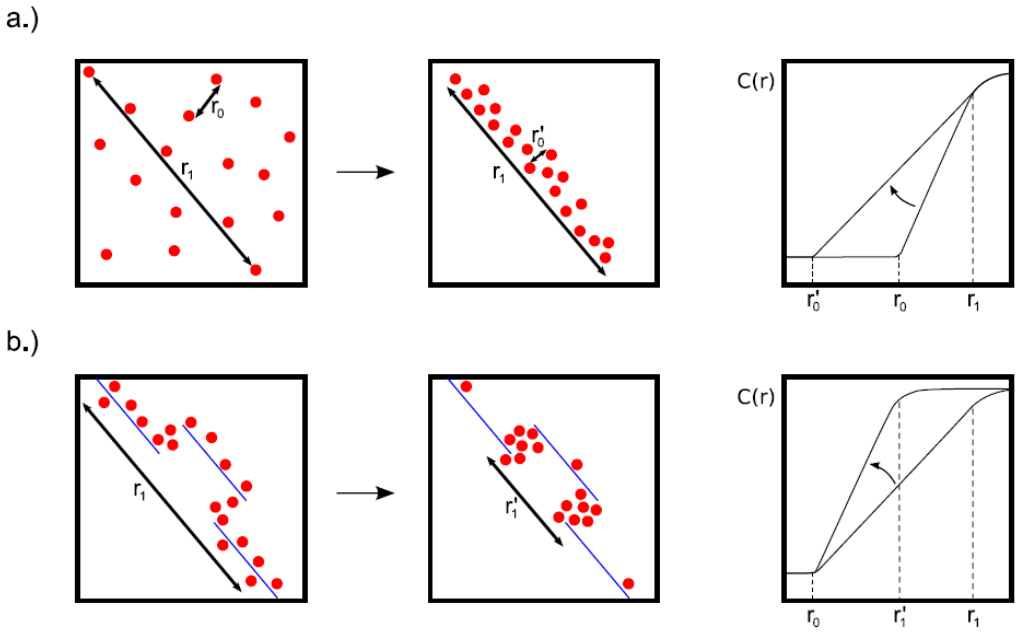

Figure 4.10. Two possible types of damage localisation, after Main (1992). a.) Uniformly distributed damage along an incipient fault plane, b.) Damage clustered about asperities and jogs, on a pre-existing fault plane.

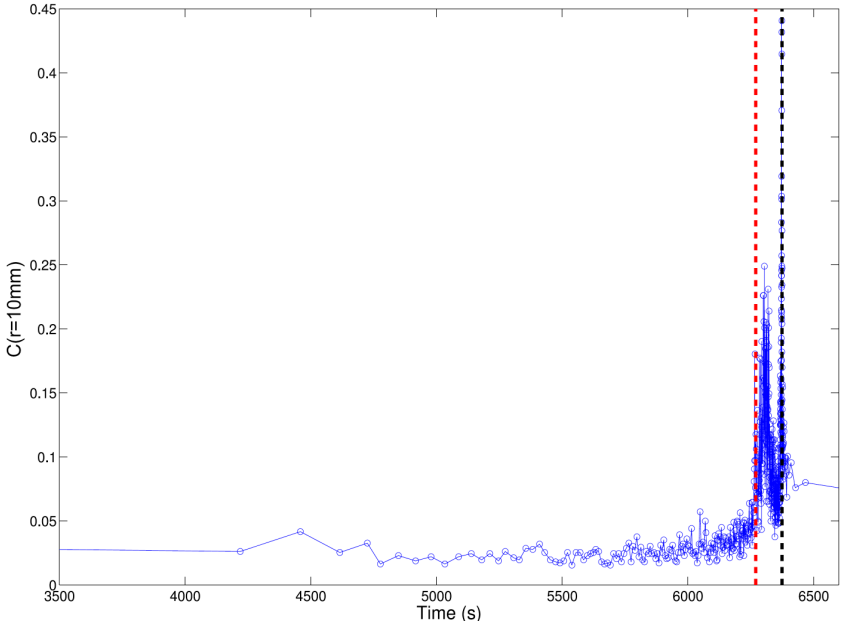

Figure 4.11. Temporal variation in spatial clustering of new damage. The correlation coefficient was determined for pairs of a distance of 10mm or less, over windows fifty events long. The red and black dashed lines indicate the times of peak stress and failure respectively.

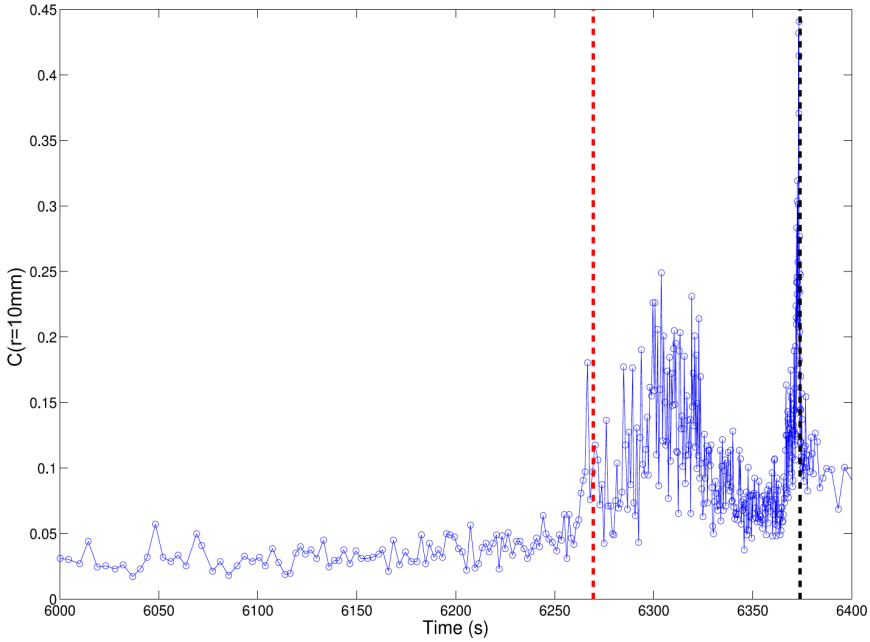

Figure 4.12. Temporal variation in spatial clustering of new damage, during the final stages of loading. The correlation coefficient was determined for pairs of a distance of 10mm or less, over windows fifty events long. The red and black dashed lines indicate the times of peak stress and failure, respectively. Two distinct peaks in the correlation coefficient indicate periods of intense clustering of new, AE-associated damage.

4.3.3 Source mechanisms

Moment tensor inversion and decomposition was carried out for acoustic emissions with a magnitude over 200mV. Events were then automatically classified into source mechanisms that are predominantly shear, tensile, mixed-mode and collapse in nature, as described above in section 4.2.4 (also see Fig. 4.8, section 4.3.2.1 for hypocentre locations). The relative proportion of each source type, normalised with respect to the total number of events, was then determined for rolling windows a hundred events long, with a quarter length overlap. The results are shown in Figure 4.13. In section 3.5.2, this method was applied to acoustic emission data from the triaxial loading of granite. In that instance, the results indicated that the dominant microscale mechanisms for strain accommodation were *tensile* microcracking and microshearing. However, in the case of a porous Aeolian sandstone, the results indicate that the brittle deformation is dominated by microshearing and microscale events of the '*collapse*' type (negative trace). Such an observation is consistent with both microstructural work (*Menéndez et al*., 1996) and first motion polarity studies of AE waveforms from deformation of sandstone at similar effective pressures (*Fortin et al*., 2009).

In the early stages of AE activity the dominant sources are collapses. At this stage, tensile microcracking is slightly more prevalent than microshearing. However, by approximately 4750s, these proportions are reversed as the AE rate begins to accelerate and microshearing increases. The relative proportion of collapse events is also observed

to decrease slightly as microshearing increases. The vast majority of collapse sources have a very significant shear component to their motion. Such behaviour is consistent with microstructural observations in this thesis (section 5.3) and other studies (*Menéndez et al.*, 1996; *Bésuelle et al.*, 2003; *Fortin et al.*, 2009), where intense grain-crushing has been observed in shear localisation of sandstone.

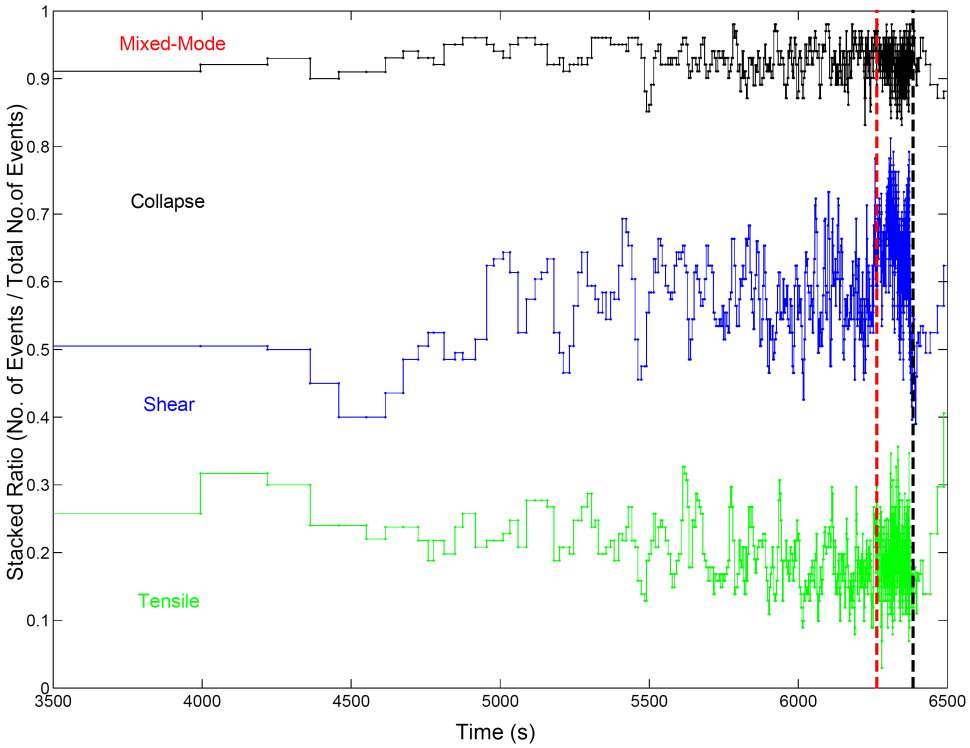

Figure 4.13. Temporal variation in source type dominance, determined from decomposition of AE moment tensors. Collapse sources constitute a primary mode of microscale deformation, particularly during the earlier stages of AE activity. Shear sources increase in dominance as failure is approached.

4.3.4 Inelastic strain localisation process from AE

In order to investigate the role of specific microscale mechanisms in the localisation process, the correlation coefficient was calculated (equation 4.7) for different AE source types (Fig. 4.14), at a constant distance of 10mm between pairs (r=10mm). This was carried out for every one hundred events of the selected source type, as described in section 4.3.2.2. The results clearly indicate significantly differing spatial behaviour, during the localisation process, for different source types.

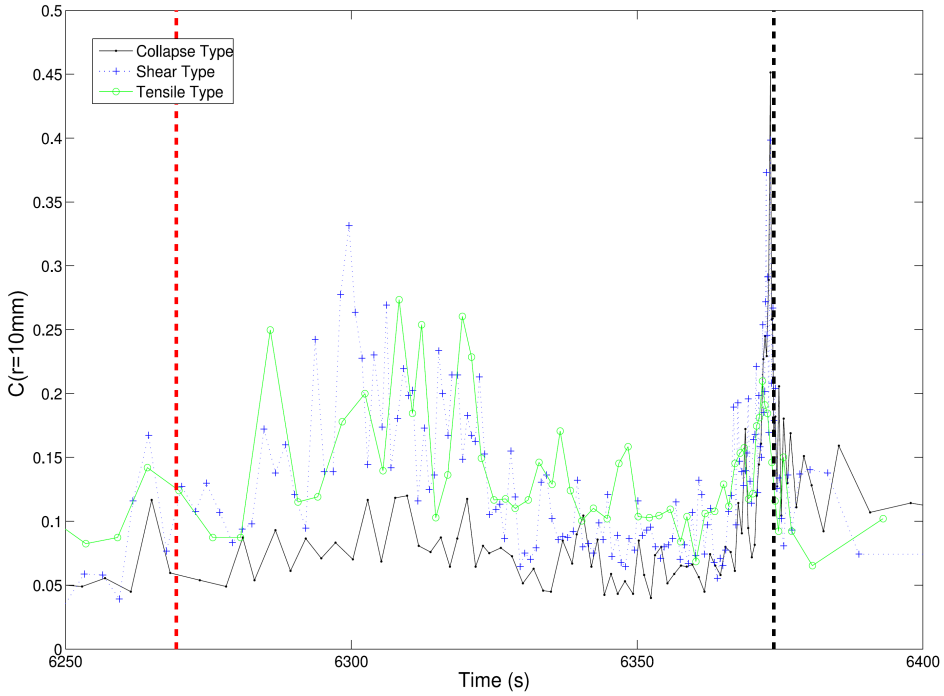

Figure 4.14. Temporal variation in spatial clustering of different source types during the final stages of loading. The correlation coefficient was determined for pairs of a distance of 10mm or less, over windows fifty events long. The red and black dashed lines indicate the times of peak stress and failure respectively. Shear and tensile sources display two periods of notable source clustering, but collapse sources only demonstrate significantly correlated behaviour in the final period of damage coalescence.

During phase C_1, an increase in the correlation coefficient for tensile sources and, in particular, shear sources is observed. In contrast to this, collapse sources show very little coalescence during this time interval. There is then a marked period of more dispersed, delocalised damage, for all source types, before a further period of damage coalescence (phase C_2) and sample failure. During this second and more pronounced phase of localisation, all source types demonstrate a significant increase in their spatial correlation, including the collapse sources. This implies one of two possibilities; i.) clustering of collapse-type damage is required before the sample can fail, or ii.) clustering of collapse-type damage is a natural consequence of the final approach to failure. De-coupling these two possibilities seems unlikely, but it is possible to at least infer that significant coalescence of collapse sources is *only* observed during the final progression to failure.

Differing rates of acoustic emission are also observed for different source types (Fig. 4.15). In particular, there is a distinct deceleration in AE rate for collapse sources during the C_1 phase. In contrast, the AE rate of tensile sources does not accelerate, but remains constant until the C_2 phase occurs. Any lag between the source types at failure cannot be resolved with certainty, due to a brief period of masking of low-magnitude events during the recording process. However, by breaking the AE rate curves down into different source types, it is clear that the AE rate curve for all sources is a superposition of a number of different behaviours occurring in the rock at any given time.

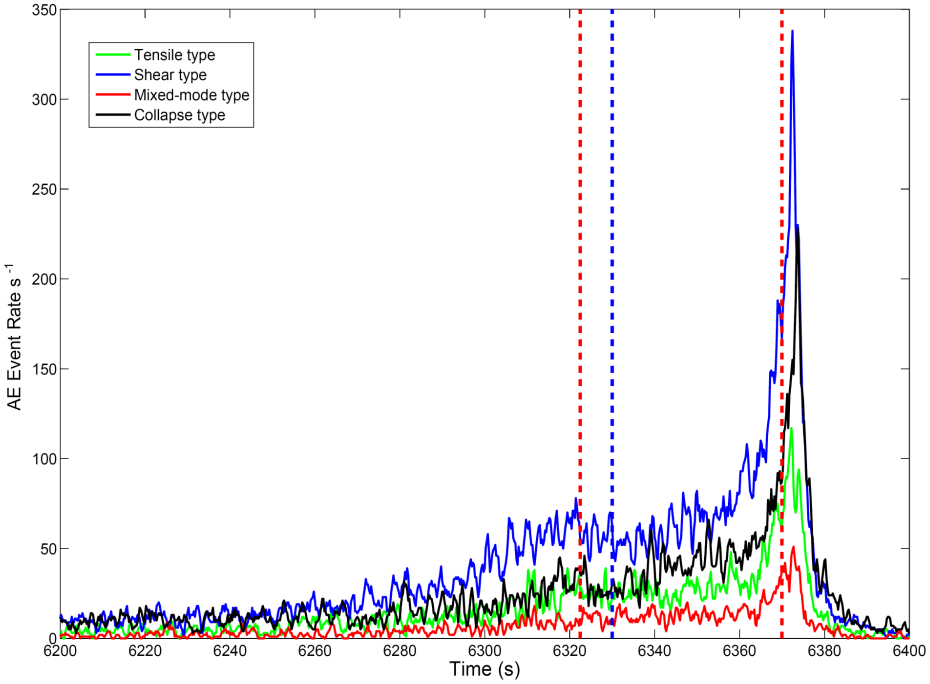

Figure 4.15. Temporal variation in the rate of acoustic emissions, for different source types, during the final stages of loading. The red dashed lines indicate the peaks in AE source coalescence for periods C_1 and C_2 and the blue dashed line indicates the time of the correlation minimum between the two coalescence peaks.

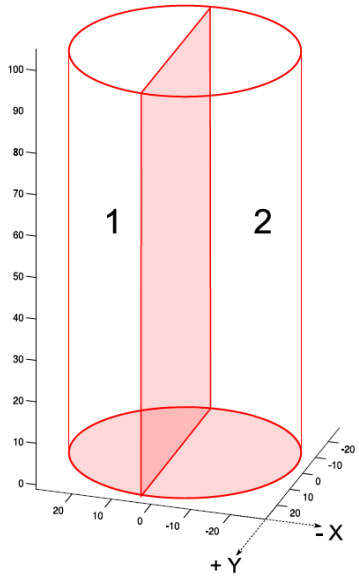

Figure 4.16. Schematic of the sample cylinder, indicating the two volumes selected for independent analysis; region 1 and region 2. This schematic has the same orientation as the hypocentre plots in Figures 4.8a and 4.8c. For reference to the failure plane, see Fig. 4.7, which is orientated with the Y axis directly out of the page.

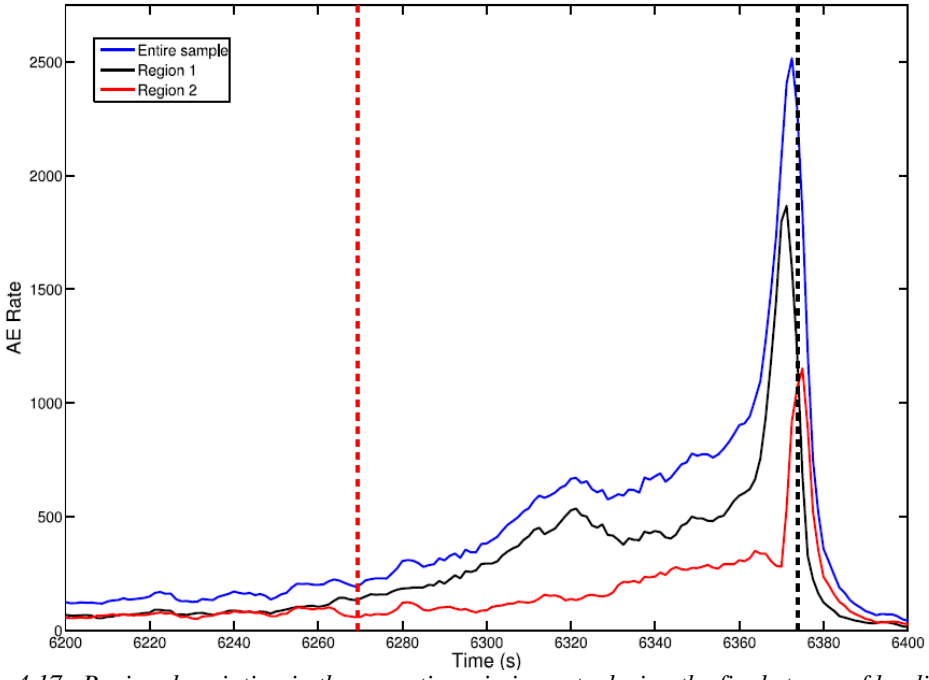

Figure 4.17. Regional variation in the acoustic emission rate during the final stages of loading. The red and black dashed lines indicate the times of peak stress and failure respectively.

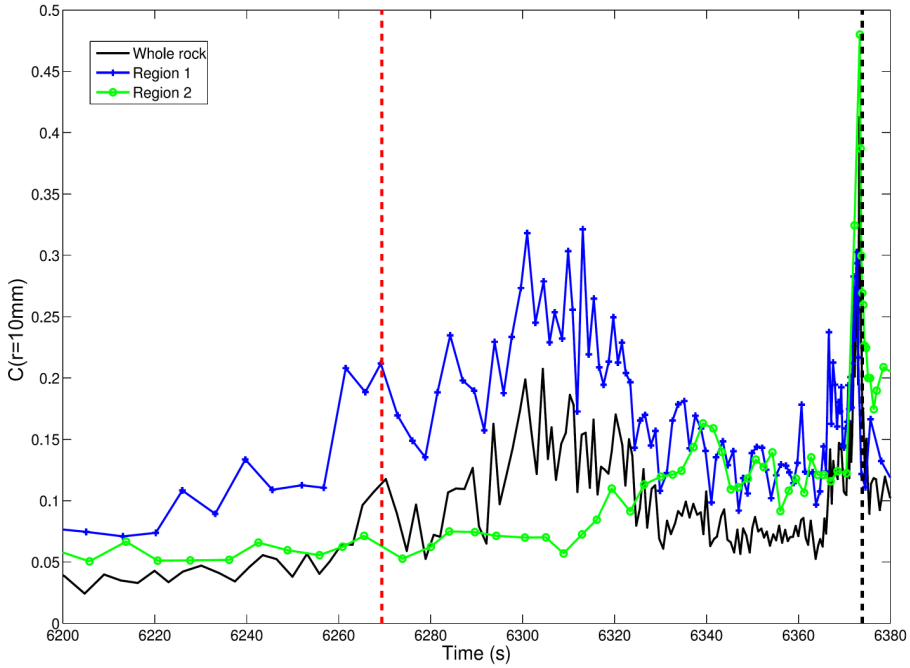

Figure 4.18. Regional variation in spatial clustering of damage with time. The correlation coefficient was determined for pairs of a distance of 10mm or less, over windows fifty events long. The red and black dashed lines indicate the times of peak stress and failure respectively.

In order to investigate the progression from the first phase of damage acceleration to the second and then finally to failure, the sample was divided into two regions (Fig. 4.16). These regions were selected by careful inspection of AE hypocentre locations plotted and rotated in 3D, from different time intervals throughout the course of the experiment. Region 1 contains the damage process initiation zone and appears to be the most active region during the C_1 phase (Fig. 4.8). Region 2 appears, from hypocentre locations (Fig. 4.8), to have been more quiescent during the C_1 phase, before becoming involved in more localised and intensive damage during the C_2 phase and sample failure. This is confirmed by plotting the AE rates for these two separate sample regions, which clearly show a marked acceleration and deceleration, during the C_1 phase, for region 1 and a more typical acceleration to failure in region 2, at a significantly later stage (Fig. 4.17).

In addition, the correlation coefficient for a constant distance interval (r=10mm) was determined for every fifty events within region 1 and again for events within region 2 (Fig. 4.18). Region 1 clearly displays two periods of coalescence with a marked reduction in the clustering of AE hypocentres during the intervening time period. However, region 2 does not show this hiatus in the localisation process, instead exhibiting a relatively steady increase in the correlation coefficient, before increasing more sharply prior failure. This suggests that we are observing the progression of localisation from one part of the sample to another. Consequently, this provides us with the opportunity to explore the behaviour of the participating damage mechanisms during a hiatus in the process zone evolution (region 1), as compared to a more typical, uninterrupted process zone evolution (region 2).

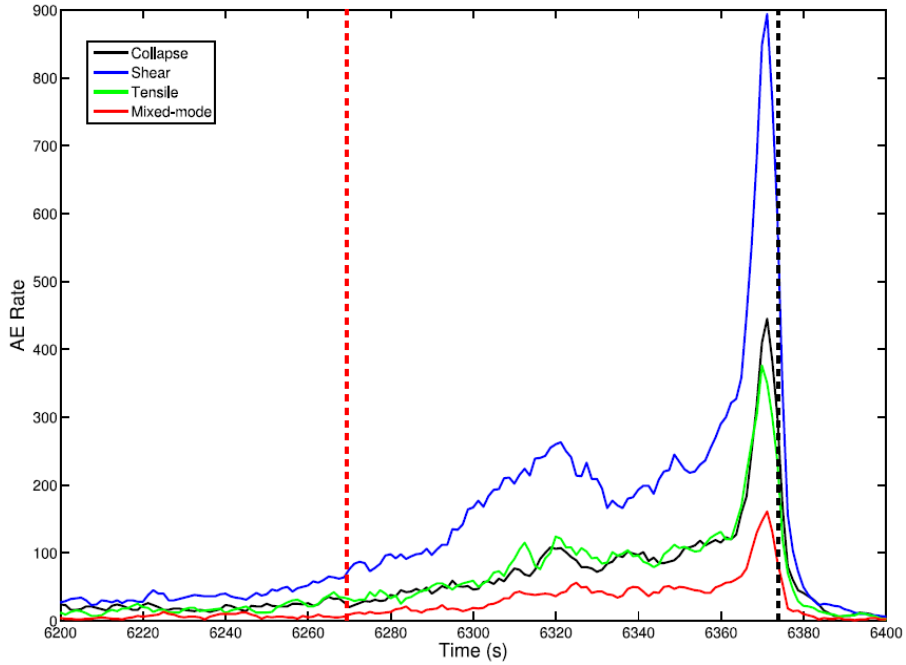

Figure 4.19. Temporal variation in the rate of acoustic emissions in region 1 during the final stages of loading. The AE rate is shown for different source types. The red and black dashed lines indicate the times of peak stress and failure respectively.

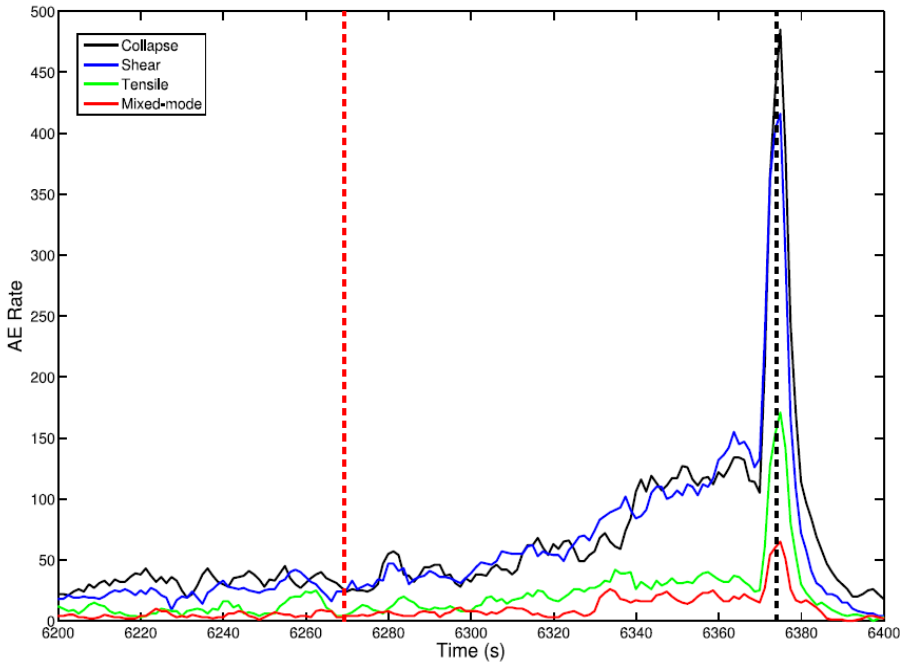

Figure 4.20. Temporal variation in the rate of acoustic emissions in region 2 during the final stages of loading. The AE rate is shown for different source types. The red and black dashed lines indicate the times of peak stress and failure respectively.

By determining AE rates for each source type in both region 1 and region 2, marked differences in the activity of different micromechanisms are indicated. In region 1 (Fig. 4.19), the first acceleration in the rate of damage is particularly marked for the shear-type sources, with very little involvement from the other source types. In clear contrast to this (Fig. 4.20), region 2 only exhibits one marked acceleration in AE rate, during phase C_2, which is displayed by all source types. Furthermore, in region 2, the activity of the collapse sources is very similar to that of the shear sources, whereas in region 1 the collapse sources behave in a markedly different fashion to the shear sources. This suggests that intensive, localised microshearing is not sufficient to lead to fault propagation without ongoing localised collapses, perhaps indicative of grain-crushing.

4.4 Discussion

During the brittle faulting of crystalline, non-porous rock under confinement, strain is primarily accommodated by shear and tensile microfractures, which coalesce to form a localised zone of intense damage that may become a failure plane. The micromechanics of this process have been studied in detail, by way of both microstructural and AE source analysis (*Reches and Lockner*, 1994; *Moore and Lockner*, 1995; *Shah and Labuz*, 1995; *Zang et al*., 2000; *Stanchits et al*., 2006, see also section 3.5). This study considers the role of different microscale mechanisms, in the process of shear localisation, when there is a significant *pre-existing* porosity. The micromechanical evolution of damage in sandstone has been studied using a number of techniques,

including optical and SEM analysis (*Menéndez et al*., 1996), velocity anisotropy studies (*Zang et al*., 1996) and AE polarity studies (*Fortin et al*., 2009). However, we are unaware of any attempt to characterise damage evolution in triaxially loaded sandstone, using moment tensor inversion of acoustic emission data.

Acoustic emissions not only give us an insight into the spatial coalescence of damage, but the *type* of damage that is occurring during the laboratory deformation of samples. Moment tensor inversion and decomposition of AE sources indicates markedly different micromechanical behaviour for sandstone compared to non-porous rock, with a considerable contribution from sources with a significant implosive component. The majority of such 'pore-collapse' type behaviour contains a notable component of 'shear', which is intuitively necessary in order to accommodate the collapse of grains inwards (*Fortin et al*., 2009). Our results here are for a relatively low-porosity sandstone, which exhibits behaviour between that of a compact rock and a high-porosity sandstone. Whilst there is a notable contribution of AE sources with a high tensile component, collapse sources dominate during the early stages of AE activity. It has been previously suggested that this phase of emissions in brittle deformation tests of sandstone may be related to the rupture of grain boundaries, leading to a loss of cohesion that then allows slip or rotation along these boundaries (*Menéndez et al*., 1996). Further discussion of the physical mechanisms behind these events can be found in chapter 5. Once the strain-softening phase has been reached and localisation begins, microscale damage is dominated by sources which are primarily shear in nature.

In addition, the spatial distribution of damage in the sample appears to have involved two distinct periods of increased clustering; both during the post-peak stress phase. These periods of coalescence correlate with peaks in the acoustic emission rate, whilst the interval between them is associated with a notable deceleration in the rate of acoustic emissions. This suggests that the drop in AE rate here is due to a transient hiatus in the localisation process, possibly due to some heterogeneity acting as a temporary barrier to damage progression.

This data set therefore provides us with an opportunity to characterise the involvement of different microscale mechanisms during such a hiatus in damage coalescence, as well as during the final stages of localisation before sample failure. Damage characterisation, through moment tensor inversion of AE data, indicates that
different source types can exhibit individual and distinct clustering behaviour during the strain-softening phase. During the first period of damage coalescence, shear and tensile sources showed significant clustering, whilst collapse sources remained relatively delocalised. In contrast, during the second period of AE hypocentre coalescence, both shear *and* collapse type sources displayed marked clustering, as did, to a lesser extent, the tensile sources. These correlation values were determined for hypocentre pairs of the chosen source type *only* and therefore do not include any clustering between different source types, brought about by their interaction. However, the results do indicate that failure only occurs once there is significant localisation of collapse events, presumably during the final stages of shear band formation.

This behaviour is also made apparent comparing AE rates for different source types. Prior to peak stress, both shear and collapse sources display similar emission rates. However, a significant increase in the rate of collapse type events is only observed during the second, and final, period of coalescence, perhaps relating to grain-crushing and gouge formation. Whilst this later episode of localised damage affected the whole sample, the earlier period of pronounced AE clustering only occurred in the region where faulting eventually nucleated. We suggest that here we have observed an initial, failed, attempt at localisation, followed by a second, successful, one.

The development of shear localisation in porous rock is dependent upon the *interplay* between two local processes; dilatancy and compaction (*Paterson and Wong, Chapter 5*, 2005). The results of this study indicate that where significant localisation of only one of these processes has taken place, the acceleration to failure will halt until the stalled process can 'catch up'. In other words, the cascade to failure can only take place when full involvement of available damage mechanisms is occurring. Consequently, on the local scale, the approach to failure may be considered as a succession of hiatus events, of varying magnitudes. This subsequently implies that noise in the AE rate signal may contain information about heterogeneities within the sample.

This study involves an example of the shear localisation process in sandstone, where the progression to failure is non-ideal. The results indicate that, in a generalised situation, failure is not solely dependent upon the *degree* of damage alone, but also upon the *mechanism* of damage and its degree of localisation. The dominant mechanism is

dependent upon both material and environmental conditions. If a heterogeneity inhibits the involvement of one of the primary damage mechanisms, the localisation process may stall temporarily, until this inhibition can be overcome. Clearly, the damage process zone involves a complex interaction between different micromechanisms, each accommodating the other until a satisfactory rearrangement can be achieved and a fault plane formed. As a result, methods for quantifying damage localisation from all AE events provide an 'averaged' value for coalescence, which is, in reality, the superposition of a number of different micromechanisms. This highlights the need for care in the application of such localisation metrics in the modelling of the failure process, particularly in situations where the approach to failure has been non-ideal.

4.5 Summary

With modern sensors and recording systems, rock deformation experiments can produce AE data sets comparable to, or of even greater quality and resolution, than seismic records in a tectonically active region. As a result, acoustic emission records are a valuable tool for investigating damage evolution in deforming rock, to which many conventional seismological techniques can be applied. Detailed characteristics of inelastic deformation and its temporal evolution can be obtained by carrying out moment tensor inversion of acoustic emission data. In this chapter, we present source analysis results for AE produced during shear localisation in triaxially loaded Clashach

sandstone. We also apply a spatial correlation analysis, in order to investigate the role of different microscale deformation mechanisms during the localisation process.

Our findings can be summarised as follows;

i.) In contrast to compact rock 'Collapse' type AE sources are the dominant microscale mechanism in the early stages of acoustic activity. The vast majority of these events contain a notable shear component, significant enough to describe them as an *implosive* 'mixed-mode' event. AE mechanisms with a dominant shear component are also a primary mode of inelastic deformation and supersede collapse sources in dominance during the localisation phase.

ii.) The onset of AE hypocentre localisation was observed to correlate with the peak stress, and involved two periods of newly clustered damage.

iii.) A hiatus in the rate of acoustic emission was observed in the later stages of loading and correlates with the first phase of damage clustering. The first period of localised activity involves both shear and tensile sources, but collapse events display little involvement. In contrast, the second period of AE hypocentre clustering involves significant activity from all source types and the damage process accelerates until sample failure.

It is only when localisation of collapse sources, a primary mode of deformation in sandstone, is observed that the sample began a successful approach to failure. The cascade to failure involves the interplay of a number of micromechanical processes and our observations suggest that when a heterogeneity inhibits one of these processes, damage evolution will stall until a suitable balance between mechanisms can be achieved again. The detailed characterisation of acoustic emission source mechanisms, by moment tensor inversion, represents a powerful tool for elucidating such processes.

Chapter 5

Mechanisms of acoustic emission during triaxial compression of low-porosity sandstone

5.1 Introduction

Understanding the micromechanical processes that lead to the macroscopic faulting of sandstone is of primary importance in the field of rock mechanics. Such information is pertinent to the modelling of damage evolution and failure in rock, as well as informing our understanding of the processes that may lead to natural faulting. In particular, the modification of pore-space geometry due to deformation and the consequent alteration of macroscopic permeability properties, is of interest in a number of areas, including ground water flow studies, the hydrocarbons industry and planning of carbon dioxide sequestration schemes. At low effective pressures, compressed sandstone may undergo failure as a consequence of shear localisation. There have been a significant number of microstructural studies relating to microscale deformation generated by shear localisation for both natural samples (*Aydin,* 1978; *Aydin and Johnson*, 1978; *Anders and Wiltschko*, 1994; *Antonellini et al*., 1994) and those deformed in the laboratory (*Menéndez et al*., 1996; *El Bied et al*., 2002; *Bésuelle et al*., 2003). However, such an approach has two particular disadvantages: i.) the sandstone can only be examined after unloading, rather than at a number of intervals during the loading process, and ii.) some

micromechanical processes likely to occur during shear-enhanced-dilation, such as cement rupture and grain rotation, are difficult to detect by microscopic inspection.

In contrast, another physical indication of the inelastic deformation of sandstone, during its deformation in the laboratory, is the emission of high-frequency pressure disturbances termed 'Acoustic Emissions' (AE). The rate of these emissions has been observed to correlate with the inelastic strain experienced by a deforming sample (*Lockner*, 1993) and has been attributed to the formation of microcracks during the irreversible damaging of the material (*Scholz*, 1968a; *Ohnaka and Mogi*, 1982). In experiments on compact rock, this damage is thought to be primarily dilational after the onset of significant AE activity; relating to the delocalised, tensile microfracturing of the sample (*Reches and Lockner*, 1994; *Moore and Lockner*, 1995). As loading progresses, microshearing becomes more significant and is the primary mode of microscale deformation at the time of failure (*Stanchits et al*., 2006). Whilst AE are also regularly detected during the brittle deformation of high-porosity sandstones (*Ohnaka and Mogi*, 1982), the resulting acoustic emissions during dilation are instead thought to be primarily associated with the rupture of grain contacts, and the sliding and rotation of grains (*Lockner et al*. 1992; *Menéndez et al*., 1996). Intuitively, one might therefore expect that the micromechanical deformation of low-porosity sandstone under compressive loading, lies somewhere between these two extremes of behaviour.

Analysis of the source mechanisms of acoustic emissions, therefore, provides us with an opportunity to investigate the transition between these two pathways to shear

localisation. In the past, AE source analysis has generally involved the broad classification of AE into a number of source 'types', based on first motion polarity of waveforms (*Zang et al*., 1998; *Lei et al*., 2000; *Stanchits et al*., 2006; *Fortin et al*., 2009). However, a number of recent studies (*Chang and Lee*, 2004; *Carvalho and Labuz*, 2002; *Shah and Labuz*, 1995; *Benson et al*., 2008) have involved a more complete characterisation of AE sources, by adapting the moment tensor inversion approach developed in the field of seismology.

The forces acting at the source of an earthquake can generally be approximated by the action of two pairs of 'force-couples', acting orthogonally to one another. This is termed a 'Double-Couple' (DC) mechanism, the orientation of which can be estimated by fitting to waveform data recorded at a number of locations on the earth's surface (section 2.3.4.2). Such a mechanism represents slip along a planar surface and inherently involves no change in volume at the source. However, in reality seismic sources may contain a volumetric component, for example in volcanically active regions (*Julian*, 1983; *Nettles and Ekström*, 1998). To characterise a Non-Double-Couple (NDC) event, a seismic source may be represented by a set of nine force-couples; three tensile and six shear, in nature. As a result, a displacement continuity may be described by a three-by-three tensor known as the moment tensor, M, the elements of which can be inverted for from waveform data. The moment tensor inversion (MTI) approach is regularly utilised, in the field of seismology, to fully characterise NDC sources (*Dziewonski et al*., 1981; *Frohlich*, 1995).

Moment tensor inversion has also been applied to acoustic emissions generated by geomaterials in the laboratory, although the focus has been primarily on non-porous rock types (*Shah and Labuz*, 1995; *Chang and Lee*, 2004; *Manthei et al*., 2001; *Manthei*, 2005; *Benson et al*., 2008). A detailed description of other source analysis methods that have been applied to laboratory acoustic emissions, is given in section 3.2. In general, these studies involve the classification of sources into a range of categories relating to their general behaviour. However, very little work appears to have been done charactersing these source 'types', and their associated physical mechanisms, or investigating how distinct the boundaries are between each classification. Are AE produced by only one or two types of mechanism? Are their source signatures simple, involving only one mode, or do they result from more complicated multi-mode behaviour? Do they arise from similar mechanisms to those determined by microstructural observation or do they represent 'atypical' deformation. In this paper, we investigate and characterise the micromechanisms responsible for acoustic emission activity, during the process of shear localisation, within a low-porosity sandstone.

This paper utilises a combined approach of moment tensor inversion of AE data and microstructural imaging to illustrate the broad range of source mechanisms that produce acoustic emissions and proposes idealised physical mechanisms that may be responsible for their generation. A single rock deformation experiment may produce thousands of AE events, comparative to a highly detailed earthquake catalogue in terms of the amount of available information. Whilst the sources, due to their NDC nature, display a more complicated spectrum of behaviour than earthquakes, this data provides an as-yet not

fully explored source of information on the highly complicated micromechanical evolution of a deforming porous rock.

5.2 Methodology

This section briefly summarises the experimental set-up used in this study, including a description of the sample, and then goes on to outline the approach utilised for source analysis of the resulting acoustic emissions.

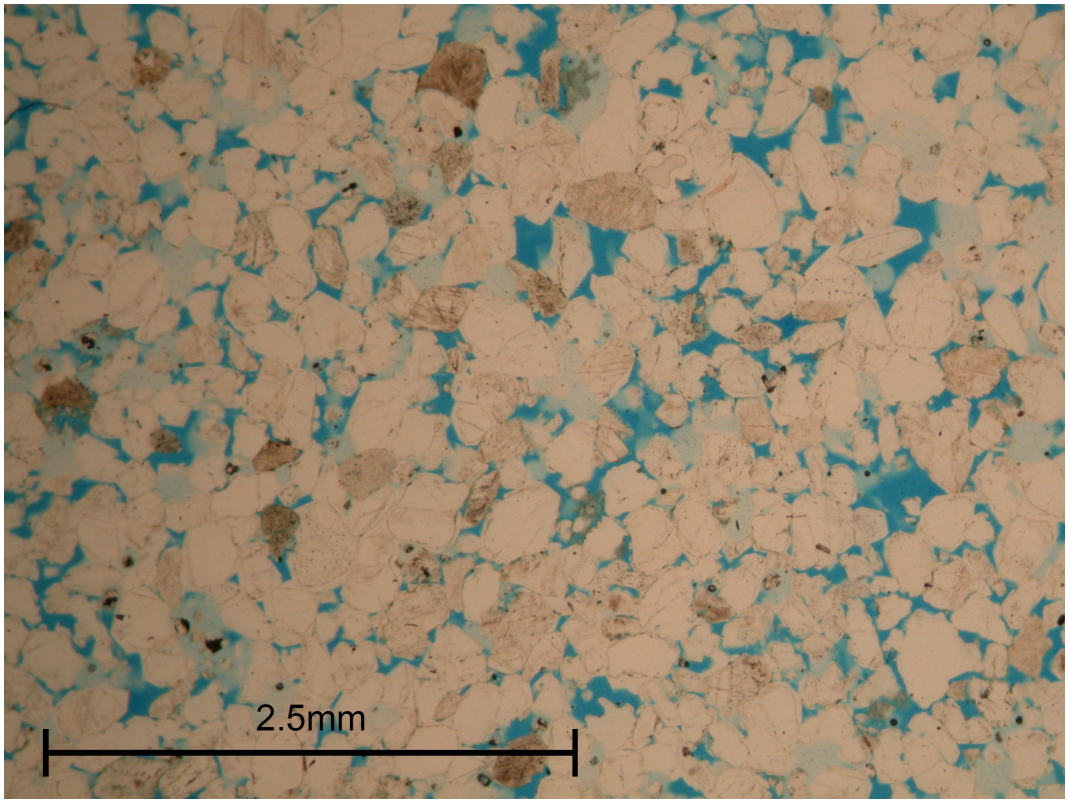

Figure 5.1. Photomicrograph of the Clashach sandstone in thin section. The sample was impregnated with blue resin to highlight porosity. The width of the field of view is 5mm.

5.2.1 Sample description

The rock selected for this study is the Clashach sandstone, from Hopeman in the Northeast of Scotland. This Permo-Triassic aeolian sandstone was selected for three primary reasons; i.) its well-sorted, massive nature provides an excellent material for rock deformation testing; ii.) it is cemented by secondary quartz-overgrowths that can provide information about grain rotation during microstructural analysis, iii.) it is an onshore analogue for petroleum reservoir rocks in the Moray Firth. This medium-coarse grained, subarkosic arenite has a simple mineralogy (Figure 5.1) with low clay-content, and sub-rounded quartz (89%) and feldspar (11%) grains (*Crawford et al*., 1995). It has a porosity of around 13% and a uniaxial strength of 105.8MPa. The sample was cored perpendicular to the large-scale bedding within the unit, with a cylinder length of 105mm and diameter of 50mm. Whilst visible bedding could not be discerned on the scale of the sample, the orientation of coring was chosen so as to be comparable to a reservoir scenario. A more detailed characterisation of the Clashach sandstone is provided by (*Crawford et al*., 1995).

5.2.2 Experimental approach

The experimental methodology for this study has been previously described in chapter 4 and, as such, is more briefly summarised here. The experiment was carried out in the Deformation and Rheology laboratories of the GeoForschungsZentrum, Potsdam. A

saturated sample of the Clashach sandstone was loaded to failure under triaxial compression. The maximum compressive stress was provided by a servo-operated MTS 4600N loading frame, and hydraulic oil within the pressure vessel provided a confining pressure of 50.5MPa. Pore fluid pressure was maintained at 10.5MPa, resulting in an effective pressure of 40MPa. The Clashach sandstone has notably high uniaxial strength for a sandstone, of 105.8MPa (*Crawford et al*., 1995) and exhibits significant dilatancy before failure at such effective pressures (Fig. 5.2b).

Acoustic emissions (Fig. 5.2c) were monitored by twenty piezoelectric transducers (PZT), which were either epoxied to the sample surface inside brass housings, or embedded in the pistons. Section 4.2.2 (Figure 5.4.2) gives a more detailed description of the sensor arrangement. Eight of the PZTs were S-wave sensors and twelve were P-wave sensors, five of which also acted as transmitters to allow monitoring of ultrasonic velocities within the sample on a minute by minute basis. A constant strain rate of 1.7×10^{-6} s^{-1} was applied to the sample, resulting in failure by shear localisation (Fig. 5.2a). Automatic algorithms picked P-wave arrival times and amplitudes and then located hypocentres, for all AE detected at a minimum of eight sensors, with an estimated accuracy of ±1mm (*Stanchits et al*., 2006).

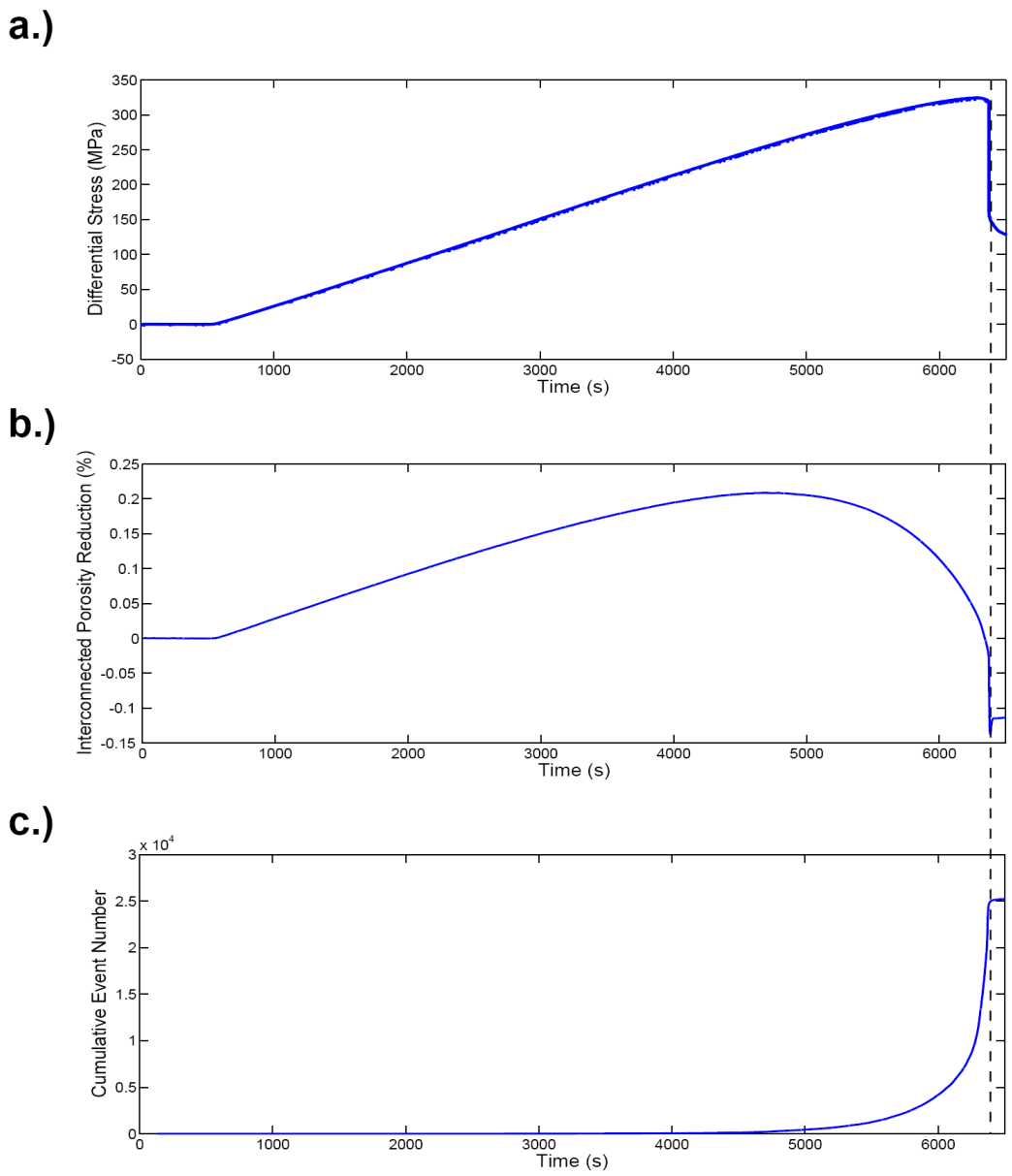

Figure 5.2 a-c) Evolution of physical properties of the Clashach sandstone, during triaxial compression. a.) Differential Stress (MPa), b.) Interconnected porosity reduction (%), c.) Cumulative number of acoustic emissions.

5.2.3 Moment tensor inversion of acoustic emissions

After the location of acoustic emission hypocentres, source analysis of each event could then take place. In this study we utilise a moment tensor inversion approach developed specifically for acoustic emissions by *Ohtsu* (1991). As with earthquakes in the field of seismology, the source mechanism of an acoustic emission can be represented by the action of six force-couples acting in unison (Fig. 5.3a). The resulting mechanism can therefore be represented by a three-by-three tensor termed the moment tensor, **M**, which is a function of the size and the orientation of the source. The elements along the diagonal of the tensor represent normal force-couples, whilst the remaining elements describe shear force-couples (*Aki and Richards*, 2002). The moment tensor can therefore describe a wide range of sources, from those involving only shear (when the trace of **M** is zero), to those with a significant volumetric component, whether it be explosive or implosive. This makes the moment tensor particularly useful for describing AE sources, which may often involve a notable volumetric component.

Utilising the approach of *Ohtsu* (1991), if we know the P-wave amplitudes generated by an AE event, at a minimum of six sensors, we can invert for the moment tensor. This chapter focuses primarily on the character and physical meaning of AE mechanisms. Further detail of the technical approach to the moment tensor inversion can be found in section 3.4.2. Once **M** has been determined, the source can be decomposed into three parts (Fig. 5.3b); i.) the double-couple (DC) part, which is essentially the shear component (eg. edge mode in Fig. 5.3b), ii.) the isotropic part (ISO), which is the

isotropic volumetric component to the source and may be either explosive or implosive, and iii.) the deviatoric or 'Compensated Linear Vector Dipole' (CLVD) part, which was proposed by *Knopoff and Randall* (1970) to allow for a volumetric component leading to a net volume change of zero. The contribution of each of these components to the source behaviour was then determined from the eigenvalues of **M,** as described in section 3.4.2.

AE events were then classified into different source types dependent upon their decomposition. Those with a DC component greater than 60 % or less than 40% were designated 'shear type' and 'tensile type' respectively. Events with an intermediate DC component, between 40% and 60% are described as 'mixed-mode' in nature. 'Collapse' events, with a net loss in volume, were selected if they involved a low to intermediate DC component, but a negative trace of **M**. In section 3.5.2 (Fig. 3.8), it was observed that this type of AE source is only of minor significance during shear localisation in granite, but is expected to play a much greater role in the deformation of porous rock, such as the Clashach sandstone.

In addition to aiding source classification, the focal mechanism of an acoustic emission can be plotted from its moment tensor. These visual characterisations of a source are regularly used in seismology to interpret faulting behaviour and represent the resulting pressure disturbance associated with the event. Regions which experience compression are shaded in black, whilst those that are subjected to dilatation are white. Figure 5.3b gives some example focal mechanisms and their associated physical sources.

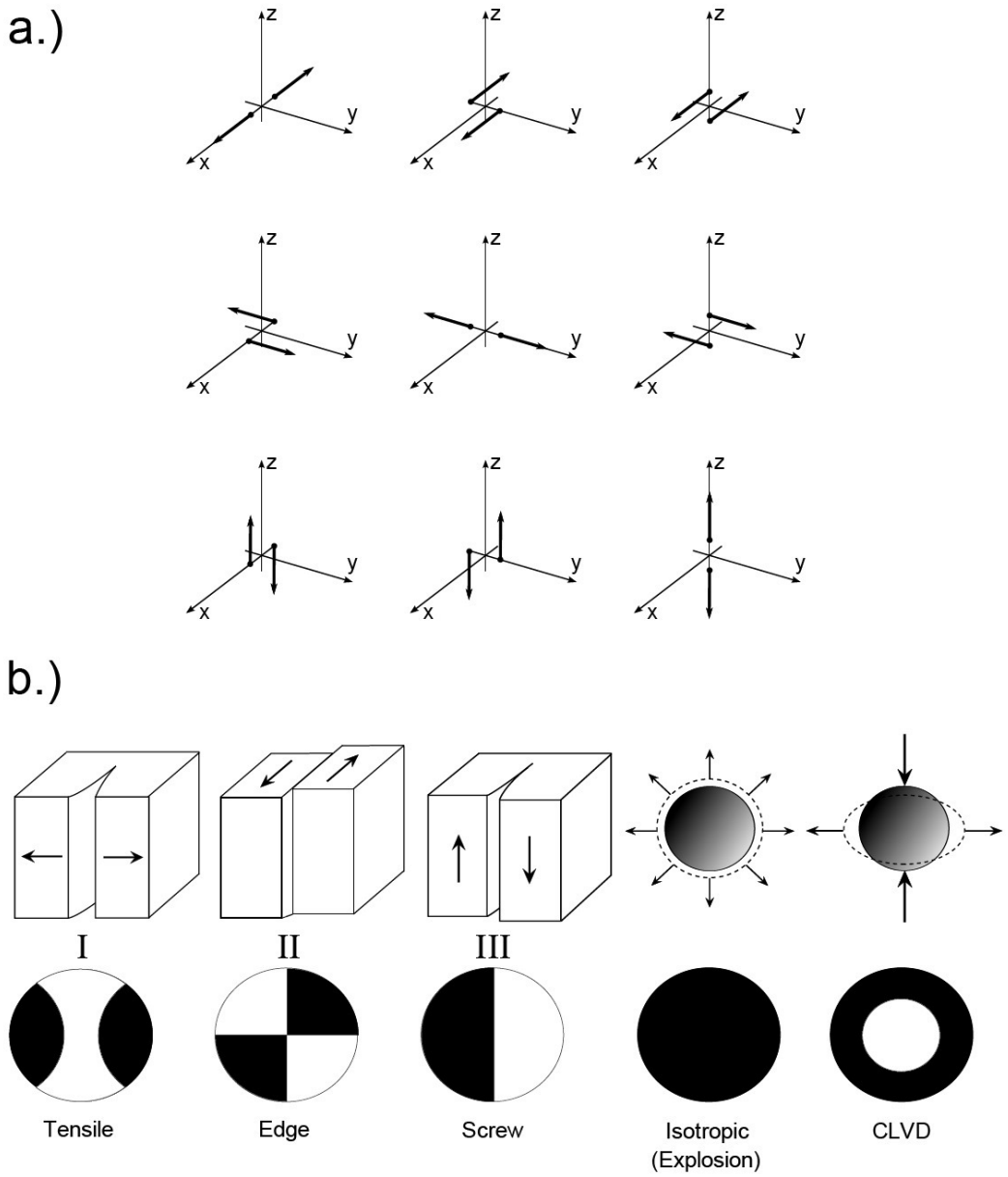

Figure 5.3. a.) The nine force couples that make up the seismic moment tensor. The diagonal elements are tensile force-couples, whilst the remaining force-couples are shear in nature. b.) Idealised acoustic emission sources and their associated focal mechanisms.

5.3 Microstructural observations

The sample failed by shear localisation along a fault plane orientated at an angle of approximately 30º from the maximum compressive stress. After unloading, the sample was injected with blue epoxy whilst under vacuum, so as to preserve microstructure within the failure plane. Thin sections were then cut, perpendicular to the fault plane, and polished for microscopic imaging.

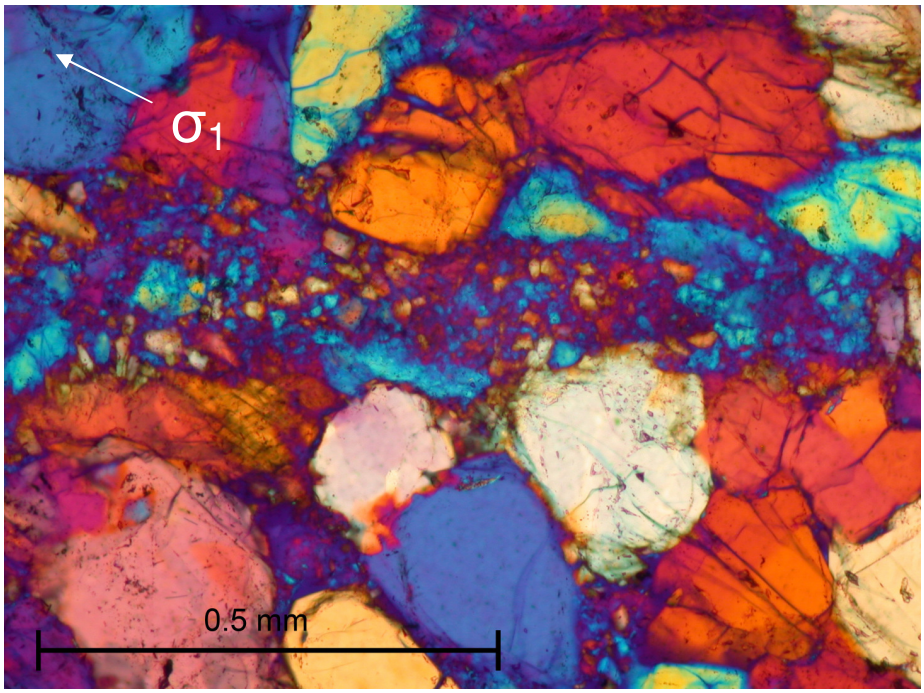

Figure 5.4. Photomicrograph of the shear band formed during triaxial compression of the Clashach sandstone. The image was taken using a petrological microscope in cross-polarised light using a sensitive plate to highlight different grains. The shear band runs E-W across the image at an angle of approximately thirty degrees from the maximum compressive stress. A zone of intense grain-crushing can be clearly observed, surrounded by significantly microcracked grains.

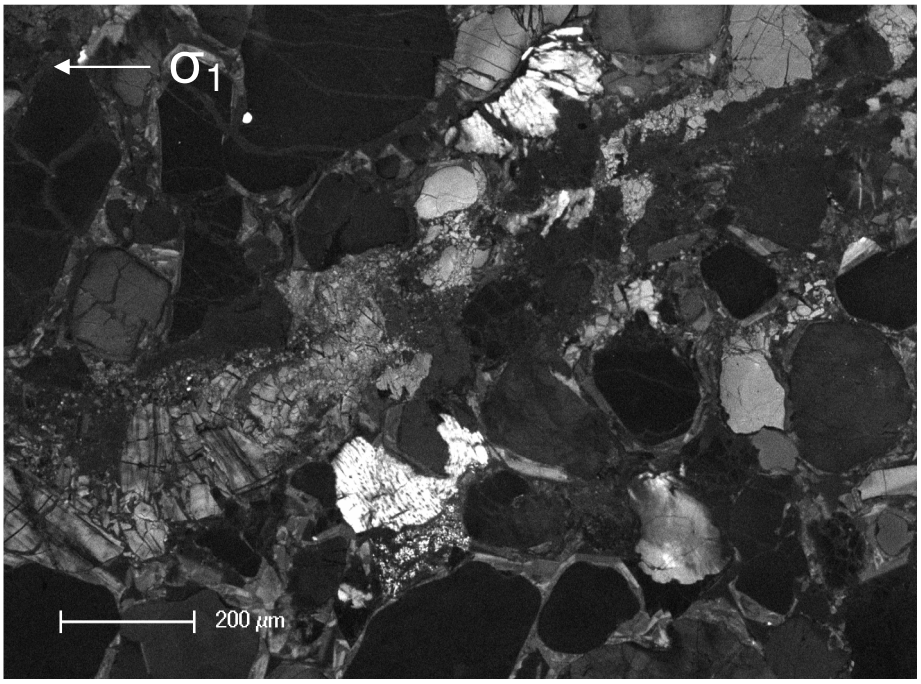

Figure 5.5. SEM Cathodo-Luminescence image of the shear band formed during triaxial compression of the Clashach sandstone. Quartz overgrowths are clearly observable around grains.

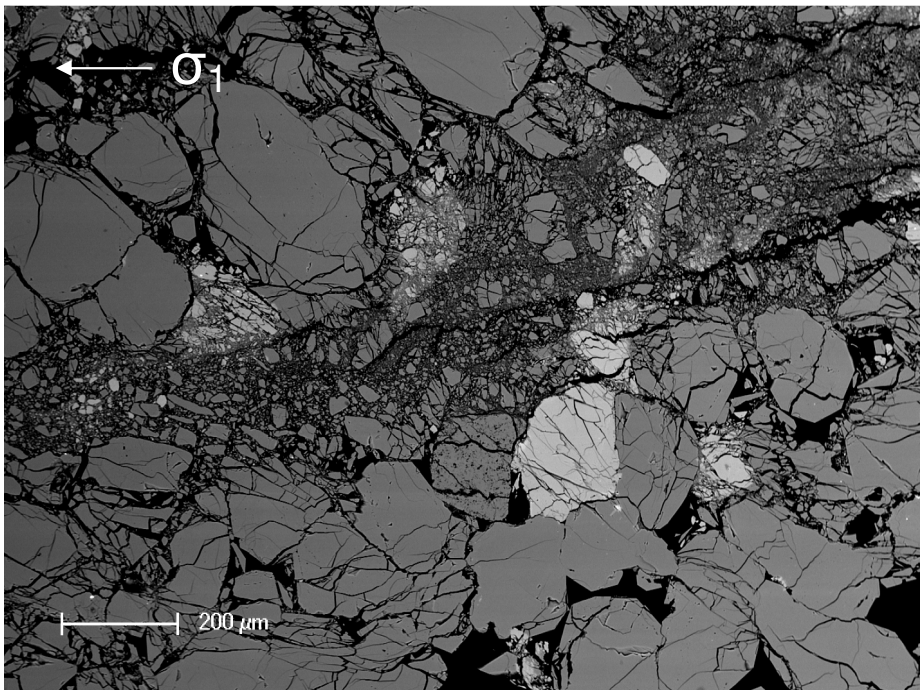

Figure 5.6. SEM Backscattered electron image of the shear band formed during triaxial compression of the Clashach sandstone. The whiter grains are feldspars, whilst most other grains are quartz.

Photomicrographs were taken under a petrological microscope, using a sensitive-tint plate to aide distinction between grains. A shear band was clearly observed to bisect the sample, containing a zone of intense grain-crushing and deformation (Fig. 5.4). However, out with the vicinity of the shear band, microcracking was also observed, though significantly less pervasive.

The thin sections were then carbon-coated for analysis using a Scanning Electron Microscope (XL30CP) in the School of Geosciences at the University of Edinburgh. A Cathodo-Luminescence (CL) image of the shear band highlights the presence of the pre-existing quartz overgrowths, within the Clashach sandstone (Fig. 5.5). Characterisation of the damage within the sample was then carried out using Backscattered Electron (BSE) imaging, which was found to highlight fractures well in the relatively compositionally unvarying sandstone. A BSE image of the shear band is shown in Figure 5.6. This study was aimed at investigating the mechanisms involved in shear localisation of sandstone and here we briefly describe some of those observed microscopically.

Significant tensile transgranular (Fig. 5.7) and intragranular fracturing was observed, often apparently as a result of impingement and generally in close association with the zone of shear localisation. *Menéndez et al*. (1996) observed intragranular fracturing in samples of Berea sandstone, but only predominantly after peak-stress and the onset of localisation.

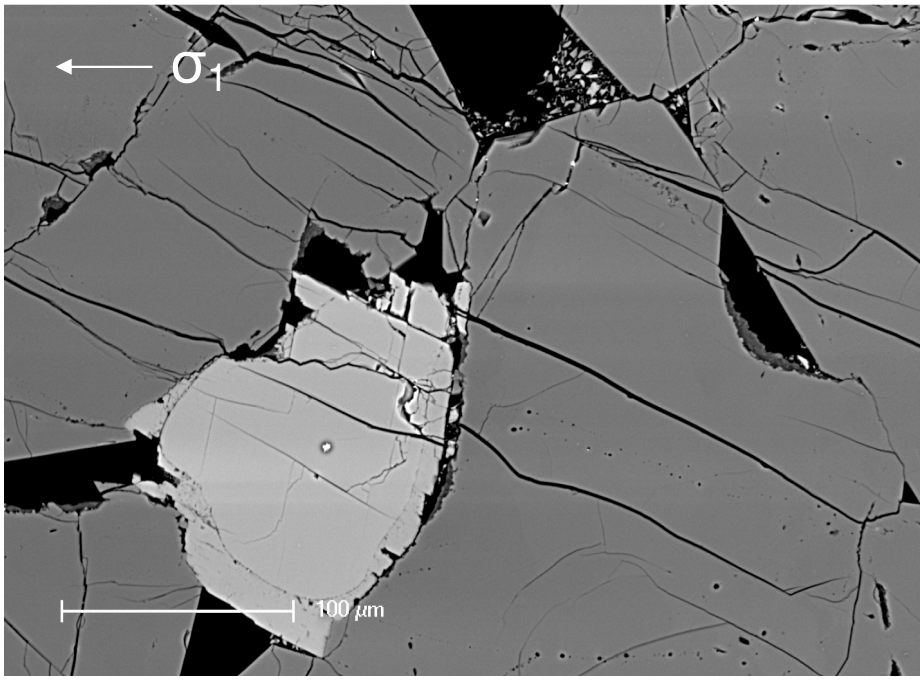

Figure 5.7. SEM BSE image of tensile microcracks through grains. The image was taken with the E-W direction parallel to the shear band, indicating that the tensile fractures are axially orientated.

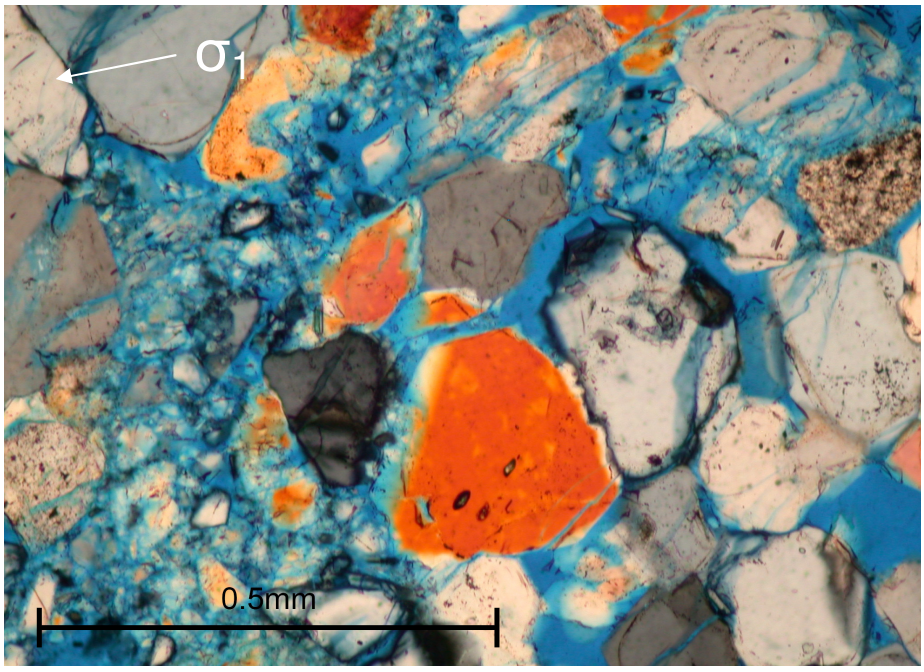

Figure 5.8. Photomicrograph of intergranular tensile fracture, due to failure of cement between a group of grains. The image was taken under a petrological microscope, using a 1/4λ plate to highlight individual grains.

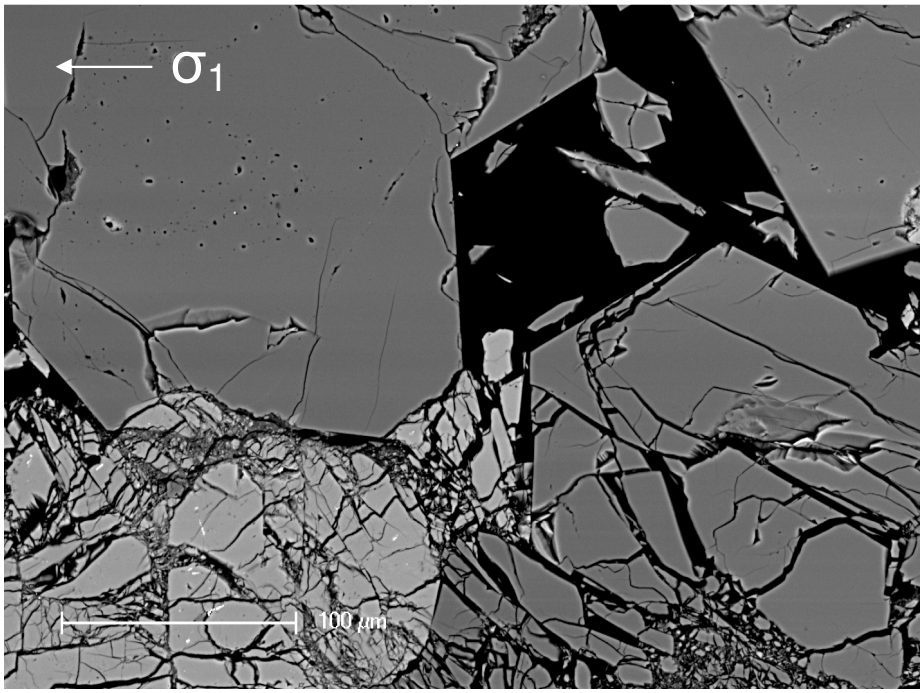

Figure 5.9. SEM BSE image of a potential source with an explosive volumetric component. Here, the sharp grain corners due to rupturing along quartz overgrowths indicates the original position of the grain.

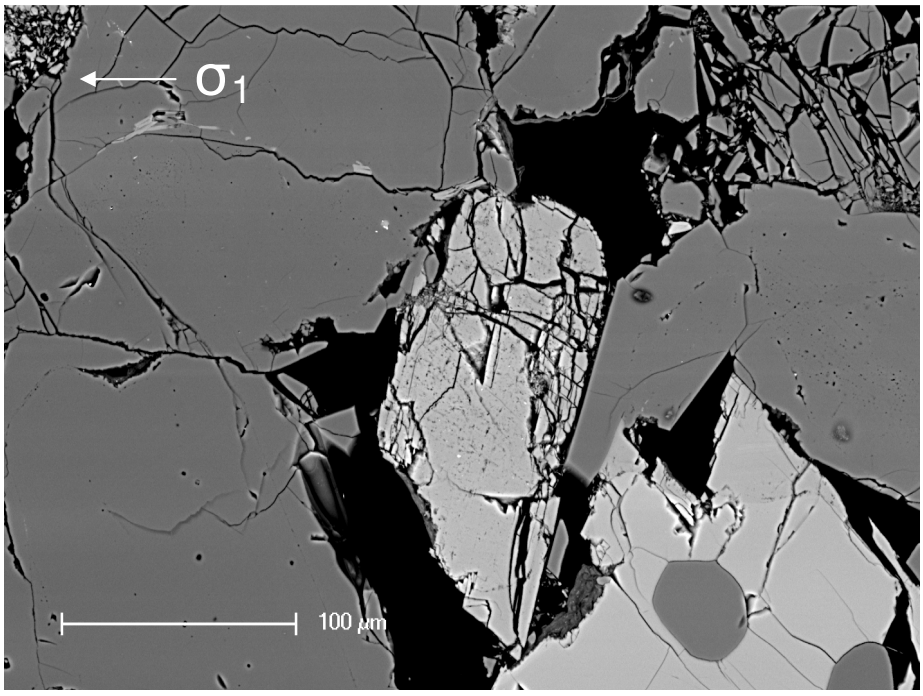

Figure 5.10. SEM BSE image of a crushed feldspar grain (lighter shade due to its composition).

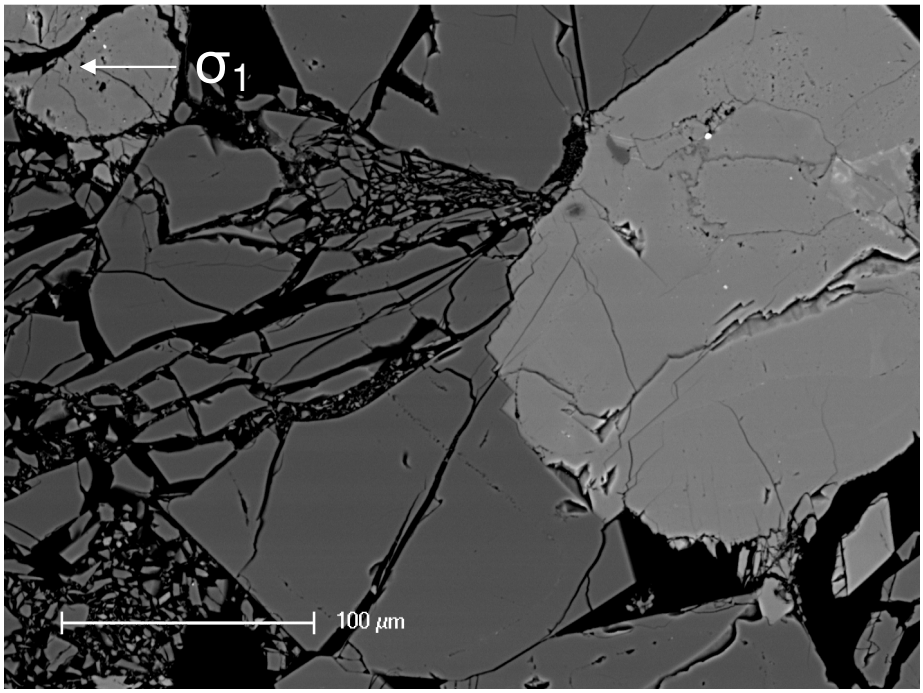

Figure 5.11. SEM BSE image of a crushed quartz grain, with fractures radiating outward from a contact with a neighbouring grain.

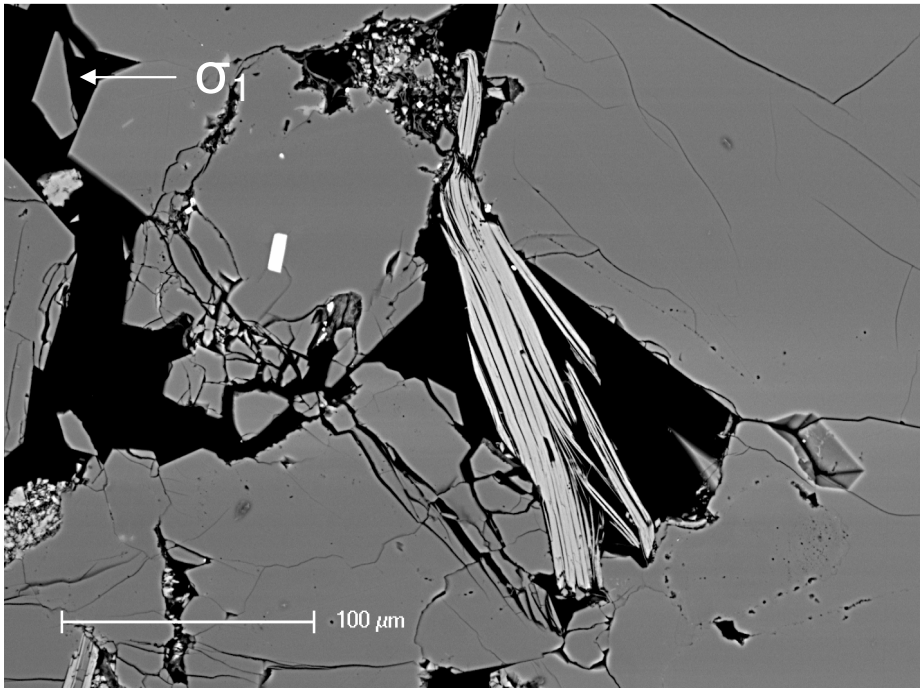

Figure 5.12. SEM BSE image of a deformed mica grain, due to displacement of surrounding quartz grains, and indicating pore-space reduction. Fracturing has preferentially occurred along the cleavage planes of the grain.

However, *Wu et al.* (2000) reported that intragranular microcracking was a significant contributor to dilatancy, during the triaxial compression of the Darley Dale sandstone, which has a porosity comparable to that of the Clashach sandstone. In addition, clear evidence was found of tensile fracturing between grains, along the quartz cement boundaries (Figs. 5.8 and 5.9), leading to local dilation. Whilst such behaviour is not necessarily easily observed during microimaging, there is potential for an acoustic emission to be generated, as will be discussed in section 5.4. A number of examples of cement fracture followed by probable grain-rotation were also observed; the sharp edges along ruptured quartz overgrowth boundaries indicating potential previous locations for grains prior to rotation.

Within the zone of localised damage, significant deformation by intragranular fracturing and grain-crushing was observed. Figure 5.10 shows a feldspar grain, which has been partially crushed between two quartz grains. An example of observed intragranular fracture is given in Fig. 5.11, where impingement cracks radiate outward through a quartz grain, from a point on its boundary adjacent to a feldspar grain. In Fig. 5.12, a single mica crystal has been trapped by adjacent quartz grains and deformed within a pore-space, leading to intragranular fracturing along cleavage planes. There was also some observed evidence for combined shear and tensile movement, or possible reactivation along pre-existing fractures, although the ordering of these events could not be directly determined by microstructural analysis alone.

5.4 Acoustic emission source analysis

Here we describe the acoustic emission source types detected during the triaxial compression of Clashach sandstone. Then we discuss the characteristics of these sources and present some example focal mechanisms.

5.4.1 Progression to failure

The damage progression to failure, during this experiment, is the subject of detailed investigation in chapter 4. This paper is instead designed to give a qualitative description of the breadth of the AE source behaviour observed in a low-porosity sandstone. Therefore, the emphasis is not on temporal or spatial evolution of various 'classes' of source types. However, to provide context, the general behaviour of these classes is briefly described here.

The dominant AE source types detected during the deformation of the Clashach sample are the 'shear' and 'collapse' types, as defined in section 5.2.3. During the early stages of AE activity, collapse sources dominate, although in the post-peak stress phase it is sources with a high shear component which are most prevalent. A significant proportion of events with a dominant tensile component were also recorded, although these decreased in prevalence over the course of loading. In addition, a number of explosive mixed-mode sources were detected, though far less common than the other source types.

5.4.2 Source mechanisms of acoustic emissions

Once the moment tensor of each event has been found, the AE source can be represented by plotting its focal mechanism. Figure 5.13 shows example focal mechanisms (without their isotropic part) for each of the chosen 'classes' of event produced during the deformation of the Clashach sample. Many of the shear events were extensional in nature, although a significant number of compressional sources were also observed. As expected, the collapse sources show compressional behaviour, whilst the mixed-mode and tensile AE show dilatational behaviour. However, with over twenty-thousand AE produced during one experiment, examination of individual mechanisms does not easily provide a holistic view of micromechanical behaviour. The degree of source mechanism variation within different classifications is, therefore, summarised in terms of the AE decompositions in histogram form (Figure 5.14a-b).

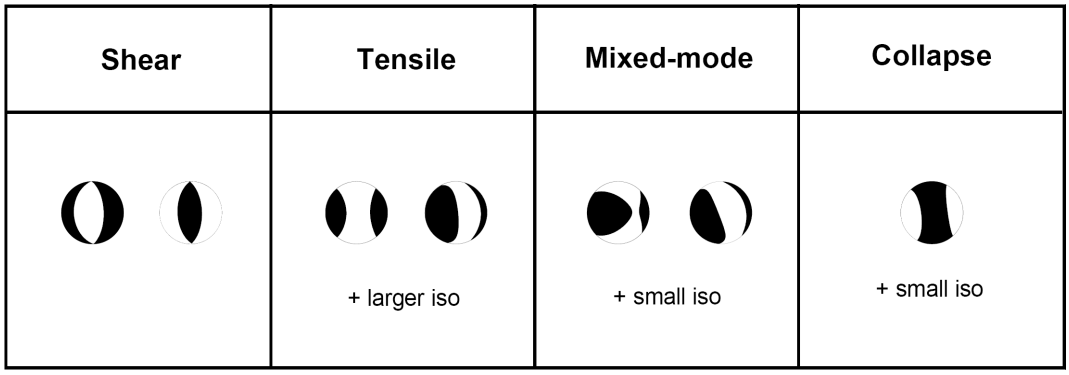

Figure 5.13. Example focal mechanisms for a number of different classes of acoustic emission. Black areas indicate regions of compression, whilst white areas represent regions of dilatation. ISO=isotropic component.

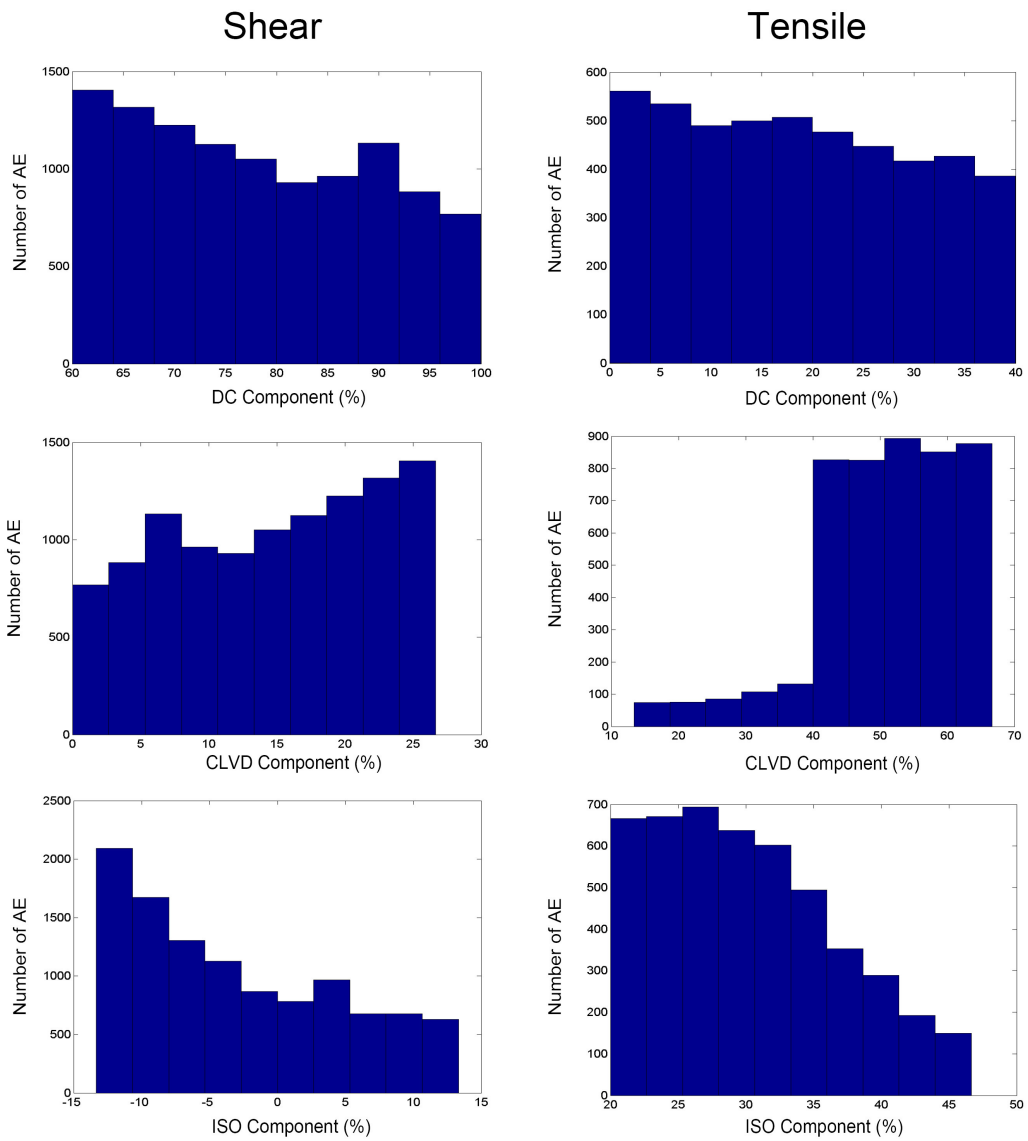

Figure 5.14. a.) Histograms indicating the distribution of source components for different classes of acoustic emission source. DC=double-couple component, CLVD=Compensated Linear Vector Dipole component (or deviatoric part), ISO=Isotropic component.

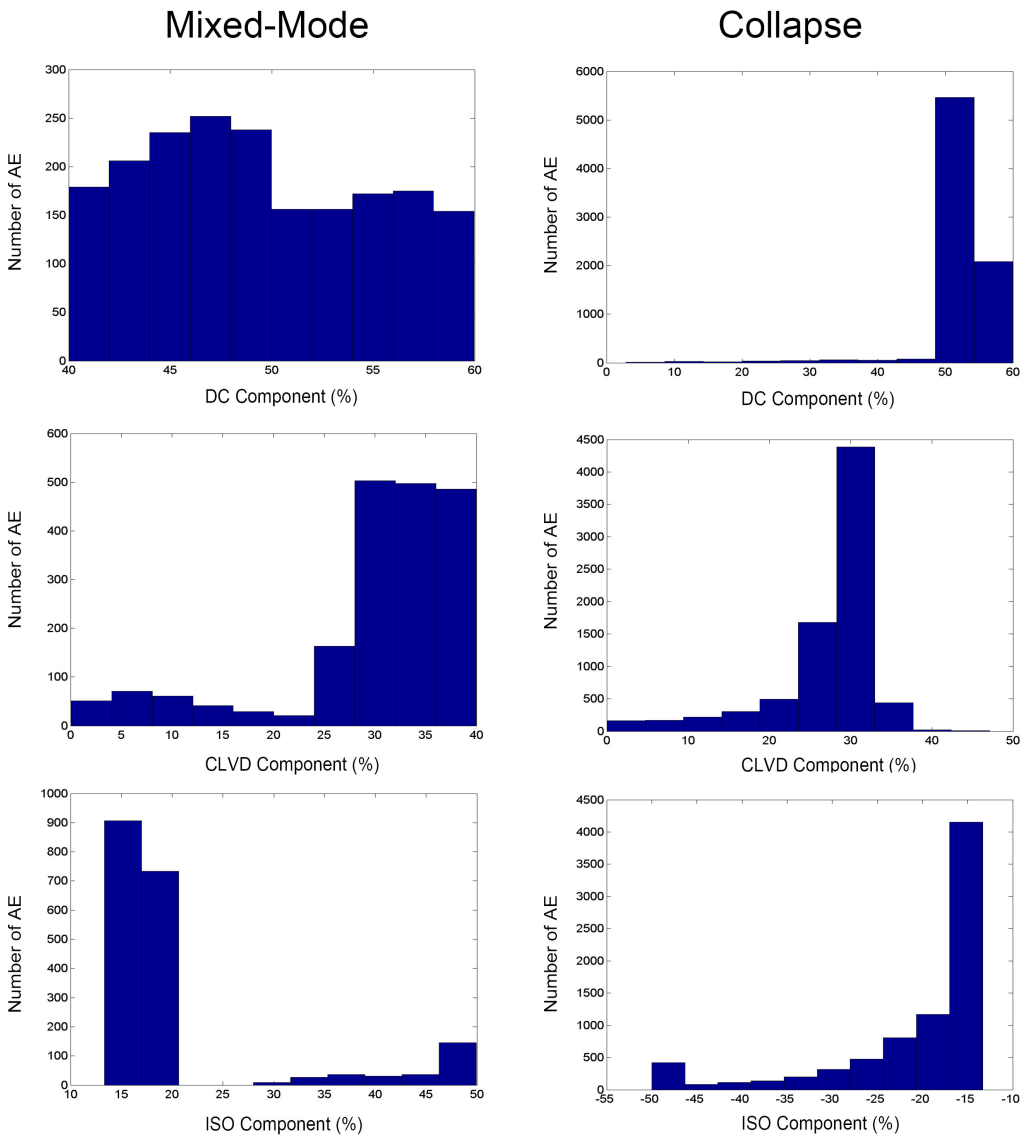

Figure 5.14. b.) Histograms indicating the distribution of source components for different classes of acoustic emission source. DC=double-couple component, CLVD=Compensated Linear Vector Dipole component (or deviatoric part), ISO=Isotropic component.

Here, the source is considered to be the sum of three components: i.) a double-couple (DC) part, which is essentially the proportion of shear involved, ii.) an isotropic part (ISO), which is the net implosive or explosive volumetric component, and is equal in all directions, and iii.) a deviatoric, or CLVD part, which is the remaining volumetric component, with a net change in volume of zero.

Figure 5.14 indicates that whilst the tensile and mixed-mode sources detected during the experiment can have relatively similar anisotropic focal mechanisms, the tensile sources tend to have a much larger explosive, isotropic part. Such source behaviour can be explained by microscopic observations of transgranular and intragranular microcracking, described in section 5.3 (Figs. 5.7 and 5.11), as well as by grain boundary rupture (Fig. 5.8). All source types display a wide range of possible DC component percentages, except the collapse sources. Looking at just the DC component, it would be very difficult to differentiate between the shear, tensile and mixed-mode sources without applying an arbitrary cut-off between each classification bin (40% and 60% were used in this study).

Collapse sources generally involve a relatively high shear contribution (50% or higher), in relation to the CLVD part, and as such are similar to the mixed-mode sources, but with an implosive volumetric component. This is consistent with the proposal by *Fortin et al*. (2009) that a pore-collapse event would, in reality, require significant shearing between grains, along intragranular microfractures or grain boundaries. However, we are not aware of any previous evidence for the involvement of shearing in collapse type

AE sources. Grain-crushing, as in Fig. 5.10, is also a potential source of such collapse events. There are also a small number of collapse sources with a very small DC component. Their contribution to shear localisation appears to be relatively insignificant, but may play a more important role during compaction localisation (see section 6.7).

The decomposition of shear sources (Fig. 5.14b) indicates that they can involve an *explosive* or an *implosive* isotropic component (as denoted by the sign of the percentage). Those events involving the latter are similar in nature to collapse type AE, but with a dominant DC component. As a result, their focal mechanisms are compressional in appearance, as with the collapse category sources, and can be explained by rearrangement of grain fragments (such as those shown in Fig. 5.11) leading to a net reduction in pore-space. In contrast, shear sources with a particularly low volumetric component are most likely to be associated with grain rotation and sliding.

The component characteristics of different source types, shown in Figure 5.14, display very little variation during the course of the experiment and exhibit similar distributions from the early stages of AE activity through to the failure of the sample. Only the shear sources display any notable change in characteristics, which is a slight increase in the DC component, at the expense of the isotropic component, as failure is approached. After failure, a significant drop in the isotropic component of AE is observed, which is intuitively to be expected. The decomposition of acoustic emissions produced during

this experiment clearly demonstrates that their sources involve a wide range of characteristics and represent a broad spectrum of microscale deformation mechanisms.

5.5 Discussion

Microstructural analysis highlights the complexity of microfracturing in sandstones. Unlike other techniques, moment tensor inversion provides a full description of the source characteristics of acoustic emissions across the continuum of possible mechanisms. This demonstrates that acoustic emissions *also* have complicated sources, and directly reflect the complexity of the observed microstructure. In this section we discuss the physical meaning of these source characteristics.

5.5.1 Common mechanisms for AE generation

There is a widely accepted correlation between the rate of accumulation of inelastic strain, during loading of rock in the brittle regime, and the rate of acoustic emissions produced by the material (*Mogi*, 1962; *Scholz*, 1968a; *Lockner*, 1993; *Paterson and Wong*, 2005). This correlation is generally attributed to the production of acoustic emissions during the microcracking of the deforming sample and has led to the development of techniques that apply AE-derived parameters to damage mechanics models. (*Cox and Meredith*, 1993; *Ojala et al*., 2003) In compact rocks, whilst the

production of AE by pore-collapse processes may sometimes lead to uncertainty in picking the onset point of microcracking, the majority of emissions during the course of an experiment can be attributed to microcracking processes. In porous rocks, however, the physical meaning of AE is complicated by the addition of pore-space and there are a number of ongoing microscale processes which may be responsible for emission, including pore-collapse and grain-crushing. Here, we present a number of acoustic emission source types, produced during the brittle compression of the Clashach sandstone, and suggest potential physical mechanisms that may lead to their generation (Fig. 5.15).

The most common acoustic emission sources detected during the course of the experiment were 'collapse' and 'shear' type events. Collapse sources (Fig. 5.15e. i.-iii.) involve an implosive volumetric component and, in general, a significant shear component. As such, they are most likely to be generated by pore-collapse and grain-crushing events. A very few collapse AE have a low shear component and are likely to be closer to compaction in nature, involving the collapse of pore-space, but with less significant sliding between grains (Fig. 5.15e. i.).

In contrast, shear type AE require a significant component of grain-grain interaction in order to generate a large DC component. This may be either extensional (Fig. 5.15b) or compressional (Fig. 5.15c) in nature, and involve intergranular motion, such as sliding and rotation (Fig. 5.15b-c, i.-ii.), or intragranular movement, such as pore-collapse and grain-crushing (Fig. 5.15b-c, iii.-iv.).

AE Mechanism Type	Physical Mechanisms	Examples
a.) Tensile Example focal mechanism:  + larger iso	i.) Intergranular fracturing between grains/through cement ii.) Rotation with tensile component ii.) Intragranular cracking, e.g., Hertzian iv.) Rotation on intragranular microcracks	i.) ii.) iii.) iv.) 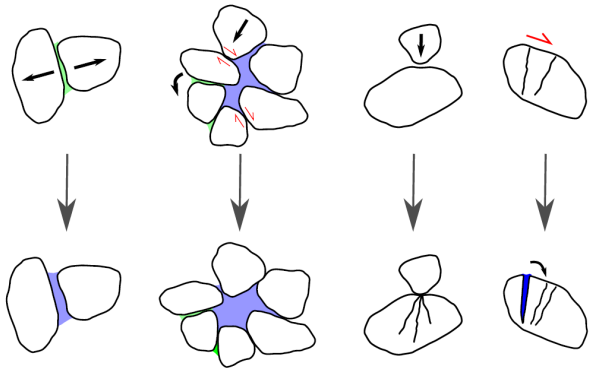
b.) Extensile shear Example focal mechanism: 	i.) Sliding between grains ii.) Rotation of grains iii.) Intragranular cracking/ grain-crushing	i.) ii.) iii.) iv.) 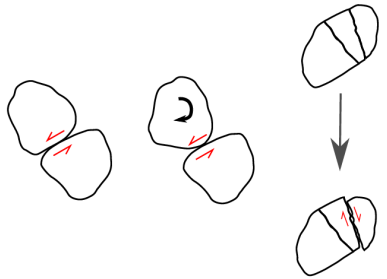 Rotation as in a.), ii.) with larger DC component

Figure 5.15 (Continued overleaf). Potential physical mechanisms for generation of acoustic emissions in low porosity sandstone. Porosity is indicated by blue shading and cement by green.

c.) Compressional shear Example focal mechanism: 	i.) Sliding between grains ii.) Rotation of grains iii.) Intragranular cracking/ grain-crushing	i.) ii.) iii.) iv.) 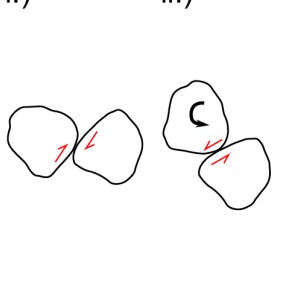 Collapse as in e.), ii.), with larger DC component
d.) Mixed-mode Example focal mechanism:  + small iso	i.) Cement fracturing with high tensile and shear components ii.) Rotation of grains iii.) Wing cracks?	i.) ii.) 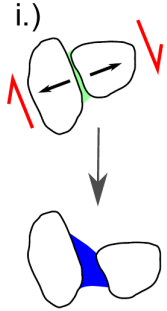 Rotation as in a.), ii.), with smaller tensile component
e.) Collapse Example focal mechanism:  + small iso	i.) Compaction ii.) Pore-collapse with intergranular sliding iii.) Pore-collapse/ grain-crushing, with intragranular sliding/rotation	i.) ii.) iii.) 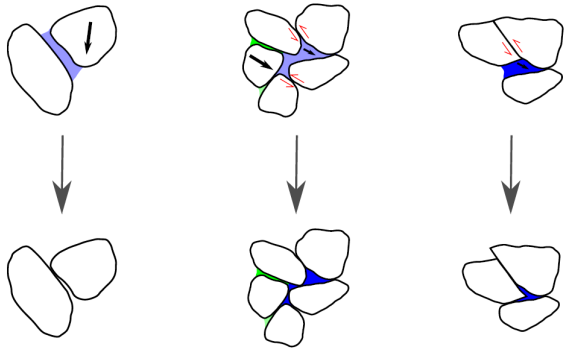

Figure 5.15 (Continued). Potential physical mechanisms for generation of acoustic emissions in low porosity sandstone.

Pore-collapse and grain-crushing events may therefore, be classified as either a 'collapse' event or a 'shear' event; the only distinction being the ratio of shear to volumetric strain. In reality, these events represent a continuum of behaviour from pore-collapse with significant reduction in pore-space, and a smaller degree of sliding between grains, to pore-collapse with only a small reduction in pore-space, and a more significant degree of intergranular sliding.

In addition, two further types of sources are described here, although they play a secondary role in the damage evolution of the sample. 'Mixed-mode' events may possibly have been produced during the fracturing of cement between grains, where both a significant shear and tensile component were involved simultaneously (Fig. 5.15d. i.), or perhaps during dilating rotation events that required a significant degree of intergranular sliding (Fig. 5.15d. ii.). However, the small proportion of mixed-mode sources detected during the course of the experiment would suggest that this is not a primary mechanism for deformation in low-porosity sandstone. Such mixed-mode deformation is known as 'trans-tensional' on a much larger scale, in structural geology and tectonics. It is relatively common in situations where plate tectonic forces are oblique to plate boundaries. We might expect it to be less important here since there is no strong pre-existing structure, apart from bedding. Consequently, it is possible that this small proportion of mixed-mode events are preferentially orientated in relation to the bedding orientation.

A more significant event is the 'tensile' type emission. Such AE may be related to the fracture of cement or grain rotation events, but are also likely to be produced during intragranular microcracking. In chapter 4, section 3.3, it was observed that the relative proportion of these events, in relation to other forms of AE, decreases during the course of the experiment. However, the mechanisms associated with tensile AE sources may be relatively crucial in allowing other forms of micromechanical behaviour and, hence, the onset of shear localisation, to occur.

The reality is that a wide range of mechanical behaviour can produce AE. This lends credence to the idea that the noted discrepancy in AE numbers in relation to microscopically determined crack densities (*Lockner*, 1993) is a consequence of the physical limits of detection, including the attenuation of small magnitude events, rather than being the result of AE representing an 'uncommon form of microcracking' (*Lockner*, 1993).

5.5.2 AE-associated damage in Clashach sandstone

Two primary types of acoustic emission were detected during the triaxial compression of Clashach sandstone. Collapse sources are dominant before the onset of localisation and generally involve a significant component of shear (Fig. 5.15e. ii. and iii. are much more common than i.). In their majority they are, therefore, likely to be the product of pore-

collapse and grain-crushing events where the change in volume occurring is more significant than the proportion of shear.

The other primary class of AE is the shear type event. These may lead to either dilation or compaction, although the isotropic component is more often negative than positive, indicating that the latter effect is the most predominant over the entire duration of the experiment. The relative proportion of their shear to volumetric components is also observed to increase slightly during the course of the experiment, which may be the result of increased grain-crushing, after the onset of shear localisation. The relative increase in shear type AE as failure is approached, and the associated decrease in collapse type events, may also be related to an increase in grain-crushing behaviour, relative to pore-collapses, as the volumetric component of such sources decreases.

Furthermore, whilst a significant proportion of tensile AE events may be the result of intergranular processes such as cement fracture and grain rotation, the majority of tensile events involve only a relatively small shear component, indicating that the most dominant mechanism for their generation is intragranular fracture. Whilst the quantitative microstructural analysis of *Menéndez et al*., 1996 indicated that significant intragranular fracture was not detected in Berea sandstone before peak stress was attained, the Clashach sandstone has a significantly lower porosity, the micromechanical behaviour of which may share characteristics with compact rock (*Paterson and Wong*, 2005). This hypothesis is consistent with the findings of *Wu et al.* (2000), who carried out quantitative microstructural analysis of the Darley Dale sandstone, which has a

comparatively similar porosity to the Clashach sandstone. They compared stress-induced anisotropy predicted by the sliding wing crack model with microstructural data laboratory experiments. Whilst they expected this approach to be inconsistent with the micromechanical behaviour of high porosity Berea sandstone, they also observed a significant discrepancy between microstructural observations and model predictions for the Darley Dale sandstone. The results of this study suggest that shear localisation in low-porosity sandstone involves a broad range of micromechanical behaviour, such as intragranular fracture and grain-sliding/rotation. As a consequence, it seems likely that the damage evolution is an intermediate process between two end-member approaches to failure, involving elements of micromechanical behaviour observed in both compact rocks and high-porosity sandstones. Moment tensor inversion analysis of AE from a higher porosity sandstone may help to further elucidate this.

The results of this study clearly demonstrate the breadth of mechanisms capable of producing acoustic emissions, the corollary of which is that AE are generated by a wide range of competing micromechanical processes during the brittle deformation of low-porosity sandstone, some of which are compactive and some dilational in nature. This has implications for damage mechanics models that incorporate AE-based parameters to estimate microcrack evolution. In seismotectonics, the inelastic deformation of plates can be investigated by summing the moment tensors of earthquakes within a selected volume of crust (*Jackson and McKenzie*, 1998). In this way, the net-contribution of different types of faulting to regional strain can be determined. *Shah and Labuz* (1995) utilised a not dissimilar technique to this by developing a tensorial measure of damage,

from MTI of AE produced during uniaxially compressed Charcoal granite, based on the ratio of axially orientated damage (described as 'normal' microcracking) to randomly orientated damaged (described as 'shear' microcracking). *Carvalho and Labuz* (2002) applied a similar approach to AE from plane-strain compression of Red Wildmoor sandstone. However, the results of this study suggest that such a separation of damage into two such distinct types of micocracking, purely based on orientation, may not be a reasonable assumption where pre-existing porosity is present, at least for sandstone under triaxial compression. Further work on the effectiveness of tensorial damage characterisation in sandstone, as carried out here, may help to further elucidate this problem.

5.6 Summary

Moment tensor inversion of acoustic emissions is of particular benefit to the study of porous media micromechanics, where some source characteristics such as sliding and rotation, cannot easily be detected by microstructural analysis and are too complicated to be determined by simpler forms of source analysis. In this study, such an approach was utilised to characterise the sources of AE generated from the triaxial compression of Clashach sandstone, in the brittle regime. The results indicate that a wide range of mechanisms are responsible for the production of acoustic emissions, comparable in scope to those observed by inspection with a scanning electron microscope. Microscale evolution of damage, during shear localisation in low-porosity sandstone, is highly

complex and may represent an intermediate form of micromechanical behaviour, between a compact rock and a high-porosity sandstone, incorporating elements of microscale deformation from both.

The most dominant forms of damage detected were 'collapse' sources, which generally also involve a significant shear component, and 'shear' sources that often involved a notable volumetric component. A continuum of behaviour between these two source types was displayed by the AE. Both types of AE are likely to be generated by pore-collapse and grain-crushing events, involving differing ratios of collapse to shear parts to their source mechanisms. It is proposed that a notable increase in the shear component of shear type sources, after peak stress is reached, is due to increased grain-crushing during the shear localisation process. Shear type sources with a particularly low volumetric component were also detected and these are attributed to sliding and rotation of grains, which may contribute to dilation, as suggested for the Berea sandstone by *Menéndez et al*., 1996. Finally, tensile type AE sources are interpreted as intragranular fracture, with a low shear component, and intergranular microcracking such as cement fracture, with a more significant shear component. This is consistent with microstructural observations that suggest that intragranular fracture may play a significant role in dilatancy of low-porosity sandstones (*Wu et al*., 2000). Comparison with moment tensor inversion results for acoustic emissions generated in a high-porosity sandstone may help to elucidate this.

Acoustic emissions are generated by a wide range of mechanisms during shear localisation in low-porosity sandstone. They exhibit a broad range of source mechanisms, indicating that the sources responsible for their emission involve a continuum of different micromechanical components. This has implications for models of rock failure that incorporate damage parameters estimated from the acoustic emissions detected. It also demonstrates that the micromechanics of brittle deformation is a highly complex process, whi ch may be further elucidated by accessing the detailed and temporally complete data-set that laboratory acoustic emissions provide.

Chapter 6

Discussion

6.1 Introduction

Acoustic emissions offer considerable information on the internal state of a deforming rock, during laboratory testing in the brittle field. The application of seismological source analysis methods to acoustic emission (AE) waveform data is a powerful tool for characterising evolving damage processes leading up to sample failure. The moment tensor inversion technique utilised in this thesis produces results that are both intuitively realistic and consistent with microstructural observations. In addition, comparison of moment tensor inversion results with those produced by a more simplistic approach to source analysis, indicate remarkably similar results for the same data set. However, in addition, the moment tensor inversion technique provides a full multi-component description of AE sources and is also therefore capable of dealing with complex mixed-mode sources, such as those generated during the compression of porous rock. It is also relatively straightforward to compare with the stresses and strains of the bulk sample.

6.2 Synopsis of damage evolution

This thesis is primarily concerned with utilising acoustic emission data to examine the evolution of the micromechanical processes that lead to brittle failure in triaxially compressed rock. The data discussed comes from experiments conducted on: i.) a compact rock with no pre-existing porosity or significant damage, known as the Aue granite from Germany, and ii.) a low-porosity sandstone, from the Clashach quarry in Scotland. These materials were selected so as to enable comparison of the micromechanical evolution of damage, up to and during shear localisation, in samples of varying porosity, specifically the transition from virtually no porosity to a relatively low-porosity material. As the focus of the hydrocarbons industry shifts to extraction from non-ideal reservoir rocks with lower permeability, improving our understanding of the process of fault formation in low-porosity sandstones becomes of increasing importance. The Clashach sandstone is an onshore analogue for the Moray Firth Basin and has a reduced porosity due to the diagenetic formation of quartz overgrowths.

The primary findings of this study are illustrated in Figure 6.1, which summarises the mechanistic changes in microscale deformation during compressive loading of granite and sandstone, as determined from source analysis of acoustic emissions. Unlike microstructural analysis, these diagrams are not compiled from instantaneous points on the loading curve, but are derived from a continuous stream of data, as AE were generated during the course of sample loading. In both compact and porous rock, significant changes in source characteristics are observed before failure.

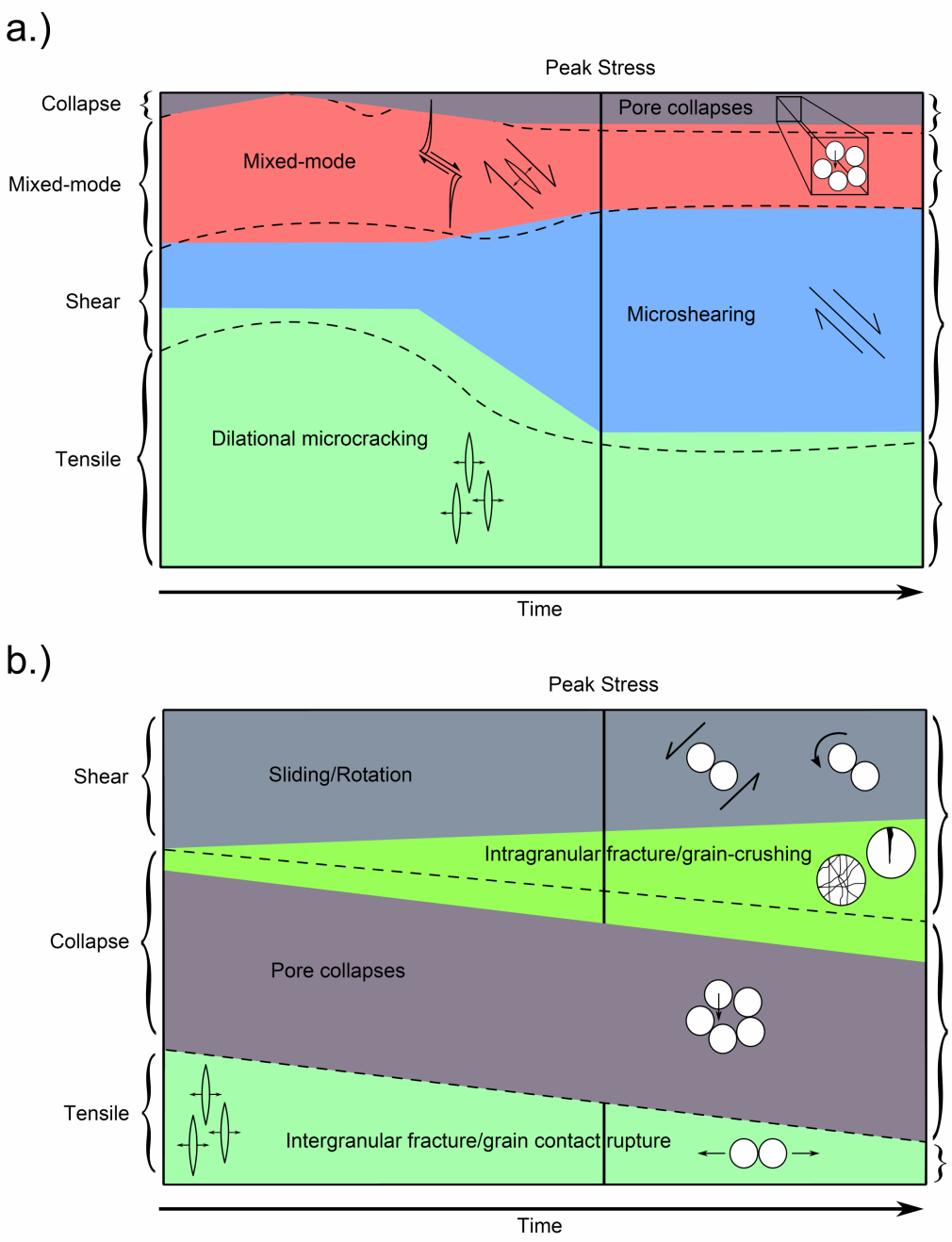

Figure 6.1. Summary diagram illustrating the micromechanical evolution of inelastic deformation, as inferred from acoustic emission source characteristics, for a.) triaxial compression of Aue granite, and b.) triaxial compression of Clashach sandstone. Colours indicate types of physical mechanisms, whilst dashed lines highlight boundaries between AE source types (indicated by brackets). For example, the physical process of intragranular fracture/grain-crushing is shaded in lime green and may be generated both shear and collapse source types (as indicated by the dashed line which transects this area).

Decomposition of AE sources produced by the Aue granite indicate a significant proportion of events that involve both substantial shear and volumetric components. Such mixed-mode behaviour is not easily detected from first motion polarities alone, but is clearly differentiable by inverting for the full moment tensor, highlighting a major advantage of the method for laboratory tests where macroscopic strain has a clear volumetric component. Implosive events were also detected, but they represent only a small fraction of the total number of detected AE. Although not presented in the body of this thesis, determination of the orientation of tensile fractures from the eigenvectors of their moment tensors indicates that they have a preferred orientation aligned with the maximum compressive stress (see Appendix B). In addition, the standard deviation from this orientation was observed to decrease during the course of loading (Appendix B), indicating greater alignment of tensile cracks with the maximum principal stress at higher stresses. The onset of shear localisation is notably correlated with a significant increase in the relative proportion of microshearing events, and a concurrent decrease in the tensile microcracking. This is consistent with models such as that proposed by *Reches and Lockner* (1994), where increased tensile microcrack density leads to the onset of localised shearing and unstable microfracturing, cascading to failure.

In contrast, AE events with an implosive volumetric component do contribute significantly to inelastic deformation during the approach to failure in the more porous Clashach sandstone. Moment tensor analysis demonstrates that these events are not simple sources but also involve a significant shear component. This result is in agreement with the suggestion that pore-spaces generally require a degree of shear

motion in order to collapse *(Fortin et al*., 2009). This has not previously been demonstrated, again highlighting the utility of the detailed moment tensor analysis to discriminate between competing hypotheses for damage evolution. A notable increase in double-couple behaviour is also observed during the approach to failure, perhaps related to an increase in grain-crushing processes and coupled with a decrease in the volumetric component of events. Such a shift in behaviour is also consistent with an acceleration in macroscopic shear strain.

Decomposition of AE produced by the Clashach sandstone, and inspection of their focal mechanisms, indicate that the processes leading to shear localisation in the Clashach sandstone represent an intermediate behaviour between that of a compact rock, illustrated by the Aue granite, and a high-porosity sandstone, as described by the microstructural observations of *Menéndez et al*. (1996). This is consistent with the high uniaxial compressive strength of the Clashach sandstone of 105.8MPa (*Crawford et al*., 1995; see table 2.1, chapter 2 for comparison) and the argument made by *Wong et al*. (1997), based on mechanical data, that the onset of grain-crushing in a lower-porosity rock requires a higher critical pressure. As such, dilatancy and shear localisation occur over a broader array of confining pressures, leading to in essence a more 'brittle' behaviour than a higher-porosity sandstone would have. As a consequence three different approaches to failure, by shear localisation, can be described for compact, high-porosity and low-porosity rock, respectively;

i.) Tensile microcracking leads to significant dilation. As they increase in spatial density, interaction develops between microcracks, leading to the formation of an unstable process zone. Further dilation is accommodated by microshearing within a localised region, leading to the formation of a macroscopic fracture and sample failure.

ii.) Intergranular fracture, such as grain-contact rupture, allows dilation to occur by sliding and rotation of grains. Significant intragranular fracture only initiates near peak stress and intensifies post-peak, during grain-crushing within the forming shear band.

iii.) A combination of the processes observed in i.) and ii.). Dilation by both inter- and intragranular cracking. Significant grain-crushing during shear band formation.

It therefore seems feasible that the ratio of implosive to explosive sources may be a useful quantity for determining the internal behaviour of a compressed rock. In the case of the Aue granite, a greater number of acoustic emissions have an explosive volumetric source than an implosive one, due to the high proportion of tensile microcracking and the small number of collapse sources. In contrast, the Clashach sandstone exhibited slightly more implosive sources than explosive sources. Moreover, temporal changes in the ratio of positive to negative volumetric source components were also observed during the loading process; increasing in sandstone after peak stress and decreasing in granite after peak stress. However, it seems reasonable to assume that these changes need to be weighted with respect to the magnitude of each event, and hence their total contribution to the inelastic strain taken into consideration. As such, further

investigation of these changes is required, as well as comparison with analysis of AE data from a high-porosity sandstone.

The results presented in this thesis represent the first comparison of the moment tensor characteristics of AE generated by compact versus porous rock. In addition, the Clashach results represent a detailed characterisation of acoustic emission-associated damage, produced during the deformation of a low-porosity sandstone, and integrating both mechanical and microstructural observations. The following sections of this chapter go on to further discuss the findings of this study and potential applications, before suggesting some possible directions for further work.

6.3 Synopsis of spatial evolution

The spatial evolution of AE hypocentres has been investigated in detail for compact rock (*Lockner et al*., 1991; *Reches and Lockner*, 1994). The results presented in this thesis for the Aue granite, are consistent with previous micromechanical interpretations of the shear localisation process. Fig. 6.2 summarises the spatial and mechanical development of damage, in terms of the associated AE source types, for both the Aue granite and the Clashach sandstone. The primary focus in the investigation of this localisation process was on the sandstone data set, as the spatial development of AE source mechanisms in low-porosity sandstone is not fully understood. As such, Fig. 6.2a illustrates qualitative findings of the spatio-mechanical damage development of the Aue granite, rather than

the quantified results presented for the sandstone. Nevertheless, qualitative findings indicate two primary phases of development, during the period of significant AE activity; i.) a period of spatially distributed damage, where tensile sources are dominant, but shear and mixed-mode sources are also occurring in significant quantities, and ii.) a period of spatially localised damage, which is dominated by shear type damage, though also involving tensile and mixed-mode sources. The transition from phase i.) to ii.) occurs rapidly during the post-peak region of the stress-strain curve and is observed to propagate through the sample, initiating at its side.

In contrast, mechanical changes observed during shear localisation in the Clashach sandstone, also involve a significant proportion of implosive mechanisms. Figure 6.2b summarises the findings of the spatial analysis carried out for different AE mechanisms. Initially, all mechanisms exhibit a delocalised distribution, although the proportion of shear sources increases during loading, whilst tensile sources were observed to decline in relative dominance before the peak stress is reached. Localisation was observed to correlate with the onset of strain-softening. Initial hypocentre clustering involved both shear and tensile sources, although failure did not take place until the collapse sources also localised. Whether this behaviour is a symptom or a cause of failure is unclear. However, these results do indicate that a significant compactive component to microscale deformation must take place in the vicinity of the shear band for failure to occur, perhaps as a consequence of gouge formation along the developing macroscopic fault.

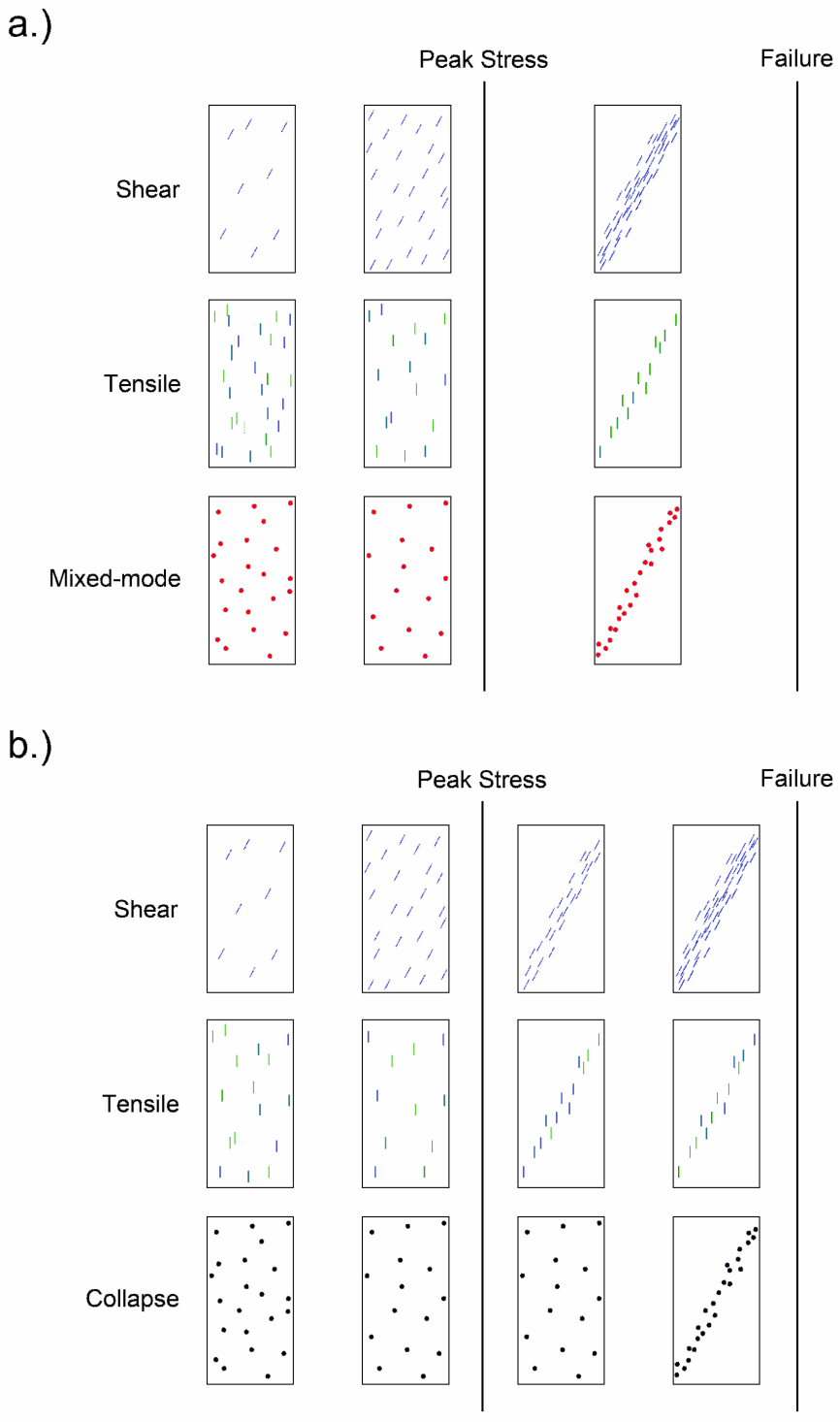

Figure 6.2. Summary diagram illustrating the spatio-mechanical evolution of inelastic deformation, as inferred from acoustic emission source characteristics, for a.) triaxial compression of Aue granite, and b.) triaxial compression of Clashach sandstone. Each box contains an instantaneous snap-shot of the nature and degree of processes occurring at a given stage in the damage evolution process and does not include previously accumulated damage.

In addition, during the strain-softening phase, the rate of acoustic emission and the degree of localisation were observed to be closely interlinked; regions with significant hypocentre clustering also exhibited notably higher AE rates. In order to sustain localised behaviour, rapidly escalating damage is required, leading to instability and the cascade to failure. Consequently the AE rate curve may be considered to be the superposition of many interlinking 'failures' on the microscale. If this process is inhibited, for example by heterogeneity, the AE rate curve will exhibit a hiatus, until a new pathway can be developed.

6.4 Source complexity

The first moment tensor inversion results of AE data generated during shear localisation in sandstone are presented in this thesis. Analysis of acoustic emission focal mechanisms clearly reveals the complexity of event sources in deforming sandstone. Decomposition of events into DC, CLVD and ISO parts demonstrates that the micromechanisms involved in the generation of AE are not made of up of a few, discrete types of fracture, but in reality represent a broad continuum of behaviours. The practice of using source type 'bins' for classification purposes is generally applicable because it allows the evolution of different 'bulk' behaviours to be monitored. However, one should always be aware of the breadth of each bin's 'contents'. For example, during the compression of Aue granite, the 'collapse' type was sufficient to describe AE with an

implosive volumetric component. However, during the deformation of a high-porosity sandstone, at a high effective pressure, it may be necessary to separate collapse sources into those with a dominant volumetric component and those with a significant shear component (see section 6.7 below), so as to distinguish between pore compaction and grain-crushing type processes.

The results of this study suggest that changes in the relative proportions of different source categories can provide us with an indication of the onset of localisation that would be otherwise masked within the bulk behaviour. However, such 'averaging' of source behaviour should always be done with consideration of the actual range of source complexities, as information is essentially lost during this process.

6.5 Potential applications

Understanding the evolution of shear localisation in compressed rock is of importance for three particular reasons; i.) informing failure models that incorporate micromechanical processes, ii.) investigating potential methods of monitoring compressed rock in man-made underground structures, iii.) informing fluid migration models in reservoirs by improved understanding of microstructural development of faulting. In addition, laboratory observations of localisation may provide some insight into large scale localisation of faulting.

6.5.1 General applications

This study provides a detailed characterisation of the micromechanical evolution of damage in a compact versus a porous rock. In particular, the mechanisms that generate AE in sandstone are examined in detail and compared to microstructural observations. The results indicate that acoustic emissions are generated by a continuum of mechanisms that are *typical*, as opposed to atypical, of those mechanisms exhibited by sample microstructure, post-loading. As such, it is argued that AE mechanisms *are* representative of the microcrack population as a whole. In addition, a clear association between the clustering of AE sources and the onset of strain-softening is observed. It is also suggested that fluctuations in the rate of AE activity may be associated with local weakening and strengthening events in the material; this implies that information about sample heterogeneity may be contained within the AE rate curve.

The results of this study indicate that moment tensor inversion of AE may potentially provide a method for determining the degree of compactive to dilative processes occurring during the deformation of a rock sample in the laboratory. Clear differences in the proportion of explosive to implosive sources were determined for a compact versus a low-porosity rock. Moreover, changes in this proportion were observed during the course of deformation of each sample. Decoupling dilatant and compactive behaviour using volumetric strain curves can be non-trivial for a porous material, particular if its hydrostatic behaviour is not known. However, the results of this study

suggest that the development of AE source analysis, by moment tensor inversion, may enable quantification of these competing processes.

6.5.2 Time-dependent failure modelling

Most conventional AE-derived damage parameters are isotropic. In addition, the assumption is made that all AE are produced by '*damage*' in the literal sense; an inelastic deformation that irreversibly *weakens* the material. However, in reality the physical mechanisms that generate acoustic emissions may also act to *strengthen* the rock on a local scale. For example, tensile microcracking may *weaken* the material in which it occurs, yet collapse of grains into a pore space may instead act to *strengthen* the material. Whilst leading to the same end-point, the microscopic route to macroscopic fault formation may vary from one material to another, depending on a range of internal and external factors, most notably the porosity of the compressed rock.

The use of an isotropic damage parameter has proven to be a generally effective tool for predicting stress-strain behaviour as it provides an estimate of the 'average' behaviour of the microcrack population (*Cox and Meredith*, 1993). However, discrepancies between the predicted and observed behaviour may occur when the effective microcrack behaviour wanders from the 'average' behaviour. This may occur when damage becomes spatially localised, involves a preferred orientation, or when the balance between one type of microscopic deformation and another shifts. These processes may

be intrinsically related to the material being loaded, the stress arrangement applied and any pre-existing heterogeneities or material anisotropy.

Shah and Labuz (1995) attempted to account for the problem of preferred orientation in uniaxial loading by defining a tensorial damage parameter and separating AE events into axially-orientated and randomly-orientated sources. A number of studies involving source analysis of AE generated in compact rock indicate that this is a reasonable approximation for such a material (*Reches and Lockner*, 1994; also see section 6.2 above). However, analysis of moment tensors produced in the Clashach sandstone, and consequent results presented in chapters 4 and 5 of this thesis, indicate that such an assumption cannot be made when a significant porosity is present. The breadth of source behaviours generated is such that separation of source behaviours for moment tensor summation is a non-trivial task.

However, further investigation into the effects of porosity upon micromechanical behaviour and source orientations may allow the development of a tensorial damage parameter for porous rock. The results of this investigation indicate that moment tensor inversion of AE waveforms is a powerful tool for informing failure models that incorporate the micromechanical behaviour of damage. This approach would be particularly useful when investigating materials that exhibit a considerable anisotropy, such as foliated metamorphic rocks and sedimentary rocks with a significant degree of bedding; for example shale ‘cap rocks’, involved in trapping of hydrocarbons or stored carbon dioxide.

In addition, *Ojala* (2003) reported that, during stress-corrosion of Clashach sandstone and the more porous Locharbriggs sandstone, the Clashach sandstone exhibited a power-law rheology, whilst the Locharbriggs behaviour was best described by an exponential or logarithmic form. These two rock types have a similar bulk mineralogy, yet displayed notably different stress-corrosion behaviour, indicating that the importance of small quantities of diagenetic material (iron in this case) can have a disproportionate effect. However, the findings presented in chapters 4 and 5 imply that damage evolution within the Clashach sandstone represents an intermediate step between that observed in a compact rock (see chapter 3) and a high-porosity sandstone (*Menéndez et al*., 1996). It therefore seems feasible that the microfracture surface area available in the Clashach and Locharbriggs sandstones differs, due to the relative proportions of different micromechanisms acting within the materials. For example, tensile fracture will increase available grain surface area, whilst collapse sources may decrease the proportion of grain surfaces exposed to pore-fluids. Further AE source characterisation studies might, therefore, aid investigation of these different behaviours.

6.5.3 Monitoring of stressed rock

The moment tensor inversion results for granite, presented in chapter 3, suggest that there is potential for estimating the state of compressed compact rock from the ratio of tensile to shear events, which drops significantly before peak stress is achieved. Whilst

such an effect seems unlikely to scale as far as large magnitude microseismics, the phenomenon might be of potential use in situations where acoustic emissions can be monitored in the near-field of rock where the stress-field has recently been perturbed; for example in the monitoring of Excavation Damaged Zones (EDZ) in underground radioactive storage facilities. Aside from the effects of scale, a limitation in such situations, however, is the physical and practical constraints on array geometry, which may make accurate source characterisation non-trivial.

6.5.4 Development of microstructures

This thesis provides a detailed analysis of spatial and temporal changes in the micromechanisms that generate acoustic emissions, during shear localisation in sandstone. In addition, a physical grounding for these findings is provided by comparison with microstructural observations. The result is an integrated study of the evolution of these processes in a fracturing porous rock, which is based on a *temporally continuous* data set. Findings suggest that significant changes in source characteristics can be detected during the onset of localisation.

Further investigation of the effect of porosity and effective pressure upon these characteristics may lead to the development of a better three-dimensional understanding of the microstructures that are generated for given materials and conditions (see section 6.7). Such information is of particular use for the prediction of permeability changes in

reservoir rock, as a consequence of hydrofracture. In addition the results of this study suggest that there is potential for source characterisation of acoustic emissions, recorded in boreholes during the hydrofracture process, to provide detailed information about the nature of induced fracturing. However, as with monitoring of underground structures, significant technical challenges relating to array distribution and source proximity may need to be overcome.

6.6 Outstanding questions

When firstly considering the Aue granite, the source analysis findings for triaxial compression indicate that there is a clearly observable change in the relative proportion of different AE mechanisms that correlates with the onset of damage localisation and the strain-softening phase. This raises the possibility that applying a metric based on the ratio of shear to tensile sources, to a time-dependent failure model, might improve stress-strain predictions of time-dependent failure in the vicinity of the peak stress. However, this switch in predominantly tensile to predominantly shear behaviour is not significantly pronounced for the Clashach sandstone, where the presence of an appreciable porosity notably affects the mechanisms of the microscopic deformation before failure.

Nevertheless, significant changes in the composition of AE sources were observed before failure in the sandstone. As such, might the proportion of double-couple to

volumetric behaviour of events, or a summation of the traces belonging to the moment tensors of the sources, be applied in a similar fashion? Furthermore, how are such temporal changes in deformation mechanisms affected by confining pressure, and does the sandstone exhibit the same spatio-mechanical development at different confining pressures?

Of particular interest is the nature of the transition from the micromechanical progression of damage observed in compact rock, to that exhibited by a higher porosity material. Low-porosity rock, such as the Clashach sandstone, represents an intermediate step between these two behavioural end-members. Such behaviour is likely to be representative of reservoir rocks that have experienced significant cementation during basin burial, leading to a lower porosity and greater cohesion. One resulting question, arising from the damage characterisation carried out in this study, is what form this transition in AE source mechanisms takes, as porosity is increased? Further investigation of damage characteristics in high-porosity sandstone is required in order to answer this question fully. How do MTI source characteristics of shear localisation in high-porosity sandstone differ from low-porosity sandstone? Does a high-porosity sandstone exhibit a greater number of collapse sources and fewer tensile sources than the Clashach sandstone? Do they exhibit similar temporal changes and spatial behaviour? Furthermore, if differences are detectable can they be used to infer the porosity of the material? In addition, if volumetric strain behaviour was monitored, the changes in the ratio of explosive to implosive events, observed in this study, might be further investigated and their relationship to local and regional strain better understood

The results presented in this thesis have been for relatively brittle conditions leading to a high degree of unstable shear localisation. However, the micromechanical development of deformation during this process has been shown to be considerably different for compact and porous materials. One consequent further question is how significantly does AE source behaviour during shear localisation differ from that which occurs during compaction localisation? If significant differences are detectable then moment tensor inversion may provide an opportunity to improve our understanding of the transition from shear to compaction localisation. Moment tensor inversion of AE data from compaction localisation experiments is discussed further in the following section.

6.7 Suggested further work

The results presented in this thesis indicate that a wealth of information is accessible by moment tensor characterisation of laboratory acoustic emissions, relating to the micromechanics of inelastic deformation prior to brittle failure. Such methodology might be applied to a wide range of problems in the study of brittle deformation of rock. Of particular interest is the effect of porosity upon the microscopic approach to failure. It is therefore suggested that similar methodology be applied to AE data from shear localisation of a number of sandstones, across a range of porosities. The effects of grain size and type/degree of cementation would also have to be considered. Such an

investigation might help to elucidate the mechanisms behind the relative strengths and the degree of 'brittle' behaviour observed in these materials. Furthermore, if volumetric strain behaviour was monitored, the changes in the ratio of explosive to implosive events observed in this study might be further investigated and their relationship to local and regional strain better understood. With an improved understanding of the effect of porosity, and well-calibrated AE magnitude data, it may be possible to develop an AE-derived tensorial measure of damage that improves stress-strain predictions for materials with differing initial porosities.

An additional area recommended for further study is the influence of effective pressure on the micromechanical evolution of damage. In particular, if AE sources generated during hydrostatic loading of sandstones exhibit any unique moment tensor characteristics, it may be possible to separate the majority of them from other forms of damage produced during differential compression experiments, and hence aide the diagnosis of the onset of dilation. Furthermore, detailed moment tensor analysis of acoustic emissions produced at high effective pressures might better elucidate the transition from shear to compaction localisation with increasing effective pressure.

As such, I have already started to investigate the mechanisms involved in compaction localisation, by analysing AE data from a suite of experiments carried out by Sergei Stanchits at the GFZ Deformation and Rheology in Potsdam. Source characterisation by moment tensor inversion has been carried out for data from triaxial loading of the high-porosity Bleurswiller sandstone, at confining pressures of 60, 80 and 100MPa. The

temporal evolution of a number of AE source types for each of these experiments is presented in Appendix (A). The results clearly indicate that collapse sources are the dominant form of deformation, with explosive events, such as tensile sources, taking up only a small percentage of the AE-generating damage. The majority of collapse sources have a significant shear component. However, collapse events with a dominant volumetric component are also a significant contributor to AE generation; notably more so than for shear localisation in the Clashach sandstone. In addition, this latter type of collapse event exhibits a significant decrease in its relative proportions that correlates notably with the onset of localisation. This change is observed for all three confining pressures and is synchronous with an increase in the relative proportion of shear type events.

The initial interpretation of this phenomenon is the decline in compaction-dominated behaviour, relative to grain-crushing behaviour, as porosity is reduced in the region of the forming compaction bands. Initial analysis also indicates that the relative proportions of these two types of collapses is related to the effective pressure, with compaction-dominated sources aided by high confining pressure. If a relationship between these two variables can be established, it may be possible to infer effective pressure from acoustic emission data alone. In addition to further investigation of this data set, analysis of AE data detected during shear localisation in the same high-porosity sandstone, at low confinement, should establish under what conditions this behaviour becomes apparent. Examination of the spatial clustering of these two source types might

also clarify their involvement in the transition from failure by shear localisation to failure by compaction localisation.

Chapter 7

Conclusions

This thesis presents a detailed analysis of acoustic emission data generated during the laboratory deformation of rock. The results given are for failure by shear localisation in a compact material, the Aue granite, and a low-porosity rock, the Clashach sandstone. To summarise, the findings of this study are:

- Source analysis of acoustic emissions can passively provide detailed, continuous information about the internal state of a loaded rock sample in laboratory experiments. Moment tensor inversion of AE waveform data produces similar results to other, more simplistic, source analysis methods, whilst giving a full tensor description for each individual event.
- During the triaxial compression of the Aue granite, decomposition of AE source mechanisms indicates a notable transition from axially-orientated, tensile microcracking to predominantly shear micro-deformation. This change correlates with the transition from spatially distributed to more localised damage. These two types of sources dominate the deformation process, although a significant contribution is also made by sources with approximately comparable volumetric and shear components.

- During the triaxial compression of the low-porosity Clashach sandstone, the majority of AE sources are dominated by shear and implosive volumetric components. The latter dominate in the early stages of AE activity and the majority contain a significant shear component, displaying 'mixed-mode' *implosive* behaviour. However, shear-dominated sources supersede collapses as the primary microscale deformation mechanism during shear localisation.
- The onset of significant acoustic emission hypocentre clustering was observed to coincide with peak stress, for the Clashach sandstone.
- Spatial analysis for different AE source types during a hiatus in the acoustic emission rate, and during the final stages of failure, indicates that not all micromechanisms need coalesce in synchrony. Collapse sources were observed to localise only in the final escalation to failure and remained uncorrelated during an earlier phase of damage localisation. This final episode of clustered collapse sources may be a consequence of gouge formation during the formation of a macroscopic fault.
- The results of this analysis suggest that the cascade to failure involves the ongoing interplay of a number of micromechanisms, which must flow continuously in order for the cascade to failure to take place. If the balance between these processes is disrupted then the process will temporarily stall until the balance can be restored.
- A clear correlation between localised damage and higher acoustic emission rates was observed. The results indicate that the AE rate curve should be considered

as a superposition of many consecutive 'break-through' events that result in instability and failure.

- Acoustic emissions generated in compressed, low-porosity sandstone, exhibit a broad spectrum of source mechanisms, involving a range of double-couple and volumetric components.
- The generation of these acoustic emissions can be explained by physical mechanisms that are similar to those observed by microstructural analysis, leading to the conclusion that AE are generated by '*typical*' inelastic deformation processes. No new microstructural processes were required to explain the data. The previously identified discrepancy between the proportion of detected AE to microscopically observed microcracks, is therefore most likely to be a consequence of not all microcracking generating detectable acoustic emissions, rather than AE representing an '*atypical*' form of damage.
- The micromechanical evolution of inelastic deformation in Clashach sandstone, as interpreted from acoustic emission source mechanisms and microstructural observations, represents an intermediate behaviour between that of a compact rock and a high-porosity sandstone.
- The results of this study demonstrate that moment tensor inversion of acoustic emission is a powerful tool for elucidating the micromechanics of inelastic deformation in the laboratory testing of rock.

Bibliography

Aki, K., and P. G. Richard (2002), *Quantitative Seismology*, Second ed., University Science Books.

Anders, M. H., and D. V. Wiltschko (1994), Microfracturing, paleostress and the growth of faults, *Journal of Structural Geology*, *16*, 795-815.

Anderson, D. L. (1974), The effect of orientated cracks on seismic velocities, *Journal of Geophysical Research*, *79*(26).

Anderson, E. M. (1942), *The dynamics of faulting and dyke formation with applications to Britain*, Oliver and Boyd, Edinburgh/London.

Antonellini, M., A. Aydin, and D. D. Pollard (1994), Microstructure of deformation bands in porous sandstones at Arches N, *Journal of Structural Geology*, *16*, 941-959.

Aydin, A. (1978), Small faults formed as deformation bands in sandstone, *Pure and Applied Geophysics*, *116*, 913-930.

Aydin, A., and A. M. Johnson (1978), Development of faults as zones of deformation bands and as slip surfaces in sandstones, *Pure and Applied Geophysics*, *116*, 931-942.

Ayling, M. R., P. G. Meredith, and S. A. F. Murrell (1995), Microcracking during triaxial deformation of porous rocks monitored by changes in rock physical properties, I. Elastic wave propagation measurements on dry rocks, *Tectonophysics*, *245*, 205-221.

Baud, P., T. Reuschlé, and P. Charlez (1996), An improved wing crack model for the deformation and failure of rock in compression, *International Journal of Rock Mechanics, Mining Science and Geomechanics Abstracts*, *33*(5), 539-542.

Baud, P., A. Schubnel, and T.-f. Wong (2000), Dilatancy, compaction, and failure mode in Solnhofen limestone, *Journal of Geophysical Research*, *105*(B8), 19,289-19,303.

Bažant, Z. k. P. (1986), Mechanics of distributed cracking, *Applied Mechanics Reviews*, *39*(5), 675-705.

Benson, P. M., and B. D. Thompson (2007), Imaging slow failure in triaxially deformed Etna basalt using 3D acoustic-emission location and X-ray computed tomography, *Geophysical Research Letters*, *34*(L03303).

Benson, P. M., P. G. Meredith, E. S. Platzman, and R. E. White (2005), Pore fabric shape anisotropy in porous sandstones and its relation to elastic wave velocity and

permeability anisotropy under hydrostatic pressure, *International Journal of Rock Mechanics and Mining Sciences*, *42*, 890-899.

Benson, P. M., V. S., P. G. Meredith, and R. P. Young (2008), Laboratory simulation of volcano seismicity, *Science*, *322*, 249-252.

Blenkinsop, T. (2000), *Deformation microstructures and mechanisms in minerals and rocks*, Kluwer Academic Publishers.

Boness, N. L., and M. D. Zoback (2004), Stress-induced seismic velocity anisotropy and physical properties in the SAFOD pilot hole in Parkfield, CA, *Geophysical Research Letters*, *31*(L15S17).

Brace, W. F., B. W. Paulding, and C. Scholz (1966), Dilatancy in the fracture of crystalline rocks, *Journal of Geophysical Research*, *71*(16), 3939-3953.

Bruner, W. M. (1976), Comment on 'Seismic velocities in dry and saturated cracked solids' by Richard J. O'Connell and Bernard Budiansky, *Journal of Geophysical Research*, *81*(14), 2573.

Burlini, L., S. Vinciguerra, G. Di Toro, G. De Natele, P. Meredith, and J.-P. Burg (2007), Seismicity preceding volcanic eruption: new experimental insights, *Geology*, *35*(2), 183-186.

Bésuelle, P. (2001), Evolution of strain localisation with stress in a sandstone: brittle and semi-brittle regimes, *Physics and Chemistry of the Earth A*, *26*(1-2), 101-106.

Bésuelle, P., P. Baud, and T.-F. Wong (2003), Failure mode and spatial distribution of damage in Rothbach sandstone in the brittle-ductile transition, *Pure and Applied Geophysics*, *160*, 851-868.

Caristan, Y. (1982), The transition from high temperature creep to fracture in Maryland diabase, *Journal of Geophysical Research*, *87*(B8), 6781-9790.

Carvalho, F. C. S., and J. F. Labuz (2002), Moment tensors of acoustic emissions in shear faulting under plane-strain compression, *Tectonophysics*, *356*, 199-211.

Chang, S.-H., and C.-I. Lee (2004), Estimation of cracking and damage mechanisms in rock under triaxial compression by moment tensor analysis of acoustic emission, *International Journal of Rock Mechanics & Mining Sciences*, *41*, 1069-1086.

Colombo, I. S., I. G. Main, and M. C. Forde (2003), Assessing damage of reinforced concrete beam using "b-value" analysis of acoustic emission signals, *Journal of Materials in Civil Engineering*, *15*(3), 280-286.

Cook, N. G. W., and K. Hodgson (1965), Some detailed stress-strain curves for rock, *Journal of Geophysical Research*, *70*(12), 2883-2888.

Cox, S. J. D., and P. G. Meredith (1993), Microcrack formation and material softening in rock measured by acoustic emissions, *International Journal of Rock Mechanics & Mining Sciences & Geomechanical Abstracts*, *30*(1), 11-24.

Crawford, B. R., B. G. D. Smart, I. G. Main, and F. Liakopoulou-Morris (1995), Strength characteristics and shear acoustic anisotropy of rock core subjected to true triaxial compression, *International Journal of Rock Mechanics & Mining Sciences & Geomechanical Abstracts*, *32*(3), 189-200.

Dahlen, F. A., and J. Tromp (1998), *Theoretical global seismology*, Princeton University Press, Princeton, New Jersey.

Dahm, T., G. Manthei, and J. Eisenblatter (1999), Automated moment tensor inversion to estimate source mechanisms of hydraulically induced micro-seismicity in salt rock, *Tectonophysics*, *306*, 1-17.

Dziewonski, A. M., and F. Gilbert (1974), Temporal variation of the seismic moment tensor and the evidence of precursive compression for two deep earthquakes, *Nature*, *247*, 185-188.

Dziewonski, A. M., T.-A. Chou, and J. H. Woodhouse (1981), Determination of earthquake source parameters from waveform data for studies of global and regional seismicity, *Journal of Geophysical Research*, *86*(B4), 2825-2852.

El Bied, A., J. Sulem, and F. Martineau (2002), Microstructure of shear zones in Fontainebleau sandstone, *International Journal of Rock Mechanics & Mining Sciences*, *39*, 917-932.

Evans, B., J. T. Fredrich, and T.-f. Wong (1990), The brittle-ductile transition in rocks: recent experimental and theoretical progress, in *The brittle-ductile transition in rocks: the Heard volume*, edited by A. G. Duba, W. B. Durham, J. W. Handin and H. F. Wang, pp. 1-20, American Geophysical Union, Washington, D.C.

Feignier, B., and P. Young (1992), Moment tensor inversion of induced microseismic events: evidence of non-shear failures in the $-4 < M < -2$ moment magnitude range, *Geophysical Research Letters*, *19*(14), 1503-1506.

Fischer, G. J., and M. Paterson, S. (1989), Dilatancy during rock deformation at high temperatures and pressures, *Journal of Geophysical Research*, *94*(B12), 17,607-617.

Fortin, J., S. Stanchits, G. Dresen, and Y. Gueguen (2009), Acoustic emissions monitoring during inelastic deformation of porous sandstone: comparison of three modes of deformation, *Pure and Applied Geophysics*, *166*, 823-841.

Frohlich, C. (1995), Characteristics of well-determined non-double-couple earthquakes in the Harvard CMT catalog, *Physics of the Earth and Planetary Interiors*, *91*, 213-228.

Gilbert, F. (1971), Excitation of the normal modes of the Earth by earthquake sources, *Journal of the Royal Astronomical Society*, *22*, 223-226.

Gilbert, F. (1973), Derivation of source parameters from low-frequency spectra, *Philisophical Transactions of the Royal Society of London A.*, *274*(1239), 369-371.

Gottschalk, R. R., A. K. Kronenberg, J. E. Russell, and J. Handin (1990), Mechanical anisotroy of gneiss: failure criterion and textural sources of directional behaviour, *Journal of Geophysical Research*, *95*(B13), 21,613-634.

Graham, C. C., S. Stanchits, I. G. Main, and G. Dresen (2010), Comparison of polarity and moment tensor inversion methods for source analysis of acoustic emission data, *International Journal of Rock Mechanics and Mining Sciences*, *47*, 161-169.

Griggs, D., and J. Handin (1960), Observations on fracture and a hypothesis of earthquakes, in *Rock deformation: a symposium*, edited by D. Griggs and J. Handin, pp. 347-364, Geological Society of America.

Gutenberg, B., and C. F. Richter (1949), *Seismicity of the Earth*, Princeton University Press, Princeton, New Jersey.

Guéguen, Y., T. Reuschle, and M. Darot (1990), Single-crack behaviour and crack statistics, in *Deformation processes in minerals, ceramics and rocks*, edited by D. J. Barber and P. G. Meredith, pp. 48-71, Unwin Hyman, London.

Hadley, K. (1975), Vp/Vs anomalies in dilatant rock samples, *Pure and Applied Geophysics*, *113*.

Hadley, K. (1976), Comparison of calculated and observed crack densities and seismic velocities in westerly granite, *Journal of Geophysical Research*, *81*(20), 3484-3494.

Haimson, B., C. Chang (2000), A new true triaxial cell for testing mechanical properties of rock, and its use to determine rock strength and deformability of Westerly granite, *International Journal of Rock Mechanics and Mining Sciences*, *37*, 285-296.

Haimson, B., C. Chang (20002), True triaxial strength of the KTB amphibolite under borehole wall conditions and its use to estimate the maximum horizontal in situ stress, *Journal of Geophysical Research*, *107 (B10)*, 2257.

Hirata, T. (1987), Omori's Power law aftershock sequences of microfracturing in rock fracture experiment, *Journal of Geophysical Research*, *92*(B7), 6215-6221.

Hirata, T., T. Satoh, and I. Keisuke (1987), Fractal structure of spatial distribution of microfracturing in rock, *Geophysical Journal of the Royal astronomical Society*, *90*, 369-374.

Hirth, G., and J. Tullis (1994), The brittle-ductile transition in experimentally deformed quartz aggregates, *Journal of Geophysical Research*, *99*(B6), 11,731-747.

Hobbs, B. E., W. D. Means, and P. F. Williams (1976), *An outline of structural geology*, John Wiley and Sons, Inc.

Jackson, J., and D. McKenzie (1988), The relationship between plate motion and seismic moment tensors, and the rates of active deformation in the Mediterranean and Middle East, *Geophysical Journal*, *93*, 45-73.

Jaeger, J., N. G. W. Cook, and R. Zimmerman (2007), *Fundamentals of rock mechanics*, Fourth edition ed., Blackwell Publishing.

Ju, J. W. (1990), Isotropic and anisotropic damage variable in continuum damage mechanics, *Journal of Engineering Mechanics*, *116*(12), 2764.

Julian, B. R. (1983), Evidence for dyke intrusion earthquake mechanisms near Long Valley caldera, California, *Nature*, *303*, 323-325.

Kachanov, L. M. (1986), *Introduction to continuum damage mechanics*, Martinus Nijhoff Publishers, Kluwer Academic Publishers Group, Dordrecht/Boston/Lancaster.

Katz, O., and Z. e. Reches (2004), Microfracturing, damage, and failure of brittle granites, *Journal of Geophysical Research*, *109*(B01206).

Klein, E., P. Baud, T. Reuschle, and T.-F. Wong (2001), Mechanical Behaviour and failure mode of Bentheim sandstone under triaxial compression, *Physics and Chemistry of the Earth (A)*, *26*(1-2), 21-25.

Knopoff, L., and M. J. Randall (1970), The compensated linear-vector dipole: a possible mechanism for deep earthquakes, *Journal of Geophysical Research*, *75*(26), 4957-4963.

Kostrov, V. V. (1974), Seismic moment and energy of earthquakes, and seismic flow of rock, *Izv. Acad, Sci. USSR Phys. Solid Earth*, *1*, 23-44.

Kranz, R. L. (1983), Microcracks in rocks: a review, *Tectonophysics*, *100*, 449-480.

Kranz, R. L., and C. H. Scholz (1977), Critical dilatant volume of rocks at the onset of tertiary creep, *Journal of Geophysical Research*, *82*(30), 4893-4898.

Kranz, R. L., T. Satoh, O. Nishizawa, K. Kusunose, M. Takahashi, K. Masuda, and A. Hirata (1990), Laboratory study of fluid pressure diffusion in rock using acoustic emissions, *Journal of Geophysical Research*, *95*(B13), 21,593-607.

Lawn, B., and R. Wilshaw (1975), Indentation fracture: principles and applications, *Journal of Materials Science*, *10*, 1049-1081.

Lei, X. (2003), How do asperities fracture? An experimental study of unbroken asperities., *Earth and Planetary Science Letters*, *213*, 347-359.

Lei, X., K. Kusunose, M. V. M. S. Rao, O. Nishizawa, and T. Satoh (2000), Quasi-static fault growth and cracking in homogeneous brittle rock under triaxial compression using acoustic emission monitoring, *Journal of Geophysical Research*, *105*(B3), 6127-6139.

Lei, X., K. Masuda, O. Nishizawa, L. Jouniaux, L. Liu, W. Ma, T. Satoh, and Kusunose (2004), Detailed analysis of acoustic emission activity during catastrophic fracture of faults in rock, *Journal of Structural Geology*, *26*, 247-258.

Leonard, D. A., and B. L. N. Kennett (1999), Multi-component autoregressive techniques for the analysis of seismograms, *Physics of the Earth and Planetary Interiors*, *113*(1-4), 247-263.

Li, H. B., J. Zhao, and T. J. Li (1999), Triaxial compression tests on a granite at different strain rates and confining pressures, *International Journal of Rock Mechanics and Mining Sciences*, *36*, 1057-1063.

Lockner, D. (1993), The role of acoustic emission in the study of rock fracture, *International Journal of Rock Mechanics and Mining Sciences & Geomechanics Abstracts*, *30*(7), 883-899.

Lockner, D. A., J. D. Byerlee, V. Kuksenko, A. Ponomarev, and A. Sidorin (1991), Quasi-static fault growth and shear fracture energy in granite, *Nature*, *350*(39-42).

Lockner, D. A., J. D. Byerlee, V. Kuksenko, A. Ponomarev, and A. Sidorin (1992), Observations of quasistatic fault growth from acoustic emissions, in *Fault mechanics*

and transport properties of rock, edited by B. Evans, T.-F. Wong and W. F. Brace, pp. 3-31, Academic Press, University of California.

Main, I., G. (1992), Damage mechanics with long-range interactions: correlation between the seismic b-value and the fractal two-point correlation dimension, *Geophysical Journal International*, *111*, 531-541.

Main, I. G., P. G. Meredith, and C. Jones (1989), A reinterpretation of the precursory seismic b-value anomaly from fracture mechanics, *Geophysical Journal*, *96*, 131-138.

Main, I. G., O. Kwon, B. T. Ngwenya, and S. C. Elphick (2000), Fault sealing during deformation-band growth in porous sandstone, *Geology*, *28*(12), 1131-1134.

Mair, K., I. Main, and S. Elphick (2000), Sequential growth of deformation bands in the laboratory, *Journal of Structural Geology*, *22*, 25-42.

Mair, K., S. Elphick, and I. Main (2002), Influence of confining pressure on the mechanical and structural evolution of laboratory deformation bands, *Geophysical Research Letters*, *29*(10).

Manthei, G. (2005), Characterization of acoustic emission sources in a rock salt specimen under triaxial compression, *Bulletin of the Seismological Society of America*, *95*(5), 1674-1700.

Manthei, G., J. Eisenblatter, and T. Dahm (2001), Moment tensor evaluation of acoustic emission sources in salt rock, *Construction and Building Materials*, *15*, 297-309.

Masuda, K. (2001), Effects of water on rock strength in a brittle regime, *Journal of Structural Geology*, *23*, 1653-1657.

McEwan, T. J. (1981), Brittle deformation in pitted pebble conglomerates, *Journal of Structural Geology*, *3*, 25-37.

McGarr, A. (1992), Moment tensors of ten witwatersrand mine tremors, *Pure and Applied Geophysics*, *139*(3/4), 781-800.

Menéndez, B., W. Zhu, and T.-F. Wong (1996), Micromechanics of brittle faulting and cataclastic flow in Berea sandstone, *Journal of Structural Geology*, *18*(1), 1-16.

Meredith, P. G., I. G. Main, and C. Jones (1990), Temporal variations in seismicity during quasi-static and dynamic rock failure, *Tectonophysics*, *175*, 249-268.

Mogi, K. (1959), Experimental study of deformation and fracture of marble. (1st Paper) On the fluctuation of compression strength of marble and the relation to the rate of stress application, *Bulletin of the Earthquake Research Institute*, *37*, 155-170.

Mogi, K. (1962), Study of elastic shocks caused by the fracture of heterogeneous materials and its relations to earthquake phenomenon, *Bulletin of the Earthquake Research Institute*, *40*, 125-173.

Mogi, K. (1967), Earthquakes and fractures, *Tectonophysics*, *5*(1), 35-55.

Moore, D. E., and D. A. Lockner (1995), The role of microcracking in shear-fracture propagation in granite, *Journal of Structural Geology*, *17*(1), 95-114.

Nelder, J. A., and R. Mead (1965), A simplex method for function minimization, *The Computer Journal*, *7*(4), 308-313.

Nettles, M., and G. Ekström (1998), Faulting mechanism of anomalous earthquakes near Bardarbunga Volcano, Iceland, *Journal of Geophysical Research*, *103*(B8), 17,973-983.

Ohnaka, M., and K. Mogi (1982), Frequency characteristics of acoustic emission in rocks under uniaxial compression and its relation to the fracturing process to failure, *Journal of Geophysical Research*, *87*(B5), 3873-3884.

Ohtsu, M. (1991), Simplified moment tensor analysis and unified decomposition of acoustic emission source: application to in situ hydrofracture test, *Journal of Geophysical Research*, *96*(B4), 6211-6221.

Ohtsu, M. (1995), Acoustic emission theory for moment tensor analysis, *Research in Nondestructive Evaluation*, *6*(3), 169-184.

Ojala, I. O. (2003), Stress corrosion crack growth in porous sandstones, University of Edinburgh.

Ojala, I. O., B. T. Ngwenya, I. G. Main, and S. C. Elphick (2003), Correlation of microseismic and chemical properties of brittle deformation in Locharbriggs sandstone, *Journal of Geophysical Research*, *108*(B5), 2268.

Paterson, M. S., and T.-f. Wong (2005), *Experimental rock deformation - the brittle field*, Second edition ed., Springer-Verlag, Berlin Heidelberg.

Peng, S. S., and A. M. Johnson (1972), Crack growth and faulting in cylindrical specimens of Chelmsford granite, *International Journal of Rock Mechanics and Mining Science*, *9*, 37-86.

Pittman, E., D. (1981), Effect of fault-related granulation on porosity and permeability of quartz sandstone, Simpson Group (Ordovician), Oklahoma, *AAPG Bulletin*, *65*(11), 2381-2387.

Ranalli, G. (1995), *Rheology of the earth*, Second edition ed., Chapman and Hall, London.

Rao, M. V. M. S., and K. Kusunose (1995), Failure zone development in andesite as observed from acoustic emission locations and velocity changes, *Physics of the Earth and Planetary Interiors*, *88*, 131-143.

Reches, Z., and D. A. Lockner (1994), Nucleation and growth of faults in brittle rocks, *Journal of Geophysical Research*, *99*(B9), 18,159-173.

Sangha, C. M., C. J. Talbot, and R. K. Dhir (1974), Microfracturing of sandstone in uniaxial compression, *International Journal of Rock Mechanics and Mining*, *11*, 107-113.

Schock, R. N., H. C. Heard, and D. R. Stephens (1973), Stress-strain behavior of a granodiorite and two graywackes on compression at 20 Kilobars, *Journal of Geophysical Research*, *78*(26), 5922-5941.

Scholz, C. H. (1968a), Microfracturing and the inelastic deformation of rock in compression, *Journal of Geophysical Research*, *73*(4), 1417-1432.

Scholz, C. H. (1968b), Experimental study of the fracturing process in brittle rock, *Journal of Geophysical Research*, *73*(4), 1447-1454.

Scholz, C. H. (1968c), The frequency-magnitude relation of microfracturing in rock and its relation to earthquakes, *Bulletin of the Seismological Society of America*, *58*(1), 399-415.

Scholz, C. H. (2003), *The mechanics of earthquakes and faulting*, Second edition ed., Cambridge University Press, Cambridge.

Shah, K. R., and J. F. Labuz (1995), Damage mechanisms in stressed rock from acoustic emission, *Journal of Geophysical Research*, *100*(B8), 15,527-515,539.

Shigeishi, M., and M. Ohtsu (2001), Acoustic emission moment tensor analysis: development for crack identification in concrete materials, *Construction and Building Materials*, *15*, 311-319.

Simmons, G., and D. Richter (1976), Microcracks in rock, in *The physics and chemistry of minerals and rocks*, edited by R. G. J. Strens, Wiley, New York.

Stanchits, S., S. Vinciguerra, and G. Dresen (2006), Ultrasonic velocities, acoustic emission characteristics and crack damage of basalt and granite, *Pure and Applied Geophysics*, *163*, 974-993.

Stanchits, S. A., D. A. Lockner, and A. V. Ponomarev (2003), Anisotropic changes in P-wave velocity and attenuation during deformation and fluid infiltration of granite, *Bulletin of the Seismological Society of America*, *93*(4), 1803-1822.

Stein, S., and M. Wysession (2003), *An introduction to seismology, earthquakes and Earth structure*, Blackwell Publishing Ltd.

Tapponnier, P., and W. F. Brace (1976), Development of stress-induced microcracks in Westerly granite, *International Journal of Rock Mechanics and Mining Science*, *13*, 103-112.

Tullis, J., and R. A. Yund (1977), Experimental deformation of dry westerly granite, *Journal of Geophysical Research*, *82*(36), 5705-5718.

Vernik, L., and M. D. Zoback (1992), Estimation of maximum horizontal principal stress magnitude from stress-induced well bore breakouts in the Cajon pass scientific research borehole, *Journal of Geophysical Research*, *97*(B4), 5109-5119.

Vinciguerra, S., P. G. Meredith, and J. Hazzard (2004), Experimental and modeling study of fluid pressure-driven fractures in Darley Dale sandstone, *Geophysical Research Letters*, *31*(L09609).

Walsh, J. B. (1965), The effect of cracks on the compressibility of rock, *Journal of Geophysical Research*, *70*(2), 381-389.

Wong, T.-f., H. Szeto, and J. Zhang (1992), Effect of loading path and porosity on the failure mode of porous rocks, *Applied Mechanics Reviews*, *45*(8), 281-293.

Wong, T.-f., C. David, and W. Zhu (1997), The transition from brittle faulting to cataclastic flow in porous sandstones: mechanical deformation, *Journal of Geophysical Research*, *102*(B2), 3009-3025.

Wu, X. Y., P. Baud, and T.-F. Wong (2000), Micromechanics of compressive failure and spatial evolution of anisotropic damage in Darley Dale sandstone, *International Journal of Rock Mechanics and Mining Sciences*, *37*, 143-160.

Yuyama, S. (2005), Acoustic emission for fracture studies using moment tensor analysis, *Journal of strain analysis*, *40*(1).

Zang, A. (1999), Akustische Emissionen beim Sproudbruch von Gestein, *Habilitationsschrift, University of Potsdam, Scientific Technical Report*(STR97/19).

Zang, A., C. F. Wagner, and G. Dresen (1996), Acoustic emission, microstructure, and damage model of dry and wet sandstone stressed to failure, *Journal of Geophysical Research*, *101*(B8), 17,507-521.

Zang, A., F. C. Wagner, S. Stanchits, C. Janssen, and G. Dresen (2000), Fracture process zone in granite, *Journal of Geophysical Research*, *105*(B10), 23,651-661.

Zang, A., C. Wagner, S. Stanchits, G. Dresen, R. Andresen, and M. A. Haidekker (1998), Source analysis of acoustic emissions in Aue granite cores under symmetric and asymmetric compressive loads, *Geophysical Journal International*, *135*, 1113-1130.

Appendix A

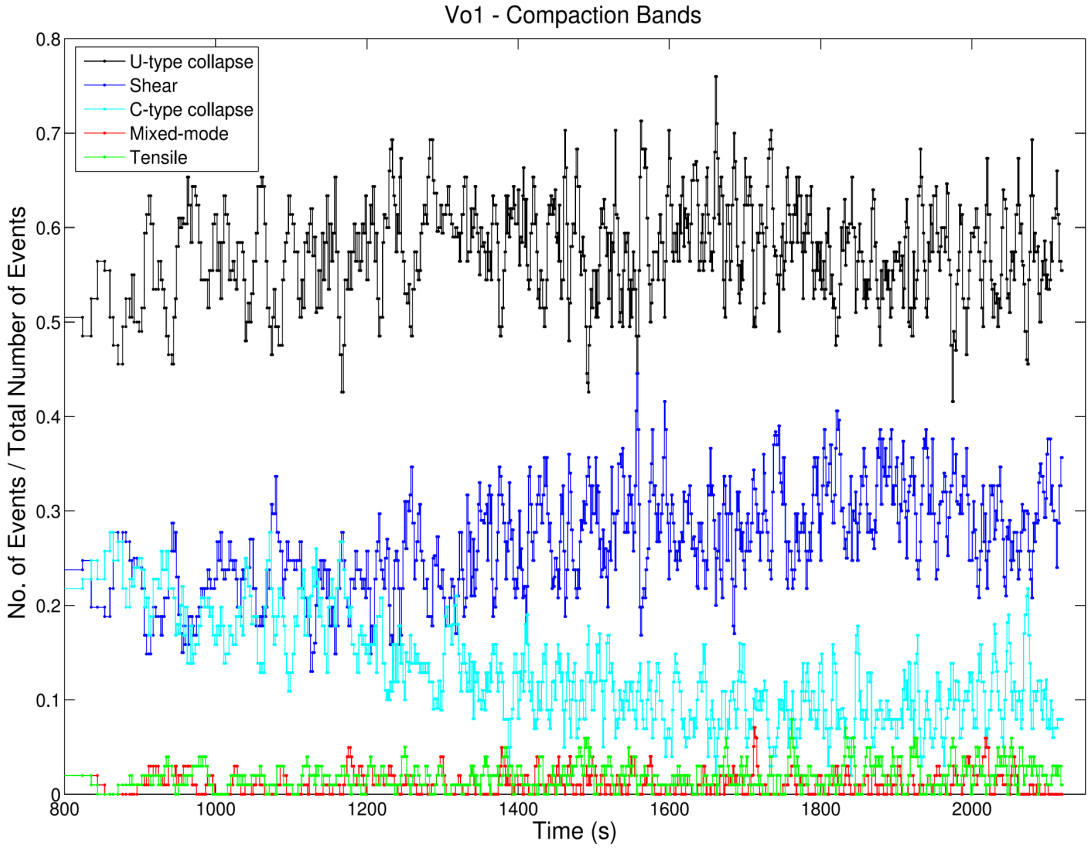

Figure illustrating the evolution of acoustic emission source types during compaction band formation in Bleurswiller sandstone at a confining pressure of 100MPa. U-type collapse contain a significant shear component, whilst C-type collapses are dominated by volumetric change. A clear reduction in the relative proportion of C-type sources is observed during the progression of compaction localisation.

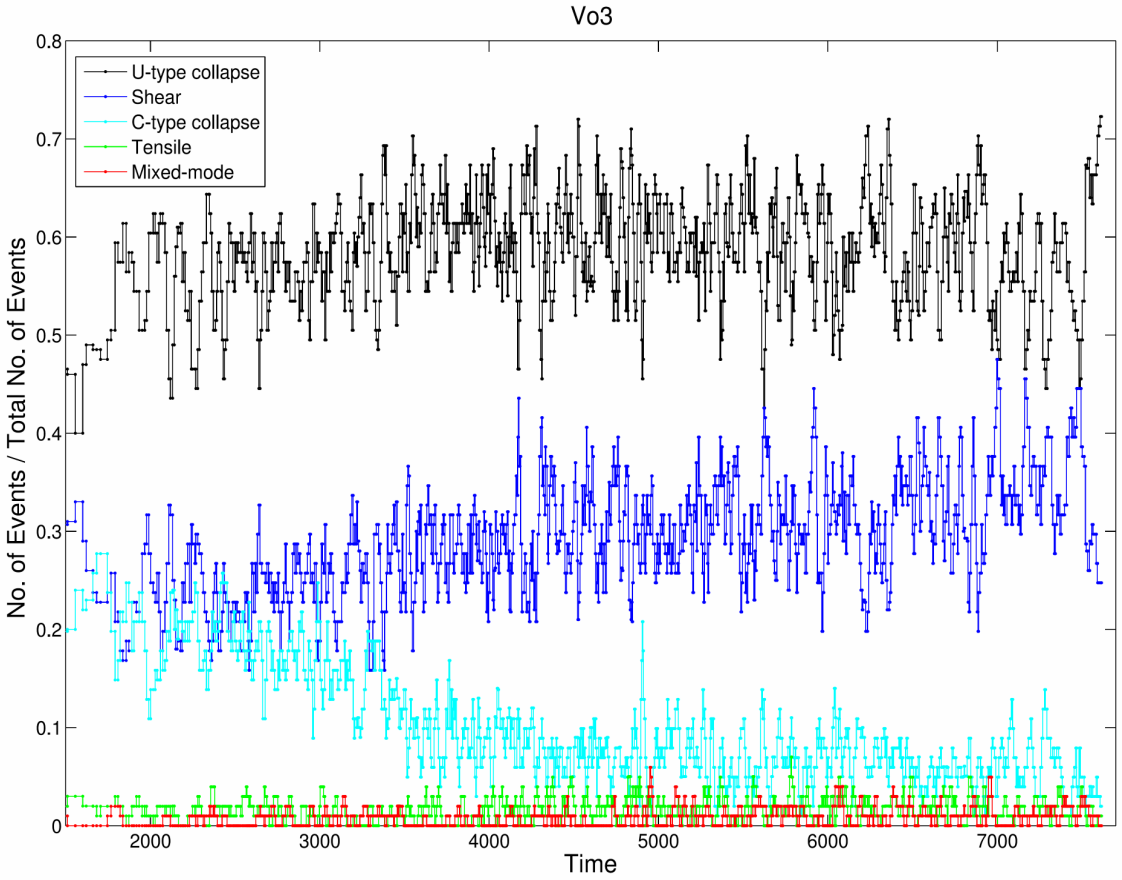

Figure illustrating the evolution of acoustic emission source types during compaction band formation in Bleurswiller sandstone at a confining pressure of 80MPa. U-type collapse contain a significant shear component, whilst C-type collapses are dominated by volumetric change. A clear reduction in the relative proportion of C-type sources is observed during the progression of compaction localisation.

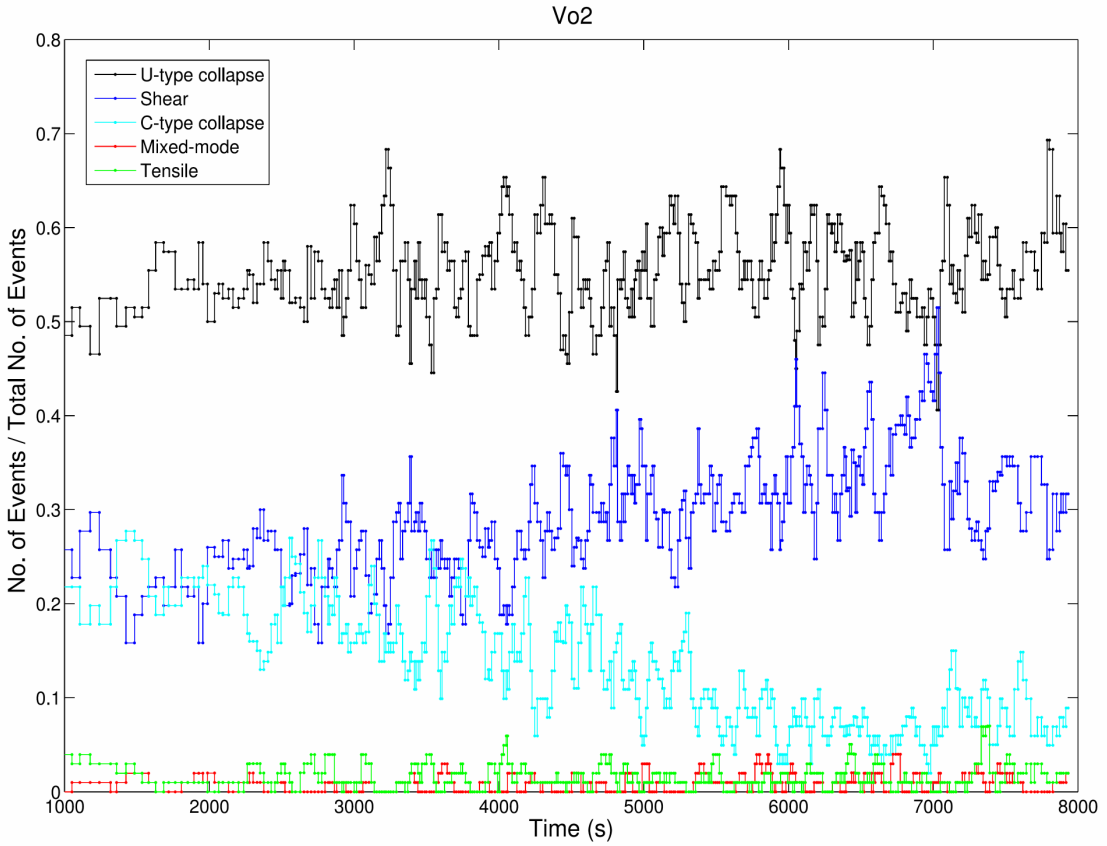

Figure illustrating the evolution of acoustic emission source types during compaction band formation in Bleurswiller sandstone at a confining pressure of 60MPa. U-type collapse contain a significant shear component, whilst C-type collapses are dominated by volumetric change. A clear reduction in the relative proportion of C-type sources is observed during the progression of compaction localisation.

Appendix B

Figure illustrating the orientation of tensile AE sources, during the final stages of damage localisation in the Aue granite. The image is a 3D projection with x, y, z axes labelled in millimetres. Each line represents a crack vector, with the colour denoting its orientation in relation to the maximum compressive stress; dark blue is approximately parallel to σ_1, whilst yellow is perpendicular to σ_1 During the final stages of fault nucleation, a wave of increasingly darker blue damage can be seen to propagate across the sample, indicating an increase in the number of tensile AE sources in close association with the maximum compressive stress.

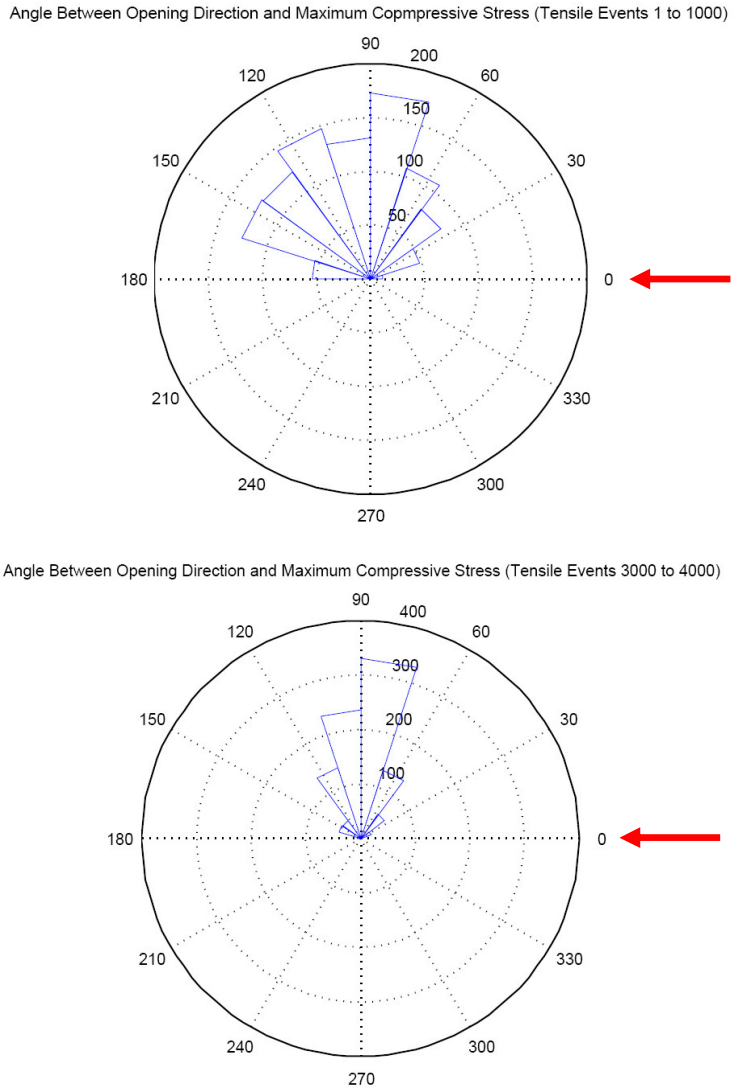

Rose diagrams illustrating the angle between the maximum compressive stress and the opening direction of tensile AE sources in the Aue granite; during the early stages of acoustic emission activity (top) and during the onset of damage localisation (bottom). The orientation of σ_1 is indicated by the red arrows. These results demonstrate that a preferred tensile opening direction, perpendicular to the maximum compressive stress, becomes increasing developed as localisation takes place.

Appendix C

Provided for non-commercial research and education use.
Not for reproduction, distribution or commercial use.

This article appeared in a journal published by Elsevier. The attached copy is furnished to the author for internal non-commercial research and education use, including for instruction at the authors institution and sharing with colleagues.

Other uses, including reproduction and distribution, or selling or licensing copies, or posting to personal, institutional or third party websites are prohibited.

In most cases authors are permitted to post their version of the article (e.g. in Word or Tex form) to their personal website or institutional repository. Authors requiring further information regarding Elsevier's archiving and manuscript policies are encouraged to visit:

http://www.elsevier.com/copyright

Author's personal copy

International Journal of Rock Mechanics & Mining Sciences 47 (2010) 161–169

Contents lists available at ScienceDirect

International Journal of Rock Mechanics & Mining Sciences

journal homepage: www.elsevier.com/locate/ijrmms

Technical Note

Comparison of polarity and moment tensor inversion methods for source analysis of acoustic emission data

Caroline C. Graham [a,*], Sergei Stanchits [b], Ian G. Main [a], Georg Dresen [b]

[a] School of Geosciences, University of Edinburgh, Grant Institute, The King's Buildings, West Mains Road, Edinburgh EH9 3JW, UK
[b] GFZ German Research Centre for Geosciences, Section 3.2, Telegrafenberg D423, 14473 Potsdam, Germany

ARTICLE INFO

Article history:
Received 15 December 2008
Received in revised form
22 April 2009
Accepted 9 May 2009
Available online 17 June 2009

1. Introduction

During rock deformation tests, energy may be released as high-frequency acoustic emissions (AE) from microfractures within the sample. These emissions provide a passive indicator of the progression of inelastic damage, during the approach to sample failure. Characterisation of the sources that produce AE can provide us with an insight into the microscopic processes that are involved in the initiation and coalescence of damage within a loaded rock sample. Such work has relevance within the field of seismology and earthquake physics; earthquakes and acoustic emissions display similar, power law, frequency–magnitude distributions [1,2] and Omori law aftershock behaviour [3]. Laboratory AE waveforms also exhibit some remarkable similarities with large scale seismological events, and monitoring and characterisation of them during experiments can improve our understanding of a wide range of processes, including fault asperity rupture [4] and volcano–seismic events [5,6]. In addition, as the search for new prospects leads to exploration in increasingly deeper underground mines, so our need to understand fracture system evolution, and the processes that lead to mining-induced earthquakes, likewise increases. However, in such field-based situations, placement of sensor arrays is governed by physical constraints and may be non-ideal. Acoustic emission studies in the laboratory can give us an insight into the fracture network evolution processes that take place in such situations and provide us with an opportunity to develop laws suitable for testing at larger scales.

This note describes two techniques used to characterise microscale fracturing, using acoustic emission data, generated within triaxially compressed granite. These microscopic processes show significant spatial and temporal development up to, and during, the period of macroscopic sample failure. Comparing the results produced by both methods shows that they are consistent with one another and demonstrates the value of the moment tensor inversion approach.

2. Current source analysis methods

Detailed information relating to fracture network evolution, and the onset of sample failure, can be obtained under controlled conditions during rock fracture experiments. The behaviour of this material does not depend solely upon mean field properties, such as crack density, but also the microscopic processes and feedbacks involved in cracking, how the cracks are organised and how they interact under different external conditions. In order to understand these effects, we need to have reliable information about the location, geometry and orientations of these cracks, the type of motion associated with them and the evolution of these properties with loading. Whilst samples compressed under brittle conditions will fail in a shear fashion along a macroscopic fault, microscopic analysis indicates that damage by tensile fracture also occurs on the microscale. One such study [7] focused on dry samples of triaxially compressed Mount Scott granite. Microstructural analysis indicated predominantly tensile microcracks in the early stages of loading, whilst shear fracturing became more intense and spatially concentrated with increasing load.

However, microstructural observations have the disadvantage of only being recoverable after sample unloading and do not provide us with real-time information about microcrack evolution. Alternatively, variations in horizontal and vertical ultrasonic velocities, across different regions of the sample, can be measured during the course of an experiment. As a result, the observed

* Corresponding author. Tel.: +44 131 6505916; fax: +44 131 6683184.
E-mail address: c.c.graham@sms.ed.ac.uk (C.C. Graham).

1365-1609/$ - see front matter © 2009 Elsevier Ltd. All rights reserved.
doi:10.1016/j.ijrmms.2009.05.002

Author's personal copy

increase in seismic anisotropy can be used to monitor changes in bulk physical properties of the sample. P- and S-wave velocities may be significantly decreased by the presence of microcracks [8], providing us with an opportunity to infer crack density values [9].

A complementary approach is the study of high-frequency pressure disturbances, termed acoustic emissions, which may be recorded during deformation experiments, exhibit a rate of occurrence that is correlated with the inelastic strain rate [10]. These emissions have been attributed to the dynamic release of energy during microcracking events [2,11] and provide us with passively collected information about damage processes occurring within laboratory samples. Such processes can be highly complicated in nature, for instance being related to the collapse of pore spaces and crushing of grains at high confining pressures.

In [12], a model of fault nucleation and growth in brittle rocks was proposed, based on observations of AE hypocentre distributions and stress-field modelling. They suggest that the nucleation and propagation of faults in granite is a consequence of the interaction of tensile microcracks, prior to the peak stress, within a 'process zone'. The dilating microcracks lead to changes in the local stress-field which, in turn, cause the interaction of cracks to spread unstably, resulting in the propagation of the process zone. As this zone grows, the material yields in a shear fashion within its central part and this creates a 'fault nucleus', which then proceeds to grow behind the process zone as it propagates through the rock. However, as mechanisms and orientations of microcracks were obtained from microstructural analysis, real time data were not available.

Improving our knowledge of these mechanisms is essential in any attempts to understand progression towards brittle failure. Source analysis of AE can elucidate the temporal and spatial evolution of these processes. A number of approaches to the characterisation of laboratory AE sources have been taken. One such technique [13] utilises the distribution of P-wave first motions to classify sources coarsely into four categories. A distinction is made between tensile sources and all other AE types, by finding the ratio between up (dilatational) and down (compressional) first motions. A similar method to this [14] assigns an average 'polarity' to each event.

Alternatively a more quantitative approach to AE source analysis is that of moment tensor inversion (MTI), which provides a tensor that describes the forces acting at the source. Such inversion has been widely utilised in the field of seismology, particularly for analysing events with a large non-double-couple (NDC) component [15,16], such as those observed in volcanically active regions [17,18]. It has the advantage of providing information about, not only the type of motion acting at the source, but also the associated change in volume. One study [19] applied moment tensor inversion to microseismic events recorded in the Underground Research Laboratory (URL) in Pinawa, Manitoba, where a tunnelling operation was underway. They found evidence for failure mechanisms with a non-shear component to them and reported a correlation between the location of a breakout in the tunnel roof and a region of failure mechanisms with a high tensile component. Similarly, McGarr [20] inverted for moment tensors from ground motions in two of the South African gold mining districts. He found two very distinct sets of mechanisms; the first, predominantly double-couple (DC) in nature, the second, displaying a substantial, coseismic reduction in volume. In addition, moment tensor decomposition has been carried out [21] using AE waveforms recorded during an in situ hydrofracture test. It was shown that sources could be separated into those that were primarily shear in nature, and those with a significant tensile component.

Inversion of laboratory AE data for moment tensors has also been carried out for material deformation experiments. For example, Shigeishi and Ohtsu [22] utilised moment tensor analysis to characterise microcracking events in unconfined mortar and concrete plates. They determined crack types, orientations and volumes using this method and demonstrated a technique for damage evolution estimation from moment tensor data. AE source analysis by moment tensor inversion has also been applied successfully to other laboratory media, including salt rock [23–25], granite and marble [26].

Whilst a number of source analysis techniques have been proposed for AE laboratory data, the authors are unaware of any studies applying and comparing inversion with other approaches, whilst utilising the same data set. This study compares the application and results of two methods of first motion analysis and source classification, using AE data collected during the triaxial compression of granite in the brittle regime. It is a polarity technique [14] and the 'simplified Green's function moment tensor analysis' [21], which are compared in this study. The former is a simple method for estimating the predominant source movement, based on the mean polarity of the first motions recorded across an array of AE sensors. Whilst this approach is simple and fast, it can only provide limited information about the source type. The latter approach is a moment tensor inversion method that utilises first motion amplitudes to invert for a moment tensor. The tensor can then be decomposed and classified depending on the predominance of its constituent parts. A moment tensor inversion approach has the advantage of providing detailed information about the source mechanism of an event, including the associated degree of volume change, which is of particular use in the application of damage mechanics [26]. Furthermore, eigenvalue analysis of the moment tensor allows the determination of source orientations and opening directions for all source types; information which is not obtained without a moment tensor inversion approach. A more detailed description of the methods used is given in Section 4 (below).

In this study we compare the results of these two techniques using the same data set, in order to test the robustness and values of both an inversion approach and a more simplified method.

3. Experimental technique

In this section, sample selection, characteristics and preparation are discussed. This is followed by a description of the experimental set-up, the data acquisition system and the method of location of acoustic emission hypocentres.

3.1. Sample description

Due to the large number of acoustic emissions produced in laboratory experiments, their classification into specified source mechanisms relies on selecting generalised categories into which, in reality much more complicated, microscale events are placed. Rock types with a significant porosity will exhibit dilatant behaviour, shear localisation and compaction during compressional loading. For the purposes of this study, a low porosity crystalline rock, in this case a granite, was utilised so as to focus primarily on the two former processes. By choosing a crystalline rock with very little pre-existing damage, this study focuses on AE source type evolution from the initiation of the damage process, through the creation of dilatancy, to the onset of localisation and eventual failure. The relatively simple source mechanisms observed in such a scenario provide a suitable data set for comparing source analysis techniques. In a material such as sandstone, with a significant porosity present, pore-collapse type sources become a major mechanism for microscopic deformation. The application of the moment tensor inversion technique

Author's personal copy

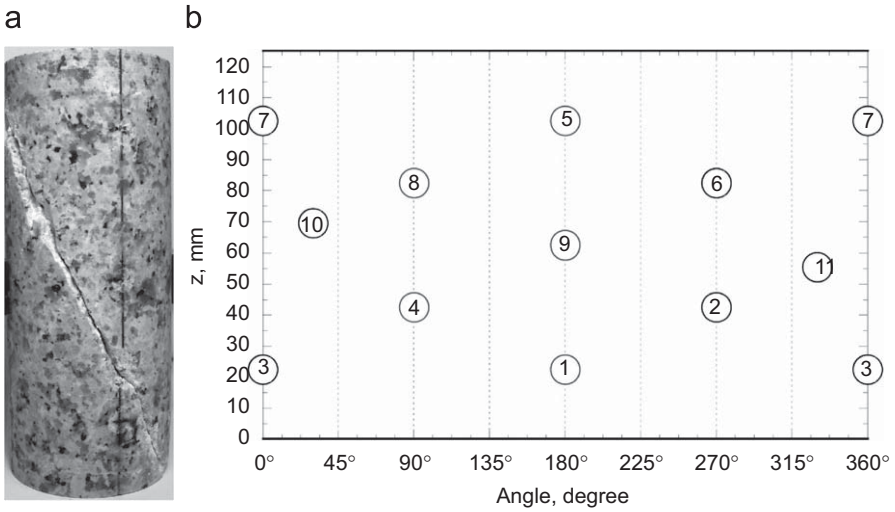

Fig. 1. (a) Aue granite sample after failure and unloading (125 mm height). (b) Projected sample surface showing position of AE sensors during testing. Sensors 1, 4, 5, 8 and 9 were used as transmitters for ultrasonic velocity measurement.

discussed in this paper, to AE from sandstone in compression, will be presented elsewhere.

The rock used in this work is a red granite, sourced from Aue, Erzgebirge, Germany. It is composed of 30% quartz, 40% plagioclase, 20% K feldspar and 10% mica [14]. The grain size within this rock type varies between 0.9 and 1.8 mm, with an average value of 1.3 mm. The uniaxial compressive strength of the Aue granite is in the range of 127–141 MPa [27]. Porosity was measured as 1.3%, and Poisson's ratio was estimated as 0.17. A cylindrical sample was used with a length, l, of 125 mm and diameter, d, of 50 mm, giving a ratio $l/d = 2.5$. The sample failed in a brittle fashion at a confining pressure of 20 MPa, with relatively localised damage. The resulting fault trace was orientated at an angle of approximately 30° from the maximum compressive stress (Fig. 1a).

3.2. Equipment set-up

A servo-operated MTS 4600 kN loading frame (MTS Systems Corporation, 1996) was used to apply the maximum stress to a cylindrical sample of red Aue granite. The surrounding hydraulic oil within the pressure vessel provided a confining pressure of 20 MPa to the sides of the cylinder whilst the sample was protected in a rubber jacket. The loading frame and pressure vessel are shown in Fig. 2. Eleven piezoelectric crystal transducers (PZT) were contained within brass housings with conformably shaped bases, so as to give a tight contact with the sample. These housings were then bonded to the sample surface with epoxy in the arrangement shown in Fig. 1b. The transducers, with a frequency range of 0.1–2 MHz, provided acoustic emission waveforms, which were then subjected to an amplification of 40 dB by Physical Acoustics Corporation preamplifiers. The waveforms were then digitised and recorded by a 16-bit data acquisition system (DaxBox, Prökel GmbH). The amplitude recording threshold was set to ± 300 mV. However, a further, floating threshold was applied during the P-wave arrival time picking procedure, which is described below. Following [28], the rate of acoustic emissions was used as a feedback control for the press, thereby drawing out the length of the failure process and allowing a greater number of the AE to be successfully located, up to and during the post-peak stress phase.

Variations in P-wave velocity were monitored during loading by applying an electrical pulse to three PZTs at minute intervals. The resulting arrival times and amplitudes were then recorded at each sensor in the array, allowing vertical and horizontal velocities to be determined for a number of different regions within the sample. P-wave arrival times of AE waveforms were then picked automatically, using an Akaike information criterion (AIC) based approach [29]. A floating threshold was applied, depending on the local noise level for each particular channel. A more detailed account of the set-up for this experiment, and the onset time picking process, can be found in [9].

Fig. 2. The MTS loading frame and confining pressure vessel used for the triaxial compression of the Aue granite.

3.3. Event location

Source location was based on automatic picking of P-waves for a minimum of eight sensors. After selection of P-wave arrival times and amplitudes, as described in Section 3.2, hypocentre determination was carried out automatically using a procedure based on the downhill simplex algorithm [30], which includes consideration of changes in the anisotropic velocity field. The resulting location precision was estimated at ± 2.5 mm.

Author's personal copy

4. Methodology

After successful location of events was carried out, two different techniques for characterising and classifying sources were applied to the data. The first method used is that of [14], where events are classified according to the polarity of the first motions at each sensor. The second approach involves a full moment tensor inversion, the methodology for which is described by [21]. In this section, a description of both of these approaches is given.

4.1. Polarity technique

The polarity classification method used in this study is described by [14]. Here, the first motion amplitude, A_i, at k sensors, is used to find an average polarity for each event, according to

$$pol = \frac{1}{k}\sum_{i=1}^{k} \mathrm{sign}(A_i), \tag{1}$$

This provides us with an estimate of the net polarity of the volume change at the location of the source. Classification is then carried out within three selected ranges, which are ascribed to the formation of different types of microcracks. AE are described as S-type events (shear) for a polarity between −0.25 and +0.25, T-type (tensile) for $pol < -0.25$, or C-type (collapse) for $pol > +0.25$. Once sources have been classified, the best-fitting double-couple total mechanism can be fitted to the first motion amplitudes for those events identified as shear. Orientations of shear fractures can then be determined from the resulting focal mechanisms [14], as they should correspond to one of the two nodal planes. This assumption (pure double-couple) is analogous to the typical focal mechanism in earthquake seismology, prior to the digital era. For natural tectonic seismicity it is often a very good assumption. However, this is not the case for laboratory or mining-scale induced events.

4.2. Moment tensor inversion technique

Moment tensor inversion has been regularly applied in the field of seismology, since the advent of digital recordings, and allows analysis of the mechanism acting at the source of the earthquake [15,16]. The source is represented as a 3×3 matrix, known as the moment tensor, **M**, which is a function of the orientation and size of the source. Each element in the array represents one of nine force-couples acting at the source. To conserve angular momentum **M** is symmetric and, therefore, contains six independent elements: three tensile or compressional couples along the diagonal, and three shear couples off the diagonal. The scalar moment M_0 gives us the magnitude of the moment tensor and is the product of the shear modulus, μ, rupture area, A, and average scalar slip on the fault, $\bar{u}$:

$$M_0 = \mu \bar{u} A. \tag{2}$$

The full moment tensor describes a range of source types that include shear, tensile, mixed-mode and compaction events. A number of methods have been developed to invert for these elements from seismic waveforms, using arrival times and amplitudes of, generally, several seismic phases.

However, for acoustic emission waveforms the effects of reflections and ringing within the sample often lead to a complicated coda, or tail, to the seismograms, where shear and surface waves/normal modes are not readily distinguishable. Therefore, any moment tensor inversion based on laboratory measurements should, preferably, require only P-wave data; the only reliable phase. If the double-couple approximation holds (i.e. the source is pure or simple shear) then there will be no volumetric change at the source and the trace of **M** will be zero. For macroscopic earthquakes, the volumetric component is rarely distinguishable from zero. However, microstructural analysis of experimentally deformed rock samples, regularly demonstrates that such sources can be much more complicated than most earthquake sources and are often associated with a significant volume change. A great advantage of moment tensor inversion of AE is that it determines a volumetric component, where one exists above the detection limit. Furthermore, unlike some techniques, it can provide information on the orientation of all sources.

Standard elastic wave theory [31] allows us to express the elastic displacement $\mathbf{u}(\mathbf{x},t)$, recorded at position **x** and time t and due to a displacement continuity $\mathbf{b}(\mathbf{y},t)$ at position **y**, as a function of the moment tensor **M**. Let us consider **M** to be the product of the initial discontinuity and the elastic constants of the medium, such that

$$M_{pq} = C_{pqkl} b_k n_1, \tag{3}$$

where **n** is the normal vector, defined positive outward from the surface of the crack. We can then represent the resultant waveform as

$$u_i(\underline{x},t) = G_{ip,q}(\underline{x},\underline{y},t) M_{pq} * S(t), \tag{4}$$

where the product of **M** and the spatial derivative of the associated Green's functions, is convolved with the source-time function $S(t)$. Green's function describes the impulse response of the medium to a spike, measured at location **x** on the sample boundary. In the SiGMA method [21,22,32], only the P-wave part of the full-space Green's function is selected, allowing for a simplification of the problem when applied to an isotropic, homogenous medium. We are then left with an equation for P-wave amplitude, dependent upon **M**, but not upon time:

$$A(\underline{x}) = \frac{C_s \mathrm{Ref}(\underline{t},\underline{r})}{4\pi\rho R v_p^3}(r_1,r_2,r_3)\begin{pmatrix} m_{11} & m_{12} & m_{13} \\ m_{12} & m_{22} & m_{23} \\ m_{13} & m_{23} & m_{33} \end{pmatrix}\begin{pmatrix} r_1 \\ r_2 \\ r_3 \end{pmatrix}, \tag{5}$$

where A is the displacement produced by an AE source (Fig. 3a) at point **y** and recorded at a position, **x**, which is a distance R away, in a direction $\mathbf{r} = (r_1, r_2, r_3)$. It is important to note that in the notation here, **t** is not time but the direction of AE sensor sensitivity, such that $\mathrm{Ref}(\underline{t},\underline{r})$ is the reflection coefficient at the observation surface. In addition, ρ is the density of the medium, v_p is the P-wave velocity and C_s is a calibration coefficient. With observations of P-phase amplitudes from six or more receivers, it is therefore possible to solve for the unique moment tensor elements. Ohtsu [21] argues that, since they are not dependent upon time, the resulting solutions are inherently stable.

Once the moment tensor of a source has been found, decomposition can be carried out using its eigenvalues ($\lambda_{\max}$, λ_{int}, $\lambda_{\min}$), to resolve the double-couple and non-double-couple parts of the source (Fig. 3b). For example [33], the tensor can be split into a double-couple component, an isotropic component (ISO) and a deviatoric or 'compensated linear vector dipole' component (CLVD). In [21] the maximum shear and CLVD components are defined as X and Y, respectively, giving a DC part (X, 0, $-X$) and a CLVD part (Y, $-0.5Y$, $-0.5Y$). This leaves the remaining isotropic part in all directions, Z. The relative proportions of X, Y and Z can then be found by first normalising with respect to the maximum eigenvalue, such that

$$\lambda_{\max}/\lambda_{\max} = 1 = X + Y + Z, \tag{6}$$

and then solving simultaneously with;

$$\lambda_{\mathrm{int}}/\lambda_{\max} = 0 - 0.5Y + Z, \tag{7}$$

$$\lambda_{\min}/\lambda_{\max} = -X - 0.5Y + Z. \tag{8}$$

Author's personal copy

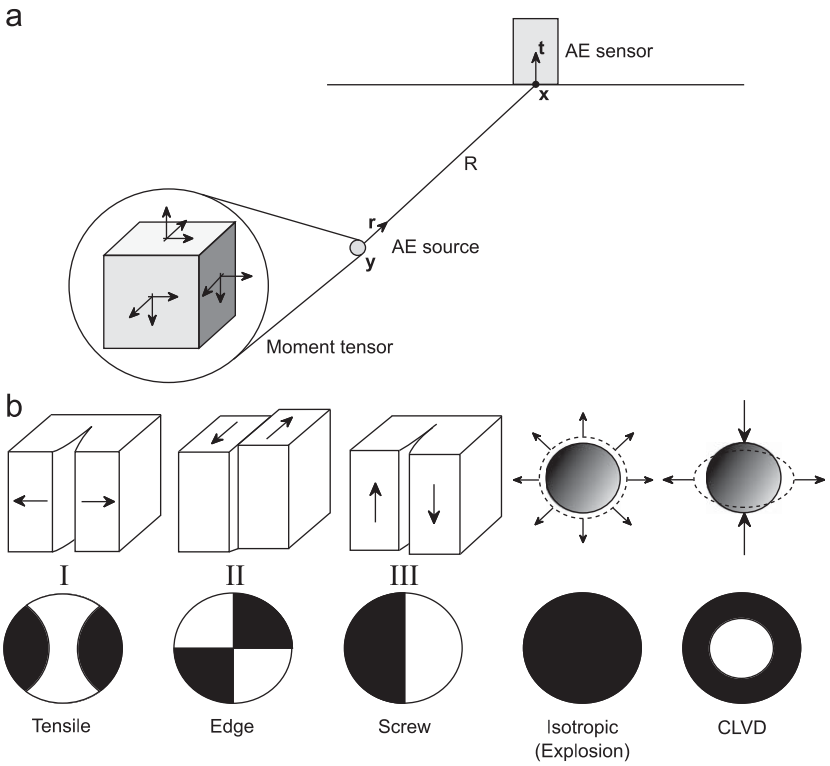

Fig. 3. (a) Source–receiver geometry assumed for the moment tensor inversion. (b) Idealised acoustic emission sources and their associated focal mechanisms.

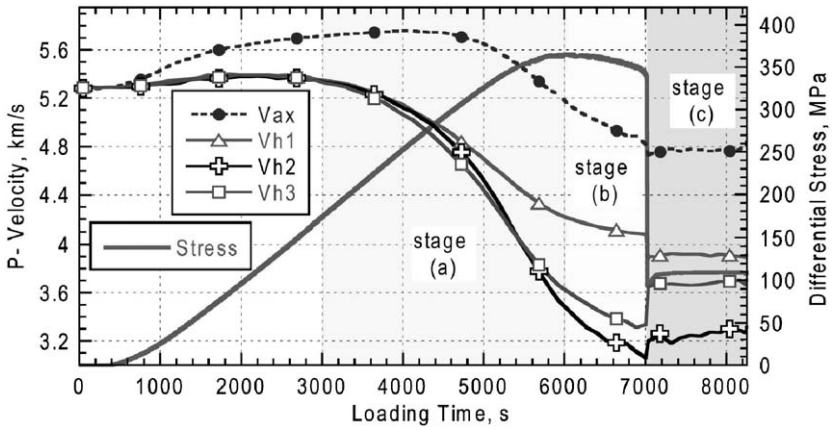

Fig. 4. Differential stress applied to the sample during the course of the experiment. P-wave velocities are also shown for three horizontal zones (V_{h1}, V_{h2}, V_{h3}) and the axial P-wave velocity (V_{ax}). Three stages (a–c) of the loading process are highlighted.

Hence, values of $X=0$, $Y+Z=1$, would represent an entirely tensile source, whilst a purely shear source would lead to $X=1$ and $Y=Z=0$. Sources can then be classified using criterion suggested and tested by [32]; for $X>60\%$ the source is considered to be predominantly shear, for $X<40\%$ it is classified as tensile and for $40\%<X<60\%$ it is termed 'mixed-mode' in nature, having both significant shear and tensile components.

Finally, in this study the trace of the moment tensor was used to find those events leading to a net loss in volume, which are classified as 'collapse' sources. It should, however, be noted when interpreting the results that this, by definition, excludes collapse sources with a significant CLVD component, which lead to no net change in volume. There also remains the possibility of some aseismic component to a source, which cannot be determined. However, the major advantage of the moment tensor technique is that the associated eigenvectors can then be used to obtain crack opening directions for *all* source types. Having the full tensor also allows detailed comparison of the inferred fracture or fault directions with microstructural data, or principal components with applied strain direction.

5. Results

5.1. Spatial progression of fracture

Triaxial compression was carried out on a cylindrical sample of red Aue granite with AE feedback controlling loading rate. The peak differential stress applied during the test was 365 MPa and failure occurred just before 7000 s, along a macroscale fault plane with an orientation of approximately 30° to the maximum principal stress. During this process a very significant increase

Author's personal copy

in the rate of acoustic emissions was observed before failure. Fig. 4 shows the loading curve for the experiment and the variation in the vertical and horizontal P-wave velocities through the sample, V_{ax}, V_{h1}, V_{h2}, V_{h3}, respectively.

Hypocentre locations (Figs. 5 and 6) of large magnitude events, from different time windows during the loading process, show a progressive change from diffuse (stage a) to more localised (stage b) AE-associated damage, concentrated near the eventual

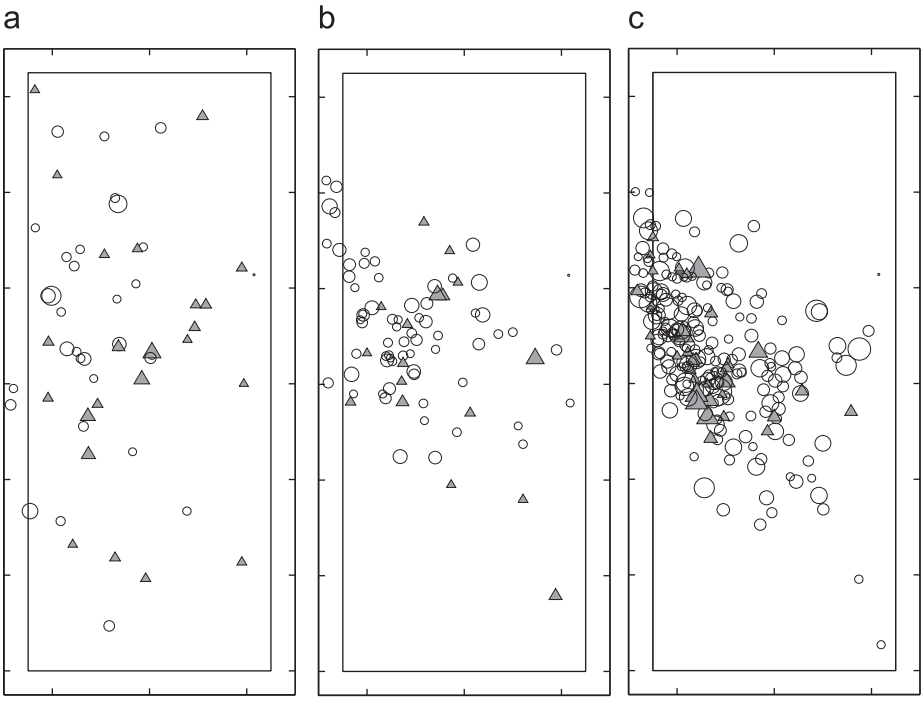

Fig. 5. (a–c) Hypocentre locations for granite sample, Ag72r. Source types are shown as derived by the average polarity technique. Predominantly shear and tensile source types are indicated by open circles and closed triangles, respectively. Symbol size is directly related to event magnitude and small magnitude events are not shown, for clarity. Slices are through the *Y–Z* plane during different time intervals: (a) 3000–6000 s (stage a), (b) 6000–7000 s (stage b) and (c) 7000–8620 s (stage c). The inner rectangle denotes the location and size of the sample.

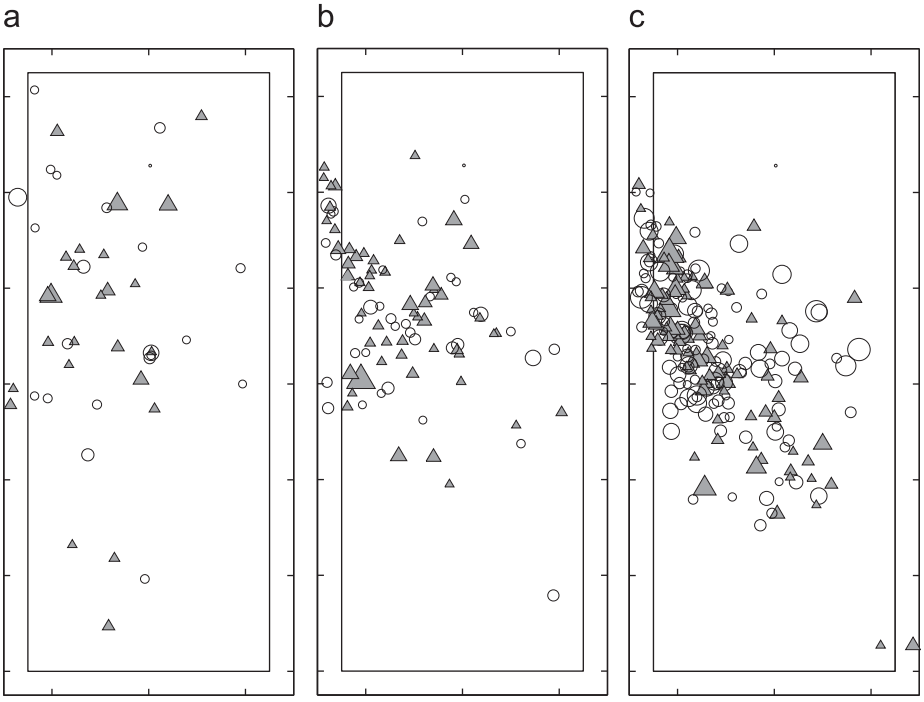

Fig. 6. (a–c) Hypocentre locations for granite sample, Ag72r. Source types are shown as derived by moment tensor inversion. Predominantly shear and tensile source types are indicated by open circles and closed triangles, respectively. Symbol size is directly related to event magnitude and small magnitude events are not shown, for clarity. Slices are through the *Y–Z* plane during different time intervals: (a) 3000–6000 s (stage a), (b) 6000–7000 s (stage b) and (c) 7000–8620 s (stage c). The inner rectangle denotes the location and size of the sample.

Author's personal copy

macroscopic fault plane. Localised fracturing starts at the side of the cylinder, and progresses towards its bottom corner during failure. It should be noted that the uncertainty in source location is clearly visible, as some events are located out with the sample box. The variation in event locations and source types are shown for both the polarity (Fig. 5a–c) and MTI methods (Fig. 6a–c). Both indicate a significantly higher proportion of tensile to shear events in the initial loading phase, followed by an increase in microshearing over time. Only shear and tensile sources are shown here for clarity, but other events were also classified as collapses (both techniques) or mixed-mode sources (MTI only). *t* should also be noted that both techniques indicate a degree of tensile activity within the failure zone, even during the final stages of loading. This is consistent with observations of a dynamic dilation 'suction pump' mechanism for fluid flow observations during slip [34].

5.2. Temporal variation of sources

Due to the large number of AE events produced during loading of the Aue granite, the source mechanisms were analysed in terms of temporal variation in the relative proportions of each mechanism type. After events were classified into different source types, a rolling average of the number of events for each source type was calculated, for every hundred events and with a quarter overlap between windows. As the inversion process requires a number of events to be discarded, due to the lack of a well-fitting solution, the number of events for each source type was normalised by the total number of events within each window. The resulting plots (Figs. 7 and 8), derived from both the polarity and MTI classifications have many similarities. Both techniques clearly show that, during the early stages of acoustic emission (stage a), predominantly distributed tensile motion is the preferred mode of fracture on the microscopic scale. However, close to peak strength (stage b), a change to primarily shear microfracture, localised near the eventual fault plane, is also observed. Similar findings have been reported in a number of other studies involving low porosity materials with little pre-existing damage [9,12].

Figs. 9 and 10 show the similarity between the resulting source type variability determined by both methods, with tensile sources initially dominating, before being superseded by shear sources. The results for the behaviour of shear sources are particularly similar, and this may be a reflection of the simplicity of the source type. In other words, a relatively shear dominant source is more common than a relatively tensile dominant source. In addition,

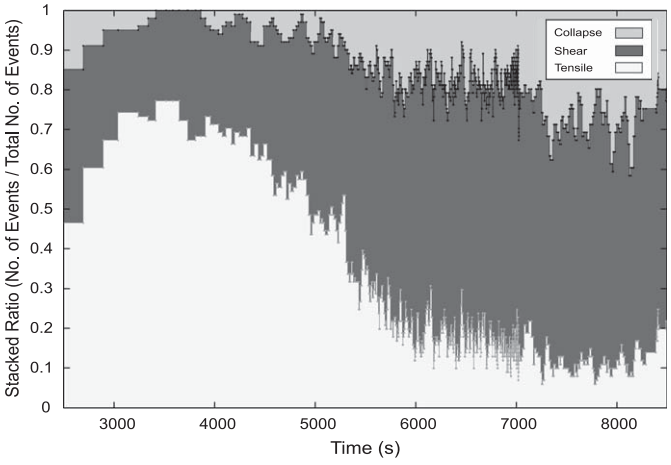

Fig. 7. Temporal variation in source type dominance, as classified by the average polarity method.

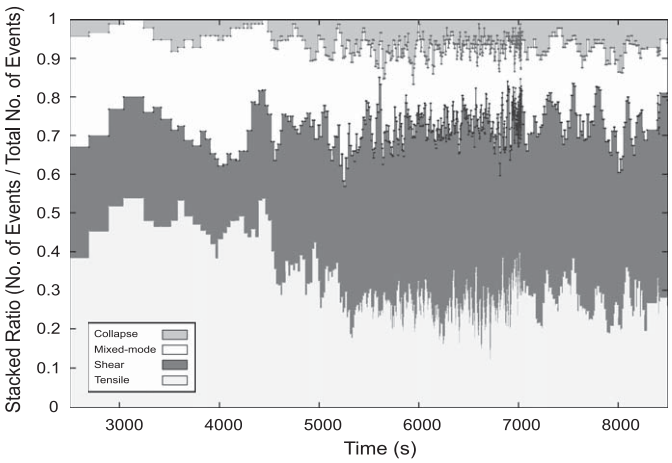

Fig. 8. Temporal variation in source type dominance, as classified using moment tensor inversion.

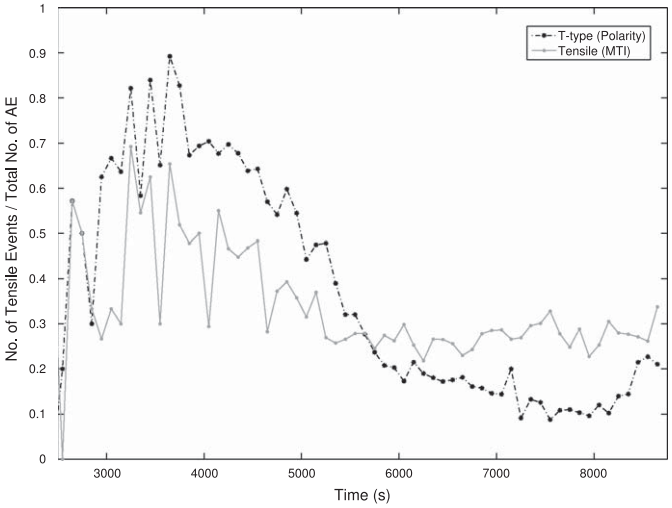

Fig. 9. Variations in the proportion of tensile to total number of AE events. The dotted line and crosses represent results of the average polarity method. The straight line and circles indicate the results for moment tensor inversion.

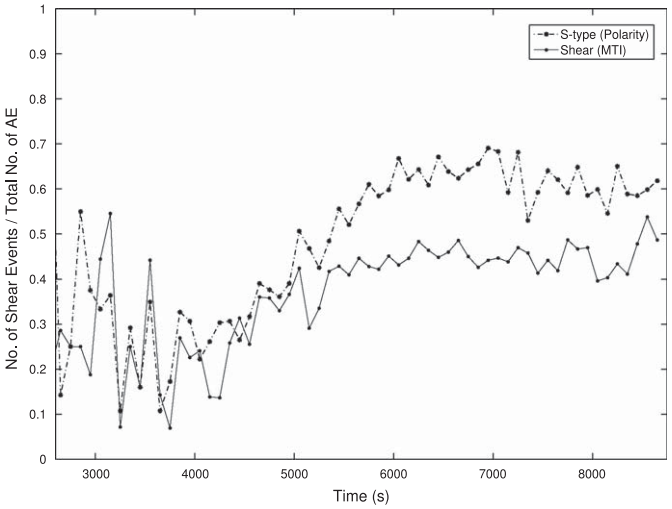

Fig. 10. Variations in the proportion of shear to total number of AE events. The dotted line and crosses represent results of the average polarity method. The straight line and circles indicate the results for moment tensor inversion.

Author's personal copy

the peak in tensile events in Fig. 9 is somewhat smaller for the MTI method, and is attributed to the addition of a 'mixed-mode' source type, with both a significant shear and tensile component. Although the gradient in the variation in MTI tensile events is shallower, the general trends are still very similar in both Figs. 7 and 8. In addition, the percentage of 'collapse' type sources is somewhat smaller in the MTI case, as is discussed below (Section 6.1).

6. Discussion

6.1. Physical mechanisms

Whilst we can separate sources into different classes, using either of the techniques described in this paper, we must also consider the physical mechanisms that generate such signals before attempting to utilise the results. In the case of the average polarity technique, we must be aware that we cannot necessarily, for example, differentiate between a shear source with no tensile component and a shear with a small tensile component. Equally, C-type events that are described as 'collapse' mechanisms are sources containing a predominant collapse component, yet they will also require shearing between grains to be physically achievable in reality. Conversely, the moment tensor technique allows those events with an implosive net volume change to be identified as collapse sources, by using the trace of **M**. As a consequence, we would expect the average polarity technique to classify somewhat different proportions of event types. Additionally, the presence of a third class of source, the mixed-mode type, in the MTI method must reduce the percentage of shear or tensile sources that are identified. This illustrates the advantages of the full moment tensor technique for discriminating in more detail between competing microstructural processes.

6.2. Comparison of the two techniques

The results of this study are encouraging for the field of AE source analysis. When applying two dissimilar techniques to an AE laboratory data set, we see a concurrent set of results from both methods. For large datasets, finding the average polarity of events provide a quick and simple method to analyse sources, demonstrating similar results, albeit less informative results, to the full moment tensor inversion. Unlike the polarity technique of [14], the SiGMA approach may not always produce a solution, as it is more sensitive to issues such as the uncertainty in source location. This uncertainty is of the order of ± 2.5 mm, meaning that it is possible for an event near the sample edge to be located out with the cylinder. However, where a solution is achievable, MTI provides a greater degree of information about the source involved, such as orientations of non-DC events and a full description of the source in terms of its six independent force-couples. In addition, moment tensors provide a description of the volumetric change at the source and can be used to sum up AE-associated damage within the rock, during the loading process [22,26]. Such an approach is clearly a powerful tool when investigating damage progression, in terms of the characteristics, organisation and evolution of microcracking.

One of the major challenges within this field is that of processing increasing amounts of data. In order to overcome this during analysis, a wide range of sources with a spectrum of different mechanism components must be reduced to a small number of source types, by placing them into a number of broad categories. The tendency is to consider them as specific and distinct mechanisms, whereas the reality is closer to a continuum of source types, which are placed in certain classification 'bins', associated with common behavioural elements. This should always be considered when using such an approach, particularly when comparing data from distinctly different materials. Further work into the nature of such sources in different media and under different laboratory conditions would help to elucidate any differences.

7. Conclusions

Temporal and spatial changes in acoustic emissions in rock deformation experiments can elucidate the processes that produce microseismic events in the earth, such as those observed in mining structures and hydrocarbons reservoirs. In order to properly understand the evolution of these changes, the micro-scale mechanisms involved must also be considered. This can, in part, be done by analysing experimentally produced AE sources. A number of techniques have been applied in this way, but with very little comparison between methods. In this study, two different methods were applied to the same data set in order to make such a comparison: one based upon polarity of first motions, the other involving a moment tensor inversion from the amplitudes of the first motions.

Sources were located, analysed, classified and their varying proportions plotted against time. Whilst the categories that sources were sorted into, for each technique, are somewhat different in their meaning, the results are still encouragingly similar. Both indicate that for this data set, produced during the triaxial compression of a granite, tensile sources dominate during the early stages of loading, but are superseded by shear sources prior to failure. It is important to note that such behaviour is only expected in materials with a low porosity and no pre-exisiting crack fabric. The results from this study suggest that both the average polarity and SiGMA methods provide useful information about the characteristics of AE sources and, hence, the associated damage within a deforming rock. We conclude that source analysis of acoustic emissions, and moment tensor inversion in particular, show significant potential for characterising and elucidating the processes involved in brittle damage in laboratory rock fracture tests.

Acknowledgements

This work was funded by the National Environment Research Council, award no. NER/S/S/2005/13745. We thank Mitsuhiro Shigeishi and Masayasu Ohtsu for granting us access to their inversion code, SiGMA. We also thank Sergio Vinciguerra and an anonymous reviewer for their constructive comments and suggestions on an earlier version of this manuscript.

References

[1] Meredith PG, Main IG, Jones C. Temporal variations in seismicity during quasi-static and dynamic rock failure. Tectonophysics 1990;175:249–68.
[2] Scholz CH. The frequency–magnitude relation of microfracturing in rock and its relation to earthquakes. Bull Seismol Soc Am 1968;58(1):399–415.
[3] Hirata T. Omori's power law aftershock sequences of microfracturing in rock fracture experiment. J Geophys Res 1987;92(B7):6215–21.
[4] Lei X. How do asperities fracture? An experimental study of unbroken asperities. Earth Planet Sci Lett 2003;213:347–59.
[5] Benson PM, Vinciguerra S, Meredith PG, Young RP. Laboratory simulation of volcano seismicity. Science 2008;322:249–52.
[6] Burlini L, Vinciguerra S, Di Toro G, De Natale G, Meredith P, Burg JP. Seismicity preceding volcanic eruption: new experimental insights. Geology 2007;35(2):183–6.
[7] Katz O, Reches Z. Microfracturing, damage, and failure of brittle granites. J Geophys Res 2004;109:B01206.

Author's personal copy

[8] Hadley K. Comparison of calculated and observed crack densities and seismic velocities in westerly granite. J Geophys Res 1976;81(20): 3484–94.
[9] Stanchits S, Vinciguerra S, Dresen G. Ultrasonic velocities, acoustic emission characteristics and crack damage of basalt and granite. Pure Appl Geophys 2006;163:974–93.
[10] Lockner D. The role of acoustic emission in the study of rock fracture. Int J Rock Mech Min Sci Geomech Abstr 1993;30(7):883–99.
[11] Ohnaka M, Mogi K. Frequency characteristics of acoustic emission in rocks under uniaxial compression and its relation to the fracturing process to failure. J Geophys Res 1982;87(B5):3873–84.
[12] Reches Z, Lockner DA. Nucleation and growth of faults in brittle rocks. J Geophys Res 1994;99(B9):18,159–73.
[13] Lei X, Kusunose K, Rao MVMS, Nishizawa O, Satoh T. Quasi-static fault growth and cracking in homogeneous brittle rock under triaxial compression using acoustic emission monitoring. J Geophys Res 2000;105(B3): 6127–39.
[14] Zang A, Wagner C, Stanchits S, Dresen G, Andresen R, Haidekker MA. Source analysis of acoustic emissions in Aue granite cores under symmetric and asymmetric compressive loads. Geophys J Int 1998;135:1113–30.
[15] Dziewonski AM, Chou T-A, Woodhouse JH. Determination of earthquake source parameters from waveform data for studies of global and regional seismicity. J Geophys Res 1981;86(B4):2825–52.
[16] Frohlich C. Characteristics of well-determined non-double-couple earthquakes in the Harvard CMT catalog. Phys Earth Planet Inter 1995;91: 213–28.
[17] Julian BR. Evidence for dyke intrusion earthquake mechanisms near Long Valley Caldera, California. Nature 1983;303:323–5.
[18] Nettles M, Ekstrom G. Faulting mechanism of anomalous earthquakes near Bardarbunga Volcano, Iceland. J Geophys Res 1998;103(B8):17973–83.
[19] Feignier B, Young RP. Moment tensor inversion of induced microseismic events: evidence of non-shear failures in the $-4<M<-2$ moment magnitude range. Geophys Res Lett 1992;19(14):1503–6.
[20] McGarr A. Moment tensors of ten Witwatersrand mine tremors. Pure Appl Geophys 1992;139(3/4):781–800.
[21] Ohtsu M. Simplified moment tensor analysis and unified decomposition of acoustic emission source: application to in situ hydrofracture test. J Geophys Res 1991;96(B4):6211–21.
[22] Shigeishi M, Ohtsu M. Acoustic emission moment tensor analysis: development for crack identification in concrete materials. Constr Build Mater 2001;15:311–9.
[23] Dahm T, Manthei G, Eisenblatter J. Automated moment tensor inversion to estimate source mechanisms of hydraulically induced micro-seismicity in salt rock. Tectonophysics 1999;306:1–17.
[24] Manthei G. Characterization of acoustic emission sources in a rock salt specimen under triaxial compression. Bull Seismol Soc Am 2005;95(5): 1674–700.
[25] Manthei G, Eisenblatter J, Dahm T. Moment tensor evaluation of acoustic emission sources in salt rock. Constr Build Mater 2001;15:297–309.
[26] Chang S-H, Lee C-I. Estimation of cracking and damage mechanisms in rock under triaxial compression by moment tensor analysis of acoustic emission. Int J Rock Mech Min Sci 2004;41:1069–86.
[27] Zang A. Akustische Emissionen beim Sproudbruch von Gestein. Habilitationsschrift, Scientific Technical Report STR97/19, University of Potsdam; 1999.
[28] Lockner DA, Byerlee JD, Kuksenko V, Ponomarev A, Sidorin A. Quasi-static fault growth and shear fracture energy in granite. Nature 1991;350:39–42.
[29] Leonard M, Kennett BLN. Multi-component autoregressive techniques for the analysis of seismograms. Phys Earth Planet Inter 1999;113(1–4):247–63.
[30] Nelder JA, Mead R. A simplex method for function minimization. Comput J 1965;7(4):308–13.
[31] Aki K, Richard PG. Quantitative seismology. Sausalito: University Science Books; 2002.
[32] Ohtsu M. Acoustic emission theory for moment tensor analysis. Res Nondestr Eval 1995;6(3):169–84.
[33] Knopoff L, Randall MJ. The compensated linear-vector dipole: a possible mechanism for deep earthquakes. J Geophys Res 1970;75(26):4957–63.
[34] Grueschow E, Kwon O, Main IG, Rudnicki JW. Observation and modeling of the suction pump effect during rapid dilatant slip. Geophys Res Lett 2003;30(5):1226.